Amidinate, NHC, and Thioamide-based Ligands for the Construction of Luminescent Mono- and Heterobimetallic Transition Metal Complexes: Synthesis, Structure, Luminescence, and Catalytic Applications

Zur Erlangung des akademischen Grades eines

DOKTORS DER NATURWISSENSCHAFTEN

(Dr. rer. nat.)

von der KIT-Fakultät für Chemie und Biowissenschaften

des Karlsruher Instituts für Technologie (KIT)

genehmigte

DISSERTATION

von

M.Sc. Shubham

1. Referent: Prof. Dr. Peter W. Roesky
2. Referentin: Prof. Dr. Silke Behrens

Tag der mündlichen Prüfung: 18.07.2025

This document is licensed under a Creative Commons Attribution 4.0 International License (CC BY 4.0): https://creativecommons.org/licenses/by/4.0/deed.en

I hereby solemnly declare that I have authored the present work independently. I have not used sources other than those specified and cited in the bibliography. This thesis has not been submitted to any other university.

The presented work was carried out in the period from 15.11.2021 to 04.06.2025 at the Institute for Inorganic Chemistry of Karlsruhe Institute of Technology (KIT) under the supervision of Prof. Dr. Peter W. Roesky.

Table of Contents

1. Introduction 1

1.1 Group 11 elements: copper, silver and gold 1

1.1.1 Background 1

1.1.2 Physical and chemical properties 4

1.1.3 Relativistic effects 11

1.1.4 Metallophilic interactions 13

1.2 Photoluminescence 16

1.3 Ligand systems 20

1.3.1 Amidinate ligands 20

1.3.2 *N*-heterocyclic carbene (NHC) based ligands 24

1.3.3 Thioamidinate ligands 29

2. Objectives 31

3. Results and discussion 32

3.1 Luminescent Cu(I)–Au(I) heterobimetallic complexes: Selective coordination within a phosphine acetylide amidinate ligand framework 32

3.1.1 Introduction 32

3.1.2 Synthesis and characterization of Cu(I)–Au(I) complexes 34

3.1.3 Photophysical Studies 44

3.2 Synthesis and characterization of heterobimetallic Cu(I)–Rh(I) and Cu(I)–Ir(I) complexes: Photophysical studies and catalytic application 49

3.2.1 Introduction 49

3.2.2 Synthesis and characterization of Cu(I)–Rh(I) and Cu(I)–Ir(I) complexes 51

3.2.3 Catalytic applications 59

3.2.4 Photophysical properties 63

3.3 Synthesis and photophysical properties of coumarin substituted NHC-Au(I) complexes 66

3.3.1 Introduction 66

3.3.2 Synthesis and characterization of NHC-Au(I) complexes 68

3.3.3 Photophysical properties 83

3.4 Synthesis and photophysical properties of coumarin substituted NHC-transition metal complexes 91

3.4.1 Introduction 91

3.4.2 Synthesis and characterization of NHC-transition metal complexes 93

3.4.3 Photophysical properties 101

3.5 Thioamidinate zinc and lanthanide complexes 105

3.5.1 Introduction 105

3.5.2 Synthesis and characterization of Zn(II) complexes 106
3.5.3 Synthesis and characterization of Sm(III) and Y(III) complexes 112
3.5.4 Photophysical studies 115
4. Experimental section 118
4.1 General methods 118
4.2 Syntheses and analytical data 119
4.2.1 [{$Ph_2PC{\equiv}CC(NDipp)_2$}$Li(thf)_3$] (1): 119
4.2.2 [{$Ph_2PC{\equiv}CC(NDipp)_2$}$_2Cu_2$] (2): 120
4.2.3 [{$Ph_2PC{\equiv}CC(NDipp)_2$}$_2Au_2$] (3): 121
4.2.4 [{(AuCl)$Ph_2PC{\equiv}CC(NDipp)_2$}$_2Cu_2$] (5): 122
4.2.5 [{(AuC_6F_5)$Ph_2PC{\equiv}CC(NDipp)_2$}$_2Cu_2$] (6): 123
4.2.6 [{(AuBr)$Ph_2PC{\equiv}CC(NDipp)_2$}$_2Cu_2$] (7): 125
4.2.7 [{(AuI)$Ph_2PC{\equiv}CC(NDipp)_2$}$_2Cu_2$] (8): 126
4.2.8 [{(AuMes)$Ph_2PC{\equiv}CC(NDipp)_2$}$_2Cu_2$] (9): 127
4.2.9 [{(Rh(cod)Cl)$Ph_2PC{\equiv}CC(NDipp)_2$}$_2Cu_2$] (10): 128
4.2.10 [{(Ir(cod)Cl)$Ph_2PC{\equiv}CC(NDipp)_2$}$_2Cu_2$] (11): 129
4.2.11 [$Ph_2PC{\equiv}CC(NDipp)(NHDipp)]_2$ (14): 131
4.2.12 [(Rh(cod)Cl)$Ph_2PC{\equiv}CC(NDipp)(NHDipp)]_2$ (15): 132
4.2.13 [(Ir(cod)Cl)$Ph_2PC{\equiv}CC(NDipp)(NHDipp)]_2$ (16): 133
4.2.14 [Coum-Mes-Im][Br] (18): 134
4.2.15 [Coum-Mes-NHC-AuCl] (19): 135
4.2.16 [Coum-Mes-NHC-AuBr] (20): 136
4.2.17 [Coum-Mes-NHC-AuC_6F_5] (21): 137
4.2.18 [Coum-Mes-NHC-AuMes] (22): 138
4.2.19 [(Coum-Mes-NHC)$_2$Au][OTf] (23): 139
4.2.20 [Coum-Mes-NHC-Au-CCPh] (24): 140
4.2.21 [Coum-Mes-NHC-Au]$_2$ (25): 142
4.2.22 [(Coum-Mes-NHC)$_2AuI_2$][I_3] (26): 143
4.2.23 [Coum-Mes-NHC-Rh(cod)Cl] (27): 144
4.2.24 [Coum-Mes-NHC-Ir(cod)Cl] (28): 145
4.2.25 [(Coum-Mes-NHC)$_2PtCl_2$] (29): 145
4.2.26 [Coum-Mes-NHC-Pd(allyl)Cl] (30): 146
4.2.27 [Coum-Mes-NHC-Ru(*p*-cymene)Cl_2] (31): 148
4.2.28 [L^{Ph}thioamide] (32): 149
4.2.29 [(L^{Ph}thioamidinate)$_2$Zn(TMEDA)] (33): 150
4.2.30 [(L^{Ph}thioamidinate)$_4Zn_2$] (34): 151

4.2.31 [(L^{Ph}thioamidinate)(ATI)Zn] (35): 151
4.2.32 [(L^{Ph}thioamidinate)$_6Sm_2$] (36): 152
4.2.33 [(L^{Ph}thioamidinate)$_3$Y] (37): 153
5. Crystal structure measurements 155
5.1 Data collection and refinement 155
5.2 Crystal data 156
5.2.1 [{$Ph_2PC{\equiv}CC(NDipp)_2$}Li(thf)$_3$] (1) 156
5.2.2 [{$Ph_2PC{\equiv}CC(NDipp)_2$}$_2Au_2$] (3) 157
5.2.3 [{(AuCl)$Ph_2PC{\equiv}CC(NDipp)_2$}$_2Cu_2$] (5) 158
5.2.4 [{(AuC_6F_5)$Ph_2PC{\equiv}CC(NDipp)_2$}$_2Cu_2$] (6) 159
5.2.5 [{(AuBr)$Ph_2PC{\equiv}CC(NDipp)_2$}$_2Cu_2$] (7) 160
5.2.6 [{(AuI)$Ph_2PC{\equiv}CC(NDipp)_2$}$_2Cu_2$] (8) 161
5.2.7 [{(AuMes)$Ph_2PC{\equiv}CC(NDipp)_2$}$_2Cu_2$] (9) 162
5.2.8 [{(Rh(cod)Cl)$Ph_2PC{\equiv}CC(NDipp)_2$}$_2Cu_2$] (10) 163
5.2.9 [{(Ir(cod)Cl)$Ph_2PC{\equiv}CC(NDipp)_2$}$_2Cu_2$] (11) 164
5.2.10 [$Ph_2PC{\equiv}CC(NDipp)(NHDipp)]_2$ (14) 165
5.2.11 [(Rh(cod)Cl)$Ph_2PC{\equiv}CC(NDipp)(NHDipp)]_2$ (15) 166
5.2.12 [(Ir(cod)Cl)$Ph_2PC{\equiv}CC(NDipp)(NHDipp)]_2$ (16) 167
5.2.13 [Coum-Mes-NHC-AuCl] (19) 168
5.2.14 [Coum-Mes-NHC-AuBr] (20) 169
5.2.15 [Coum-Mes-NHC-AuMes] (22) 170
5.2.16 [(Coum-Mes-NHC)$_2$Au][OTf] (23) 171
5.2.17 [Coum-Mes-NHC-Au]$_2$ 172
5.2.18 [(Coum-Mes-NHC)$_2AuI_2$][I_3] (26) 173
5.2.19 [Coum-Mes-NHC-Rh(cod)Cl] (27) 174
5.2.20 [Coum-Mes-NHC-Ir(cod)Cl] (28) 175
5.2.21 [(Coum-Mes-NHC)$_2PtCl_2$] (29) 176
5.2.22 [Coum-Mes-NHC-Pd(allyl)Cl] (30) 177
5.2.23 [Coum-Mes-NHC-Ru(*p*-cymene)Cl_2] (31) 178
5.2.24 [L^{Ph}thioamide] (32) 179
5.2.25 [(L^{Ph}thioamidinate)$_2$Zn(TMEDA)] (33) 180
5.2.26 [(L^{Ph}thioamidinate)$_4Zn_2$] (34) 181
5.2.27 [(L^{Ph}thioamidinate)(ATI)Zn] (35) 182
5.2.28 [(L^{Ph}thioamidinate)$_6Sm_2$] (36) 183
5.2.29 [(L^{Ph}thioamidinate)$_3$Y] (37) 184
6. Summary (Zusammenfassung) 185

6.1 Summary 185
6.2 Zusammenfassung 191
7. References 198
8. Appendix 213
8.1 General abbreviations 213
8.2 NMR abbrevitations 215
8.3 IR abbrevitations 215
Curriculum Vitae (CV) 216
Conferences 217
Publications 218
Acknowledgements 219

1. Introduction

1.1 Group 11 elements: copper, silver and gold

1.1.1 Background

The elements of group 11 of the periodic table: copper (Cu), silver (Ag), and gold (Au) are also collectively regarded as coinage metals. These elements have historically been used to mint coins due to the ideal physical and chemical properties such as high resistance to corrosion, high malleability and ductility, good conductivity of heat and electricity, lustrous nature and their stable d^{10} electronic configuration etc. In addition to the method of payment, silver and gold have also been used as jewellery for a long time.[1-4] The name "copper" originates from the Latin term *aes Cyprium* (metal of Cyprus), later shortened to *cuprum*, giving rise to its chemical symbol “Cu”. During the early 1900s, copper demand boomed due to its use in electric telegraphy,[5] steam engines, industrial machinery,[6] and plumbing systems. Due to the low cost (USD 9.81/kg)[7] and good conductivity (5.96×10^7 S/m), it became popular with applications in electric wiring and motors,[8-9] transformers and generators,[10] telecommunication[11] and currently in the renewable energy system.[12] Copper is also widely studied in coordination chemistry, and its complexes have been employed in many fields. There have been some examples of copper complexes recently used in organic light emitting diodes (OLEDs) (Figure 1a).[13] Apart from technological applications, copper complexes are also used as antibiotics, antimicrobials or anticancer agents (Figure 1b).[14-17] Copper is an essential trace element in the human body, with around 80 mg present in adults[18] supporting haemoglobin synthesis, as shown by its effectiveness in treating anaemia.[19]

Compared to copper, silver, which possesses similar physical properties, exhibits greater electrical conductivity (6.30×10^7 S/m). However, due to limited natural abundance, silver possesses relatively high cost (USD 977.33/kg),[20] limited its widespread industrial use. Instead, silver is primarily reserved for high-value or specialized applications, including its roles in photovoltaic systems and medical technology.[21-22] Silver is an integral component in jewellery manufacturing, such as sterling silver (92.5 % silver), due to its luster and corrosion resistance.

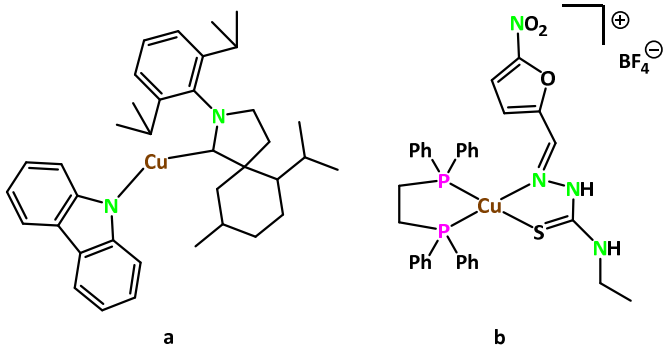

Figure 1: (a) Copper complex used in OLEDs[13] and (b) copper complex exhibiting anticancer properties.[17]

A pivotal moment came in 1868, when Justus von Liebig introduced a groundbreaking method for producing reflective surfaces in his publication *"On Silvering Glass"*.[23] This innovation revolutionized mirror production but also impacted daily life and scientific instrumentation. Even, more than 150 years later, silver remains the material of choice for high-precision optical mirrors, including those used in specialized instruments like NASA's Hubble Space Telescope.[24] Currently, silver is being used for practical applications such as weaving silver threads into the fingertips of gloves, allowing interaction with touchscreens in cold environments where direct skin contact is not feasible.[25] In the medical field, silver-coated wound dressings are used as antiseptic bandages.[26] Silver has been used in amalgam fillings in dentistry, though its mercury content has sparked ongoing safety debates.[27-28] Apart from this, silver complexes are also known to exhibit antimicrobial and antioxidant properties. Figure 2 shows selected examples of silver(I) *N*-heterocyclic carbene (NHC) complexes employed for this purpose.[29-31]

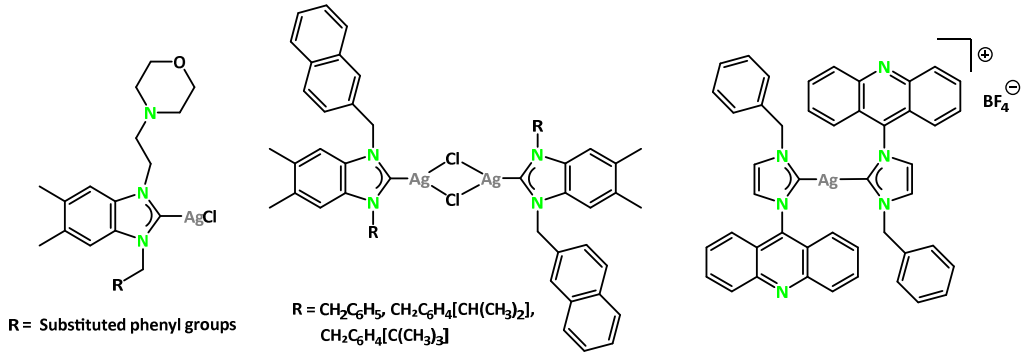

Figure 2: Silver-NHC complexes used as antimicrobial and antioxidant agents.[29-31]

Historically, gold has stood out among the coinage metals not only for its rarity but also for its unique properties. As the heaviest congener among this group, gold captures the imagination with its remarkable scarcity. It is known to exist as the stable nuclide ^{197}Au in nature. Due to its characteristic color and luster, it is widely used in the jewellery industry and is also associated with wealth because of its high cost (USD 100,136.47/kg).[20] In the electronics industry, gold find is used in circuits and circuit boards as it is a soft metal ideal for semiconductors' contact.[32-33] In the elemental form, gold is one of the most malleable and ductile of all metals, enabling the production of gold layers with thicknesses of only 0.0001 mm and 30 m^2 area from just one ounce (28.35 g).[34] By exploiting this property of gold, at the beginning of the 20th century, Ernst Rutherford irradiated a thin foil of gold with alpha particles and observed backscattering of the particles, leading to the development of Rutherford's atomic model.[35] Gold is also utilized in advanced optical technologies, especially in high-performance mirrors and zone plates for UV and infrared spectroscopy.[36-37] A notable example is the James Webb Space Telescope, whose 25 m^2 primary mirror is coated with a thin layer of gold enhancing the telescope's ability to reflect infrared light, making it exceptionally effective for deep-space observation.[38] Gold and its derivatives have attracted significant attention in medical research, particularly in the form of gold nanoparticles, which have been explored for their potential in highly sensitive diagnostic applications, such as detection of HIV.[39-40] Gold organometallic complexes have also been extensively investigated over the past years for their therapeutic potential in treating various ailments.[41-43] Gold(III) complexes adopt a square planar geometry, which is isoelectronic and isostructural to a powerful anticancer platinum complex, making gold(III) complexes a highly desirable synthetic target for medicinal purposes.[41,43-45]

Gold complexes are susceptible to ligand exchange and disproportionation under physiological conditions and therefore require suitable ligands for stabilization. Ligands such as phosphines, thiolates, and NHCs are commonly employed to stabilize linear gold(I) complexes. This is due to favourable ligand properties, including lipophilicity, chemical stability, and strong binding affinity.[41] These characteristics are also provided by porphyrin based ligands effectively stabilizing gold(III) ions and helping to preserve their structure and function in biological environments.[44] Some examples include therapeutic gold-based drugs Solganol (Figure 3a) and Auranofin (Figure 3b), which are landmark compounds approved for

treating rheumatoid arthritis since 1985.[46-47] Beyond its established use, Auranofin has shown promising potential for expanded therapeutic applications, including the treatment of cancer, HIV, neurodegenerative diseases, as well as various parasitic and bacterial infections.[48-49] In addition to medical uses, gold complexes also find application in optoelectronics, where they have been used for the fabrication of OLEDs (Figures 3d and 3e).[50-51]

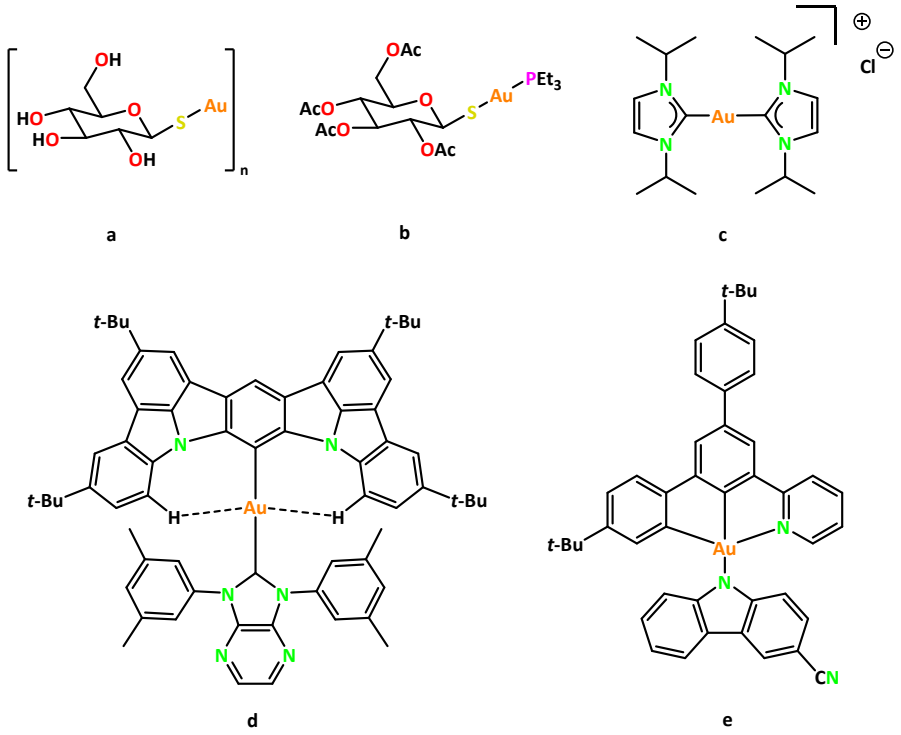

Figure 3: Examples of gold complexes: (a) Solganol,[46] (b) Auranofin,[49] (c) gold(I) NHC complex[46] used as anticancer drug and complexes (d) & (e) used in OLEDs fabrication.[50-51]

1.1.2 Physical and chemical properties

Coinage metals exhibit a high resistance to corrosion stemming from their high positive standard potential. Following a periodic trend, the standard potential increases down the group 11 culminating with gold (E^0 (Au/Au^+) = +1.69 V, E^0 (Au/Au^{3+}) = +1.50 V and E^0 (Au^+/Au^{3+}) = +1.40 V).[52] Another reason for their wide variety of applications is their low melting points (ranging from 960 °C to 1085 °C), the highest electrical conductivity of all metals, high thermal conductivity and very high malleability and ductility.[53] Silver and gold, both more ductile than copper, are unsuitable for applications subjecting them to mechanical stress and must therefore be alloyed with other metals for such applications.[54]

Copper occurs naturally in small native deposits, however, for large-scale industrial purposes, it is primarily extracted from oxide and sulfide ores, with sulfide ores playing the most crucial role in commercial copper production. Among the most important copper-bearing minerals are chalcopyrite ($CuFeS_2$), bornite (Cu_5FeS_4), and chalcocite (Cu_2S). The extraction process begins with smelting metallurgical treatment, where the iron components are separated from the ore. The resulting intermediate product, crude copper, is obtained through a roasting process, in which the sulfide ores are oxidized in air to remove sulfur and other impurities. Then, it undergoes electrolytic purification, where the impure copper is dissolved in an acidic solution and deposits onto cathodes.[55] Chemically, copper exhibits a variety of oxidation states, although it most commonly occurs in the +I (cuprous) and +II (cupric) oxidation states, with the latter being more stable under ambient conditions. Less frequently, copper can also be found in the 0,[56] +III,[57] and even +IV[58] oxidation states, although these are typically observed in more reactive compounds. Recently, there has been an example of a Cu–Mg complex, synthesized by the reaction of an NHC-ligated copper alkoxide with a dimeric magnesium(I) compound, where copper exists in the -I oxidation state (cupride anion) (Figure 4a).[59] The Cu–Mg bond acts as a source of the cupride anion, enabling the transfer of the NHC-copper fragment to electrophilic elements across the *s*-, *p*-, and *d*-block elements of the periodic table. A complex with the copper in the formal oxidation state of zero was successfully obtained in 2014 by utilizing cyclic alkyl(amino)carbene (CAAC) ligands (Figure 4b).[60] The CAAC ligands are known for their ability to form robust bonds with metal centers and possess strong π-accepting capabilities which can stabilize an electron-rich Cu(0) center and prevent it from precipitating as a metal. The two-coordinate Cu(0) species can be prepared either by reducing a Cu(I) cationic complex using metallic sodium or by treating $CuCl_2$ with potassium graphite (KC_8) in the presence of a CAAC ligand, enabling the stabilization and isolation of the low-valent copper center.

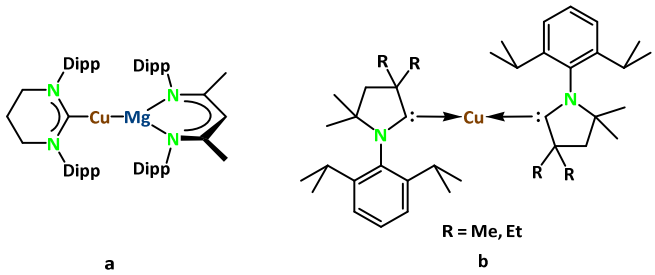

Figure 4: Examples of copper in (a) -I[59] and (b) 0[60] oxidation states.

In coordination chemistry, Cu(I) ions often adopt a coordination number of four, but three- and two-coordinate geometries are also known, depending on the ligand environment and the specific chemical context.[61-63] Although the +III oxidation state of copper is relatively rare; it has been increasingly reported in recent years.[57,64-65] This oxidation state is particularly stabilized by chelating ligand systems that incorporate cyclic NHCs or pyridine-based frameworks. In a study in 2020, Meyer *et al.* successfully isolated a series of copper complexes in +I, +II, and +III oxidation states through a stepwise oxidation process starting from a Cu(I) precursor (Figure 5).[61] Lastly, copper in the +IV oxidation state is extremely rare and has only been stabilized under high pressure conditions. One example includes the octahedral complex $Cs_2[CuF_6]$ reported by Hoppe *et al.* in 1973, which is formed through high-pressure fluorination. Additionally, copper(IV) species can be realized in certain perovskite structures when subjected to high oxygen pressure.[66-68]

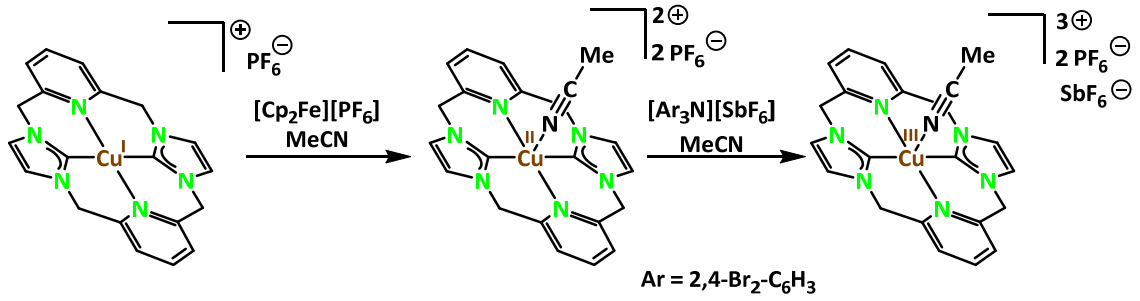

Figure 5: Systematic oxidation of a copper(I) ion in a pyridyl-NHC ligand system.[61]

The next heavier congener of group 11, silver, is found in nature both in its native metallic form and more commonly as part of sulfide mineral ore, acanthite (Ag_2S).[69] To extract raw silver, a widely used industrial method is cyanide leaching, where the metal is selectively dissolved from the ore using a cyanide solution.[70] The dissolved silver is then recovered and purified through electrochemical processes, yielding high-purity silver. Chemically, silver exhibits a range of oxidation states, spanning from +I to +IV, although the +I oxidation state is by far the most common and stable, unlike copper. Notably, silver also forms low-valent compounds with oxidation states below +I, such as silver subfluoride (Ag_2F), which exemplifies its ability to adopt unusual bonding environments in specific chemical contexts.[71] The monovalent silver cation usually prefers a linear or tetrahedral geometry[72] but there are a few examples where they exist in the trigonal planar [73] and octahedral geometry as well.[74] In 2007, Tiekink *et al.* reported an example of a silver(I) complex which comprises of a

dinuclear dication, with each Ag ion in an approximate T-shaped AgN_3 geometry (Figure 6a).[75] Another T-shaped coordination geometry around silver(I) was reported by Fernandéz and Bezuidenhout *et al.* by using carbazole-based CNC ligand (Figure 6b).[73]

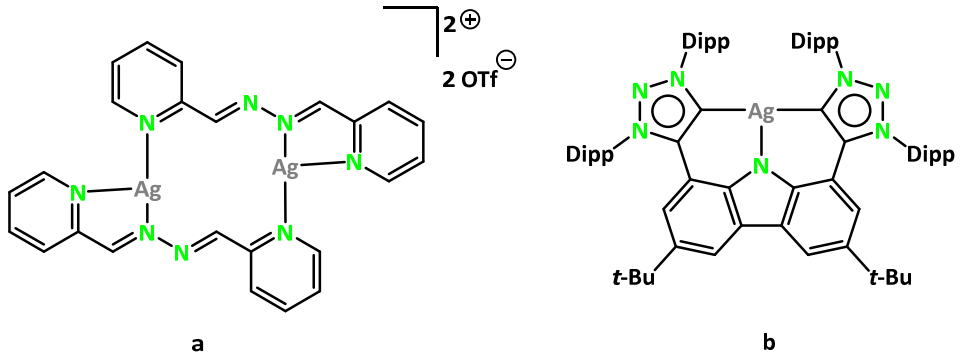

Figure 6: Examples of silver(I) complexes with T-shaped geometry: (a) a cationic complex and (b) a complex with carbazole-based CNC ligand.[73,75]

The divalent silver compounds are commonly found, as in the case of the lighter homologue copper(II), in a square planar coordination environment.[76] Rath and coworkers succeeded in the synthesis of a dinuclear silver(II)-complex using bridging porphyrins (Figure 7).[77] By oxidation of the complex, they were able to initially obtain the mixed-valent Ag(II)/Ag(III) complex and finally isolated the Ag(III)/Ag(III) complex, featuring an attractive d^8-d^8 interaction of the two Ag(III) centers.

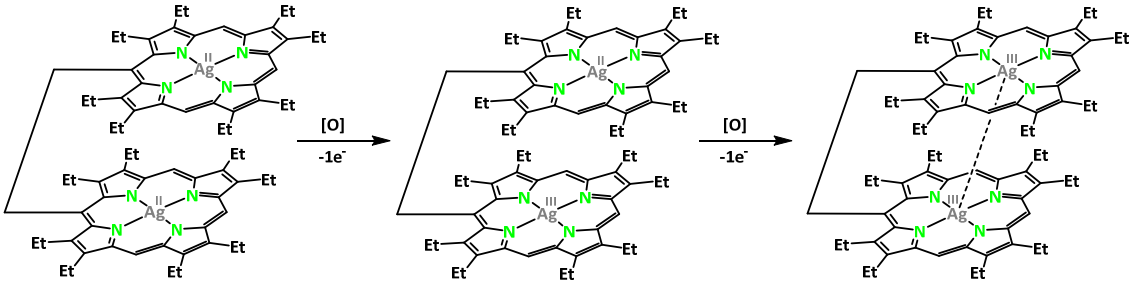

Figure 7: Stepwise oxidation of porphyrin-ligated silver cations.[77]

Gold occurs in nature mainly in the native state in the form of nuggets or grains, in rocks, veins, and alluvial deposits.[78] It also occurs in the form of alloys with silver (electrum), with other metals like copper[79] and palladium,[80-81] and mineral inclusions such as within pyrite (FeS_2).[82] Common extraction processes of gold include amalgamation or cyanide leaching.[70] The obtained gold is further purified electrochemically to isolate pure gold.

Although gold possesses the highest standard electrode potential among the coinage metals, it also displays the most diverse and versatile redox chemistry. In addition to its elemental metallic state, gold commonly exists in the +I and +III oxidation states, which are considered the most thermodynamically stable ones, unlike its lower congeners copper and silver.[72] The Au(I) cation, with its electron configuration of [Xe]4f^{14}5d^{10}, has a closed-shell valence structure, making it particularly stable and it favours a linear coordination geometry, typically resulting in complexes that exhibit 14 valence electrons. This structural preference can be understood through the lens of hybridization theory. One of the key factors influencing gold's bonding behavior is the presence of strong relativistic effects, which become especially significant for heavier elements. These effects lead to a substantial energy separation between the 6*s* and 6*p* orbitals, making it energetically favourable for hybrid orbitals to retain a high degree of *s*-character. As a result, *sp* and possibly *sd* hybridizations are favoured in Au(I) complexes, which directly contribute to the formation of the characteristic linear geometries with 14 valence electrons.[83] Despite the preference for linear coordination, there are also several examples of trigonal planar coordination environments for Au(I) cations in the literature. In 1993, Winpenny *et al.* synthesized a cationic trigonal planar gold(I) complex using a tripod-like tris(2-(diphenylphosphino)ethyl)amine (NP_3) ligand (Figure 8a).[84] Later in 2007, our group also reported Au(I) complexes in trigonal planar geometry using aminotroponiminate ligands (Figure 8b).[85] The group of Hey-Hawkins reported a cationic Au(I) trigonal planar complex using a redox-active tris-(ferrocenyl)triazine based tris-phosphane ligand (Figure 8c).[86]

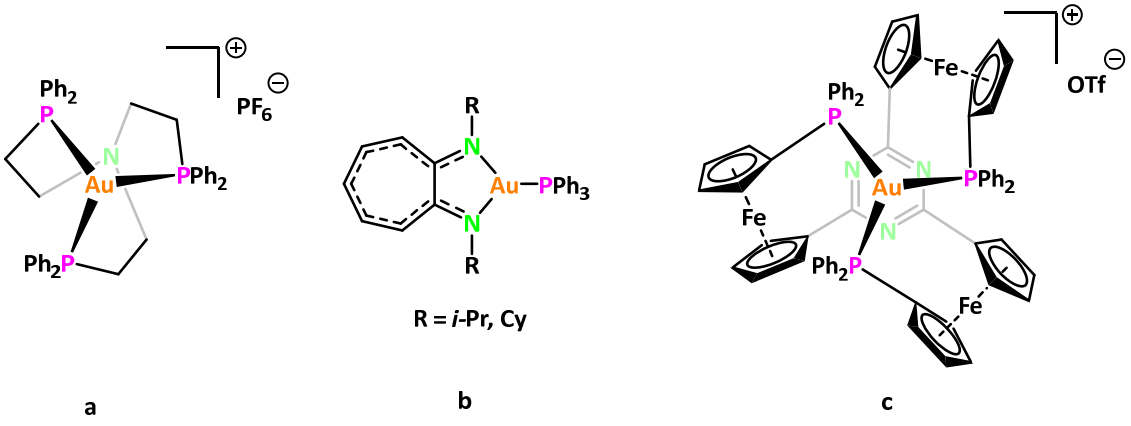

Figure 8: Examples of trigonal planar Au(I) complexes.[84-86]

In addition to the +I and +III oxidation states, -I (CsAu, $Au(NH_3)^-$ in liq. NH_3),[87] 0 (clusters),[88] +II ($[Au(S_2C_2(CN)_2)]_2^{2-}$)[89] and +V ($AuF_5$)[90] oxidation states are also known for gold. Over the past years, molecular gold(0) compounds have attracted significant attention due to their unique electronic properties and potential applications in catalysis.[91] However, the synthesis and isolation of these compounds have posed a notable challenge and difficulties lie in the instability of gold in the zero oxidation state, due to its tendency to agglomerate or form clusters.[92-93] This aggregation often leads to the spontaneous formation of gold nanoparticles, rather than the desired discrete molecular species.[94] As a result, the synthesis of gold(0) complexes requires carefully controlled conditions and the use of stabilizing ligands. In 2012, Sadighi and colleagues reported a mixed-valent Au(I)/Au(0) cluster (Figure 9a), which is stabilized by the coordination of three NHC ligands. This unique gold cluster exhibits electronic characteristics that are isolobal to the $[H_3]^+$ ion. The presence of the NHC ligands plays a crucial role in stabilizing the mixed-valent system, preventing decomposition and enabling the isolation of the gold(0) species.[95] Later, in 2013, CAAC ligands have proven to be highly effective for the successful isolation of molecular gold complexes. These ligands offer both strong σ-donation and π-accepting capabilities, which contribute significantly to the stabilization of low-valent gold species. The synthetic strategies developed by Bertrand and co-workers have enabled the preparation of such complexes. The CAAC ligands used to stabilize copper in the zero oxidation state were also employed to access mononuclear and dinuclear gold complexes in the zero oxidation state (Figures 9b and 9c).[96]

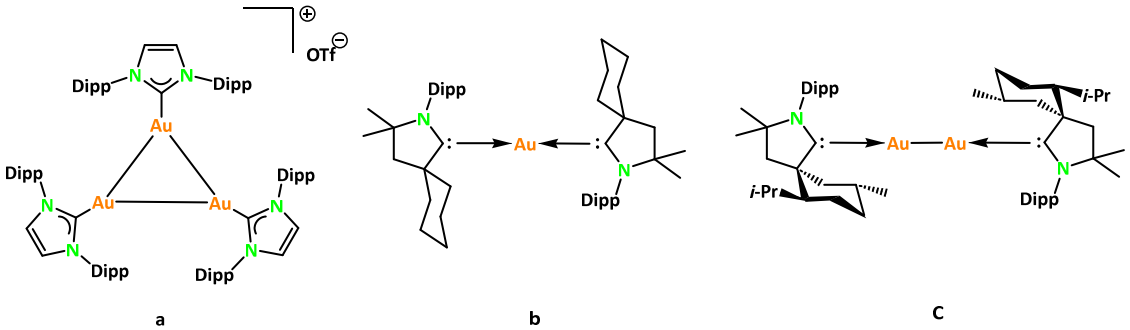

Figure 9: Structures of (a) trinuclear mixed-valent Au(I)/Au(0) cluster, (b) CAAC stabilized Au(0) mononuclear complex and (c) dinuclear Au(0) complex.[95-96]

The +II oxidation state of gold remains rare and challenging to isolate, primarily due to its inherent tendency to undergo disproportionation into the more thermodynamically stable +I

and +III oxidation states. As a result, only a handful of studies have successfully reported well-characterized Au(II) complexes. One of the earliest examples of a gold(II) complex was described in 1990 by Schröder *et al.*, where gold was stabilized in an octahedral coordination environment by two bis(1,4,7-trithiacyclononane) ligands (Figure 10a).[97] This was later followed by the discovery of the first xenon-gold(II) compound, $[AuXe_4]^{2+}([Sb_2F_{11}]^-)_2$, reported by Seppelt and Seidl in 2000, which further demonstrated the possibility of stabilizing Au(II) under specific conditions (Figure 10b).[98] In 2017, Heinze *et al.* have shown that porphyrin ligands, due to their rigid, planar structure and electron-donating capabilities, are also capable of stabilizing gold in the +II oxidation state, offering a promising platform for the design of structurally well-defined Au(II) complexes (Figure 10c).[99]

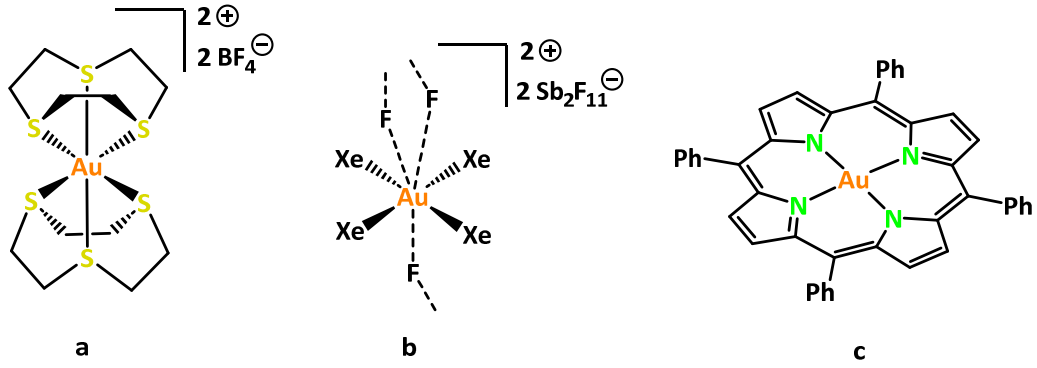

Figure 10: Examples of gold complexes in the +II oxidation state.[97-99]

Gold, in addition to its commonly observed positive oxidation states, is also notable for its rare but chemically interesting negative oxidation state of -I. This unusual state arises from gold's exceptionally high electron affinity, which allows it to accept electrons. The formation of gold(-I) species typically requires the use of strong reducing agents, such as cesium metal.[87] While the number of organometallic complexes featuring gold in a formally negative oxidation state is still quite limited. One notable contribution came in 2016, when Kinjo and co-workers published a study on the synthesis of a 1,2,3-triazaborol-3-yl gold complex.[100] In this compound, the electronegativity difference between the gold and boron atoms gives rise to a highly polarized bond, in the form of an $Au^{\delta-}$–$B^{\delta+}$ interaction. Despite this polarization and the formal negative charge on gold, the gold center does not exhibit classical nucleophilic behavior in this particular system. In contrast, an exceptional breakthrough was reported in 2019 by Goicoechea, Aldridge, and collaborators, where they isolated the first gold complex

that acts as a genuine nucleophile. This work was based on the use of the NON pincer-type ligand 4,5-bis(2,6-diisopropylanilido)-2,7-di-*t*-butyl-9,9-dimethylxanthene, a structurally robust and electron-donating framework they had previously employed in 2018 to develop a nucleophilic aluminyl anion.[101] By extending this ligand system to gold, they successfully created a nucleophilic gold center, which opens up exciting new reactivities in the field of main group and transition metal chemistry.[102] The gold center reacts with CO_2 and diisopropylcarbodiimide by insertion into the Al–Au bond, with the gold forming the bond to the electrophilic carbon atom and acting as a nucleophilic center (Figure 11).

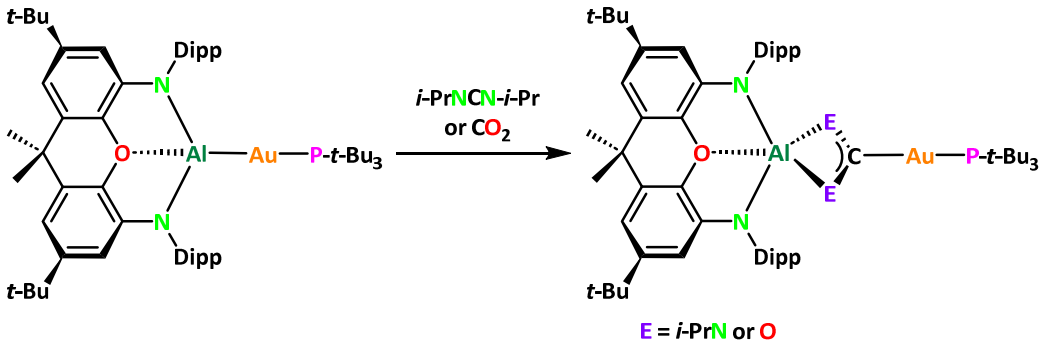

Figure 11: Nucleophilic gold(-I) complex and its reactivity with electrophilic carbon centers.[102]

1.1.3 Relativistic effects

Gold exhibits a number of distinctive physical and chemical properties which are often different from its lighter group 11 homologues, silver and copper. While all three are classified as coinage metals and share several properties due to their closed-shell d^{10} electron configurations, gold's behavior frequently deviates in many ways, for instance, in its characteristic yellow luster, its exceptional resistance to oxidation, and its unique behavior in coordination chemistry.[103] These unusual properties of gold can be rationalized by relativistic effects, which become increasingly relevant as we move down the periodic table. In general, relativistic effects refer to the alterations in the behavior of electrons, particularly those close to the nucleus, due to the high nuclear charge (Z) of heavy atoms. The magnitude of these effects tends to scale approximately with the square of the atomic number (Z^2), meaning they become dramatically more pronounced for heavier elements such as gold (Z = 79), and especially for those beyond the lanthanides (Z > 71).[104]

For the simplified understanding of these effects, the electron is considered as a particle orbiting the nucleus. As per Einstein's theory of relativity, the mass of an elementary particle depends on the speed with which it moves through the space.[105] Accordingly, when electrons, particularly *s*-orbitals, experience the intense electrostatic attraction of a high- *Z* nucleus, they must travel at very high velocities to maintain their orbitals. For an electron, this mass increase can be calculated using the equation below:

$$m_{rel} = \frac{m_0}{\sqrt{1 - \frac{v^2}{c^2}}}$$

where m_{rel} - relativistic mass, m_0 - rest mass, v - velocity of the electron and c - speed of light.

In the case of gold, the 1*s* electrons are estimated to move at roughly 58 % of the speed of light. This rapid movement results in a relativistic increase in mass, about 22 % greater than their non-relativistic mass.[103,106] The Bohr's radius of an electron can be calculated using the equation below,[107] assuming that it is approximately in a circular orbit around the nucleus:

$$a_0 = \frac{4\pi\varepsilon_0\hbar^2}{Ze^2m_{rel}}$$

where a_0 - Bohr's radius, ε_0 - electric field constant in vacuum, $\hbar = (h/2\pi)$ - reduced Planck's quantum of action, m_{rel} - mass of an electron taking relativity theory into account, Z - nuclear charge and e - elementary charge.

Here, Bohr's radius is inversely proportional to the mass of an electron (taking relativity theory into account) and if it is calculated for both m_0 and m_{rel}, the orbital radius for the electrons close to the nucleus is up to 20 % smaller ($m_0/m_{rel} \approx 0.82$).

All of the higher energy *s*-orbitals, including those in the valence shell, undergo contraction due to relativistic effects. While *p*-orbitals are also influenced by relativistic factors, the impact on them is comparatively less. This contraction of inner orbitals is known as the direct relativistic effect. As a consequence of this contraction, the inner *s*- and *p*-orbitals provide more effective shielding of the nucleus. This improved shielding, in turn, reduces the effective nuclear attraction experienced by electrons in the *d*- and *f*-orbitals, causing these outer orbitals to expand and attain higher energy. This phenomenon is referred to as the indirect relativistic effect or relativistic expansion.[108-109] An important result of the contraction of the 6*s* orbital in gold is a significant increase in ionization energy for the 6*s* electrons compared to the non-relativistic case. The high first ionization energy of the 6*s* electron also results in gold's

well-known and valued corrosion resistance. These electrons become less available for bonding and show a reduced tendency to participate in chemical reactions. This reduced tendency of *s*-electrons in heavy elements to participate in bonding is described as the inert-pair effect.[110-111]

The relativistic effects significantly influence the unique properties of gold, one of the most striking being its distinctive metallic color. In a non-relativistic framework, the excitation energy required for an electron transition from the 5*d* band to the partially filled 6*s* conduction band (Fermi level) would be approximately 3.6 eV. This energy lies in the ultraviolet region of the electromagnetic spectrum. As a result, in the absence of relativistic effects, visible light would be reflected and gold would appear silver-white, much like its lighter homolog silver.

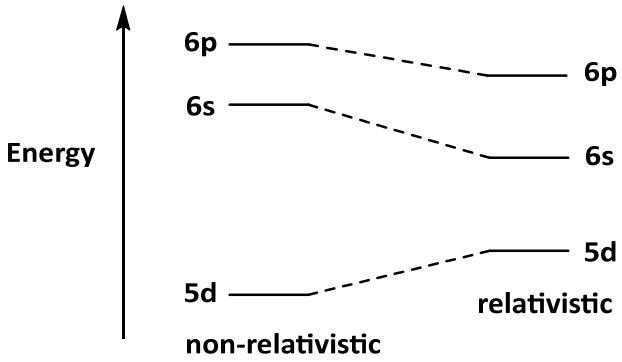

Figure 12: Schematic representation of the influence of relativistic effects on the energetic position of the gold atomic orbitals.[109]

However, due to relativistic effects, the 5*d* orbitals are destabilized (increased energy) while the 6*s* orbital is stabilized (decreased energy). This narrowing of the energy gap between the 5*d* and 6*s* orbitals reduces the excitation energy to approximately 2.4 eV, which falls within the blue-green region of the visible spectrum.[112] Consequently, blue and green lights are absorbed, while red and yellow light is predominantly reflected. This selective reflection of warmer hues is what imparts to gold its characteristic rich golden color, a visual manifestation of the underlying relativistic electronic structure (Figure 12).

1.1.4 Metallophilic interactions

The concept of metallophilicity or metallophilic interactions was first introduced by Pyykkö in 1994 to describe a phenomenon observed in certain metal containing compounds and it refers to the unexpected tendency of metal atoms or metal ions, particularly those with closed-shell

electronic configurations, to come into very close proximity, even closer than the sum of their van der Waals radii.[113] With the advancement of single-crystal X-ray structure analysis, chemists started noticing unusual structural features in many metal complexes. These structures revealed metal centers with closed shells are positioned much closer together than previously anticipated, despite the absence of traditional bonding interactions. Such behavior was initially unexpected as two positively charged metal cations should repel each other, according to classical electrostatic arguments,[114] particularly when they have filled outer electron shells, typically making them chemically inert. Nevertheless, such short metal-metal distances were repeatedly observed, suggesting the presence of a non-covalent attractive force overcompensating electrostatic repulsion. These metallophilic interactions are now recognized as a real and significant phenomenon in coordination and supramolecular chemistry. They occur most commonly between metal centers with electron configurations such as d^{10}–d^{10} (e.g., Au(I), Ag(I), Cu(I)), d^{8}–d^{8} (e.g., Pt(II)), or d^{10}–d^{8} combinations. Though weaker than covalent bonds, these interactions play an important role in stabilizing molecular structures.[115-121]

These types of interactions have been most commonly observed in gold(I) complexes, which possess a d^{10} electronic configuration. Reports of such close range gold-gold contacts date back as early as the 1970s. However, it was not until 1988 that the term aurophilic interactions was formally introduced by Schmidbaur to describe these phenomena in gold(I) systems where two gold atoms are separated by less than 3.5 Å, a distance shorter than what would be expected from simple van der Waals considerations. Despite involving closed-shell metal centers, these interactions can be surprisingly strong, comparable in strength to hydrogen bonds, depending on the exact interatomic distance (r).

$$D_e = 1.27 \cdot 10^6 \cdot e^{-3.5 \cdot r_{Au-Au}}$$

where D_e- interaction energy; $r_{\mathrm{Au-Au}}$- equilibrium distance in Å.

According to the formula above, with a gold-gold distance of $r_{\mathrm{Au\text{-}Au}}$ = 2.70 Å, a binding energy of about 100 kJ/mol is expected, while for an interatomic distance of 3.50 Å, the value drops to approximately 10 kJ/mol. Thus, a gold-gold contact of less than 3.50 Å is the accepted limit for the presence of aurophilic interactions.[122]

A key piece of evidence supporting the explanation is that aurophilic interactions behave in accordance with London dispersion forces, where the strength of the interaction diminishes with the sixth power of the distance between two particles.[123-124] In addition, various studies suggest that aurophilic interactions arise not solely from dispersive forces, but rather from a synergistic combination of relativistic and electron correlation effects. Some researchers also propose that there is a partial ionic character involved, meaning that electrostatic contributions may play a role alongside the typically assumed London dispersion interactions.[125-127]

Considering the type of ligands, aurophilic interactions are further divided into three types mainly: fully-supported, semi-supported and unsupported interactions (Figure 13). Fully-supported and semi-supported interactions fall under the category of intramolecular aurophilic interactions where two gold atoms are connected by either two or one bifunctional ligands, respectively. While on the other hand, unsupported interactions are a type of intermolecular gold–gold bonding.[122,127]

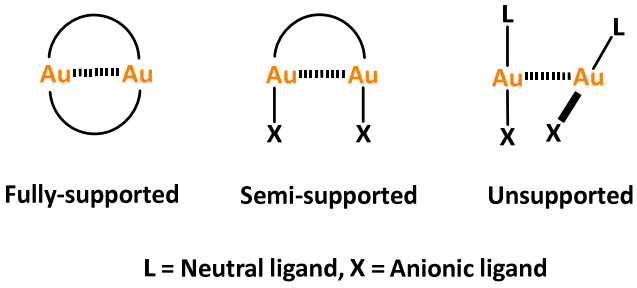

Figure 13: Classification of the types of aurophilic interactions.[122,127]

The metallophilic interactions involving the other group 11 elements, silver and copper, have been also extensively studied.[116,128] When two silver(I) cations are in close proximity, with a separation less than 3.4 Å, the interactions are termed as argentophilic interactions. These argentophilic interactions are comparable in strength to aurophilic interactions observed in gold(I) complexes, up to 40 kJ/mol.[129-130] In contrast, copper(I) cations exhibit the weakest metallophilic interactions among the group 11 elements. These are known as cuprophilic interactions and occur when the Cu–Cu distance is less than 2.8 Å. The energetic strength of cuprophilic interactions is relatively low, estimated to be around 15 kJ/mol.[131-132]

1.2 Photoluminescence

Compounds featuring metallophilic interactions are often known for their photoluminescent properties. Absorption of light promotes the chemical system into a higher energy excited state from which relaxation back to the ground state can occur *via* radiative or non-radiative pathways, where the emission observed from the radiative processes is termed photoluminescence (PL). Two subdivisions compose PL: fluorescence and phosphorescence, depending on the type of excited state.[133]

Such emissive processes can be visualized in a Jablonski diagram (Figure 14). In addition to radiative processes, an electronically excited molecule can return to the ground state through various non-radiative pathways. One such pathway is internal conversion (IC), a process in which the molecule transitions from the first excited singlet state (S_1) directly to the ground electronic singlet state (S_0) without emitting a photon or any non-radiative transition between states of the same multiplicity. Alternatively, the system may undergo intersystem crossing (ISC), where it transitions from the singlet excited state (S_1) to a lower-energy triplet excited state (T_1). From this triplet state, the system can relax to the electronic ground state (S_0), *via* a non-radiative mechanism typically transferring energy to the surrounding environment. These non-radiative transitions typically lead to the population of higher vibrational levels of the ground state, followed by vibrational relaxation (VR). This vibrational energy is dissipated, often facilitated by collisions with surrounding molecules, such as those of a solvent. This cascade of energy loss does not involve photon emission and is therefore a competing pathway to light-emitting processes.[134]

The efficiency of photoluminescence is determined by the competition between radiative (light-emitting) and non-radiative (heat-emitting) decay processes. It is quantitatively expressed as the quantum yield (or quantum efficiency), defined as the ratio of the number of photons emitted to the number of photons absorbed. A high quantum yield indicates that a majority of the absorbed energy is released *via* photon emission, whereas a low quantum yield suggests significant energy loss through non-radiative channels.[134]

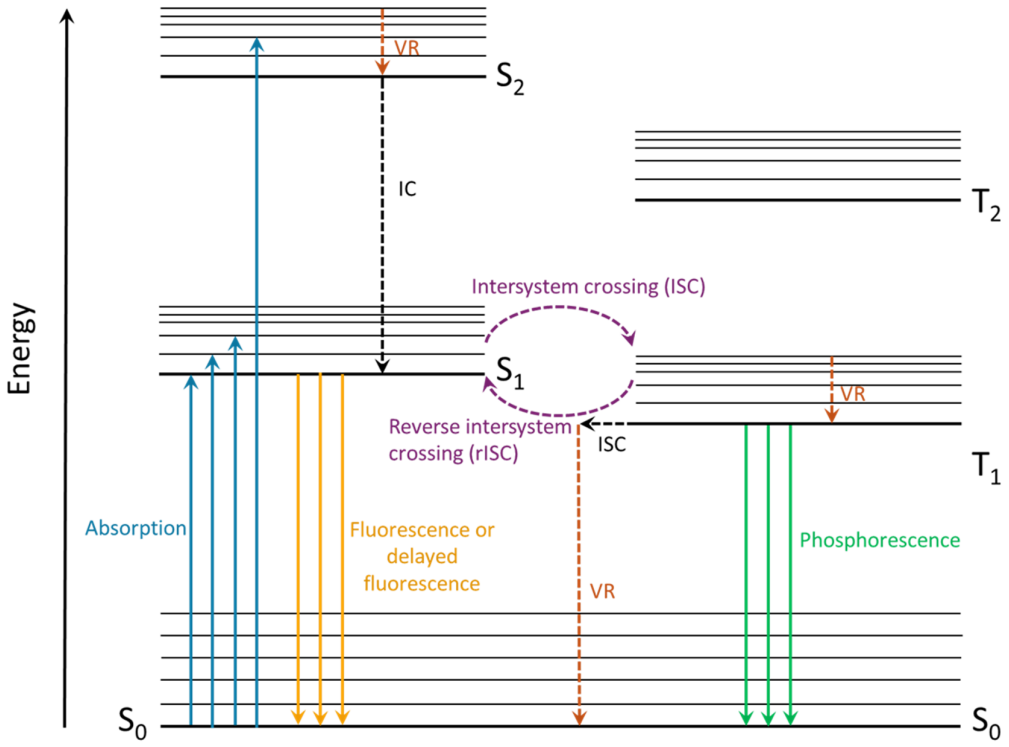

Figure 14: Jablonski diagram illustrating possible transitions between the ground and excited states. Electronic ground state S_0 and excited states (S_1: first excited electronic singlet state, T_1: first excited electronic triplet state) are visualized by thick lines and the subordinate excited vibrational states by thinner lines above them. The vertical arrows illustrate the processes of absorption, fluorescence, and phosphorescence. The non-radiative transitions such as IC, ISC, and VR are described using dashed lines.

The phenomenon of fluorescence was first documented in 1845 by Herschel, who observed the emission of blue light from a quinine solution upon exposure to ultraviolet radiation.[133,135] Fluorescence is initiated when a molecule absorbs a photon with energy corresponding to the energy gap between the electronic ground state (S_0) and an electronically excited singlet state (S_1, or sometimes higher states such as S_2). If excitation occurs to a higher singlet state (S_n, $n \geq 2$), the molecule undergoes internal conversion (IC) to the lowest vibrational level of S_1, which is non-radiative and occurs on an ultrafast timescale of ~10^{-13} to 10^{-11} seconds. Following vibrational relaxation within S_1, the molecule may return to the ground electronic state S_0 *via* radiative decay, emitting a photon in the process. This emission is termed as fluorescence and occurs on a typical timescale of ~10^{-9} to 10^{-8} seconds. The energy of the emitted photon is lower than that of the absorbed photon due to prior

non-radiative losses, resulting in an emission at a longer wavelength, an effect known as the Stokes shift. The energy gap involved in fluorescence emission corresponds to the transition from the relaxed vibrational level of S_1 to a higher vibrational level of S_0. The process is spin-allowed, hence relatively fast and efficient compared to phosphorescence. The quantum yield (Φ_F) of fluorescence is defined as the ratio of the number of photons emitted to the number of photons absorbed, and is influenced by competing non-radiative processes, like ISC to the triplet state and IC, as well as VR facilitated by interactions with the solvent or environment.[134]

Similar to fluorescence, phosphorescence is also a form of photoluminescence that begins with the absorption of a photon, promoting the molecule from the electronic ground state (S_0) to an excited singlet state (S_1). Following this initial excitation, the molecule may undergo intersystem crossing (ISC), where the electron undergoes a spin inversion to enter the lowest excited triplet state (T_1). This transition from a singlet to a triplet state is considered spin-forbidden under quantum mechanical selection rules because it involves a change in the spin multiplicity of the system, violating the conservation of total spin angular momentum. Despite its spin-forbidden nature, intersystem crossing can be significantly enhanced in molecules that contain heavy atoms (e.g., Au, Pt, or Ir). The electrons in these elements exhibit strong spin-orbit coupling, ensuring conservation of the total angular momentum when the spin state is changed by a concomitant change in orbital angular momentum, increasing the probability of ISC and making subsequent phosphorescent emission from the triplet state possible.

Phosphorescence itself refers to the radiative transition from the triplet excited state (T_1) back to the singlet ground state (S_0), which is also spin-forbidden and therefore occurs on a much longer timescale compared to fluorescence. The lifetime of phosphorescence emissions is typically in the range of microseconds to several seconds, and in exceptional cases, particularly in rigid matrices or crystalline solids, it may persist for minutes to hours due to the kinetic stability of the T_1 state.[136]

However, in solution-phase systems, effective phosphorescence is less commonly observed. This is due to enhanced non-radiative deactivation pathways and collisional quenching by solvent molecules. Since these processes are relatively fast and efficient in solution and the phosphorescent emission is slow, the energy stored in the T_1 state is often dissipated non-radiatively before photon emission can occur. Therefore, low-temperature conditions or solid-

state matrices are frequently employed to suppress non-radiative decay and observe phosphorescence effectively.[137]

The phenomenon of delayed fluorescence was first reported in 1929 by Perrin *et al.*,[138] and later examined more extensively in 1941 by Lewis and co-workers, who identified it as a form of luminescence that occurs after a time delay following photon absorption, yet still originates from a singlet excited state.[139] The term Thermally Activated Delayed Fluorescence (TADF) was formally introduced in 2012 by Adachi and co-workers, who provided a mechanistic framework that described the reversible intersystem crossing (rISC) as a key condition for efficient TADF.[140] In contrast to phosphorescence, which involves radiative decay directly from the triplet state ($T_1 \rightarrow S_0$), TADF involves a thermal upconversion process in which the electron residing in the lowest triplet excited state (T_1) is thermally promoted back to the singlet excited state (S_1) *via* reverse intersystem crossing. Subsequently, the molecule undergoes radiative relaxation from S_1 to the ground state (S_0), resulting in delayed fluorescence.[141]

This mechanism leads to a delayed but singlet derived emission, typically on the microsecond timescale, which significantly extends the duration of luminescence compared to fluorescence, occurring on the nanosecond timescale. The delayed nature of the emission gives rise to a longer fluorescence lifetime, yet the spin-allowed nature of the $S_1 \rightarrow S_0$ transition ensures that the emission remains bright and efficient, similar to the fluorescence.

For TADF to be efficient, a critical requirement is that the energy difference between S_1 and T_1 states ($\Delta E(S_1\text{-}T_1)$) must be sufficiently small. Experimental and theoretical studies have shown that an energy gap of less than 0.37 eV is generally required to allow thermal population of the singlet state from the triplet reservoir at ambient temperature. This narrow energy gap facilitates rISC by enabling ambient thermal energy ($kT \approx 25$ meV at 298 K) to overcome the energetic barrier between T_1 and S_1.[142-143]

1.3 Ligand systems

1.3.1 Amidinate ligands

In coordination chemistry, singly negatively charged, bidentate nitrogen-donor ligands have emerged as an attractive and versatile alternative to the well-established cyclopentadienyl (Cp^-) anions.[144-145] These anionic nitrogen-based ligands are highly valued for their ability to form stable chelate complexes with a wide variety of metal centers, thereby influencing the geometry, reactivity, and electronic properties of the resulting complexes.[146] Examples include amidinates,[147-148] β-diketiminate (often termed as nacnac),[149] amino-troponiminates,[150] guanidinates,[147,151] and phosphoamidinate.[152-153]

Amidinates are one of the nitrogen donor ligands in coordination and organometallic chemistry, structurally regarded as the nitrogen analogues of carboxylates. Their protonated counterparts are known as amidines (Figure 15).

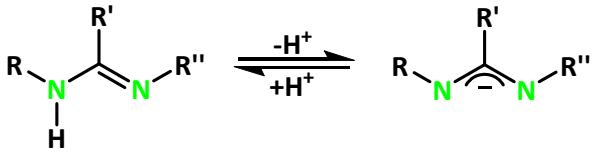

Figure 15: Interconversion of amidines and amidinates by protonation and deprotonation.

One of the key advantages of amidinates lies in their straightforward and cost-effective synthesis, as well as the wide range of structural modifications that can be introduced into the heteroallylic NCN backbone (Figure 15). These features make them one of the most widely employed *N*-based ligand systems in the modern organometallic chemistry.[146-147,154-155] The versatility of amidinates can be attributed to their ability to be tailored into symmetric, asymmetric, and even chiral derivatives, with adjustable steric and electronic properties. These adjustments enable one to optimize ligand characteristics to suit specific applications.[156-157] Such adaptability has led to their extensive use in coordination chemistry across various fields, including lanthanide-based synthesis, the chemistry of main group elements, transition metal coordination, and homogeneous catalysis.[158-161]

Among the commonly employed synthetic strategies for the synthesis of amidinates, one is the insertion of carbodiimides into metal–carbon bonds (Figure 16). This method provides robust access to diverse amidinate scaffolds.

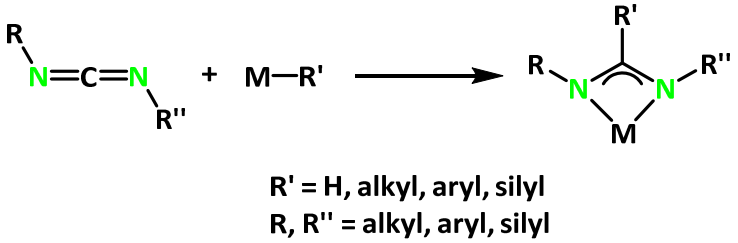

Figure 16: Amidinate synthesis by nucleophilic insertion of a carbodiimide into a metal organyl bond.

Amidinates exhibit remarkable flexibility in their coordination behavior, allowing them to adopt a variety of binding modes with the metal centers. This versatility arises from the delocalized negative charge over the central NCN unit and the potential for different spatial arrangements of substituents on the nitrogen atoms. Typically, three primary coordination modes of amidinate ligands are distinguished, each with unique structural and electronic features (Figure 17).[162]

The most common binding motif is the chelating coordination mode (Figure 17a), in which both nitrogen atoms of the amidinate ligand simultaneously coordinate to a single metal center. In this arrangement, the negative charge is delocalized across the NCN backbone, enhancing the ligand's stability and electron-donating capability. This chelation forms a four-membered ring. The monodentate coordination mode (Figure 17b) is less frequently encountered and typically occurs under sterically constrained conditions, such as when bulky substituents are present on the nitrogen atoms. In this binding mode, the metal binds to only one of the two nitrogen atoms, while the second nitrogen remains uncoordinated. Notably, in certain cases, especially when the substituents adopt an anti-configuration, additional stabilization can be achieved through secondary interactions, like coordination of a π-aryl system to the metal center. The bridging coordination mode (Figure 17c) is primarily observed in complexes containing low-valent transition metal centers. In this configuration, a single amidinate ligand bridges two metal atoms by coordinating to each through one of its nitrogen atoms. This spatial proximity can facilitate direct metal-metal interactions, either promoting

the formation of metal-metal single or multiple bonds or contributing to the stabilization of reactive metal centers or bimetallic species.

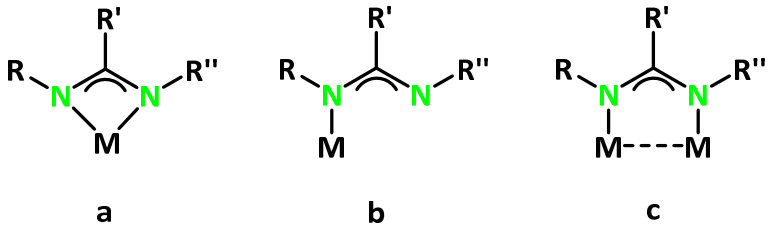

Figure 17: Different binding modes of amidinate ligands; (a) chelating, (b) monodentate and (c) bridging.

Over the years, a wide variety of amidinate ligands have been developed and structurally modified to meet the requirements of coordination and organometallic chemistry. The foundation of amidinate chemistry was laid in 1973 when Sanger first introduced benzamidinate (Figure 18a).[163] This pioneering ligand was later adapted and applied to other systems by Reed *et al.*,[164] and subsequently, it was employed by Dehnicke *et al.*[165] in the synthesis of the first dinuclear gold amidinate complex. In a further advancement, our research group extended the structural diversity of amidinates by incorporating acetylene functionalities into the NCN backbone. These modified ligands enabled the successful synthesis of a range of gold(I) complexes (Figure 18b)[166] as well as lanthanide-based compounds (Figure 18c),[167] thereby expanding the scope of amidinate coordination frameworks to different classes of metals. Moreover, the structural elaboration of amidinates has led to the synthesis of bis(amidinate) ligands, where two amidinate units are connected *via* a molecular linker, facilitating bidentate or bridging coordination modes.[168] For instance, Liu *et al.* demonstrated a strategy in which two nitrogen donor atoms are bridged using a central linker, allowing for coordination to multiple metal centers or chelation within multinuclear complexes (Figure 18d).[169] Another approach was later introduced by our group in 2022, in which the amidinate framework was combined with a ferrocene unit, resulting in a novel ligand design (Figure 18e).[170]

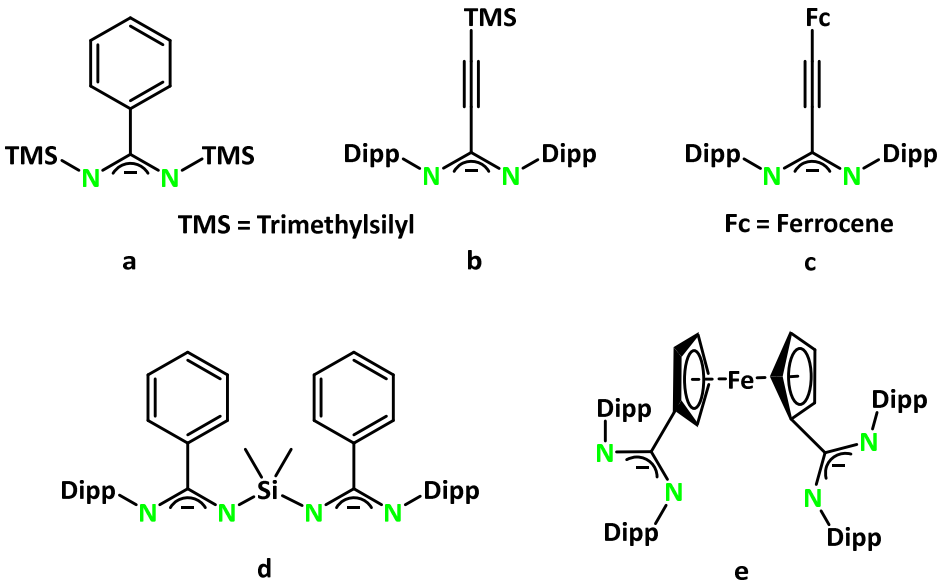

Figure 18: Selected examples of amidinate ligands.

There is another class of ligands termed as orthogonal ligands and can be defined as the type of ligands designed to interact with metal centers through two or more distinct and non-interfering coordination sites. Their defining feature is the ability to selectively and independently bind to different metal centers or molecular components without obstructing the other, that is why they are also referred to as bifunctional ligands. This unique property makes orthogonal ligands particularly valuable in the construction of complex architectures, such as multinuclear metal assemblies and heterobimetallic catalysts. By combining steric and electronic complementarity, orthogonal ligand frameworks allow for the control over coordination geometry, reactivity, and functional diversity.[116]

Specifically, there are many ligand systems exploiting the different coordination behaviors of N- and P-centers. According to hard-soft acid-base (HSAB) concept, N is a hard donor site, preferentially binding to hard metal centers (e.g. Cu) while P is a soft donor site, thus preferentially binding to soft metal centers (e.g. Au).[171-172] The first example of the use of an orthogonal ligand was published in 1998 by Che *et al.* for the synthesis of bimetallic complexes of Cu(I) and Au(I) as well as Cd(II) and Au(I).[173] In 2002, Tsukada and colleagues reported an amidinate based PNNP ligand (Figure 19a), *N*,*N*'-bis[(2-diphenylphosphino)phenyl]-formamidine (Hdpfam), for the synthesis of Pd(II) and Pt(II) complexes.[174] Later, our group utilized this ligand for the synthesis of multimetallic coinage metal complexes (Figure 19a).[175]

A β-diketimine ligand and its corresponding anion, forming a PNNP-type pocket, was also used for the synthesis of such heterobimetallic complexes (Figure 19b).[176]

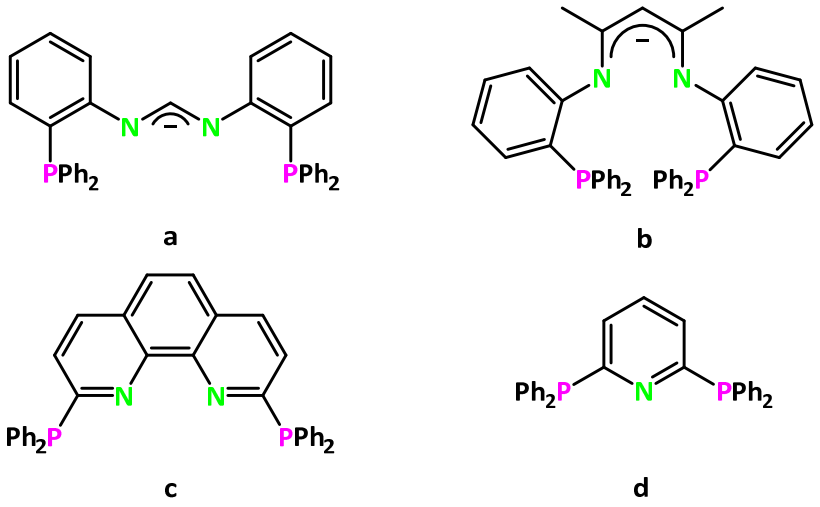

Figure 19: Examples of N- and P-based orthogonal ligands, (a) and (b): anionic ligands; (c) and (d): neutral ligands.

In 2014, Catalano *et al.* reported Cu(I)–Au(I) heterometallic complexes using a diphenyl phosphine substituted phenathroline neutral ligand (Figure 19c).[177] Another neutral ligand depicted in Figure 19d was used by Samouei *et al.* for a similar purpose.[178]

1.3.2 *N*-heterocyclic carbene (NHC) based ligands

Carbenes are typically described as divalent carbon species in which the central carbon atom has only six valence electrons, making them electronically unsaturated and highly reactive. The challenge of isolating such species has fascinated chemists since the mid-19th century, but their inherent instability and high reactivity rendered these efforts unsuccessful for many decades.[179] A significant advancement came with Wanzlick's hypothesis, that carbenes substituted with electron-donating groups could be sufficiently stabilized to exist in an isolable free form. This idea provided a new direction for carbene research and eventually led, in 1962, to the synthesis of an electron-rich olefin. This compound was later recognized as the dimeric form of an NHC (Figure 20a).[180] At the time, it was proposed that the dimer might exist in dynamic equilibrium with two free carbene units. However, experimental observations revealed that the dimer did not exhibit any tendency to dissociate under ambient conditions. A major breakthrough followed in 1968, when the first NHC-transition metal complexes were

independently synthesized and reported by Öfele[181] and Wanzlick.[182] These findings demonstrated the viability of NHCs as ligands in coordination chemistry (Figure 20b and 20c).

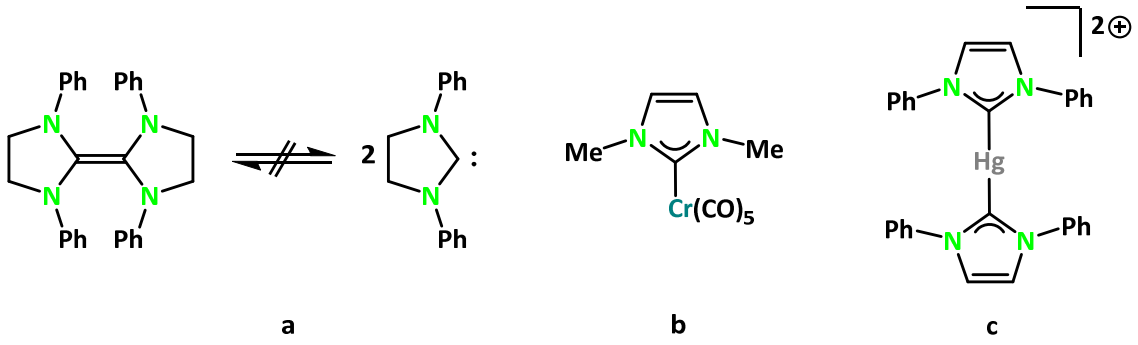

Figure 20: Early work on NHCs by Öfele and Wanzlick.[180-182]

The successful isolation of a free NHC was not realized until 1991, when Arduengo achieved this long-standing goal in carbene chemistry. A key factor that contributed to it was the strategic use of bulky adamantyl substituents. These sterically demanding groups effectively hinder dimerization of the carbene species. By preventing two carbene molecules from approaching each other closely enough to form a dimer, the adamantyl groups allowed the monomeric, free carbene to persist in a stable and isolable form under ambient conditions (Figure 21).[183]

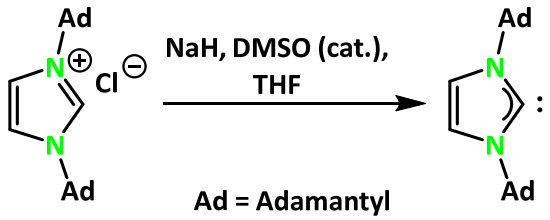

Figure 21: Illustration of the first free NHC by Arduengo.[183]

NHCs are bent carbenes with frontier orbitals consisting of an sp^2-hybridized orbital (σ) and an orthogonal p orbital (p_π). They can adopt four electronic configurations (Figure 22) but are best known for their singlet $^1A_1$ ground state with a filled σ orbital (σ^2). Excluding the higher energy $^1A_1$ state with a p_π^2 configuration, the main alternatives are the triplet $^3B_1$ and singlet $^1B_1$ states, each with singly occupied σ and p_π orbitals. The stability of NHCs depends on the singlet-triplet energy gap, $E_{S\text{-}T}$. If this gap exceeds ~40 kcal/mol, a singlet ground state is preferred.[184-185] The singlet state stability of NHCs is mainly attributed to the electron

withdrawing inductive effect of the amine substituents, which stabilizes the orbitals on the carbene carbon, thereby increasing the singlet–triplet energy gap and favouring the singlet state. Additional stabilization comes from p_π donation by the nitrogen atoms into the empty p_π orbital of the carbene carbon.[186]

In the $^1A_1$ singlet state, the lone pair in an sp^2 orbital forms the HOMO and is stabilized by the inductive effect of adjacent electronegative nitrogen atoms. The LUMO, a p_π orbital on the carbene carbon, interacts *via* π-type interactions with the nitrogen lone pairs, completing the octet and enhancing the stability. While the aromatic 6π-electron ring system offers additional stabilization, its role is secondary to the inductive and π-donation effects.[187]

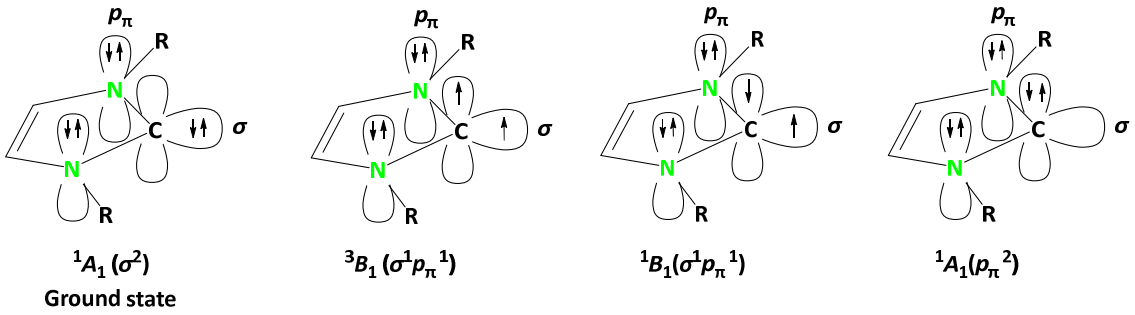

Figure 22: Electronic configurations of NHC carbenes.

Initially, it was assumed that NHCs are only σ-donors, and however this hypothesis is now outdated as it was shown that both $d \rightarrow \pi^*$ (M to NHC π^*-backdonation) as well as $\pi \rightarrow d$ (NHC to M π-donation) have to be considered to understand the details of the M-NHC bonding. Thus, the electronic structure of NHCs enables them to form three types of bonds with metals. As depicted in Figure 23, these are σ-donation (NHC → M), π^*-back-bonding (M → NHC) and π-donation (NHC → M).[187]. In the literature, 15-20 % of NHC-metal bonding contributions are attributed to π-bonds (π-donation and back bonding) and in the case of coinage metal complexes, the contribution of back bonding was determined to be about 20 %.[188-189] In the series of [NHC(MCl)] complexes with coinage metals, the calculated bond strength trend is Au > Cu > Ag.[190] This aligns with practical observations, where silver complexes are particularly effective as transmetallation reagents. The bonding is primarily ionic, driven by the interaction between the carbene's free σ-electron pair and the metal cation. However, there is also a covalent component, arising from the overlap of the lone pair with a hybrid orbital on the metal composed of d_{z^2} and *s* character.

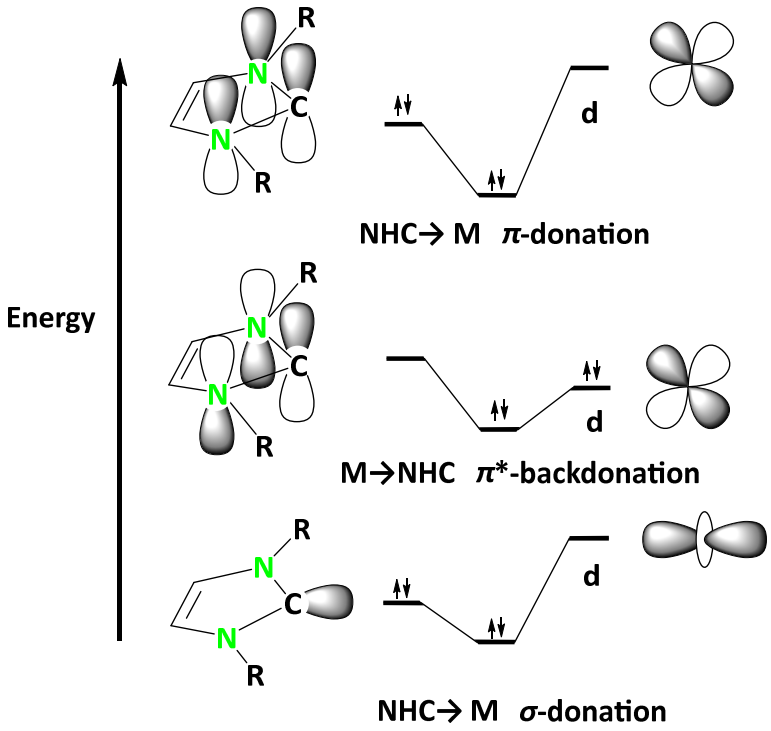

Figure 23: Types of interaction of NHCs with metals.

NHCs and phosphines are both strong σ-donors and weak π-acceptors, making the Tolman Electronic Parameter (TEP), originally developed for phosphines, useful for comparing their donor strengths (Figure 24).[191] The TEP is determined by measuring CO stretching frequency in metal carbonyl complexes, of the type [LNi(CO)$_3$]. Due to toxicity of the latter, it has nowadays been replaced by *cis*-[LIrCl(CO)$_2$] and *cis*-[LRhCl(CO)$_2$].[192-193] Stronger σ-donors increase metal electron density, enhancing π-back bonding to CO and lowering CO stretching frequencies. NMR and theoretical or electrochemical methods have been explored as alternatives but have not fully replaced IR-based TEP analysis.[194-196]

Tolman's cone angle quantifies the steric bulk of phosphines by measuring the apex angle of a cone defined by the van der Waals cloud of the phosphine substituents with the metal at the top of the cone at a distance of 2.28 Å from the phosphorus atom.[191] This concept is not applicable to NHCs, as their substituents point toward the metal, forming a shielding screen. To assess NHC steric properties, Nolan and co-workers introduced the percentage buried volume (%V_{bur}) method, which calculates the percentage of a sphere (2 Å away from the donor atom) occupied by the ligand, using the crystallographic data (Figure 24). Their electronic

properties are mainly determined by the backbone of NHC, and even with small *N*-substituents, air-stable complexes can be formed when the backbone is suitably designed.[197]

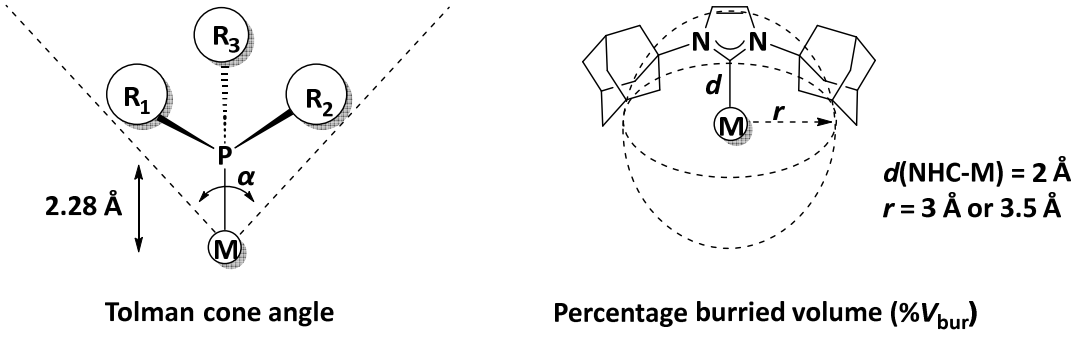

Figure 24: Tolman cone angle and percentage buried volume.[191,197]

Although stable, most NHCs cannot be stored as free carbenes, so metal complexes are typically formed using stable precursors. Early methods used tetraamines for metal insertion.[198] Later, adducts with labile groups (e.g., alkoxides, trichloromethyl radicals or borates) allowed easier handling (Figure 25).[199-200]

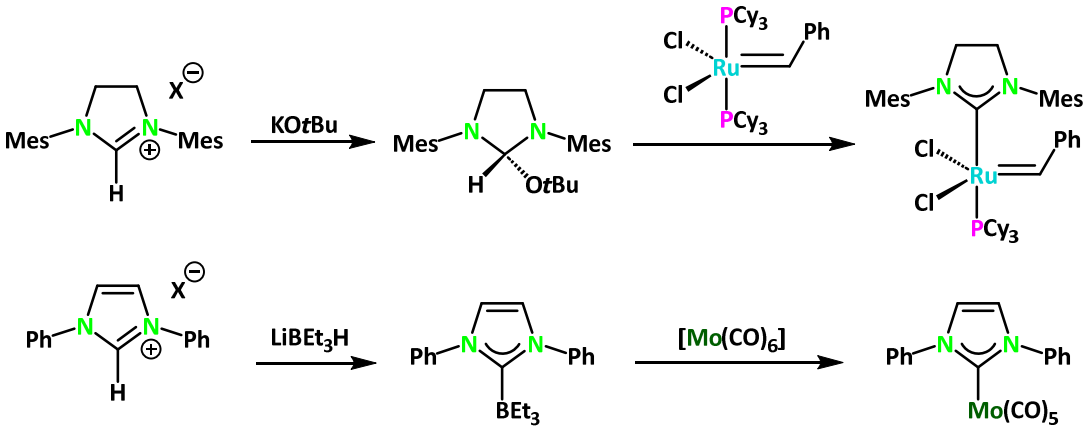

Figure 25: Synthesis of NHC metal complexes using carbene adducts.[199-200]

The most common precursor of carbenes, imidazolium salts, can be deprotonated by using bases such NaH, KO*t*Bu, KHMDS or liquid NH_3. This free NHC route enables straightforward complex formation, often displacing neutral ligands or breaking up metal aggregates.[201-202] *In situ* generation with mild bases is also possible, even with weak bases such as NEt_3 or NaOAc, when complex formation is thermodynamically favoured.[200] Alternatively, direct reaction with basic metal reagents (e.g., hydrides or acetates) is common[203]. Transmetallation from Ag or Cu complexes, formed *via* Ag_2O or Cu_2O, is now widely used due to the NHC–Ag/Cu

labile bonds and precipitation of AgCl/CuCl.[204-205] This route tolerates functional groups but may risk oxidation by Ag(I); Cr, Mo, and W complexes can also serve in transmetallation.[200]

1.3.3 Thioamidinate ligands

A thioamide (or thiourylene) is a functional group characterized by the general structural formula R–C(=S)–NR'R" (R, R' and R" are any organic groups or hydrogen atoms). Structurally, thioamides can be considered as the heavier analogues of amides, wherein the oxygen atom of the carbonyl group (C=O) is substituted by a sulfur atom, leading to the formation of a thiocarbonyl group (C=S) (Figure 26). These compounds form a bridge between organic sulfur chemistry and coordination chemistry due to their versatile bonding possibilities. Upon the formation of imine derivatives from amides, compounds known as amidines are obtained. These serve as key precursors to amidinate ligands (Figure 15).

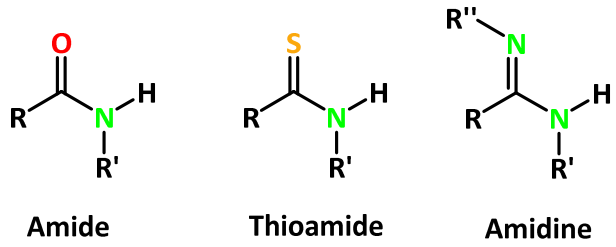

Figure 26: Representation of amide, thioamide and amidine.

In the same way, by deprotonation of a thioamide, a thioamidinate or iminothiolate ligand is obtained, depending on the location of the negative charge (Figure 27). Thioamidinates possess the general formula $[R–C(=S)–NR']^-$, where R and R' can be modified to meet desired steric and electronic demands. Structurally and functionally, thioamidinates resemble amidinates, but with the key difference that one nitrogen atom is replaced by a sulfur atom. In these ligands, both the nitrogen and sulfur atoms act as donor sites for metal coordination. This bidentate coordination behavior enables thioamidinates to chelate metal centers effectively, typically forming four-membered metallacycles in the coordination complexes.[206] Due to the presence of the soft donor sulfur, thioamidinates are categorized as soft ligands, distinguishing them from their oxygen- or nitrogen-based counterparts. This softness makes them especially suited for binding with soft metal centers, particularly the late transition metals (e.g. Ni, Pd, Pt, Au etc.).[171-172]

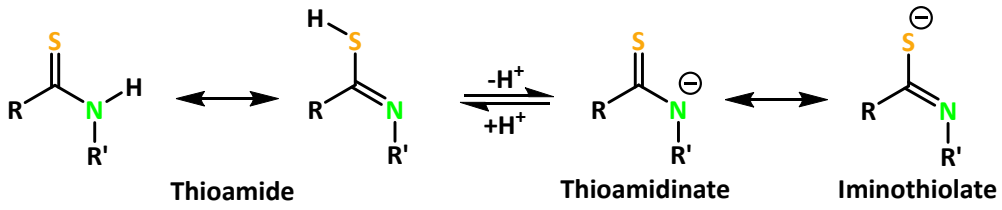

Figure 27: Conversion of thioamide into thioamidinate or iminothiolate by deprotonation.

The coordination chemistry of this class of ligands is unique due to their variety of coordination states, such as monodentate, bridging, and chelating modes, including pincer and scorpionate ligands. In recent years, several studies highlighted the advantages of using multidentate thioamidinate-based transition metal complexes in diverse fields, such as photochemistry, structural chemistry, catalyst development, polymer-based materials science, electrochemistry, and supramolecular chemistry.[206] In 1983, Castan *et al.* utilized thioamido ligands to stabilize the higher oxidation states of platinum in its complexes.[207] Beyond platinum, thioamido ligands have also been explored in complexes with other metals. For instance, Cu(II) and Hg(II) complexes have been synthesized using thiobenzanilide ligands, which tend to coordinate in a monodentate fashion exclusively *via* the sulfur atom alone (Figure 28a).[208-209] Another common ligand of this type is 2-mercaptopyridine, a commercially available compound, showcasing dual coordination behavior. It has been used for the coordination to Fe(II) as a monodentate ligand and as a bidentate ligand within Ru(II) complexes (Figure 28b).[210-211] A few examples of organotin(IV) complexes with heterocyclic thioamides were reported and consequently used in biological studies for *in vitro* cytotoxicity studies (Figure 28c).[212] Furthermore, Sn(II) complexes featuring alkyl substituted thioamidinate ligands have been employed in the deposition of tin sulfide (SnS) thin films, a material of interest for semiconductor and solar cell applications (Figure 28d). Similar ligands have also been utilized in the synthesis of cationic Ru(II) complexes, underlining the broad functional utility of thioamidinates across both materials and bioinorganic chemistry.[213-214]

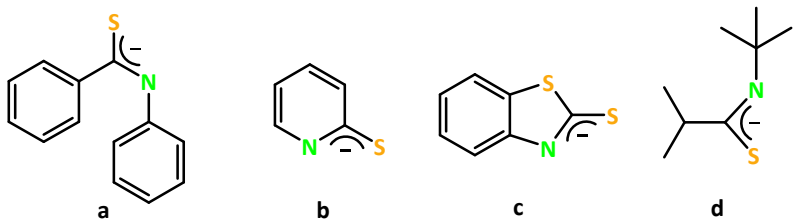

Figure 28: Examples of different thioamidinate ligands.[208-214]

2. Objectives

Over the past years, there have been many reports of coinage metal complexes studied for their photophysical properties and other transition metal complexes for catalysis and photoluminescence studies. Here, the aim is to synthesize coinage metal and transition metal complexes using different ligands.

The objectives are as follows:

1) Synthesis of a phosphine acetylide functionalized orthogonal amidinate ligand and its utilization for the synthesis of Cu(I)–Au(I) heterobimetallic complexes. Further, the photophysical properties of the complexes are to be investigated (Chapter 3.1).
2) Utilization of the phosphine acetylide amidinate ligand for the synthesis of heterobimetallic Cu(I)–Rh(I) and Cu(I)–Ir(I) complexes. Further, the catalytic activity and photophysical properties of the Cu(I)–Ir(I) complex are to be explored (Chapter 3.2).
3) Synthesis of a coumarin-substituted *N*-heterocyclic carbene (NHC) ligand and its Au(I) complexes. Additionally, the photophysical properties of the luminescent complexes both at 298 K and at 77 K are to be studied (Chapter 3.3).
4) Synthesis of Rh(I), Ir(I), Pd(II), Pt(II) and Ru(II) complexes coordinated by a coumarin-substituted NHC and the analysis of the photophysical properties of the complexes both at 298 K and at 77 K (Chapter 3.4).
5) Synthesis of a thioamidinate ligand and its use for the complexation of Zn(II) and Ln(III) ions to obtain different complexes. Additionally, the photophysical properties of the complexes are to be investigated (Chapter 3.5).

3. Results and discussion

3.1 Luminescent Cu(I)–Au(I) heterobimetallic complexes: Selective coordination within a phosphine acetylide amidinate ligand framework

3.1.1 Introduction

In recent years, the synthesis of heterobimetallic complexes has attracted growing attention due to their promising applications in diverse areas including electronics, medicine and catalysis.[215-218] These complexes are distinctive molecular systems comprising of two different metal centers incorporated within a single framework.[219-220] Their increasing appeal comes from the synergistic combination of the unique chemical characteristics of each metal, such as differences in ionic radii, oxidation states, and HSAB behavior. This metal–metal cooperativity, when paired with an appropriate ligand scaffold, often leads to the emergence of novel molecular structures and reactivity profiles that are not achievable with monometallic analogues.[221]

Depending on the nature of the metal centers involved, heterobimetallic complexes may also exhibit photoluminescence properties.[222-224] In this context, luminescent complexes featuring coinage metals have been extensively explored due to their filled d^{10} electronic configuration and the absence of low-energy, non-radiative *d-d* transitions.[225] Notably, Cu(I) and Au(I) display differing affinities for hard and soft donor atoms in accordance with the HSAB principle,[171-172,226] a feature that has been utilized in the rational design of orthogonal ligands with site-specific binding properties toward each metal.[116,227-233] Among these, ligands containing both amidinate and phosphine donor groups and featuring N and P coordination sites represent a particularly appealing scaffold for the targeted synthesis of heterobimetallic Cu(I)–Au(I) complexes.[173,177,234-235]

Coinage metal complexes in the +I oxidation state coordinated by amidinate ligands are well known to form dimeric structures of the type "L_2M_2" (L = amidinate ligand; M = Cu, Ag, Au), stabilized by attractive metal–metal interactions.[236] These weak, yet structurally significant forces, often observed between d^{10} metal centers, are referred to as metallophilic interactions.[108,122,129,132,237-240] Such interactions can dramatically influence the photophysical behavior of the complexes by facilitating a transition from simple ligand to metal charge transfer (LMCT) in mononuclear systems to ligand to metal to metal charge transfer (LMMCT)

in dinuclear systems, typically resulting in a reduced HOMO–LUMO gap and altered emission properties.[129,241-242]

There are several reported examples of Cu(I) amidinate complexes of the general formula $[(R'NC(R)NR'')Cu]_2$ (where R' and R'' = *n*-propyl, *i*-propyl, *n*-butyl, *i*-butyl, *sec*-butyl, *t*-butyl; R = methyl, *n*-butyl), as described by Gordon *et al.*, who showed that these species exist as planar dimers bridged by nearly linear N–Cu–N linkages. These complexes have been explored for atomic layer deposition.[243] Walensky *et al.* later synthesized similar dinuclear Cu(I) and Ag(I) amidinate complexes and investigated their reactivity toward CS_2, leading to the formation of Cu_4S_8 clusters,[244] as well as mixed-valent copper species *via* iodine-mediated reduction.[245] Other examples include Cu(I) complexes with zwitterionic imidazolium-2-amidinate ligands,[246] and a remarkable dodecacopper(I) extended metal atom chain supported by a hexadentate bis(pyridylamido)amidinate ligand reported in 2018.[247] Additionally, phosphaamidinate Cu(I) complexes have demonstrated catalytic potential,[248] and multinuclear Cu(I)–Ag(I) complexes bearing coumarin-functionalized aminodiphosphine ligands have also been documented.[249]

Our group has previously reported the synthesis of gold(I) amidinate complexes featuring alkyne functionalities, exploring the capacity of alkynyl groups to promote the formation of multimetallic assemblies.[166,250] The alkynyl moiety plays an important role in organometallic photophysics, often contributing to metal-to-ligand charge transfer (MLCT) involving π^*(C≡C) orbitals and enabling radiative decay upon photoexcitation.[251] In 2021, a PNNP-type ligand, *N*,*N*'-bis[(2-diphenylphosphino)phenyl]-formamidinate ($dpfam^-$), was employed for site-specific coordination of Cu(I) and Au(I) to nitrogen and phosphorus donor atoms, respectively, yielding luminescent heterobimetallic complexes.[128,175,252]

This chapter presents the synthesis of a phosphine substituted acetylide amidinate ligand featuring both an alkynyl group and a phosphine donor. The ligand's coordination behavior is explored for the synthesis of heterobimetallic Cu(I)–Au(I) complexes through both stepwise and one-pot synthetic routes. These complexes exhibit variations in coordination modes and ligand environments at the gold(I) center. Furthermore, the photophysical properties of the complexes were examined to gain insights into the role of metal–metal interactions and the ligand in modulating luminescence.

3.1.2 Syntheses and characterization of Cu(I)–Au(I) complexes

The phosphine-substituted lithium acetylide amidinate complex (**1**) was obtained *via* following a two-step synthetic procedure, as shown in Scheme 1. The first stage of the process was the preparation of diphenylphosphine substituted acetylene ($Ph_2PC{\equiv}CH$), which was obtained from the reaction of chlorodiphenylphosphine (Ph_2PCl) and ethynyl magnesium bromide ($HC{\equiv}CMgBr$) in tetrahydrofuran (THF) as a solvent at -78 °C. Following the successful formation of $Ph_2PC{\equiv}CH$, deprotonation was perfomed using an equivalent amount of *n*-BuLi and further reaction was performed with *N*,*N*'-diisopropylphenyl carbodiimide (Dipp carbodiimide) leading to the formation of the desired lithium salt of the phosphine substituted acetylide amidinate ligand **1** in quantitative yield (Scheme 1). Crystals suitable for the single crystal X-ray diffraction (SC-XRD) analysis were obtained from the concentrated solution of **1** in THF.

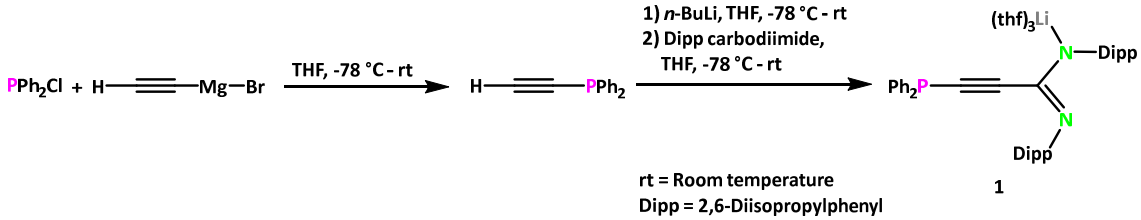

Scheme 1: Synthesis of the lithium salt of the phosphine substituted lithium acetylide amidinate (**1**).

In addition to SC-XRD (Figure 29), compound **1** was characterized by NMR and IR spectroscopy as well as elemental analysis. It was found to crystallize in the monoclinic space group $P2_1/n$ with one molecule in the asymmetric unit. From the structural analysis, it was evident that the Li ion is coordinated by one nitrogen atom of the amidinate ligand and three molecules of THF, indicating four-fold coordination around Li. The Li–N1 bond length was found to be 1.989(2) Å, similar to the previously reported Li–N bond length in $[\{Me_3SiC{\equiv}CC(NDipp)_2\}Li(thf)_3]$ (2.009(6) Å).[166] The N1–C1–N2 bond angle was observed to be 125.5(9)° similar to the reported one, 125.8(3)°.[166]

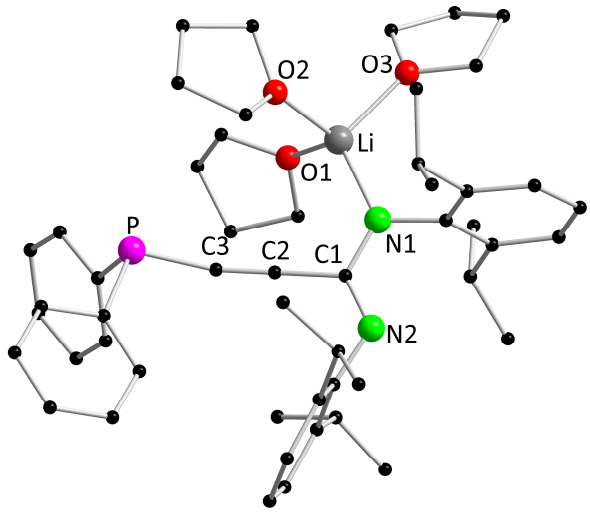

Figure 29: Molecular structure of **1** in the solid state. Hydrogen atoms and non-coordinating solvent molecules are omitted for clarity. Selected bond lengths (Å) and bond angles (°): Li–N1 1.989(2), N1–C1 1.339(1), N2–C1 1.309 (1), P–C3 1.768(1); N1–C1–N2 125.5(9).

In the ^{1}H NMR spectrum of **1** in $CDCl_3$, the coordination of THF molecules was also confirmed by the resonances at δ = 1.29 and 3.55 ppm. Additionally, a resonance at δ = 1.40 ppm was observed for the methyl groups of the Dipp substituents. The characteristic resonance in the $^{31}P\{^{1}H\}$ NMR spectrum was observed at δ = -33.6 ppm for the compound **1**. Further, infrared spectroscopy confirmed the presence of C≡C bond, the stretching vibration of which was observed at $\tilde{\nu}$ = 2165 cm^{-1}.

The obtained lithium salt of ligand **1** was reacted with copper(I) and gold(I) precursors. The reaction of **1** with CuCl was performed in an equimolar ratio at ambient temperature. After workup, the targeted product [{$Ph_2PC{\equiv}CC(NDipp)_2$}$_2Cu_2$] (**2**) was obtained as a light-yellow powder in analytically pure form in 64 % yield.

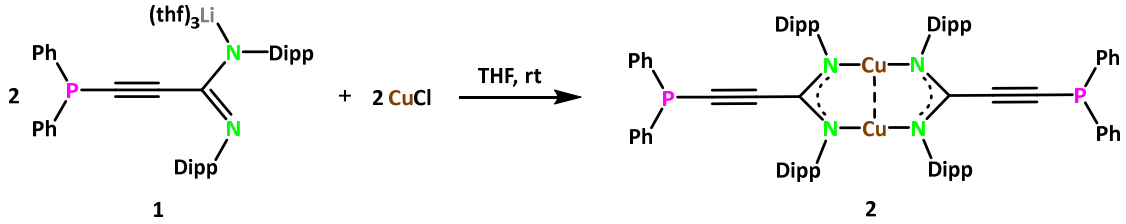

Scheme 2: Synthesis of the copper(I) amidinate complex **2**.

Although single crystals of complex **2** could not be successfully obtained, evidence for the successful synthesis was provided by the electrospray ionization mass spectrometry (ESI-MS).

The molecular ion peak at *m/z* = 1268.5018 in the ESI-MS spectrum is consistent with the expected molecular mass of complex **2**. In the ^{1}H NMR spectrum, significant changes in the chemical shifts were observed compared to the precursor **1**. The methine protons associated with the Dipp groups exhibited an upfield shift from δ = 3.78 ppm (**1**) to δ = 3.47 ppm in complex **2**. Furthermore, the resonances of the methyl protons of the isopropyl groups, which previously appeared as a single doublet at δ = 1.40 ppm in compound **1**, were resolved into two distinct doublets at δ = 1.14 and 1.06 ppm, respectively, in compound **2**. In the ^{31}P{^{1}H} NMR spectrum, the signal was downfield shifted to δ = 19.9 ppm compared to the precursor **1** (δ = -33.6 ppm). Upon excitation with ultra-violet (UV) light, complex **2** exhibited a vibrant yellow luminescence.

Two different synthetic approaches were explored to obtain the gold(I) analogue of complex **2**. However, rather than forming the expected product, both routes resulted in the formation of an unprecedented twelve-membered ring structure **3** (Scheme 3) due to HSAB interactions.[171-172] In the first synthetic approach (Route A, Scheme 3), the reaction of the lithium salt **1** was carried out with [Au(tht)Cl] (tht = tetrahydrothiophene) in THF at ambient temperature forming complex **3** in 74 % yield. In the alternative approach (Route B, Scheme 3), complex **3** could be synthesized from a previously reported acetylene functionalized amidnate Au(I) complex (**4**).[251] This route involved a two-step reaction, beginning with the deprotonation of **4** using *n*-BuLi in THF, followed by subsequent treatment with 2 equivalents of PPh_2Cl, leading to a rearrangement reaction and formation of complex **3** in 67 % yield. The success of this alternative synthetic pathway depicted that complex **3** could be accessed through different reactions, offering a flexible and versatile approach for its preparation.

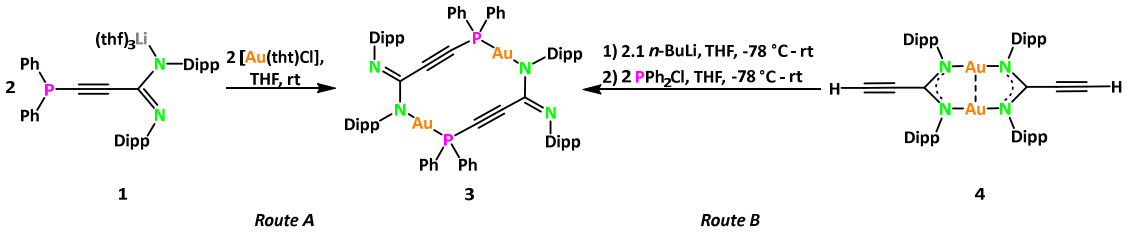

Scheme 3: Synthesis of the gold(I) amidinate complex **3** *via* two different synthetic routes.

Crystals of complex **3** suitable for SC-XRD analysis were obtained from a concentrated solution in dichloromethane (DCM). The structural analysis revealed the presence of a distinctive twelve-membered ring incorporating P–Au–N structural motif (Figure 30). The affinity of Au(I)

for the soft donor atoms played an important role in facilitating the rearrangement and formation of twelve-membered ring. Within the ring, the Au(I) center adopts a linear coordination geometry bonded to one phosphine center from one of the amidinate ligands and one nitrogen atom from the other amidinate ligand with a P–Au–N1 bond angle of 177.9(1)°. The Au–N bond length was determined to be 2.027(3) Å, while the Au–P bond length measured 2.215(10) Å. These bond distances are consistent with previously reported ones in similar gold-containing complexes, such as $[\{(PPh_3)AuC{\equiv}CC(NDipp)_2\}_2Au_2]$, which exhibits Au–N and Au–P distances of 2.020(6) Å and 2.272(2) Å, respectively.[251] Additionally, the structural analysis validated the non-equivalence of the two C–N bonds within the amidinate framework. The C1–N1 bond length was found to be 1.337(5) Å, indicative of single bond character, whereas the C1–N2 bond length, measuring 1.289(5) Å, corresponds to a double bond.

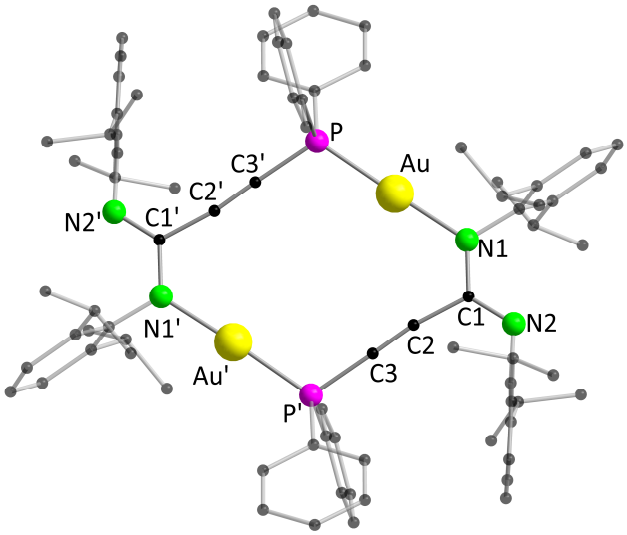

Figure 30: Molecular structure of **3** in the solid state. Hydrogen atoms and non-coordinating solvent molecules are omitted for clarity. Selected bond distances (Å) and angles (°): Au–P 2.215(10), Au–N1 2.027(3), C1–N1 1.337(5), C1–N2 1.289(5); P–Au–N1 177.8(1), Au–P–C3' 112.5(1).

Analysis of the ^{1}H NMR spectrum of complex **3** revealed that there are two distinct sets of resonances present, corresponding to the two non-equivalent Dipp moieties within the molecule. Specifically, a characteristic septet was observed at δ = 3.21 ppm, which was assigned to the methine protons of the Dipp groups attached to the nitrogen atom N1 (Figure 30). On the other hand, a second septet signal appearing at δ = 3.71 ppm corresponded to the methine protons of the Dipp groups bonded to the carbon atom that is

doubly bonded to N2. Furthermore, the resonance in the $^{31}P\{^{1}H\}$ NMR spectrum exhibited a notable shift from δ = -33.6 ppm in compound **1** to δ = 2.1 ppm in complex **3**. The rearrangement of the Au(I) centers from complex **4** to the macrocyclic structure of complex **3** resulted in the loss of aurophilic interactions, which are typically associated with emissive properties in gold complexes. This disruption in Au(I)–Au(I) interactions likely rationalizes the non-emissive nature of complex **3**.

In the next step, the concern was to explore the potential of complex **2** as a metalloligand, leveraging its ability to coordinate with other metal centers through its phosphine groups. Given the affinity of Au(I) for the phosphine ligands, the reactivity of complex **2** was investigated with Au(I) precursors as a pathway towards heterobimetallic complexes. Thus, complex **2** was reacted with [Au(tht)Cl] and [Au(tht)C_6F_5] in THF at ambient temperature. This resulted in the formation of the complexes [{Au(X)$Ph_2PC{\equiv}CC(NDipp)_2$}$_2$$Cu_2$] (X = Cl (**5**), C_6F_5 (**6**)) as heterobimetallic complexes with both Cu(I) and Au(I) centers (Scheme 4). During the course of the reactions, noticeable color changes were observed, transitioning from bright yellow to dark yellow, and the luminescent properties resembled those of the starting material. Single crystals of complexes **5** and **6** were obtained from concentrated DCM solution.

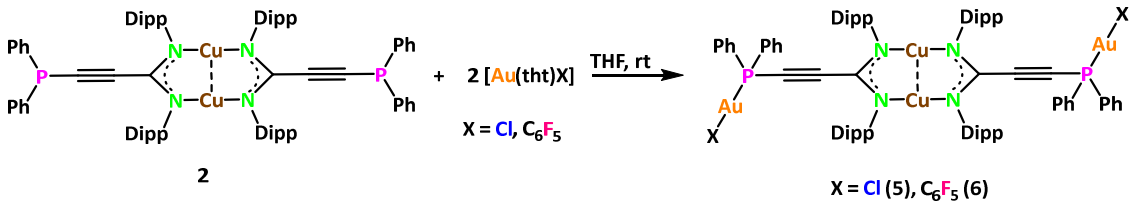

Scheme 4: Reactivity of complex **2** with [Au(tht)Cl] and [Au(tht)C_6F_5].

The analysis revealed that the Au–P bond distances in complexes **5** and **6** differ slightly, measuring 2.226(2) Å in complex **5** and 2.274(9) Å in complex **6** (Figures 31 and 32). Additionally, the Cu–N bond lengths were observed to be nearly identical in both the complexes, with values of 1.887(5) Å and 1.889(5) Å for complex **5**, and 1.876(3) Å and 1.880(3) Å for complex **6**. A notable structural feature of both the complexes was the presence of cuprophilic interactions, with a Cu–Cu separation of 2.552(1) Å in complex **5** and 2.537(8) Å in complex **6**. The Au(I) center was found to be in a nearly linearly coordinated with a bond angle of 175.9(7)° spanned by P–Au–Cl in complex **5** and P–Au–C4 bond angle of 176.5(1)° in complex **6**. Similarly, the Cu(I) centers also exhibited an almost linear coordination

environment, being bonded to the nitrogen atoms of the amidinate ligands with N–Cu–N bond angles of 173.7(2)° and 174.0(12)° in complexes **5** and **6**, respectively. The molecular ion peaks observed at *m/z* = 1732.3630 for complex **5** and *m/z* = 1996.4052 for complex **6** were in excellent agreement with the calculated masses.

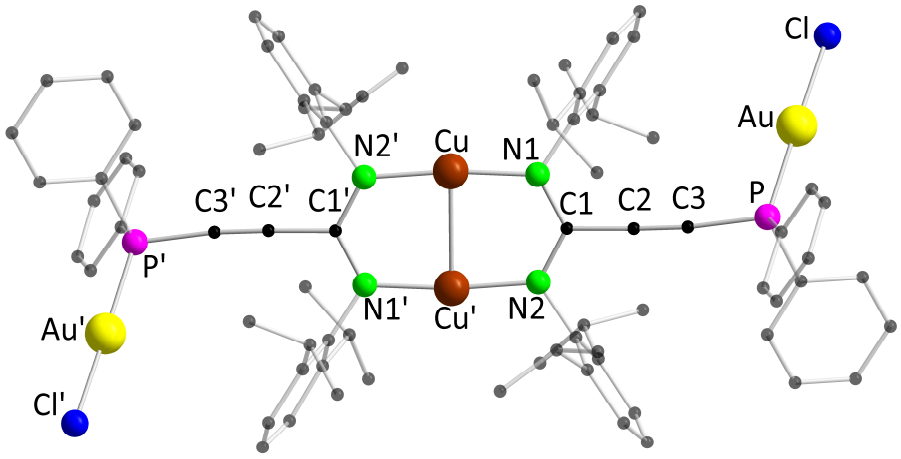

Figure 31: Molecular structure of **5** in the solid state. Hydrogen atoms and non-coordinating solvent molecules are omitted for clarity. Selected bond distances (Å) and angles (°): Au–P 2.226(2), Au–Cl 2.277(2), Cu–N1 1.887(5), Cu–Cu 2.552(13); P–Au–Cl 175.9(7), N1–Cu–N2' 173.7(2).

Additional confirmation of the identity of the synthesized products was obtained through NMR spectroscopy. The ^{1}H NMR spectra of complexes **5** and **6** resembled each other as well as precursor **2** with only minor changes in the chemical shift values. In the ^{31}P{^{1}H} NMR spectrum, phosphorus resonances were observed at δ = 2.1 ppm and δ =15.1 ppm for the complexes **5** and **6**, respectively. These values show a noticeable shift from the phosphorus resonance of the reactant **2**, which was previously observed at δ = 19.9 ppm.

As a complementary approach, an alternative reaction pathway was explored by reversing the order of the synthetic steps to obtain similar heterobimetallic complexes. Instead of introducing the Au(I) centers after the formation of the Cu(I) complex (**2**), the reactivity of the pre-formed cyclic Au(I) complex (**3**) was investigated with various Cu(I) salts.

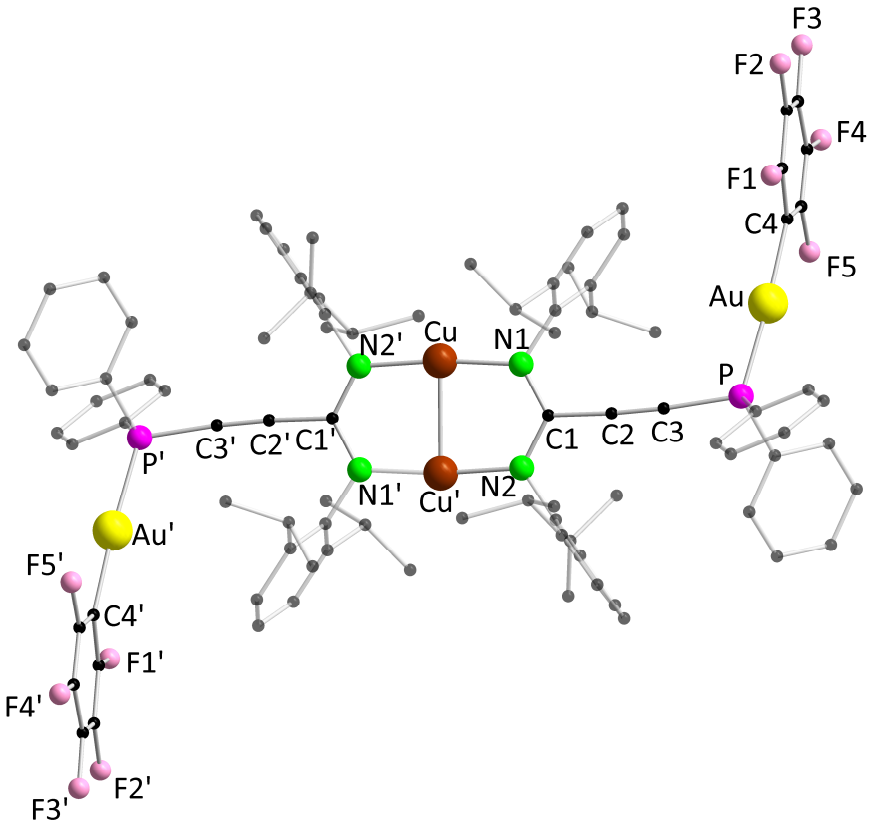

Figure 32: Molecular structure of **6** in the solid state. Hydrogen atoms and non-coordinating solvent molecules are omitted for clarity. Selected bond distances (Å) and angles (°): Au–P 2.274(9), Au–C4 2.055(3), Cu–N1 1.876(3), Cu–Cu 2.537(8); P–Au–C4 176.5(1), N1–Cu–N2' 174.0(1).

Specifically, complex **3** was treated with different CuX salts (X = Cl, Br, I, and mesityl) in THF at ambient temperature for overnight, resulting in a substantial structural rearrangement. As a result, a series of heterobimetallic Cu(I)–Au(I) complexes, denoted as $[\{Au(X)Ph_2PC{\equiv}CC(NDipp)_2\}_2Cu_2]$ (X = Cl (**5**), Br (**7**), I (**8**), Mes (**9**)), were successfully isolated (Scheme 5). These products featured the same $Cu_2(amidinate)_2$ core structure as observed in complex **2**, with the Au(I) centers selectively coordinated to the phosphorus atoms of the phosphine centers. Interestingly, complex **5** was obtained *via* both pathways, using either complex **2** or complex **3** as the precursor. Complexes **5** and **7-9** were obtained in good yields, ranging from 57 % to 67 % starting from the Au(I) precursor **3**. Throughout the course of these reactions, a distinct color change was observed, transitioning from bright yellow to a dark yellow. Furthermore, upon exposure to UV light, all the complexes **5-9** exhibited bright luminescence.

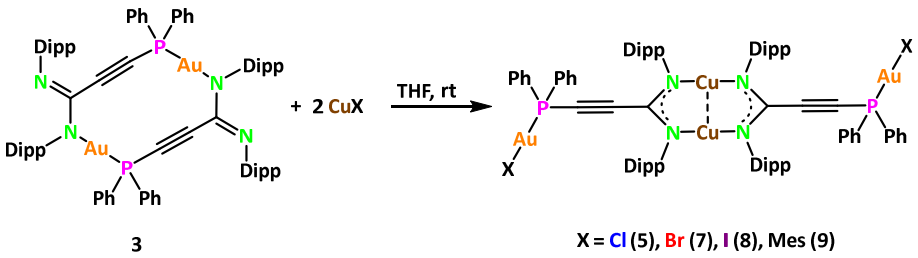

Scheme 5. Reactivity of complex **3** with different Cu(I) salts.

Compounds **7-9** were thoroughly characterized using standard analytical techniques. To gain deeper insight into their molecular architectures, SC-XRD analyses were performed and revealed that all three complexes feature an eight-membered ring at the center of the molecule composed of two amidinate ligand units and two copper ions. This structural motif was consistent with the core framework previously observed in the complexes **2**, **5**, and **6** (Figures 33, 34 and 35). Additionally, the measured Cu–Cu distances were found to be 2.569(1) Å for compound **7**, 2.526(9) Å for compound **8**, and 2.511(8) Å for compound **9**. These values were found to be well within the range typically associated with Cu–Cu distances in cuprophilic interactions.[240]

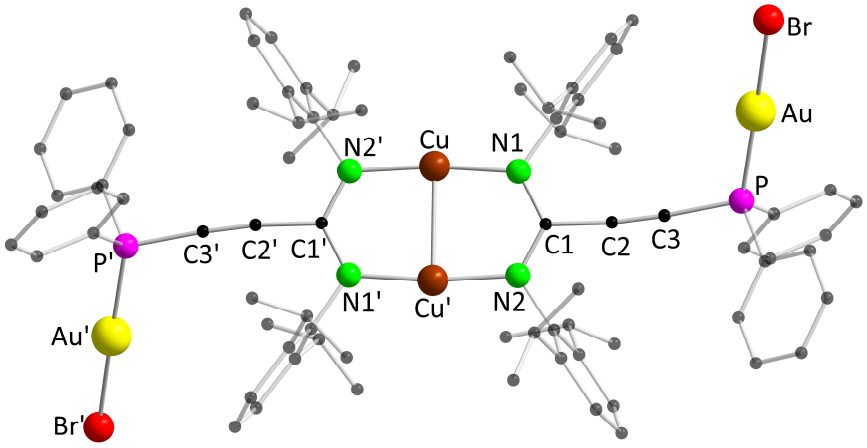

Figure 33: Molecular structure of **7** in the solid state. Hydrogen atoms and non-coordinating solvent molecules are omitted for clarity. Selected bond distances (Å) and angles (°): Au–P 2.228(2), Au–Br 2.405(7), Cu–N1 1.884(5), Cu–Cu 2.569(14); P–Au–Br 173.4(5), N1–Cu–N2’ 173.1(2).

The characterization of complexes **7-9** was further supported by NMR studies and slight differences were observed among the three complexes in the ^{1}H NMR spectra.

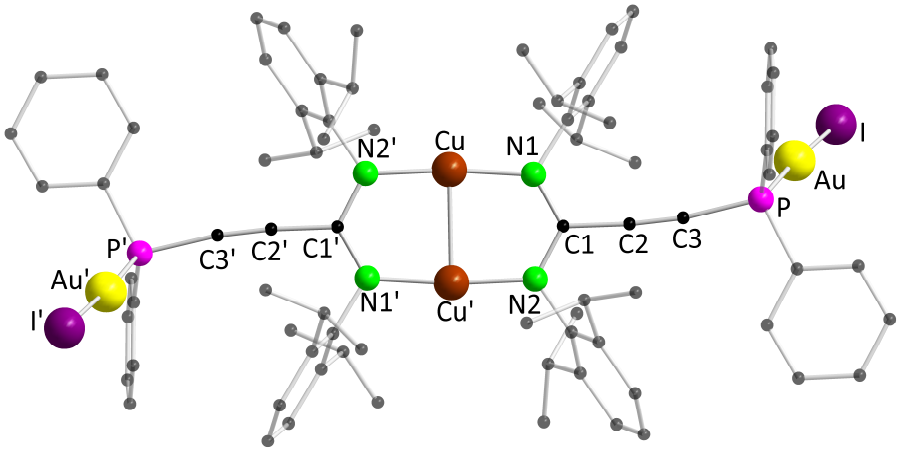

Figure 34: Molecular structures of **8** in the solid state. Hydrogen atoms and non-coordinating solvent molecule are omitted for clarity. Selected bond distances (Å) and angles (°): Au–P 2.248(1), Au–I 2.550(3), Cu–N1 1.882(3), Cu–Cu 2.526(9); P–Au–I 177.9(3), N1–Cu–N2' 174.3(1).

Notably, complex **9** exhibited additional expected resonances corresponding to the methyl groups of mesityl substituent and two distinct sets of resonances were observed for the *ortho*- and *para*-methyl groups at δ = 2.42 ppm and δ = 2.24 ppm, respectively. Additionally, resonances corresponding to the aromatic protons of the mesityl groups were also observed.

In contrast to the ^{1}H NMR spectra, more pronounced differences were evident in the ^{31}P{^{1}H} NMR spectra of these compounds. The observed ^{31}P{^{1}H} chemical shifts for compounds **7**, **8**, and **9** were δ = 4.3 ppm, δ = 8.5 ppm, and δ = 18.8 ppm, respectively. Further confirmation of the successful formation of these heterobimetallic complexes was obtained through ESI-MS. The molecular ion peaks observed at *m/z* = 1820.2576, 1916.2322 and 1900.6025 for the complexes **7**, **8**, and **9**, respectively, were in excellent agreement with the calculated masses.

Building upon the insights gained from previous reactions (Schemes 2-5), a distinct coordination preference for the metal centers within these heterobimetallic systems was observed. Specifically, Cu(I) demonstrated an affinity for bonding with the nitrogen atoms of the amidinate ligand, whereas Au(I) selectively coordinated to the phosphine group which is in accordance with Pearson's HSAB principle.

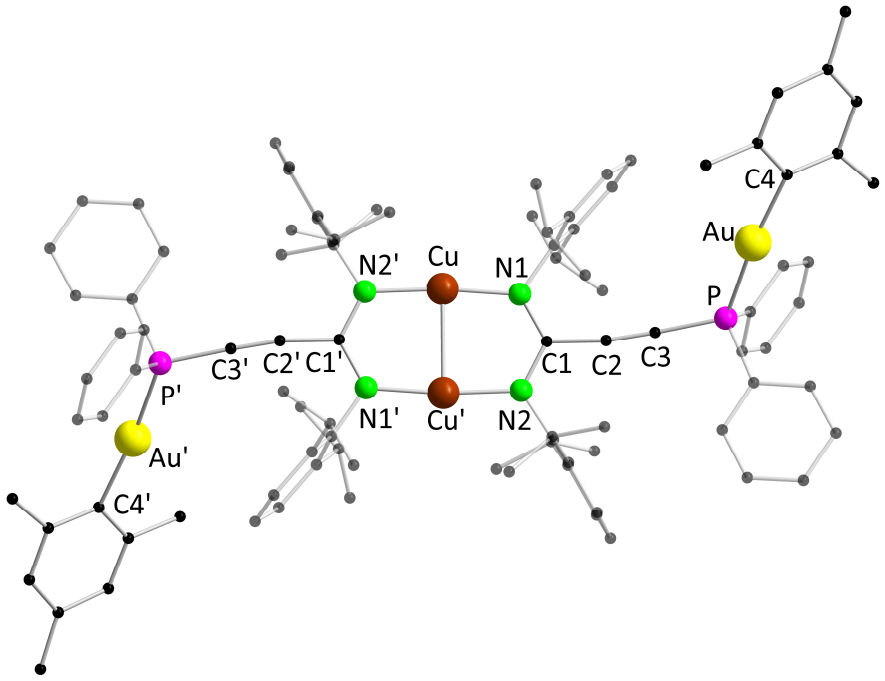

Figure 35: Molecular structure of **9** in the solid state. Hydrogen atoms and non-coordinating solvent molecules are omitted for clarity. Selected bond distances (Å) and angles (°): Au–P 2.285(2), Au–C4 2.069(4), Cu–N1 1.869(3), Cu–Cu 2.511(8); P–Au–C4 175.8(2), N1–Cu–N2' 174.5(1).

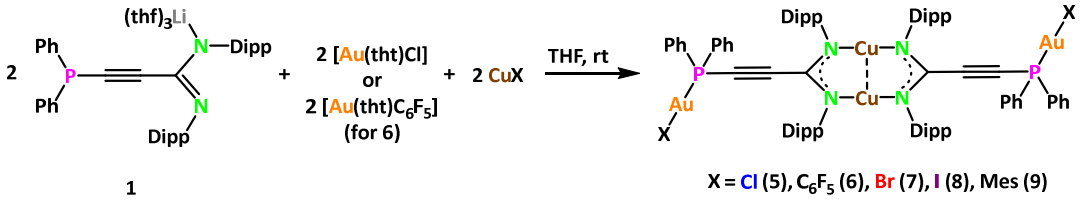

Scheme 6: One-pot synthesis of compounds **5**-**9**.

Motivated by these observations, a more efficient one-pot synthetic approach was developed incorporating all the fundamental building blocks for the formation of complexes **5-9**. In this procedure, the lithium salt precursor **1** was reacted directly with [Au(tht)Cl] or [Au(tht)C_6F_5] for complex **6**, along with a suitable CuX precursor (X = Cl (**5**), Br (**7**), I (**8**), Mes (**9**)) at ambient temperature in THF, as shown in Scheme 6. This one-pot synthetic strategy resulted in a substantial increase in the reaction efficiency, leading to higher yields of the desired heterobimetallic complexes. The complexes **5-9** were obtained in yields ranging from approximately 60 % to 85 %, which represented a considerable increase compared to the yields achieved using the conventional stepwise approach.

3.1.3 Photophysical Studies

The photophysical properties of the synthesized complexes were thoroughly investigated to gain insights into their luminescence behavior. Notably, both the lithium salt **1** and the gold(I) complex **3** did not exhibit any significant luminescence, neither in the solid state nor in solution. A detailed analysis of the absorption characteristics of complex **3** further supports this observation. The absorption onset of **3** was found to be blue-shifted (Figure 36) to about 325 nm compared to about 350 nm for the remaining complexes. This blue-shift and the absence of intense luminescence can be attributed to the lack of low-energy excited states typically associated with metallophilic interactions.[253-254] In many coinage metal complexes in the +I oxidation state, such interactions play a crucial role in stabilizing the emissive excited states.[255]

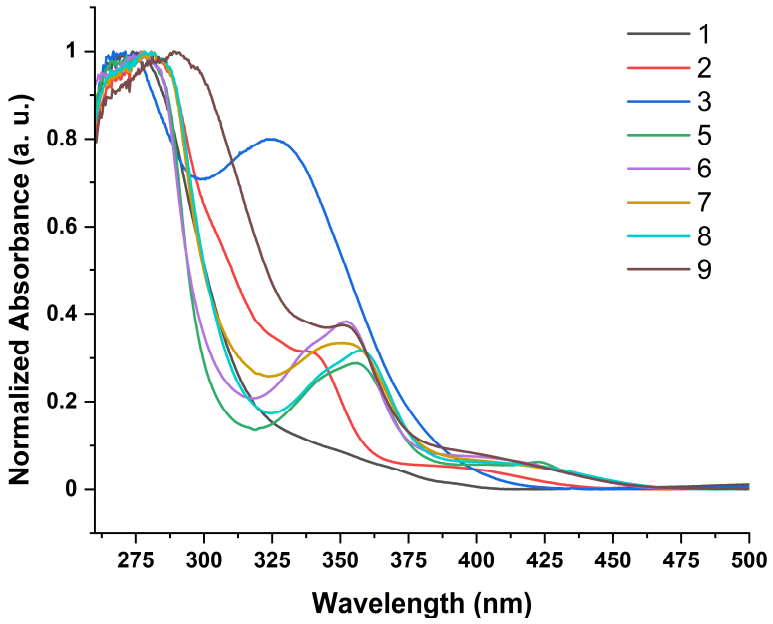

Figure 36: Absorption spectra of compounds **1**-**9** in dichloromethane at ambient temperature.

On the other hand, the luminescent metalloligand **2** and the heterobimetallic complexes **5**-**9** displayed notable photophysical properties. To evaluate their luminescence characteristics, these complexes were subjected to photoluminescence (PL) studies in both solution and the solid state. The acquired PL data, summarizing their emission wavelengths, quantum yields, and lifetimes, are compiled in Table 1.

The PL emission and excitation (PLE) spectra of the metalloligand **2** are presented in Figure 37. The emission profile of **2** exhibits a distinct vibronic structure at 77 K, observed both in

solution and in the solid state. The recorded emission spectra have the respective maximum centered at 490 nm. The analysis of the PL behavior of **2** revealed a noticeable decline in emission intensity as the temperature increased. Notably, this decrease in PL intensity was found to be more pronounced in solution than in the solid state. This difference in thermal quenching can be attributed to enhanced thermally activated non-radiative relaxation pathways in the solution, resulting in a lower emission intensity at ambient temperature.

The decay lifetimes of the excited states of **2** were determined to be 71 µs in solution and 47 µs in the solid state at 295 K. The relatively long-lived excited-state lifetimes strongly indicate that the emission originates from a phosphorescence mechanism.

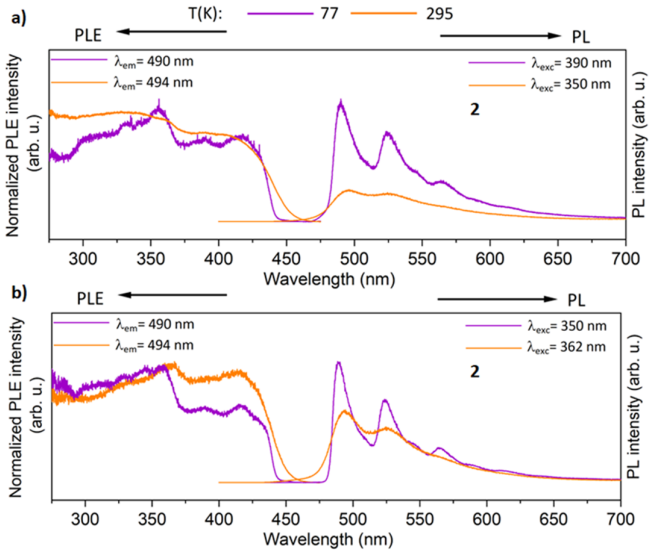

Figure 37: Normalized photoluminescence excitation (PLE) and emission (PL) spectra of the metalloligand **2** at 295 K and 77 K (a) in benzene, (b) in the solid state. PLE and PL spectra were recorded at the depicted wavelengths (λ_{em} and λ_{ex}).

The PL properties of the heterobimetallic complexes **5**, **7**, and **8**, which differ in their anionic halogen ligands (Cl, Br, and I, respectively), were investigated, and the recorded excitation and emission spectra of these complexes exhibit notable similarities in their spectral profiles. In DCM solution, these complexes display excitation maxima at around 450 nm. In addition, the shape of the excitation spectra varies depending on the selected emission wavelengths. The emission spectra at 77 K revealed a vibronic structure, whereas at 295 K, the emissions became broader. A key observation from the PL data is that the emission maxima of **5**, **7**, and **8** are red-shifted in comparison to the metalloligand **2**, suggesting that the presence of the

Au(I) and halogen ligands significantly influences the electronic transitions of these complexes.

From further analysis, a strong decrease in the PL intensity was observed with increasing temperature. A distinct trend in the emission intensity was observed among the three complexes, wherein the intensity progressively diminishes when moving from **5** (Cl) to **7** (Br) and further to **8** (I) (Figure 38a). This gradual reduction in PL intensity across the halogen series can be attributed to the heavy atom effect.[256] The presence of heavier halogen atoms enhances spin-orbit coupling, thereby promoting non-radiative relaxation processes and leading to the quenching of luminescence.[257] In addition to the solution-state studies, solid-state PL measurements were conducted using polycrystalline samples (Figure 38b).

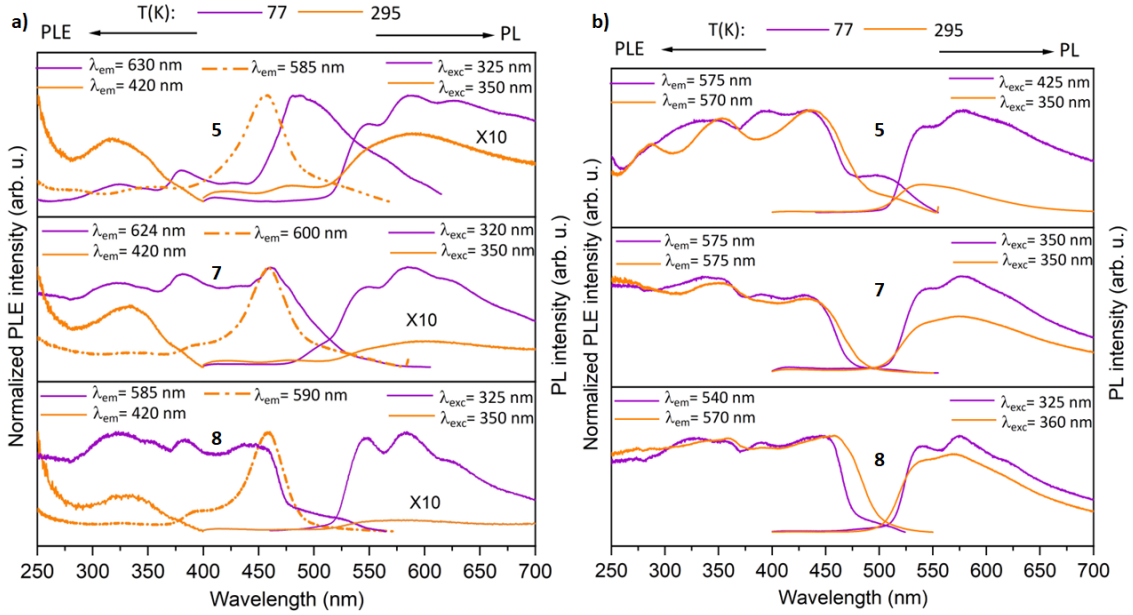

Figure 38: Normalized photoluminescence excitation (PLE) and emission (PL) spectra of the heterobimetallic complexes **5**, **7**, and **8** in (a) DCM solutions and (b) solid state at 295 K and 77 K. PLE and PL spectra were recorded at the depicted wavelengths (λ_{em} and λ_{ex}).

The emission maxima in the solid state at 77 K exhibit a slight red-shift compared to the solution phase spectra, yet the overall emission profiles remain consistent. However, an interesting reversal in PL intensity trends was noted in the solid-state measurements. Unlike in solution, the solid-state PL intensities follow the opposite pattern, increasing in the order **8** > **7** > **5** (Figure 38b). Notably, the gold(I) iodo complex **8** retains an emission intensity comparable to that observed at 77 K, whereas the chloro (**5**) and bromo (**7**) analogues exhibit

a significant decline in the luminescence at 295 K. The inverse trend in the solid-state luminescence could be primarily attributed to the dominant influence of molecular packing effects in the solid state, which appears to outweigh the impact of the heavy atom effect.

The gold(I) complex **9**, which contains a mesityl ancillary ligand, exhibits a broad emission spectrum in both solution and solid-state measurements (Figure 39). A noticeable decline in PL intensity is observed as the temperature increases, indicating a temperature-dependent quenching. In contrast, complex **6** maintains its emission efficiency in the solid state, with intensity levels remaining comparable to those observed at 77 K. The presence of fluorine groups in complex **6** results in a blue-shift in its emission spectra relative to the other bimetallic complexes which is in agreement with previously reported observations.[258]

It is also important to note that, for both complexes **6** and **9**, the emission profile remains consistent regardless of the excitation wavelength (Figure 39). Furthermore, the nature of the PL in complexes **6** and **9** has been confirmed to be phosphorescence, as evidenced by the microsecond emission lifetimes of their excited states.

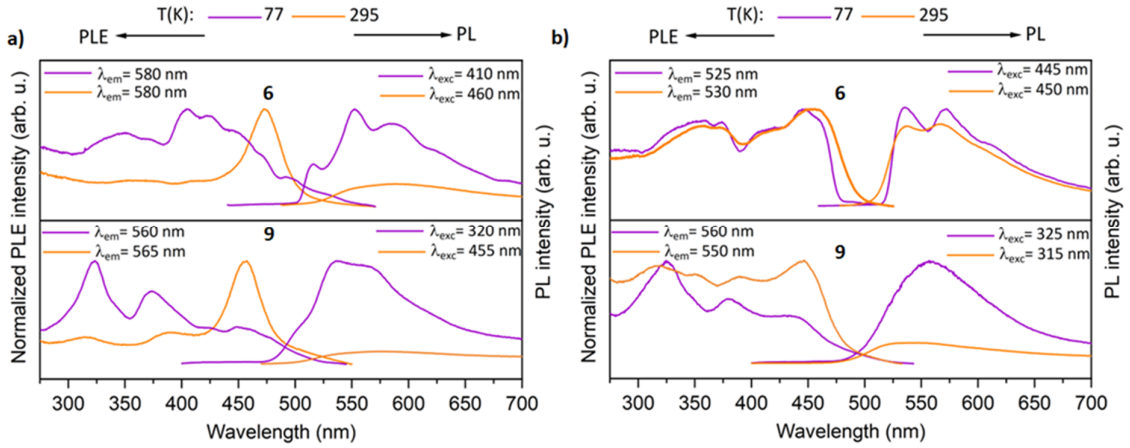

Figure 39: Normalized photoluminescence excitation (PLE) and emission (PL) spectra of the bimetallic complexes **6** and **9** in (a) DCM solutions and (b) solid state at 295 K and 77 K. PLE and PL spectra were recorded at the depicted wavelengths (λ_{em} and λ_{ex}).

The quantum yields of the synthesized complexes were found to be below 10 % at 295 K. Among these, the heterobimetallic complexes demonstrated even lower quantum yields in comparison to the metalloligand **2**, suggesting a reduced quantum efficiency in these heterobimetallic systems. Additionally, the excited states responsible for the photoactivity of

the heterobimetallic complexes exhibited significantly shorter lifetimes, decaying more rapidly than those of the metalloligand **2** (Table 1). This non-radiative quenching of luminescence observed in heterobimetallic complexes **5-9** is likely attributed to the presence of an additional metal center, which introduces extra rotational degrees of freedom within the molecular structure. These additional modes of motion can facilitate non-radiative relaxation pathways, thereby diminishing the overall luminescence efficiency.[259]

Table 1: Photophysical data of the metalloligand **2** and the bimetallic complexes **5-9** in solution and in the solid state.

Compound	**Solution**				**Solid**				
	Lifetimes of the excited state (µs)		λ_{max} (nm)		Lifetimes of the excited state (µs)		λ_{max} (nm)		QY (%)
	295 K	77 K	295 K	77 K	295 K	77 K	295 K	77 K	
2	71	153	490	490	47	144	490	490	9
5	-*	28	540	575	12	17	535	580	3
6	9	51	560	545	26	36	530,	530,	7
7	-*	20	570(br)	575	14	19	570	580	6
8	8	39	570(br)	575	15	25	570	580	6
9	-*	33	550	535	21	24	535	560	8

*– The measured values are below the detection limit of our detector.

3.2 Syntheses and characterization of heterobimetallic Cu(I)–Rh(I) and Cu(I)–Ir(I) complexes: Photophysical studies and catalytic application

3.2.1 Introduction

Heterobimetallic complexes are of great interest for applications in optoelectronics,[217] catalysis,[215-216] molecular magnetism,[260-261] and medicine.[218,262] In some cases, the complexes consist of two different metal centers, either directly bonded or bridged by orthogonal ligands.[223,251,263-264] In systems utilizing orthogonal ligands, the distinct affinities of metals for different ligand segments can be exploited, often guided by the HSAB principle.[171-172,226]

Numerous Cu(I)-based heterobimetallic complexes incorporating other transition metals have been successfully synthesized using the orthogonal ligand strategy in accordance with HSAB preferences.[265-268] In particular, copper amidinate complexes are known to predominantly form planar dimers, bridged through linear N–Cu–N units.[243-244,246-247] These dimeric structures, denoted as Cu_2L_2 (L = amidinate ligand), are stabilized by cuprophilic interactions, an intrinsic property of d^{10} metal centers, which are crucial for maintaining both structural stability and electronic characteristics.[116,240,269]

Heterobimetallic transition metal complexes offer a valuable advantage in catalysis, especially for tandem catalysis, where multiple catalytic cycles are operating sequentially or simultaneously.[270-273] This approach can enhance reaction efficiency, reduce waste, and improve overall productivity and selectivity in organic synthesis.[274-275] Copper containing heterobimetallic complexes have been employed in a variety of catalytic transformations, including hydroboration, alkynylation, CO_2 reduction to ethanol, and alcohol oxidation.[276-279] Alcohols are essential substrates or intermediates in organic synthesis,[280-281] pharmaceuticals,[282] and agrochemicals.[283] Traditionally, aldehydes and ketones are converted into alcohols using stoichiometric reducing agents such as $NaBH_4$ and $LiAlH_4$,[284-285] or through catalytic hydrogenation with molecular hydrogen.[286] As a more sustainable alternative, catalytic transfer hydrogenation (TH) allows for such conversions using hydrogen donors like formic acid, isopropanol, methanol, ethanol, or dihydroanthracene.[287] Transition metal complexes based on Co, Ni, Ru, Rh, Pd, and Ir have been extensively studied for TH applications.[288-293]

Figure 40 presents selected iridium-phosphine complexes employed in TH catalysis. Complexes a and b feature Ir(III) centers, while complexes c and d contain Ir(I) as the active metal site. In 2006, an air-stable iridium chlorodihydride complex (Figure 40a) was reported to catalyze TH of ketones in 2-propanol.[294] Later, in 2011, Ir(III) complexes with abnormal NHCs and phosphines (Figure 40b) were shown to catalyze not only TH of ketones and enones but also C–C coupling of alcohols and dehydrogenation of benzyl alcohol.[295] Ir(I) cationic complexes (Figure 40c), developed by Lugo *et al.*, were similarly active in ketone TH.[296] Notably, Andersson *et al.* in 2020 introduced Ir(I) NHC-phosphine complexes (Figure 40d) that enabled TH of ketones under ambient conditions without the need for a base additive.[297]

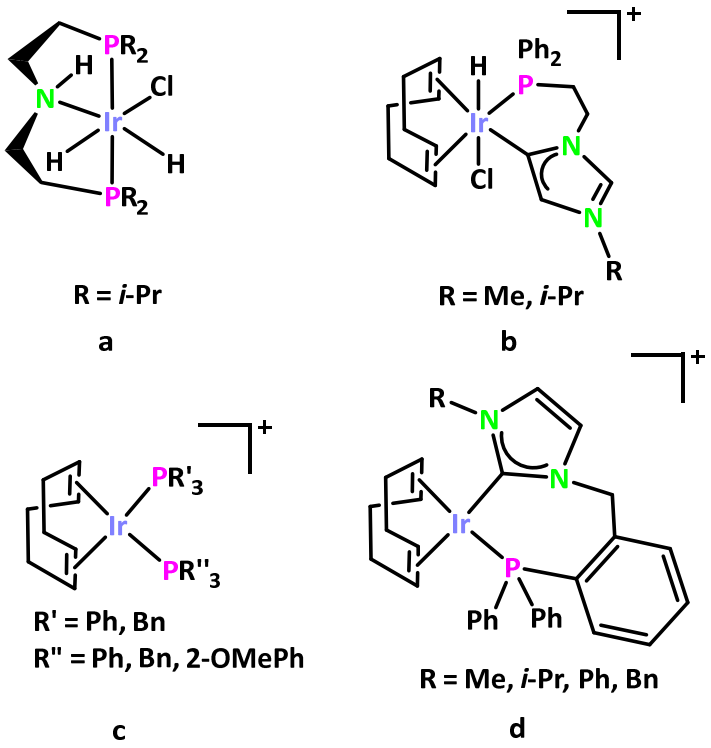

Figure 40: Selected examples of Ir(III) and Ir(I) complexes used for TH catalysis.

In this chapter, the syntheses of heterobimetallic Cu(I)–Rh(I) and Cu(I)–Ir(I) complexes stabilized by a phosphine substituted acetylide amidinate ligand have been reported. The synthetic pathway is detailed in step by step including both individual metal complex preparations and a one-pot synthetic approach. Furthermore, the application of a Cu(I)–Ir(I) complex as a catalyst for the transfer hydrogenation of aryl aldehydes has been demonstrated and studied the luminescent properties.

3.2.2 Syntheses and characterization of Cu(I)–Rh(I) and Cu(I)–Ir(I) complexes

The synthesis of the heterobimetallic complexes **10** and **11** was carried out through an overnight reaction under ambient conditions. The reaction involved a previously synthesized copper amidinate complex, Cu_2L_2 (L = $Ph_2PC{\equiv}CC(NDipp)_2$, Dipp = *N*,*N*'-2,6-diisopropyl-phenyl) (**2**), which functions as a metalloligand.[263] The reaction was conducted with an equimolar amount of either chloro(1,5-cyclooctadiene)rhodium(I) dimer ($[Rh(cod)Cl]_2$) or chloro(1,5-cyclooctadiene)iridium(I) dimer ($[Ir(cod)Cl]_2$), respectively, in THF at ambient temperature. After workup, the heterobimetallic complex Cu(I)–Rh(I) **10** was obtained as a yellow-colored solid in 79 % yield. Similarly, the Cu(I)–Ir(I) complex **11** was obtained as an amber-colored solid with an overall yield of 74 %.

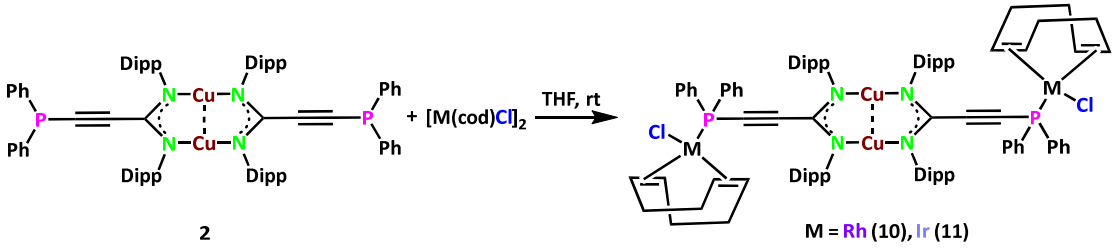

2

Scheme 7: Synthesis of heterobimetallic Cu(I)–Rh(I) (**10**) and Cu(I)–Ir(I) (**11**) complexes from a Cu(I) metalloligand (**2**).

Complexes **10** and **11** were subjected to structural and spectroscopic characterization using a combination of SC-XRD, NMR spectroscopy, IR spectroscopy, and elemental analysis. The structural analysis revealed that both the complexes are structurally similar and crystallize in the triclinic space group $P\bar{1}$. In the molecular framework of these heterobimetallic complexes, the Rh(I) and Ir(I) centers are coordinated by both the phosphine group from the metalloligand and the COD ligand, in addition to a chloride (Figures 41 and 42). One of the structural features observed in **10** and **11** is the presence of a Cu–Cu interaction within the central Cu_2L_2 unit where the Cu–Cu bond distances were determined to be 2.462(10) Å in complex **10** and 2.465(6) Å in complex **11**, which fall well within the range of cuprophilic interactions.[240]

Furthermore, the N–Cu–N units in both the structures exhibit a nearly linear geometry, with a bond angle of approximately 175° which closely resembles the geometries previously observed in Cu(I)–Au(I) systems.[263] The bond distances for the Rh–P and Ir–P interactions were measured to be 2.289(2) Å and 2.284(9) Å for complexes **10** and **11**, respectively. These values are nearly identical to each other and are in excellent agreement with those reported

for structurally related complexes.[298-301] Additionally, the P–Rh–Cl and P–Ir–Cl bond angles were found to be 91.2(6)° and 92.2(3)° in complexes **10** and **11**, respectively. These angles are close to the ideal right angle, further confirming the expected coordination geometry around the Rh(I) and Ir(I) centers.

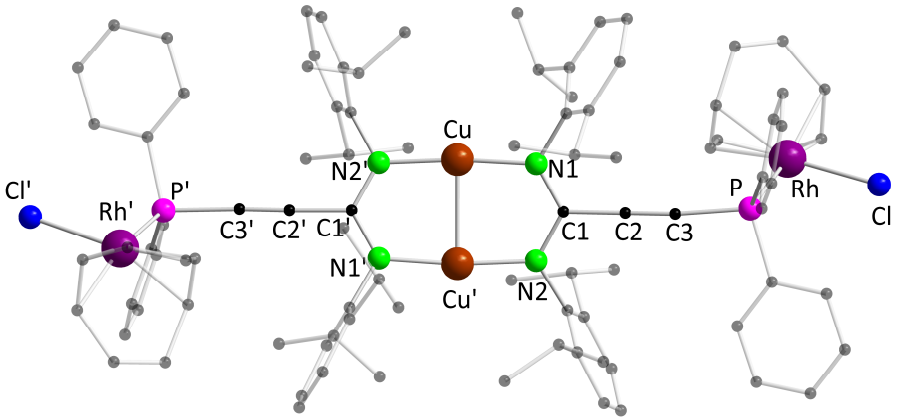

Figure 41: Molecular structure of **10** in the solid state. Hydrogen atoms and non-coordinating solvent molecules are omitted for clarity. Selected bond distances (Å) and angles (°): Rh–P 2.289(2), Rh–Cl 2.371(2), Cu–N1 1.870(5), Cu–Cu 2.462(1); P–Rh–Cl 91.2(6), N1–Cu–N2' 173.8(2).

The ^{1}H NMR spectral analysis of complexes **10** and **11** indicates that their solid-state structures are well retained in the solution containing the characteristic resonances. The Cu_2L_2 core displays resonances that closely resemble the previously reported ones, with only slight changes in the chemical shifts.[263] In these complexes, the isopropyl arms of the Dipp moiety give rise to a septet at δ = 3.28 ppm for complex **10** and at δ = 3.32 ppm for complex **11**. Additionally, the methyl groups of the Dipp moiety show a characteristic doublet around δ = 1.0 ppm in both the complexes. Additionally, three sets of signals, were observed at δ = 2.75, 2.27–2.06 and 1.98–1.78 ppm for complex **10** and at δ = 2.33, 2.11–1.88 and 1.82–1.45 ppm for complex **11** which can be attributed to cod protons.

Furthermore, in the ^{31}P{^{1}H} NMR spectrum of complex **10**, a well-defined doublet was observed at δ = 12.3 ppm, with a $^{1}J_{P\text{-}Rh}$ coupling constant of 158.5 Hz, confirming the interaction between phosphorus and the rhodium center. For complex **11**, a singlet was detected at δ = 4.1 ppm, consistent with the presence of the iridium center.

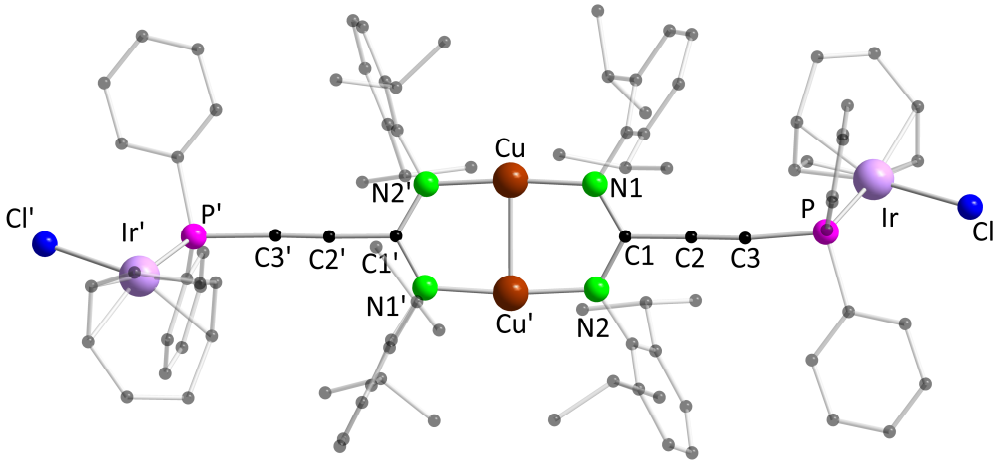

Figure 42: Molecular structure of **11** in the solid state. Hydrogen atoms and non-coordinating solvent molecules are omitted for clarity. Selected bond distances (Å) and angles (°): Ir–P 2.284(9), Ir–Cl 2.353(9), Cu–N1 1.870(3), Cu–Cu 2.465(6); P–Ir–Cl 92.2(3), N1–Cu–N2' 173.9(1).

The structural analysis of complexes **10** and **11** provided an insight into the conformation of the eight-membered metallacyclic ring, consisting of two copper atoms, two carbon atoms, and four nitrogen atoms from the amidinate ligand. The observation was made regarding the planarity of this metallacyclic framework, which differs notably from previously reported Cu_2Au_2 complex (**8**).[263] In the case of the Cu_2Au_2 system, the corresponding eight-membered ring has been reported to adopt a perfectly planar conformation, with a torsional angle of precisely 0° (Figure 43c). This indicates a completely flat arrangement of the involved atoms within the ring. However, our findings reveal that complexes **10** and **11** deviate from this behavior, exhibiting a non-planar conformation instead. For complex **10**, the torsional angle made by the four nitrogen atoms (N1–N2–N1'–N2') was determined to be 19.7° (Figure 43a). Similarly, complex **11** also displays a comparable non-planar conformation, with a slightly lower torsional angle of 19.5° (Figure 43b). This deviation from planarity signifies a noticeable structural distortion compared to the Cu_2Au_2 counterpart.

The sterically demanding cod ligand on Rh and Ir forces the Dipp groups on the amidinate to distort, so the Dipp groups on the two opposing amidinate ligands need to rearrange slightly to avoid clashing, leading to the non-zero N1–N2–N1'–N2' torsion angle in complexes **10** and **11**.

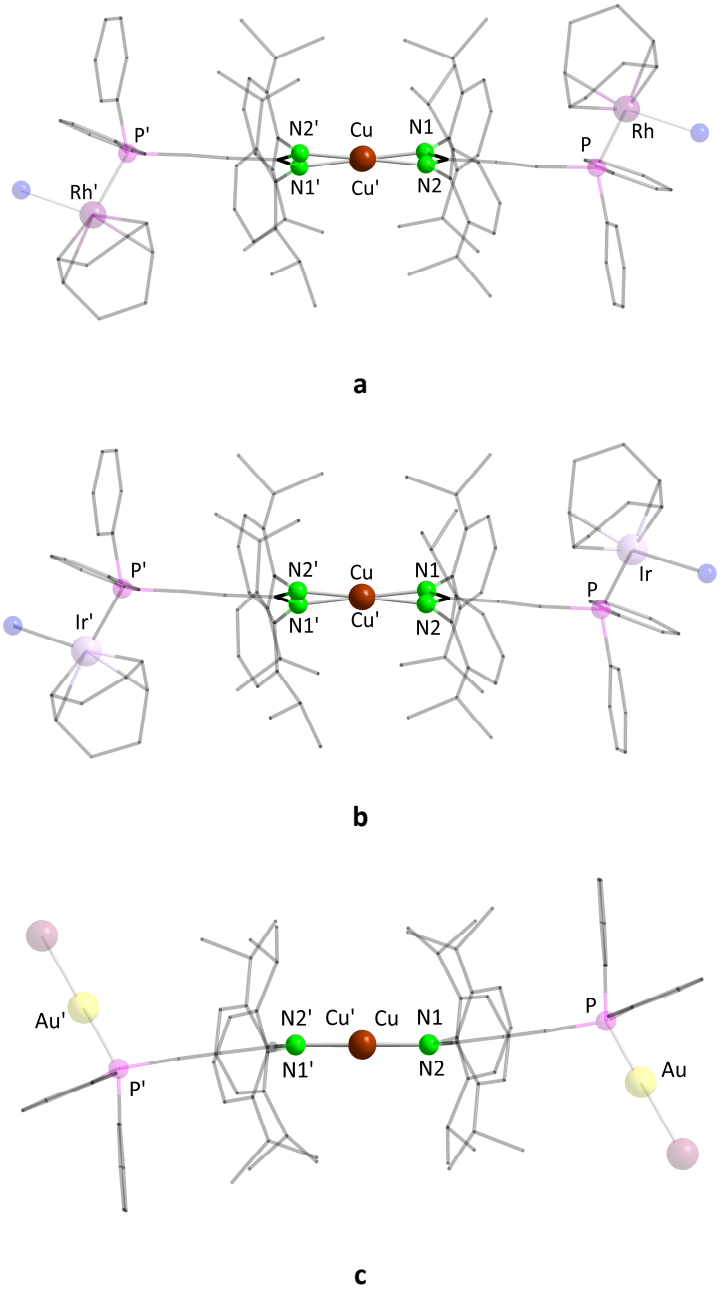

Figure 43: Comparison of the torsional angle of complexes **10** and **11** to the Cu_2Au_2 complex (**8**).

Furthermore, the lithium salt of the phosphine-substituted acetylide amidinate was reacted with $[Rh(cod)Cl]_2$ or $[Ir(cod)Cl]_2$ in THF for 12 hours, resulting in the complexes **12** and **13**, respectively, in quantitative yield (Scheme 8). Despite the successful synthesis of complexes **12** and **13**, their crystallization and full characterization proved to be challenging. The lack of suitable single crystals prevented SC-XRD analysis, and further spectroscopic characterization remained inconclusive. Thus, hydrolysis of complexes **12** and **13** was attempted to obtain their

corresponding protonated amidinate derivatives, resulting complexes **15** and **16**, respectively (Scheme 8). The complexes **15** and **16** were crystallized by layering *n*-pentane to the saturated toluene solutions. An alternative synthetic approach was also employed for the preparation of complexes **15** and **16**, which involved the reaction of the protonated amidinate ligand (**14**) with $[Rh(cod)Cl]_2$ and $[Ir(cod)Cl]_2$, respectively. The precursor, compound **14**, was synthesized by hydrolysis of the lithium salt of the ligand (Scheme 8), leading to the formation of the protonated amidinate species. After hydrolysis, compound **14** was crystallized from a concentrated solution of THF.

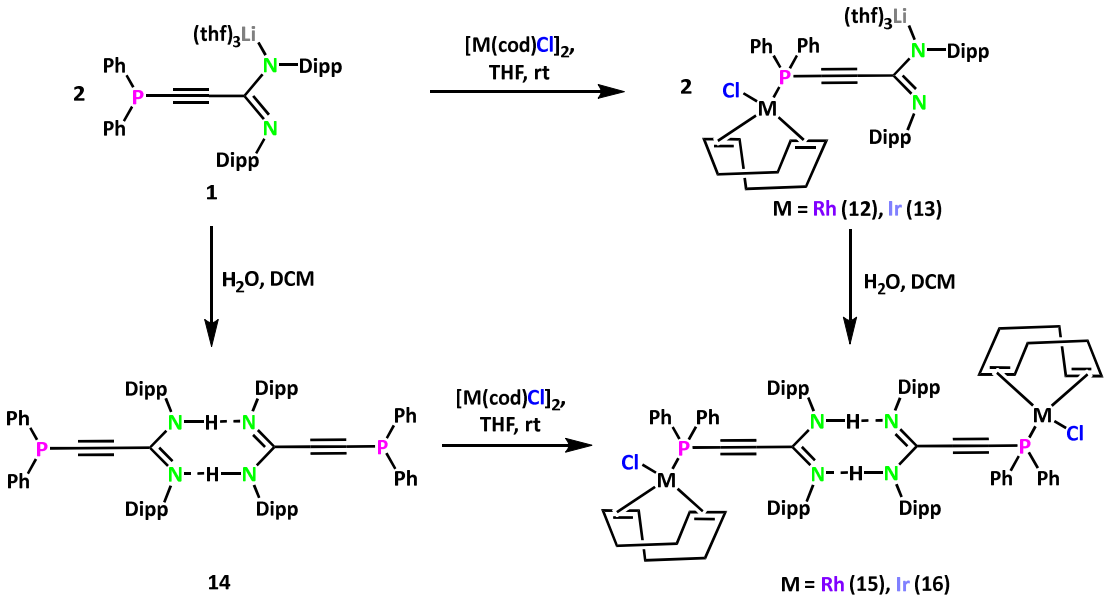

Scheme 8: Synthesis of complexes **12**-**16**.

Detailed structural analysis of compound **14** revealed that it exists as a dimeric species, wherein two ligand units are interconnected through hydrogen bonding interactions (Figure 44). The H···N bond lengths within the hydrogen-bonded dimer were measured to be 1.976(7) Å and 1.963(8) Å, indicating strong interactions between the ligand units. The N1–C1 bond length was determined to be 1.294(3) Å, while the N2–C1 bond length measured 1.321(3) Å. The difference in these bond lengths suggests distinct bonding characteristics, where the N1–C1 bond exhibits double bond character, while the N2–C1 bond length is more consistent with a single bond. Additionally, the structural data revealed that the phosphine within compound **14** is bonded to C3, with a P–C3 bond length of 1.738(3) Å and has not been

oxidized. The N1–C1–N2 bond angle was measured to be 120.5(2)°, indicative of sp^2 hybridization at the C1 carbon center.

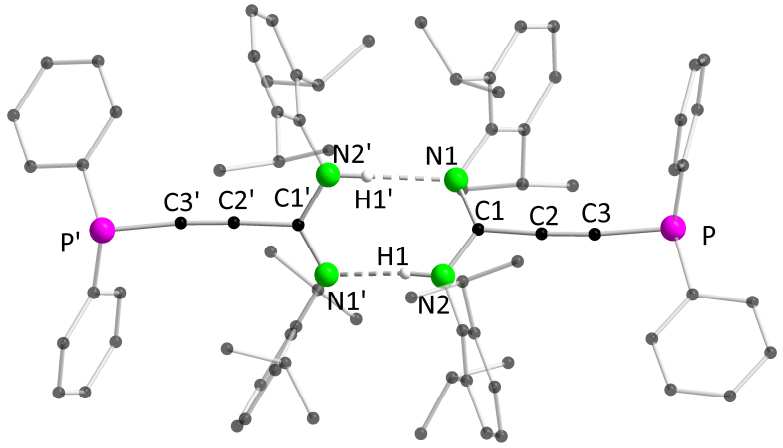

Figure 44: Molecular structure of **14** in the solid state. Hydrogen atoms (except N–H proton) and non-coordinating solvents are omitted for clarity. Selected bond distances (Å) and angles (°): P–C3 1.738(3), C1–N1 1.294(3), C1–N2 1.321(3); N1–C1–N2 120.5(2).

From a structural perspective, the overall bonding environment within complexes **15** and **16** closely resembles that observed in complexes **10** and **11**, with the key distinction being the absence of Cu ions in the molecular framework (Figure 45). Despite the structural variation, the metal-phosphorus bond distances remain consistent between the two sets of complexes. The Rh–P and Ir–P bond lengths were determined to be 2.285(2) Å and 2.289(13) Å, in complexes **15** and **16**, respectively. These values show minimal deviation when compared to the corresponding bond lengths in complexes **10** and **11**, suggesting that the absence of Cu does not significantly influence the metal-phosphorus bonding interaction. Similarly, the bond angles spanned by P–Rh–Cl and P–Ir–Cl in complexes **15** and **16** were found to be 91.2(6)° and 92.3(5)°, respectively. These values are in close agreement with those observed in complexes **10** and **11**, further underlining the structural similarity in coordination geometry across these complexes, regardless of the presence or absence of Cu.

Additionally, complexes **15** and **16** were observed to adopt a dimeric structure, similar to compound **14**, wherein the N–H···N units participate in hydrogen bonding interactions. The measured H···N bond distances were determined to be 2.056(1) Å and 2.071(1) Å in complexes **15** and **16**, respectively. Notably, these bond distances are slightly elongated compared to the corresponding H···N distances in compound **14**, yet they remain well within the range of

reported hydrogen bond lengths for similar systems.[302] This slight elongation could be attributed to subtle electronic or steric effects introduced by the metal coordination environment in complexes **15** and **16**.

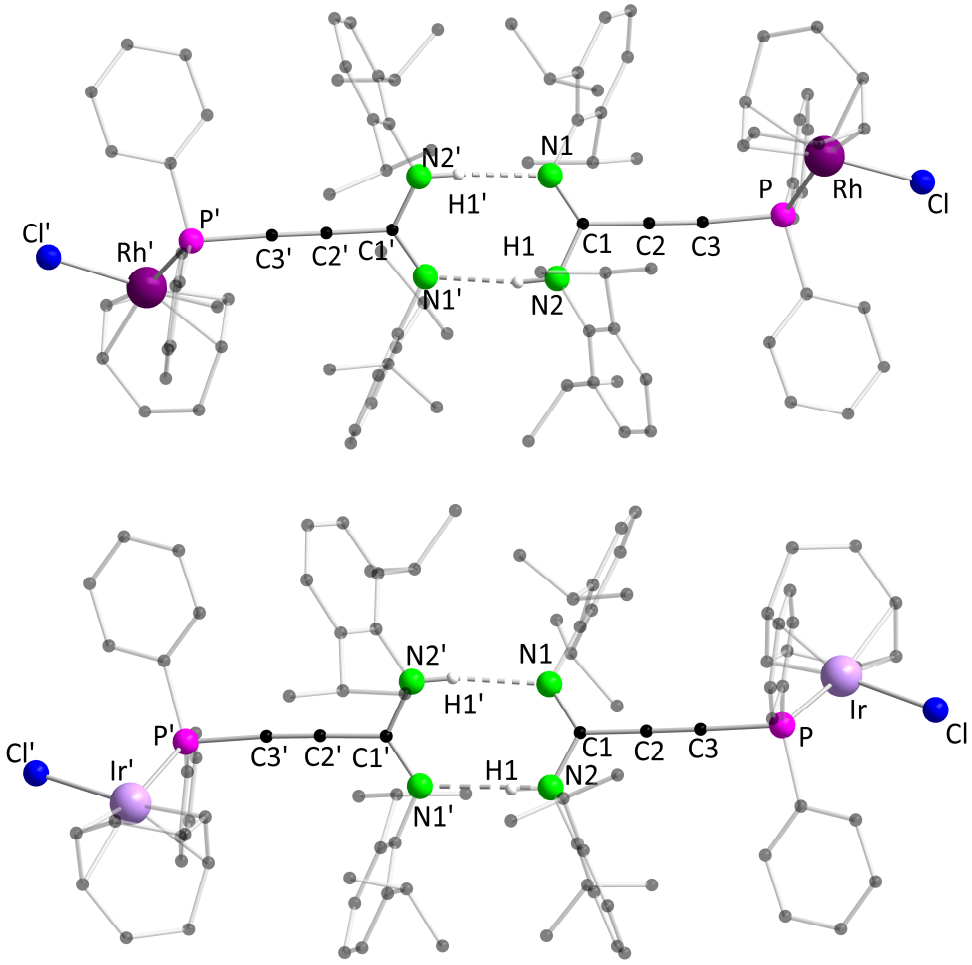

Figure 45: Molecular structure of **15** (top) and **16** (bottom) in the solid state. Hydrogen atoms (except N–H proton) and non-coordinating solvent molecules are omitted for clarity. Selected bond distances (Å) and angles (°) in **15**: Rh–P 2.285(2), Rh–Cl 2.363(2), P–C3 1.780(7); P–Rh–Cl 89.4(6). In **16**: Ir–P 2.286(1), Ir–Cl 2.354(1), P–C3 1.772(6); P–Ir–Cl 90.8(5).

The heteronuclear NMR analysis of complexes **15** and **16** provided valuable insights into their structural and electronic properties. In the $^{31}P\{^{1}H\}$ NMR spectrum, a doublet was observed at δ = 12.2 ppm for complex **15**, while a singlet appeared at δ = 4.1 ppm for complex **16**. These chemical shift values closely resemble those observed for complexes **10** and **11**, suggesting that the electronic environment around the phosphine center in these systems remains largely unaltered. Furthermore, analysis of the ^{1}H NMR spectra of complexes **15** and **16** revealed

similarities to those of complexes **10** and **11**. The characteristic proton resonances corresponding to the coordinated cod ligand and the amidinate framework remained largely unchanged. However, a notable distinction was the appearance of an additional broad resonance, which was attributed to the NH proton of the protonated amidinate ligand at δ = 3.31 ppm and δ = 3.44 ppm for complexes **15** and **16**, respectively. The presence of this additional NH signal serves as a direct confirmation of the protonation of the amidinate ligand, distinguishing these hydrolyzed complexes from their precursors, complexes **12** and **13**.

Further evidence supporting the successful formation of complexes **15** and **16** was obtained from ESI-MS spectra with molecular ion peaks corresponding to the $[M+H]^+$ species were observed at *m/z* = 819.3051 for complex **15** and at *m/z* = 909.3598 for complex **16**.

Moreover, compounds **12** and **13** served as precursors for the synthesis of the heterobimetallic complexes **10** and **11**. These target complexes were obtained by treating compounds **12** and **13** with an equimolar amount of CuCl in THF (Scheme 9). This synthetic transformation enabled the incorporation of copper centers into the ligand framework.

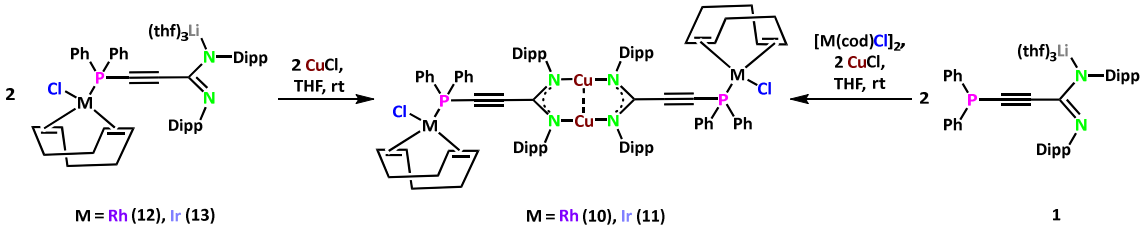

Scheme 9: Synthesis of complexes **10** and **11** from **12** and **13**, and alternative preparation of **10** and **11** via a one-pot reaction.

In addition to this stepwise approach, an alternative and more efficient synthetic strategy was employed for the preparation of complexes **10** and **11**. These complexes were successfully synthesized *via* a one-pot reaction, wherein two equivalents of the lithium salt of the ligand (**1**) were reacted with one equivalent of $[Rh(cod)Cl]_2$ or $[Ir(cod)Cl]_2$ and two equivalents of CuCl in THF (Scheme 9). Notably, the one-pot synthetic approach demonstrated remarkable efficiency, yielding higher amounts of complexes **10** and **11** compared to the stepwise synthetic procedures. The enhanced yields observed with this method underscore its effectiveness and practicality, making it a highly advantageous route for the preparation of these heterobimetallic complexes. This approach not only improves the overall synthetic efficiency but also highlights the versatility of the metalloligand system, offering a more

convenient and scalable strategy for accessing these Cu(I) containing heterobimetallic complexes.

3.2.3 Catalytic applications

Transfer hydrogenation catalysis is an important process that offers several advantages over traditional hydrogenation methods.[287] It enhances safety by eliminating the need for hazardous pressurized hydrogen gas and instead uses convenient and readily available hydrogen donors like alcohols or formic acid.[288-290] Moreover, it facilitates asymmetric synthesis and employs stable, easily accessible catalysts. Following the successful synthesis of the heterobimetallic complexes, the catalytic activity of complex **11** in the TH of aryl aldehydes was investigated. To assess the efficiency, 4-chlorobenzaldehyde was selected as a trial substrate and isopropanol (*i*-PrOH) employed as the hydrogen transfer source. The reaction progress was monitored using ^{1}H NMR spectroscopy. To establish a baseline for comparison, a control experiment in which 4-chlorobenzaldehyde was treated with *i*-PrOH and 5 mol% KOH in $CDCl_3$ at 100 °C, but without adding the catalyst, was initially conducted. After two hours of reaction, no conversion to the desired reduced product was observed (Entry 1, Table 2), indicating that the presence of the catalyst is essential for the reaction.

Next, the influence of catalyst loading on the reaction efficiency was investigated. Under the same reaction conditions, complex **11** was introduced in varying amounts ranging from 1 to 10 mol% (Entries 2-4, Table 2) with the reaction time of 120 minutes. Among the different catalyst loadings, the highest conversion was achieved using 10 mol% of complex **11**, indicating that this amount was the most effective in promoting the transfer hydrogenation reaction. Furthermore, at 10 mol% catalyst loading, the reaction was completed within 30 minutes (Entry 5, Table 2). In an effort to optimize the reaction further, the effect of different base additives was also explored and replaced KOH with KO*t*-Bu under otherwise identical reaction conditions (Entry 6, Table 2). However, this modification led to a significant drop in the reaction yield, with the conversion decreasing to only 22 %. This result suggests that KOH is a more effective as a base for the transfer hydrogenation reaction in the presence of complex **11**.

Table 2: Optimization of the reaction conditions of the catalytic TH of 4-chlorobenzaldehyde using complex **11** as catalyst.

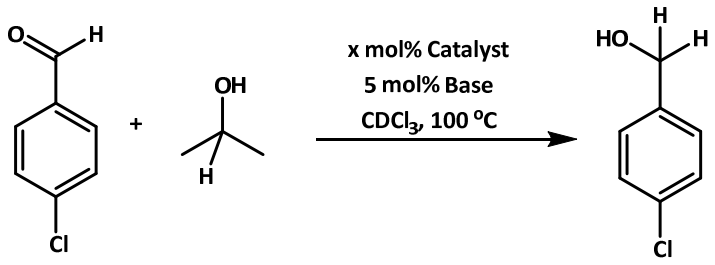

(17a)

Entry	Catalyst (mol%)	Base (5 mol%)	Time (min)	Conversion (%)
1	0	KOH	120	-
2	1	KOH	120	10
3	5	KOH	120	37
4	10	KOH	120	>99
5	**10**	**KOH**	**30**	**>99**
6	10	KO*t*-Bu	30	22

Reaction conditions: 4-chlorobenzaldehyde (10 mg, 1 eq., 71.1 µmol), isopropanol (0.1 mL, 18.4 eq., 1.3 mmol). Base, catalyst loading and time are specified in the table above. The oil bath temperature was set to 100 °C.

To gain a broader insight into the catalytic efficiency of complex **11** the catalytic activities of two other Ir-based catalysts, specifically [Ir(cod)ClPPh$_3$] and complex **16**, were additionally investigated under identical reaction conditions. Initially, a reaction was conducted using 10 mol% of [Ir(cod)ClPPh$_3$] under the standard reaction conditions, where it achieved 71 % conversion of 4-chlorobenzaldehyde to the corresponding hydrogenated product within 30 minutes (Entry 1, Table 3) while 20 mol% of [Ir(cod)ClPPh$_3$] afforded in 97 % conversion (Entry 2, Table 3). This result indicates that [Ir(cod)ClPPh$_3$] is also an active catalyst for the transfer hydrogenation reaction.

On the other hand, employing 10 mol% of complex **16**, the reaction yield was significantly decreased, with 52 % conversion after 30 minutes (Entry 3, Table 3) and 92 % conversion with 20 mol% of complex **16** (Entry 4, Table 3).

To verify that the Ir(I) center serves as the sole active catalytic site, while the Cu(I) center does not contribute to the catalytic activity in the transfer hydrogenation reaction, a control experiment under identical reaction conditions using the complex Cu_2L_2 (**2**) as the catalyst was conducted (Entry 5, Table 3). In the reaction, almost no conversion of 4-chlorobenzaldehyde to the hydrogenated product was observed.

Altogether, these results underline the comparable activity of complex **2**, with [Ir(cod)ClPPh$_3$] and complex **7**, in terms of both conversion rate and overall reaction efficiency.

Table 3: Screening of the catalysts [Ir(cod)ClPPh$_3$], complex **16** and complex **2** compared to complex **11**.

Entry	Catalyst	mol%	Time (min)	Temp (°C)	Conversion (%)
1	[Ir(cod)ClPPh$_3$]	10	30	100	71
2	[Ir(cod)ClPPh$_3$]	20	30	100	97
3	Complex **16**	10	120	100	52
4	Complex **16**	20	120	100	92
5	Complex **2**	10	30	100	–
6	**Complex 11**	**10**	**30**	**100**	**>99**

Reaction conditions: 4-chlorobenzaldehyde (10 mg, 1 eq., 71.1 µmol), isopropanol (0.1 mL, 18.4 eq., 1.3 mmol), KOH as base (5 mol%, 3.6 µmol), catalyst loading and time are specified in the table above. The oil bath temperature was set at 100 °C.

After comprehensively optimizing and screening various catalytic conditions, it was established that the most effective conditions for the TH of 4-chlorobenzaldehyde involved using 10 mol% of complex **11** as the catalyst at 100 °C for 30 minutes.

To further explore the broad applicability of this catalytic system, the substrate scope was expanded beyond 4-chlorobenzaldehyde to include a variety of aryl aldehydes with electron-donating and electron-withdrawing substituents. Interestingly, no specific trend in reactivity was observed between electron-rich and electron-deficient aldehydes. For all tested aryl aldehyde substrates, the reaction consistently delivered high yields (>70 %) of the corresponding hydrogenated alcohols. Specifically, benzaldehyde derivatives with electron-withdrawing groups like 4-Cl, 4-Br, 4-CF_3, 2-F and 2-Br substitutions on the aromatic ring

exhibited excellent conversions, affording the corresponding alcohols (**17a-17f**) in yields ranging from 79 % to 99 %.

Table 4: Screening of substrates for TH of aldehydes catalysed by **11**.

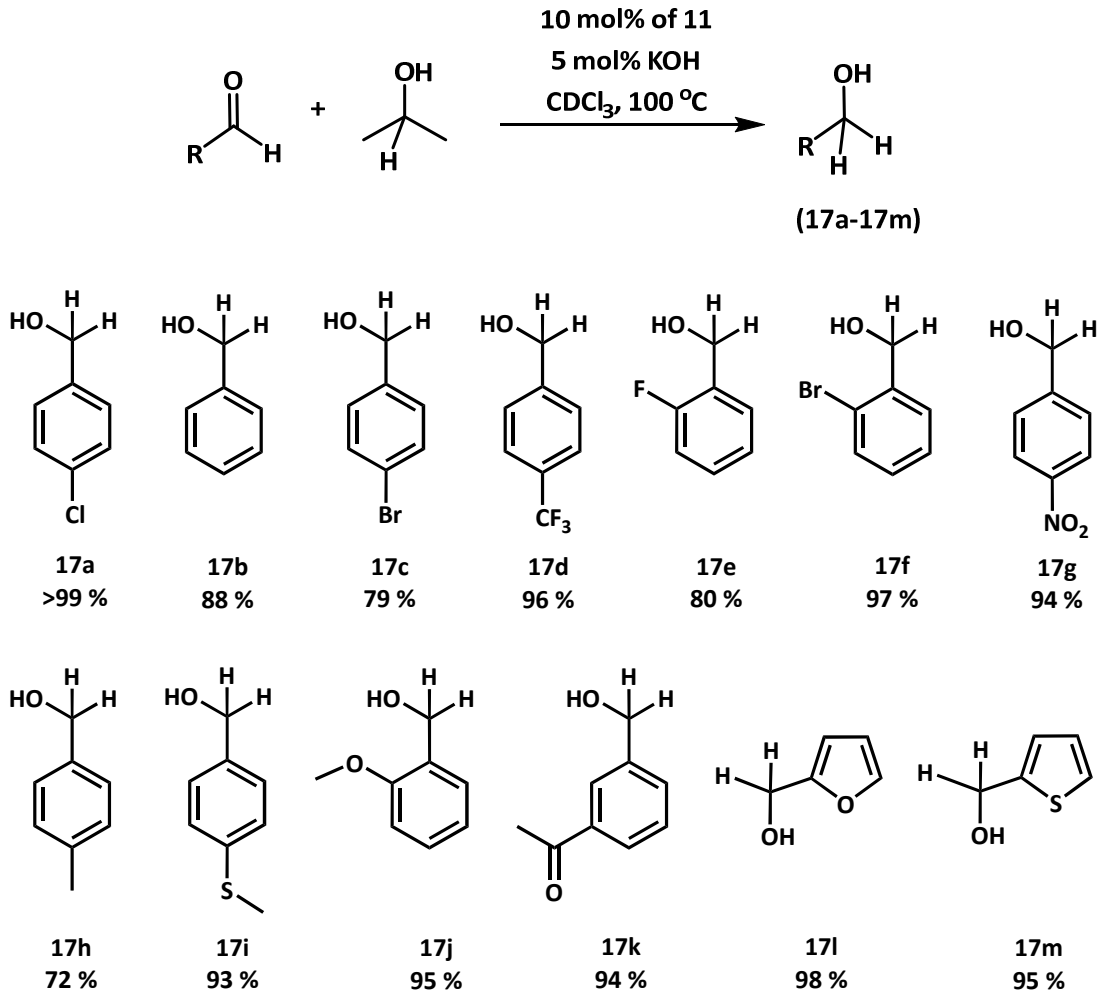

Notably, the catalyst exhibited high chemoselectivity when an aldehyde containing a nitro (-NO_2) functional group, which is usually susceptible to reduction, is used as the substrate. The catalyst exclusively reduced the aldehyde functionality, leaving the -NO_2 group intact, and provided the desired product (**17g**) in 94 % yield. To assess whether the catalytic system could also facilitate the transfer hydrogenation of ketones, a reaction was performed using acetophenone as the substrate. However, even after 24 hours, no conversion to the corresponding secondary alcohol was observed. This outcome indicates that the catalyst is selective towards aldehydes, with ketones being significantly less reactive under these conditions. Building on this observation, a competitive reduction experiment was performed

using 3-acetylbenzaldehyde, a compound containing both an aldehyde and a ketone functional group. The reaction selectively reduced only the aldehyde functionality, producing the corresponding alcohol (**17k**) in a 94 % yield.

In addition, the catalytic performance was evaluated for aryl aldehydes substituted with electron-donating groups, such as 4-Me, 4-SMe and 2-OMe. These substrates were efficiently converted to their respective alcohol products (**17h-17j**) with yields of 72, 93, and 95 %, respectively.

To further challenge the scope and efficiency of the catalytic system, its activity was tested on more electron-rich and sterically demanding heteroaromatic aldehydes, 2-acetylfuran and 2-acetylthiophene. These heterocycles are often known to coordinate to metal centers, potentially hindering catalytic performance by deactivating the active site. However, despite these challenges, the reaction proceeded efficiently, yielding the desired reduced products (**17l-17m**) in excellent yields of 95-98 %.

3.2.4 Photophysical properties

After the application of complex **11** in TH catalysis, the protonated amidinate ligand (**14**), the heterobimetallic Cu(I)–Ir(I) complex (**11**) and the amidinate Ir(I) complex (**16**) were studied for their photophysical properties both in the solid state and DCM solution at 77 K. The emission and excitation profiles reflect the influence of the ligand framework, metal centers (Cu and Ir), and environmental effects on the excited states.

In the solid state at 77 K, compound **14** showed a broad emission band with a maximum at 480 nm upon excitation at 390 nm (Figure 46, top left). This emission likely arises from a ligand-centered excited state localized on the amidine or conjugated phosphine framework, as no metal center is present to facilitate the charge transfer.[303] Complex **11**, a bimetallic Cu(I)–Ir(I) complex, shows a maximum at 585 nm upon excitation at 365 nm (Figure 46, middle left), indicating lower energy emission compared to ligand **14**. This red-shift is attributed to a mixed metal to ligand charge transfer (MLCT) state involving both the Cu(I) and Ir(I) centers, with the Ir(I) center's strong spin-orbit coupling and lower-energy *d*-orbitals.[304-305] Complex **16**, an Ir(I) complex with an amidine phosphine ligand, emits at 575 nm (λ_{ex} = 370 nm) (Figure 46, bottom left), consistent with a MLCT state localized on the Ir center, where the amidine acts as a π-acceptor, lowering the MLCT energy. The solid-state rigidity enhances radiative decay from

excited states by suppressing vibrational quenching.[306] The observed phosphorescence lifetime for the compounds **14**, **11** and **16** in the solid state were 6 µs, 7 µs and 13 µs, respectively, at 77K.

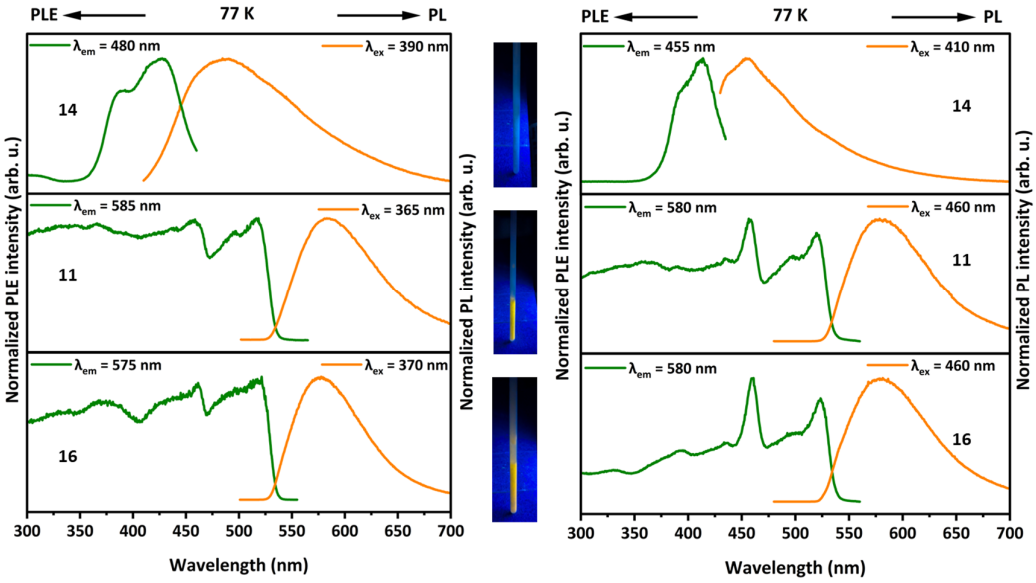

Figure 46: Normalized photoluminescence excitation (PLE) and emission (PL) spectra of solid samples (left) and DCM solutions (right) of the compounds **14, 11** and **16** at 77 K. Photographs of DCM solutions (center) of the complexes under UV illumination (λ = 365 nm) at 77 K. PLE and PL spectra were recorded at the depicted wavelengths (λ_{em} and λ_{ex}).

In DCM solution at 77 K, all three compounds exhibit blue-shifted emissions compared to the solid state (Figure 46, right). Compound **14** shows an emission upon excitation at 455 nm (λ_{ex} = 410 nm), a significant blue-shift compared to solid sample, indicating a higher energy state in solution. Compound **11**, the bimetallic Cu(I)–Ir(I) complex, emits at 580 nm, with a modest blue-shift, suggesting a mixed MLCT character.[307] Compound **16**, the Ir(I) complex, also emits at 580 nm (λ_{ex} = 460 nm), close to its solid-state value, showing the presence of the Ir(I)-centered MLCT state, which is less perturbed by solvent reorganization due to the strong ligand field and spin-orbit coupling of Ir(I).[308-309] The observed phosphorescence lifetime for the compounds **14**, **11** and **16** in DCM solution were 6 µs, 10 µs and 12 µs, respectively, at 77K.

The observed differences in emission behavior between the solid state and DCM solution shows the role of the environment in modulating the photophysical properties of these complexes.[310] In the solid state, the rigid lattice enhances MLCT emission by suppressing

vibrational relaxations, while in DCM solution, solvent effects and increased flexibility allow for contributions from higher-energy states and non-radiative decays, particularly in the compound **14**.[307] The bimetallic Cu(I)-Ir(I) complex (**11**) and the Ir(I) complex (**16**) exhibited the almost similar PL and PLE spectra, shows the independence on the cuprophilic interactions.[311]

3.3 Syntheses and photophysical properties of coumarin substituted NHC-Au(I) complexes

3.3.1 Introduction

Over the past several years, research on gold complexes coordinated by NHCs has experienced a remarkable surge. These complexes have demonstrated their utility in a range of catalytic processes, including hydroamination, hydrogenation, and various cyclization reactions.[312-317] NHCs have evolved into well-established and reliable ligands in the field of coordination chemistry and are now widely employed in both transition metal and main group element chemistry.[318-319] Compared to phosphines, NHCs exhibit distinct steric and electronic characteristics, and they can be easily functionalized by a wide variety of organic substituents on the nitrogen atoms.[320-323] As carbenes are typically monodentate σ-donor ligands, additional donor functionalities can be introduced into the ligand framework, such as phosphine groups,[242,324-326] hydroxyl groups,[327-330] thiol groups[331-332] and various other functional moieties.[333-336] These functionalized NHC systems significantly broaden the scope of applications in coordination chemistry and catalysis, as they enable the design of ligands with tailored properties for specific tasks.[332,337-338]

Besides their applications in catalysis, the coinage metal complexes of NHC have also attracted attention for their intriguing luminescent properties.[241,339-346] A key factor contributing to their luminescence is the ability of coinage metal ions to engage in close range metal-metal interactions, a phenomenon collectively referred to as metallophilicity.[121] Among these, gold(I) compounds are particularly well known for exhibiting strong d^{10}-d^{10} interactions, which were historically recognized as unique to gold and termed as aurophilicity.[122,127,239]

In addition to the substituents discussed previously which offer multidentate coordination, certain functional groups also possess inherent luminescent properties and exhibit significant biological relevance, making them highly attractive for designing multifunctional NHC-based metal complexes.[347-351] Especially, NHC-gold complexes gained attention due to their remarkable biological activity. These complexes have shown potential as anticancer agents, owing to their cytotoxic properties and their ability to interact selectively with biological targets.[344] Besides, carbazole based derivatives have also demonstrated a broad spectrum of pharmacological properties. These include, but are not limited to, anticancer, antibacterial,

anti-inflammatory and anti-psychotropic properties. Amongst the latter, *N*-thioalkyl carbazoles proved to inhibit cancer cells damaging the nuclear DNA through the inhibition of human topoisomerases.[347,351]

A particularly compelling class of substituents within this context is the coumarin scaffold. While the parent coumarin molecule itself is known to be only weakly fluorescent, its chemically modified derivatives can exhibit strong fluorescence, making them excellent candidates as fluorophores.[352] This enhancement in fluorescence behavior is supported by computational studies by Yin *et al.* and Abbas. These investigations revealed that targeted substitution at specific positions, particularly the 4- and 7-positions, on the coumarin ring can significantly lower the HOMO–LUMO energy gap. This results in enhanced absorption and emission properties, thereby giving rise to compounds with notable and tunable optical characteristics.[353-354]

In 2014, the group of Casini and collaborators synthesized NHC-gold(I) complexes with 7-methoxy-4-methylene coumarin as the substituent on the *N* atom of an NHC and investigated the biological activity in cancer cells (Figure 47a).[355] Later, Budagumpi and coworkers further explored the use of coumarin-functionalized NHC ligands to develop a series of cationic NHC-gold(I) complexes that were employed as electrocatalysts for the hydrogen evolution reaction (HER) from water, showcasing their applicability beyond the biomedical field (Figure 47b).[356]

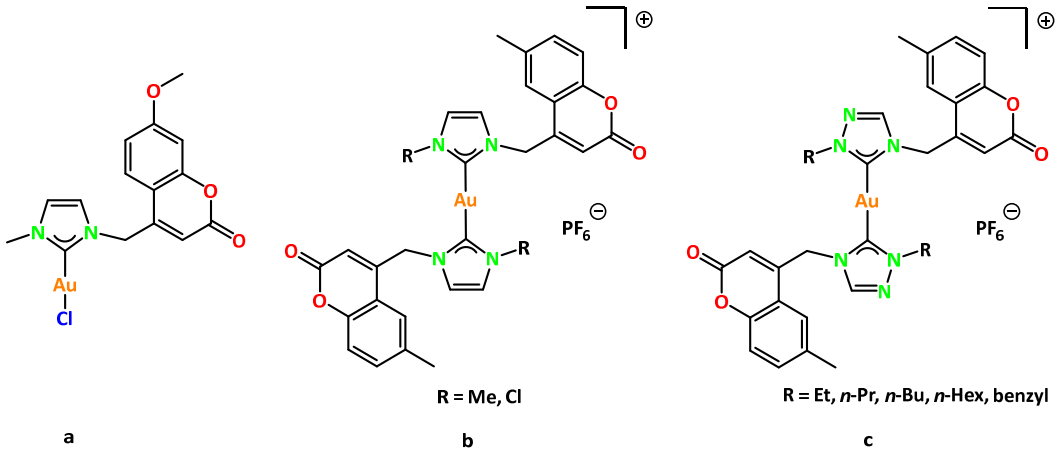

Figure 47: Examples of gold(I) complexes with coumarin substituted NHCs.

Expanding on this work, the same research group utilized the coumarin scaffold to construct triazole derived NHC ligands, which were then complexed with gold(I) to form a new class of cationic complexes. These compounds were also assessed for their biological relevance, in cancer treatment studies, underlining the versatility of the coumarin motif for applications in both catalysis and medicinal chemistry (Figure 47c).[357] Moreover, coumarin-substituted NHC-gold(I) complexes are widely studied for their photophysical properties, with several examples highlighting their unique luminescent characteristics.[249,358-360]

This chapter reports the design and synthesis of a set of NHC-gold(I) complexes functionalized with coumarin derivatives and bearing a range of anionic ligands. In addition, a novel NHC-AuCl complex was subjected to further chemical transformations to probe its reactivity profile. All the synthesized complexes were thoroughly characterized and subjected to comprehensive photophysical studies.

3.3.2 Syntheses and characterization of NHC-Au(I) complexes

For the synthesis of a coumarin substituted NHC, 1-(mesityl)imidazole was initially synthesized by a reaction of 2,4,6-trimethylaniline in methanol with an aqueous solution of glyoxal for 16 hours (Scheme 10). Subsequently, ammonium chloride and an aqueous solution of formaldehyde were added to the reaction and the mixture refluxed for 4 hours. After adjusting the pH to 9, the aqueous phase was extracted with diethyl ether to obtain the target product 1-(mesityl)imidazole. It was purified by crystallization from the concentrated diethyl ether solution. To ensure the purity of the product, a ^{1}H NMR spectrum was acquired and found to be in agreement with the literature.[361-362]

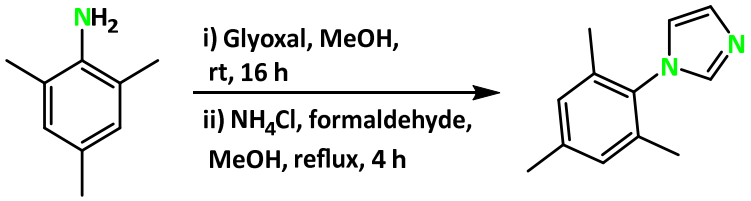

Scheme 10: Synthesis of 1-(mesityl)imidazole.

Following the successful preparation of 1-(mesityl)imidazole, it was reacted with 4-bromomethyl-7-methoxycoumarin in refluxing acetonitrile for 16 hours (Scheme 11). After workup, the desired product 1-mesityl-3-(7-methoxy)coumarin imidazolium bromide (**18**) was obtained as a white solid. It is sparingly soluble in all the organic solvents. In the ^{1}H NMR

spectrum, two singlets were observed at δ = 2.07 ppm and 2.33 ppm integrating to six and three protons, respectively, for the methyl groups of the mesityl moiety. An additional singlet was observed at δ = 3.85 ppm for the coumarin methyl group. The characteristic resonance of the N-C*H*=N proton of the imidazolium salt was observed as a singlet at δ = 10.67 ppm. The successful synthesis of **18** was additionally verified by ESI-MS, showing a molecular ion peak at *m/z* = 375.1695 for the cationic part of the imidazolium salt.

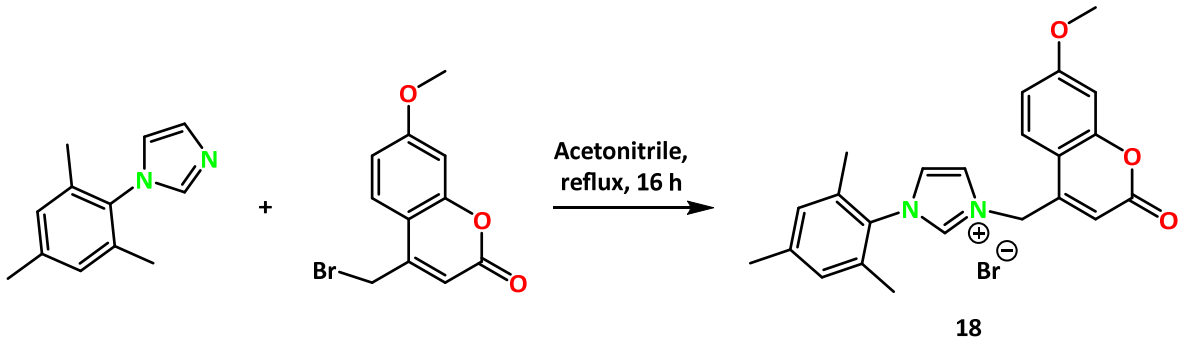

18

Scheme 11: Synthesis of 1-mesityl-3-(7-methoxy)coumarin imidazolium bromide (**18**).

Having the NHC precursor **18** at hand, its application as coumarin-substituted NHC ligand for the coordination to different metals was explored. Unlike phosphines, which can readily coordinate to metals without any prior activation, NHC precursors require an initial activation or deprotonation step before they can effectively bind to a metal center. The most widely used and effective methods for generating NHCs involve the reaction of an imidazolium salt with KO*t*-Bu, K_2CO_3 or a silver base. While, for **18** the deprotonation with KO*t*-Bu and K_2CO_3 was unsuccessful, the activation with Ag_2O proved to be feasible.

The latter reaction results in the formation of an NHC-silver(I) complex, which serves as an intermediate towards the synthesis of other metal complexes. Subsequently, the NHC ligand can be transferred from the silver complex to another transition metal in a transmetalation process. This final step successfully leads to the formation of the desired NHC-transition metal (NHC-M) complexes, which can then be utilized in various catalytic and synthetic applications.

Specifically, one equivalent of the imidazolium salt (**18**) was reacted with half an equivalent of Ag_2O in DCM for 16 hours and the light yellow-colored reaction mixture was filtered into a flask containing one equivalent of [Au(tht)Cl], followed by stirring for additional 16 hours (Scheme 12). The resulting reaction mixture was filtered again to obtain a light-yellow colored

solution. Removal of the solvent under reduced pressure, afforded the NHC-gold(I) chloride complex **19** as an off-white powder in 92 % yield. Colorless crystals were obtained by the diffusion of *n*-pentane to a concentrated solution of **19** in DCM.

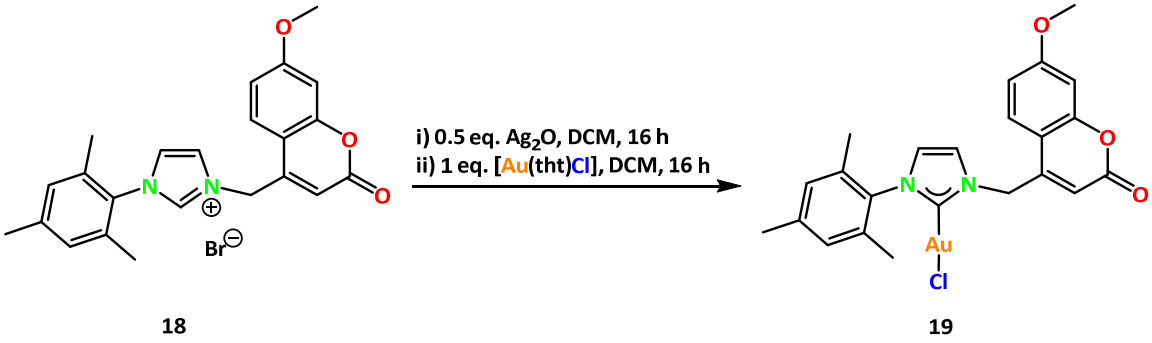

18 **19**

Scheme 12: Synthesis of NHC-AuCl complex **19**.

Complex **19** crystallized in the monoclinic space group $P2_1/n$ forming colorless prism-shaped crystals. The analysis of the crystal structure revealed that the NHC ring, consisting of three carbon atoms and two nitrogen atoms, is planar as expected (Figure 48).[317] The structural study further revealed a Au–Cl bond length of 2.318(12) Å and a Au–C bond length of 1.980(5) Å which are deviating slightly from the literature values of Au–Cl bond length 2.280(6) Å and Au–C bond length 1.910(2) Å.[363] Moreover, complex **19** exists as dimeric unit, with a Au–Au distance of 3.335(6) Å indicative of aurophilic interactions.[122,127,239] The Au(I) center is coordinated almost linearly with a C–Au–Cl bond angle of 175.7(2)° which is slightly smaller compared to the reported value of 178.1(7)° in a similar NHC-AuCl complex.[363] Furthermore, the N1–C–N2 bond angle in the NHC ring is measured to be 105.4(4)°.

The complex **19** was also characterized by ^{1}H NMR where two singlets at δ = 2.06 and 2.34 ppm for the methyl groups of the mesityl substituent and one singlet at δ = 3.90 ppm for the methoxy group of coumarin were observed. These resonances are only slightly shifted compared to the starting material. Other resonances for the mesityl and coumarin groups experienced more pronounced shifts compared to the imidazolium salt **18**. Characteristically, no resonance was observed for the carbenic proton in the range of δ = 10-11 ppm which confirms the successful deprotonation of the imidazolium salt **18** and generation of the carbene moiety. Moreover, in the ^{13}C{^{1}H} NMR spectrum, a resonance in the downfield region at δ = 174.3 ppm also confirms the carbene complex formation which is near to the literature value of similar NHC-AuCl complex at δ = 173.5 ppm (Figure 47a).[355,364-365]

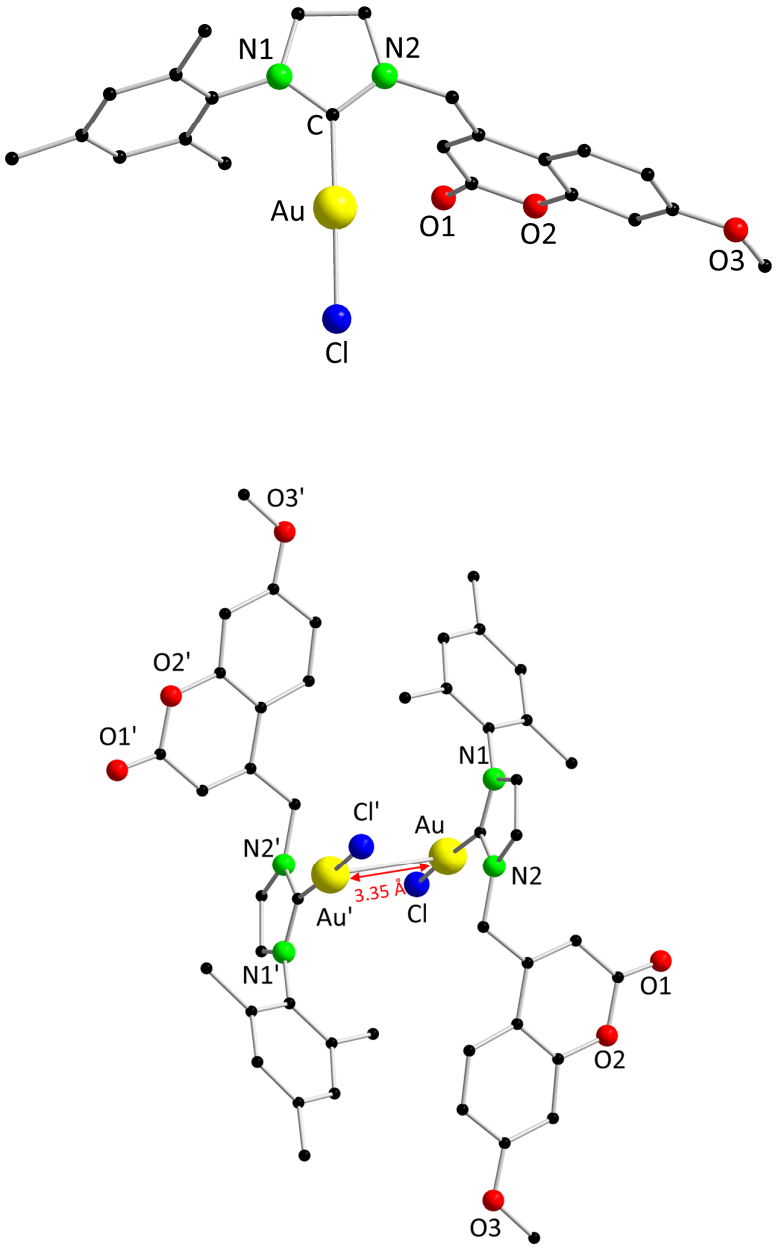

Figure 48: Molecular structure of **19** as a monomeric unit (top) and as a dimeric unit (bottom) in the solid state. Hydrogen atoms and non-coordinating solvent molecules are omitted for clarity. Selected bond distances (Å) and angles (°): Au–Au' 3.335(6), Au–Cl 2.318(1), Au–C 1.980(5), C–N1 1.349(7), C–N2 1.357(7); C–Au–Cl 175.7(2).

Employing the same synthetic procedure used for the preparation of complex **19**, the analogue NHC-AuBr complex **20** was successfully synthesized. The synthesis was carried out employing [Au(tht)Br] as a precursor instead of [Au(tht)Cl], while keeping all other reaction

conditions unchanged (Scheme 13). After completion of the reaction, complex **20** was obtained in 87 % yield.

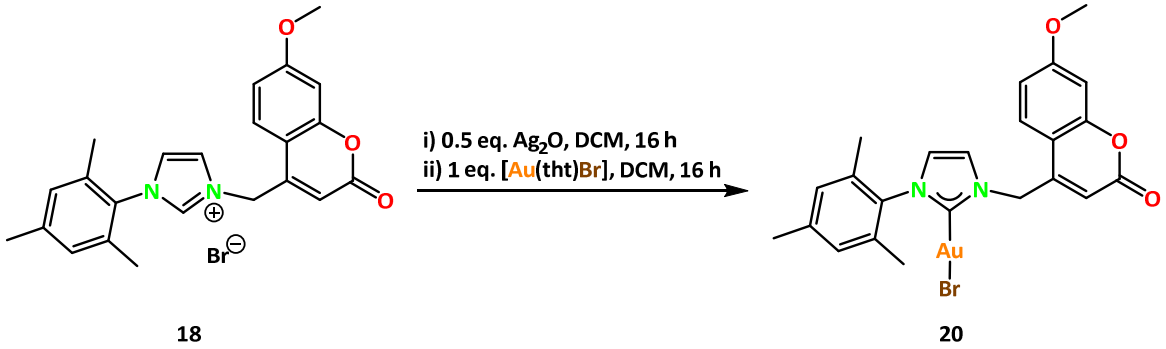

18 20

Scheme 13: Synthesis of NHC-AuBr complex **20**.

To further purify and characterize the complex, crystallization was performed from a mixture of DCM and *n*-pentane. SC-XRD analysis revealed that complex **20** crystallized in the triclinic space group $P\bar{1}$ (Figure 49). The structural features of complex **20** are similar to that of complex **19**. However, contrary to **19**, it does not form a dimer, indicating the absence of aurophilic interactions. The Au–Br bond length was measured to be 2.405(1) Å which is slightly longer than Au–Cl bond length in **19** but similar to the reported Au–Br bond length of 2.381(2) Å in a NHC-AuBr complex.[366] The Au–C bond length was 1.981(9) Å, similar to complex **19** and to the one in a NHC-AuBr complex (1.975(1) Å).[366] The Au(I) center again adopts a nearly linear geometry with a C–Au–Br bond angle of 176.3(3)°.

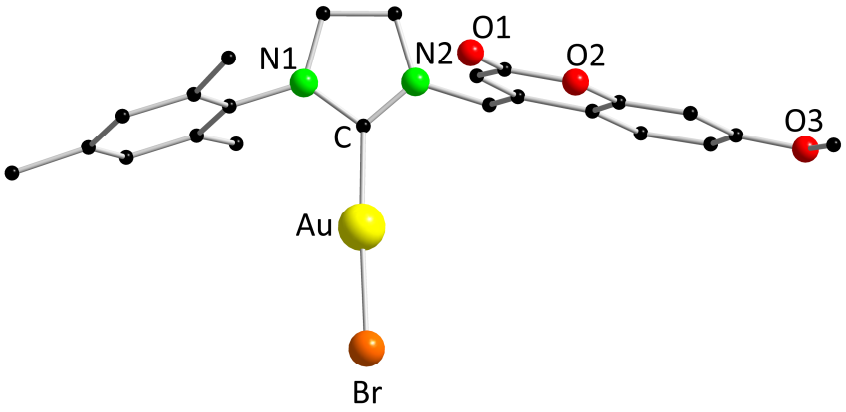

Figure 49: Molecular structure of **20** in the solid state. Hydrogen atoms and non-coordinating solvent molecules are omitted for clarity. Selected bond distances (Å) and angles (°): Au–Br 2.406(8), Au–C 1.983(7), C–N1 1.318(9), C–N2 1.392(9); C–Au–Br 176.3(2).

The ^{1}H NMR spectrum of complex **20** is reminiscent of that of complex **19** with minor deviations in the chemical shifts. In the upfield region of the spectrum, two singlets at δ = 2.06 and 2.34 ppm for the mesityl group and one singlet at δ = 3.90 ppm for the methoxy group of coumarin were observed. Other peaks in the aryl region were also found to be reminiscent to complex **19**. Additionally, a characteristic resonance in the ^{13}C{^{1}H} NMR spectrum was observed at δ = 177.5 ppm for the carbenic carbon indicating successful complex formation and is close to the reported value of δ = 176.7 ppm in a similar NHC-AuBr complex.[366]

Following a procedure similar to that used for the synthesis of the complexes **19** and **20**, the NHC-AuC_6F_5 complex **21** was successfully prepared (Scheme 14). The synthesis involved the reaction of compound **18** with half an equivalent of Ag_2O in DCM for 16 hours. Upon completion of this initial step, the reaction mixture was filtered into a flask containing one equivalent of [Au(tht)C_6F_5]. The resulting solution was stirred under similar conditions for additional 16 hours, leading to the successful formation of complex **21** with an overall yield of 88 %. Slow diffusion of *n*-pentane into a concentrated solution of complex **21** in DCM afforded colorless rod-like crystals.

The crystal data quality was insufficient for a reliable bond parameter discussion. For illustrative purposes, the preliminary structure is depicted in the Figure 50.

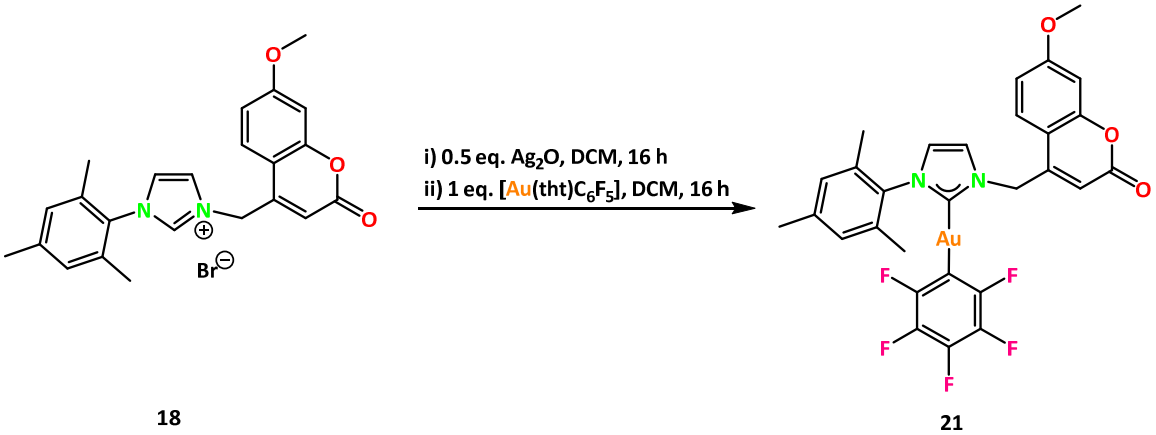

Scheme 14: Synthesis of NHC-AuC_6F_5 complex **21**.

Complex **21** was thoroughly analyzed using ^{1}H NMR spectroscopy, and the obtained spectral data indicated that all observed peaks closely resembled those of complex **19**. However, in comparison to complex **19**, the chemical shift values of complex **21** were found to be shifted downfield, suggesting electronic influences when exchanging Cl for C_6F_5. Two distinct singlets

corresponding to the methyl protons of the mesityl group appeared at chemical shift values of δ = 2.10 and 2.35 ppm. Furthermore, a singlet was observed at δ = 3.89 ppm, which was assigned to the methoxy (-OCH_3) functional group attached to the coumarin moiety.

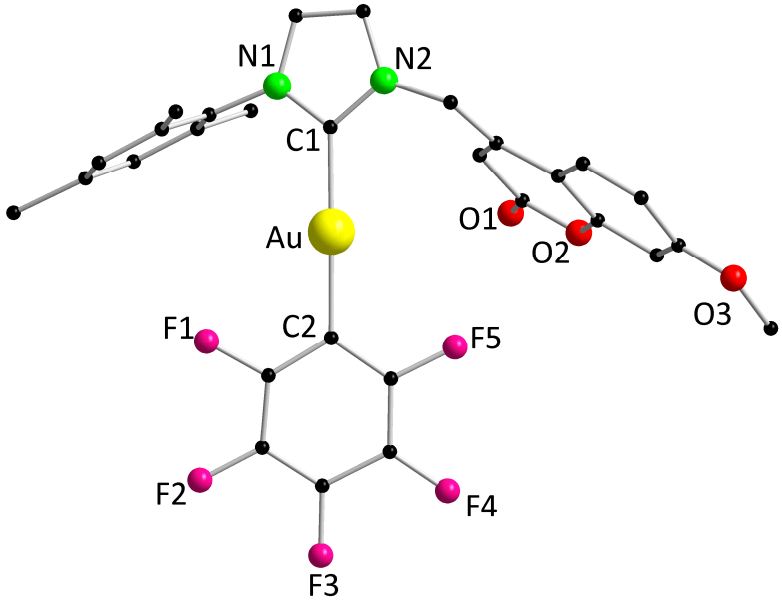

Figure 50: Molecular structure of **21** in the solid state. Hydrogen atoms and non-coordinating solvent molecules are omitted for clarity.

In addition, complex **21** was also characterized using $^{19}F\{^1H\}$ NMR to analyze the fluorines' environments within the molecule. The spectrum exhibited three distinct signals at δ = -116.3, -59.8 and -163.1 ppm corresponding to the fluorine atoms located at *ortho*, *para* and *meta* positions on the pentafluorophenyl ring, respectively. Moreover, a signal at δ = 191.0 ppm was observed for the carbene coordinating the Au(I) center in the $^{13}C\{^1H\}$ NMR spectrum of complex **21** which is highly downfield shifted compared to the complexes **19** at δ = 174.3 ppm and **20** at δ = 177.5 ppm. These spectral observations further confirmed the successful formation and structural integrity of complex **21**.

Following a similar approach as for complexes **19-21**, after the activation of the imidazolium salt **18** with Ag_2O, the intermediate was further reacted with mesityl gold(I) in DCM (Scheme 15). After filtration of the reaction mixture, the product was obtained in 85 % yield and crystals suitable for the SC-XRD analysis were obtained from the concentrated solution of complex **22** in DCM.

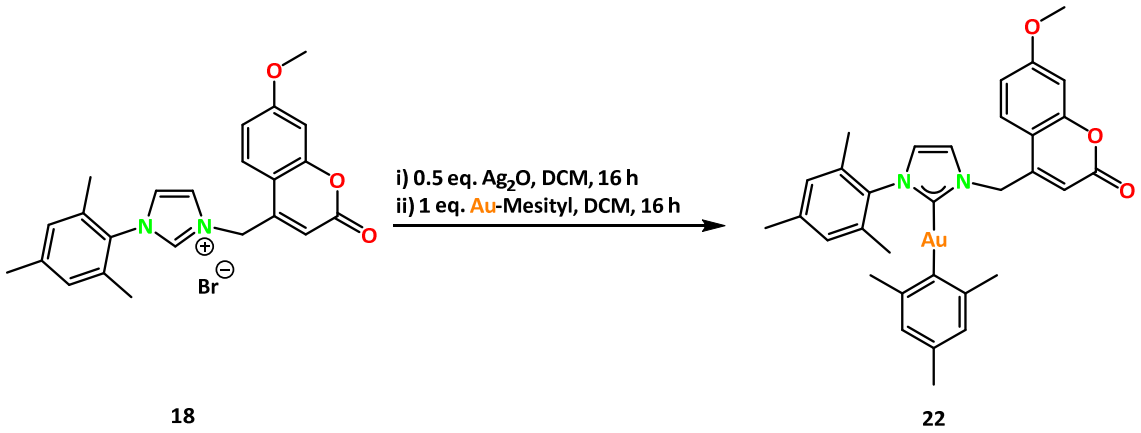

18 22

Scheme 15: Synthesis of NHC-Au(I)-mesityl complex **22**.

From the structural analysis of complex **22**, it was observed that Au(I) is bonded by two carbon atoms: one from NHC (C1) and the other one from the mesityl group (C2) (Figure 51). The Au–C1 bond length, representing the bond between Au(I) center and carbene, was found to be 2.029(3) Å while the Au–C2 bond length, between Au(I) center and the mesityl carbon, was observed to be 2.045(3) Å. The Au(I) center was observed to adopt a nearly linear coordination geometry with a C1–Au–C2 bond angle of 176.9(1)°.

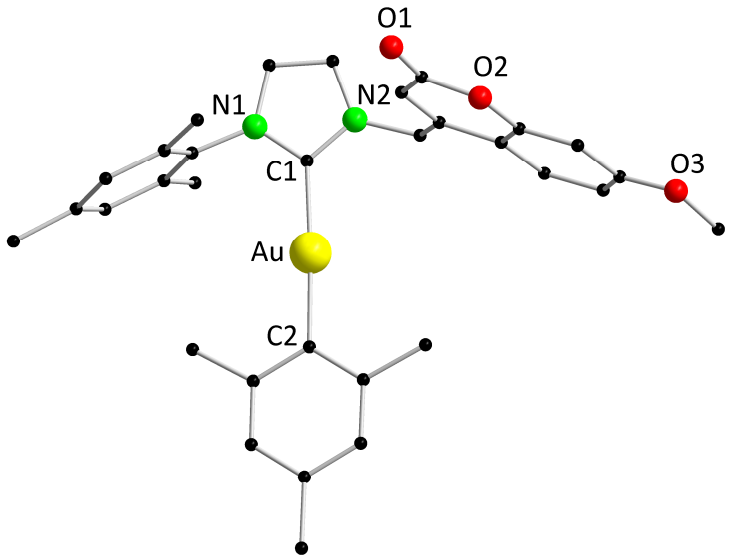

Figure 51: Molecular structure of **22** in the solid state. Hydrogen atoms and non-coordinating solvent molecules are omitted for clarity. Selected bond distances (Å) and angles (°): Au–C1 2.028(3), Au–C2 2.044(3), C–N1 1.358(4), C–N2 1.376(4); C1–Au–C2 176.9(1).

Cationic gold complexes are more electrophilic than their neutral counterparts, making them highly effective at activating π-systems like alkynes and alkenes in catalysis. They often exhibit

higher catalytic activity, better solubility in polar solvents, and enable milder reaction conditions.[367-369] As a next step to synthesize the gold(I) complexes, the aim was to prepare cationic gold(I) complex (**23**). For this purpose, the same synthetic approach was adopted as for the previously discussed neutral gold(I) complexes. However, half an equivalent of [Au(tht)$_2$OTf] instead of one equivalent of [Au(tht)X] (X = Cl, Br, C_6F_5) was used to achieve twofold NHC coordination at gold(I) center (Scheme 16).

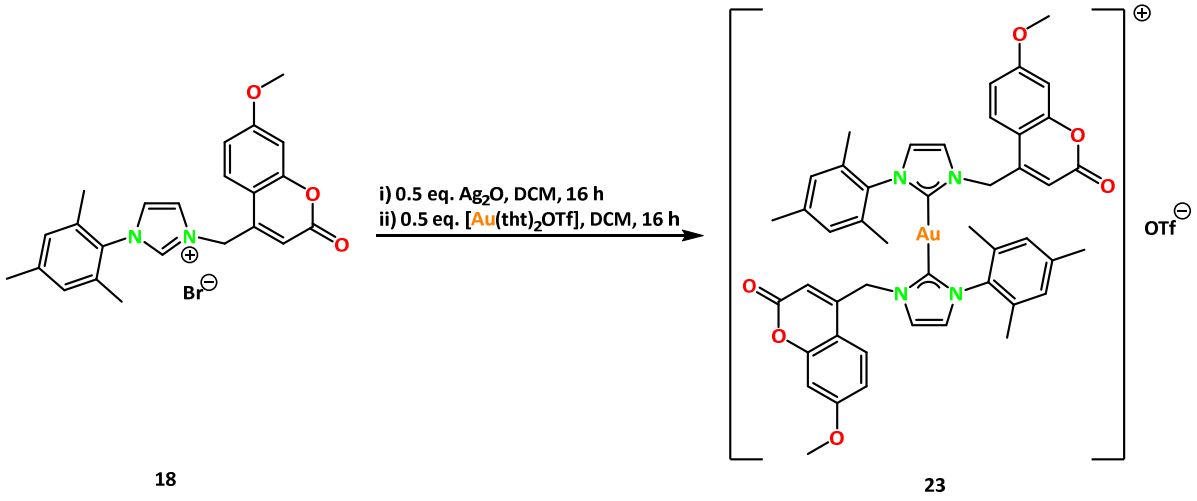

Scheme 16: Synthesis of cationic NHC-gold(I) complex **23**.

Single crystals of complex **23** were obtained from a concentrated DCM solution at ambient temperature. Complex **23** crystallized in the orthorhombic space group $P2_12_12_1$ (Figure 52). The Au–C bond distance was found to be 2.002(3) Å which is consistent with the Au–C bond length of 2.008(4) in a similar cationic NHC-gold(I) complex depicted in Figure 47b.[356,367-369] The gold(I) center is almost linearly coordinated by two NHC ligands with a C–Au–C' bond angle of 175.9(1)° which is deviating slightly from the bond angle of 173.5(2)° in a similar cationic complex.[356] The two NHC rings are not coplanar to each other, rather they adopt an inclined conformation with a N1–N2–N1'–N2' torsional angle of 107.7(1)°.

The ^{1}H NMR spectrum of complex **23** displayed two distinct singlets at δ = 1.71 ppm and 2.33 ppm which correspond to the methyl groups of mesityl functionality. These peaks integrate to twelve and six protons, respectively, reflecting the presence of two chemically equivalent mesityl environments.

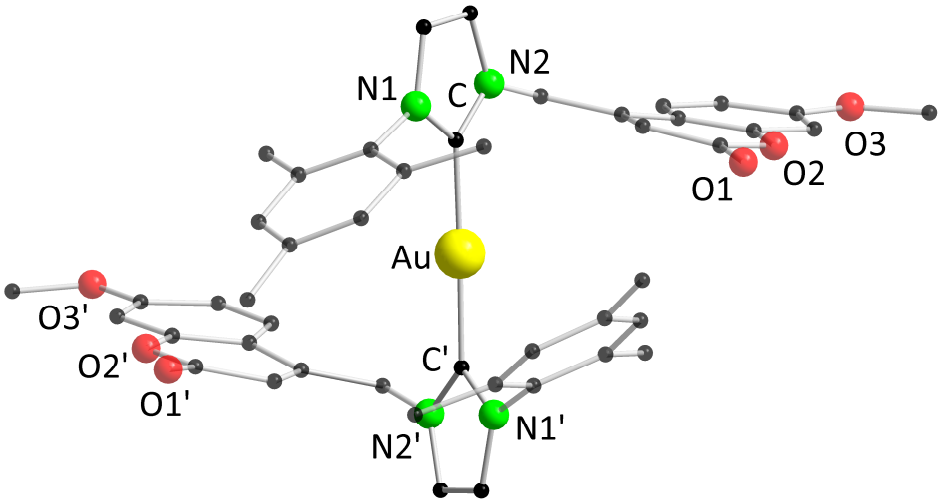

Figure 52: Molecular structure of **23** in the solid state. Hydrogen atoms, non-coordinating solvent molecules and non-coordinating anion are omitted for clarity. Selected bond distances (Å) and angles (°): Au–C 2.01(3), Au–C' 2.013(3), C–N1 1.352(4), C–N2 1.350(4); C–Au–C' 175.6(1).

A singlet resonance at δ = 3.90 ppm accounting for six protons was observed for the coumarin methoxy group. The resonances observed in the aromatic region of spectrum were consistent with the expected structural framework of complex **23**. In addition, a resonance at δ = 186.1 ppm was observed in the $^{13}C\{^{1}H\}$ NMR spectrum for the NHC-carbon coordinating the Au(I) center. Moreover, in the ESI-MS spectrum, a molecular ion peak was observed at *m/z* = 945.2876 for the cationic complex **23**.

Furthermore, the complex **19** features Au–Cl bond, thus serving as a versatile precursor for the synthesis of various gold(I) complexes with several substitutions at the Au(I) center. Given its potential for further functionalization, the reactivity of complex **19** was explored by subjecting it to a ligand exchange reaction. Specifically, the reaction of complex **19** was performed with 1.5 equivalents of K_2CO_3 and one equivalent of phenyl acetylene in DCM for 16 hours (Scheme 17). Upon completion of the reaction, the NHC-gold(I) phenyl acetylene complex **24** was obtained as an ivory colored solid in 84 % yield.

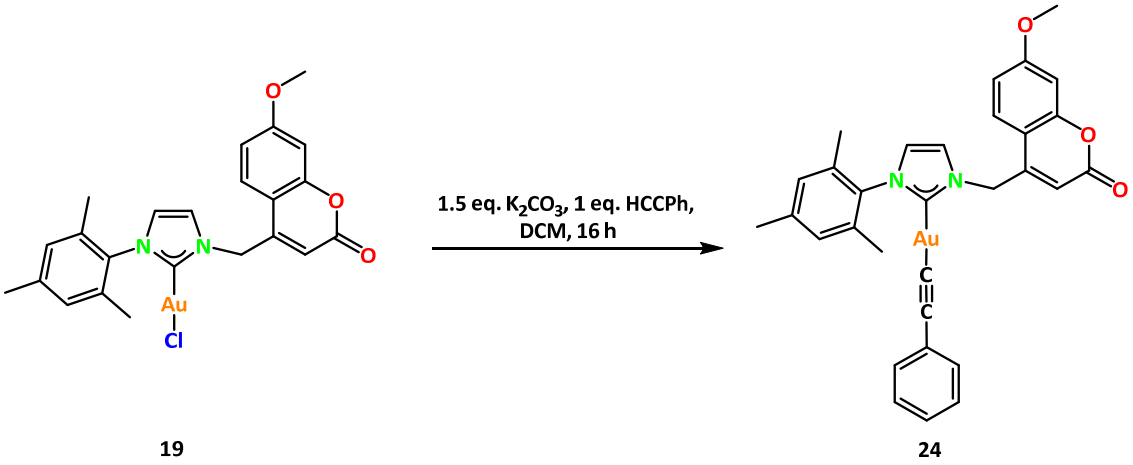

Scheme 17: Synthesis of NHC-gold(I) phenyl acetylene complex **24**.

Single crystals suitable for the SC-XRD analysis were obtained from a mixture of DCM and *n*-pentane. The crystal data quality was insufficient for a reliable bond parameter discussion. For illustrative purposes, the preliminary structure is depicted in the Figure 53.

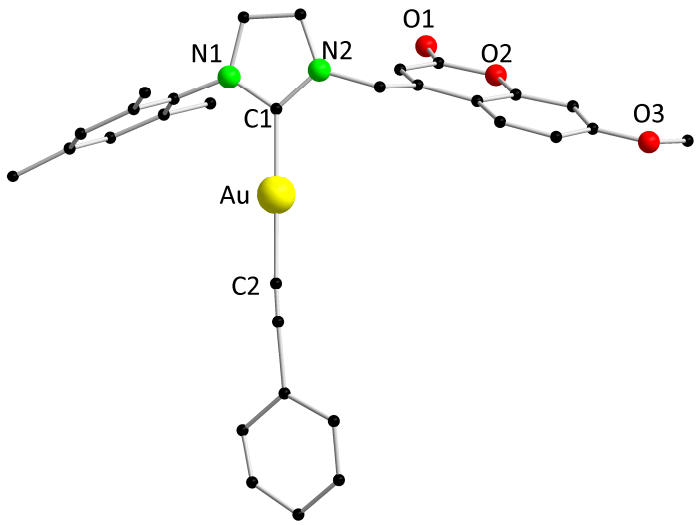

Figure 53: Molecular structure of **24** in the solid state. Hydrogen atoms and non-coordinating solvent molecules are omitted for clarity.

The complex was further analyzed by NMR spectroscopy. In the ^{1}H NMR spectrum, the resonances were found to be similar to those of the starting material (**19**) in the aliphatic region of the spectrum however, resonances of the additional five protons stemming from the phenylacetylide moiety were observed in the aromatic region of the spectrum. In the $^{13}C\{^{1}H\}$

NMR spectrum, a resonance at δ = 190.1 ppm was observed for carbenic carbon which is highly downfield shifted compared to the starting substrate complex **19** (δ = 174.3 ppm).

Complex **19** contains an active methylene group bearing two α-hydrogen atoms adjacent to the nitrogen atom of the NHC moiety, originating from the coumarin functionality. These α-hydrogens are acidic in nature, making them potential sites for deprotonation under basic conditions. They could not be deprotonated using K_2CO_3 as a base as seen from the last reaction with K_2CO_3 and phenyl acetylene to synthesize complex **24**. Instead, KO*t*-Bu, a significantly stronger base, worked well for the deprotonation at this position. To achieve this transformation, the equimolar reaction of complex **19** and KO*t*-Bu was carried out in THF overnight (Scheme 18). As the reaction progressed, a color change was observed, with the reaction mixture transitioning from off-white to dark yellow. Following the deprotonation, an *in situ* formation of the potassium salt at the active methylene center took place. This intermediate subsequently underwent a reaction, leading to chloride abstraction from the gold(I) center, ultimately resulting in the elimination of KCl as a byproduct. For further investigations, crystals of the resulting complex **25** suitable for SC-XRD analysis were obtained from a concentrated DCM solution at ambient temperature. The solubility of complex **25** was found to be comparatively low in most of the organic solvents, like THF, toluene, diethyl ether DCM etc.

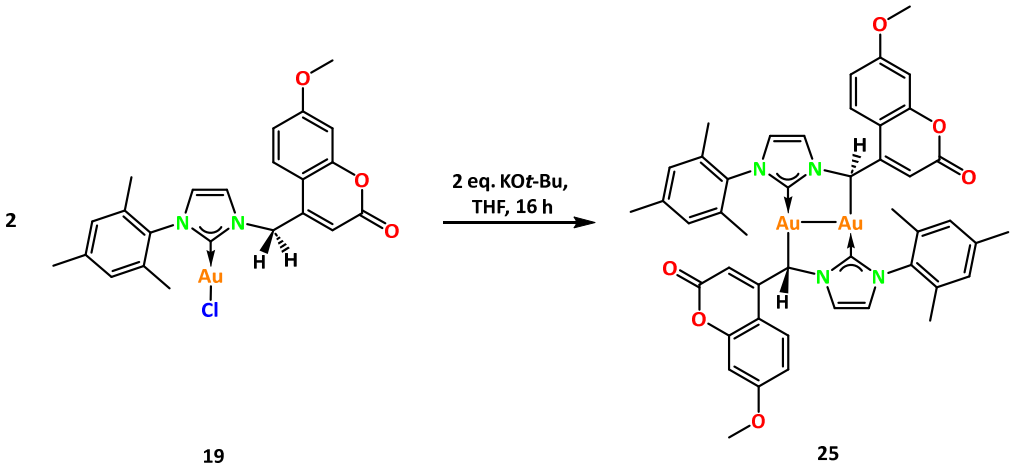

Scheme 18: Reaction of complex **19** with KO*t*-Bu, leading to the formation of complex **25**.

From the structural analysis, it was evident that complex **25** adopts a dimeric arrangement in which the Au(I) center of one molecular unit is not only coordinated to the carbene carbon

(C1) of its own NHC ligand but also forms an additional bond to the α-methylene carbon (C2') of the second molecular unit within the dimer (Figure 54). This bonding interaction results in a measured Au–C2' bond length of 2.100(3) Å, confirming the presence of an extended coordination environment in the dimeric structure.

Furthermore, within this dimeric assembly, the two gold(I) centres were found to be separated by 2.764(2) Å, which is well within the range typically associated with aurophilic interactions, potentially leading to a stabilizing effect within the dimer.[122,126-127] The Au–C1 bond distance, corresponding to the bond between the gold(I) center and the carbene carbon of the NHC ligand, was found to be 2.024(3) Å which is slightly longer than that observed in the starting substrate. Additionally, the Au(I) center was found to exhibit a slight deviation from the linear coordination geometry. The measured C1–Au–C2' bond angle was 171.2(1)° indicating a minor bending at the gold(I) center, likely influenced by steric effects and the dimerization process. A notable structural feature of complex **25** is the presence of an eight-membered metallacyclic ring, composed of two gold, two nitrogen and four carbon atoms. This ring system was found to be planar and the two NHC rings within the dimer were also found to be coplanar with the eight-membered ring.

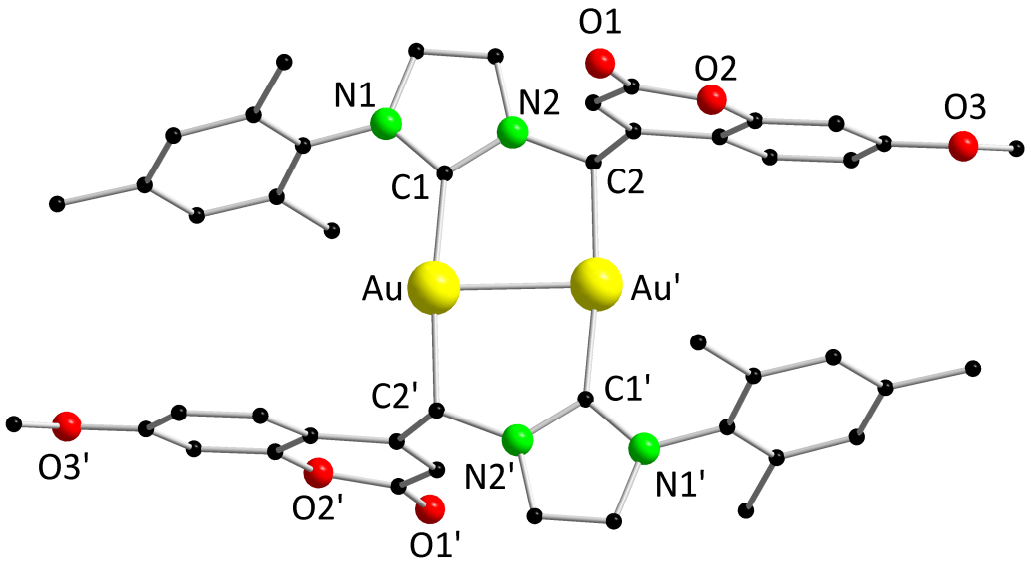

Figure 54: Molecular structure of **25** in the solid state. Hydrogen atoms and non-coordinating solvents are omitted for clarity. Selected bond distances (Å) and angles (°): Au–Au 2.763(3), Au–C1 2.028(4), Au–C2' 2.104(4), C1–N1 1.349(5), C1–N2 1.351(5); C1–Au–C2' 171.4(1).

In the ^{1}H NMR spectrum, three resonances at δ = 1.60, 2.14 and 2.36 ppm were observed as singlets, each integrating to six protons of the methyl groups on the mesityl substituents. Additionally, a singlet was observed at δ = 3.92 ppm, integrating to six protons, which was assigned to the methoxy group located on the coumarin moiety. A noteworthy feature in the spectrum was a singlet at δ = 5.27 ppm, integrating to two protons. This resonance was attributed to the proton attached to the α-methylene carbon, which confirmed the presence of the deprotonated methylene unit within the molecular framework of complex **25**.

Furthermore, in the ^{13}C{^{1}H} NMR spectrum a notable downfield shifted resonance was observed at δ = 185.6 ppm, corresponding to the carbenic carbon directly coordinated to the Au(I) center. This signal was significantly shifted downfield when compared to the starting substrate, complex **19**, which displayed its carbenic carbon resonance at δ = 174.3 ppm. Moreover, the carbon signal corresponding to the α-methylene carbon was detected at δ = 62.6 ppm, which also showed a downfield shift compared to the same carbon in complex **19**, where it appeared at δ = 51.5 ppm.

To explore the reductive capabilities of complex **19**, it was reacted with iodine as an oxidizing agent in DCM for 16 hours under ambient conditions (Scheme 19). The color of the reaction mixture changed from off-white to dark brown. The reaction mixture was filtered and crystals suitable for SC-XRD analysis were obtained from the concentrated DCM solution. The solid obtained after removing the solvent was found to be insoluble in most of the organic solvents, like THF, toluene, diethyl ether and DCM. During the course of the reaction, the Au(I) center was oxidized to Au(III) and from the crystal structure, it is evident that the resulting complex **26** exists in the cationic form where the Au(III) center is coordinated by two NHC ligands and additionally coordinated by two iodides.

A detailed structural analysis of complex **26** provided insights into its coordination environment and geometric properties (Figure 55). The Au–C bond length was found to be 2.051(5) Å, which is slightly shorter than in the precursor complex **19** and similar to the value of 1.993(5) Å in a NHC-Au(III) complex.[370] This minor contraction in bond length can be attributed to the change in oxidation state from Au(I) to Au(III), as higher oxidation states generally lead to stronger metal-ligand interactions. The Au–I bond distances were measured to be 2.561(4) Å and are consistent with previously reported values for Au(III) iodide bonds in similar coordination environments.[370-371]

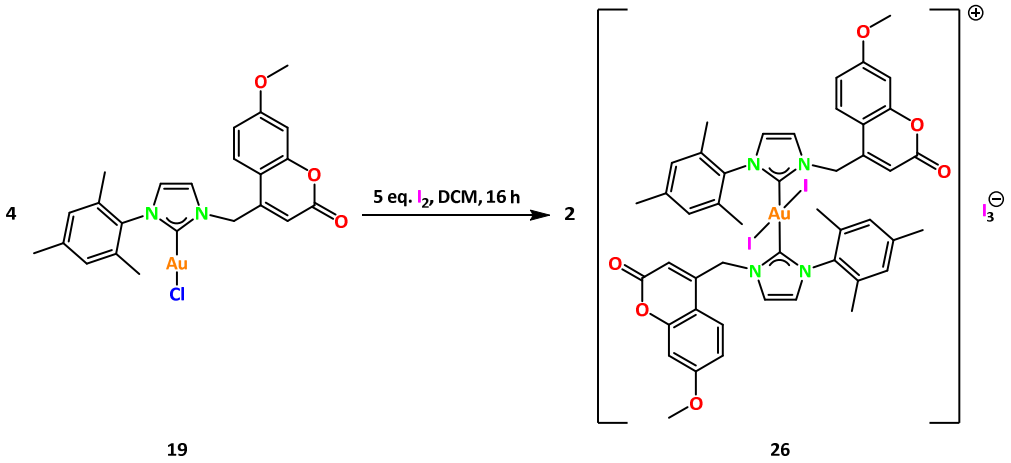

Scheme 19: Synthesis of NHC-Au(III) complex (**26**) by oxidation of complex **19** with I_2.

The geometry of the complex revealed that the Au(III) center is coordinated in a strictly linear manner by the two NHC ligands, forming a C–Au–C' bond angle of 180.0(0)°. Similarly, the two iodides are also arranged in a perfectly linear configuration, with an I1–Au–I2 bond angle of 180.0(0)°. Thus, the Au(III) center adopts a highly symmetric, square planar coordination geometry with C–Au–I1 and C–Au–I2 bond angles of 88.7(1)° and 91.3(1)°, a characteristic of d^8-configured complexes. [372-373]

A notable distinction between complex **26**, a cationic Au(III) complex, and complex **23**, a cationic Au(I) complex, lies in the relative orientation of the NHC ligands. In complex **23**, the two NHC ligands were observed to be positioned at an approximately right angle to each other, however, in complex **26**, the two NHC ligands were found to be completely coplanar.

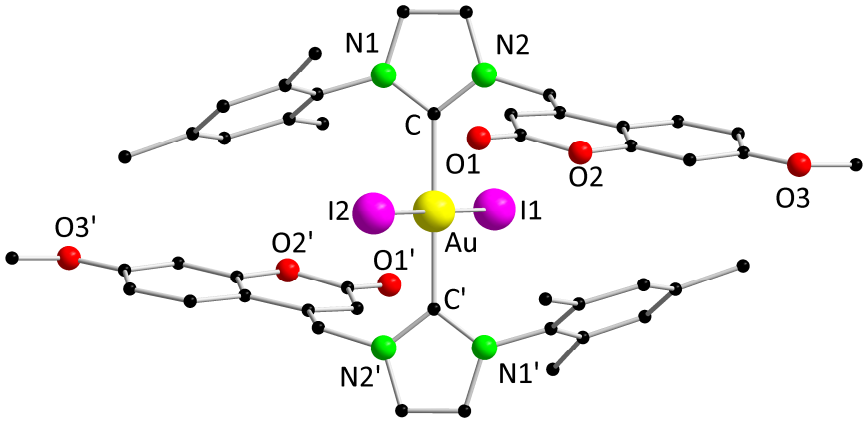

Figure 55: Molecular structure of **26** in the solid state. Hydrogen atoms, non-coordinating solvents and non-coordinating anion are omitted for clarity. Selected bond distances (Å) and angles (°): Au–I1 2.501(9), Au–C 2.061(1), C–N1 1.341(2), C1–N2 1.348(1); C–Au–C' 180.0(0), I1–Au–I2 180.0(0).

Complex **26** was further characterized by NMR spectroscopy. In the ^{1}H NMR spectrum, the resonances at δ = 2.27 and 2.35 ppm were observed for methyl groups of the mesityl substituents, which are almost similar to the precursor **19**. A resonance at δ = 3.90 ppm was obtained for the methoxy group of coumarin which is also reminiscent to the precursor **19**. Surprisingly, in the ^{13}C{^{1}H} NMR spectrum, no resonance was observed corresponding to the carbenic carbon, which was also the case in a similar complex reported.[370]

3.3.3 Photophysical properties

The PL and PLE properties of compounds **18-25** were investigated both in the solid state and in DCM solution. Measurements were conducted at ambient temperature (295 K, red lines) and at 77 K (blue lines) to probe the temperature-dependent luminescent behavior.

In the solid state (Figure 56, left), the PLE spectra of imidazolium salt **18** monitored at λ_{em} = 410 nm (295 K) and 420 nm (77 K) show distinct excitation features with stronger intensity and better spectral resolution at 77 K, indicating suppression of nonradiative pathways at lower temperature.[13,374] The corresponding PL spectra (λ_{ex} = 365 nm) also show an enhanced emission intensity at 77 K, further supporting a thermally activated nonradiative decay process in the solid.[374] The only difference between the spectra at 295 K and 77 K lies in the intensity, being higher at 77 K. The emission profiles are relatively broad, suggesting strong vibronic coupling and possible aggregation-induced effects in the solid.[375]

In the DCM solution (Figure 56, right), the compound exhibits slightly different photophysical characteristics. The PLE spectra observed at λ_{em} = 415 nm at 295 K and 580 nm at 77 K, show two different transitions, with the low-energy emission (580 nm) gaining prominence at 77 K. The PL spectra upon excitation at λ_{em} = 365 nm and 528 nm display multiband emission in the blue-to-orange range, at 77 K. The PL spectrum at the 295 K remains almost similar to that in the solid state.

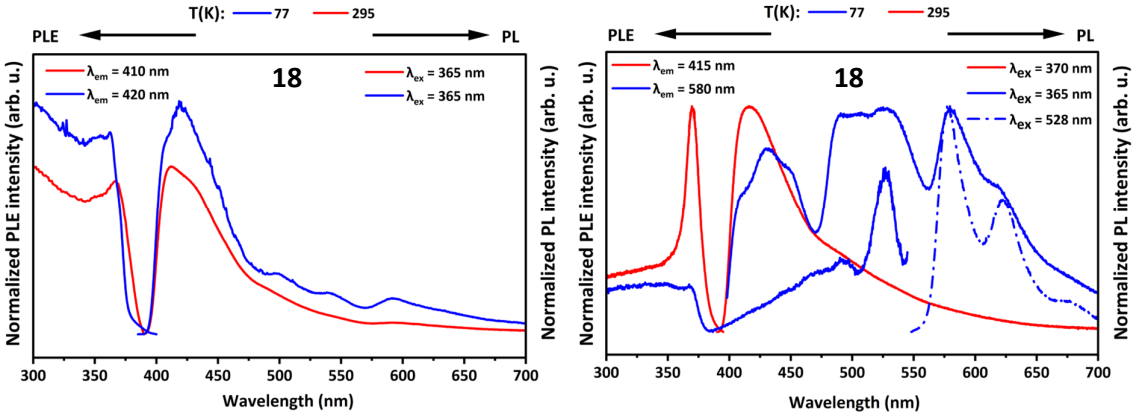

Figure 56: Normalized photoluminescence excitation (PLE) and emission (PL) spectra of solid (left) and DCM solution (right) of the imidazolium salt **18** at 295 K and at 77 K. PLE and PL spectra were recorded at the depicted wavelengths (λ_{em} and λ_{ex}).

The excited states of the imidazolium salt **18** decay with a lifetime of 6 µs at 295 K and 77 K both in solution and the solid state, indicating phosphorescence behavior.

Similarly, PL and PLE measurements were performed for complexes **19** and **20**. In the solid state, the NHC-AuCl complex **19** (Figure 57, upper left) exhibits a distinct temperature-dependent behavior. At 77 K, the PLE spectrum (λ_{em} = 520 nm) shows multiple bands, indicating more resolved excitation features compared to at 295 K. The PL spectrum at 77 K shows a red-shift and broadening relative to the sharper emission observed at 295 K (λ_{ex} = 350 nm), suggesting thermally activated non-radiative processes at higher temperatures. Similarly, the NHC-AuBr complex **20** (Figure 57, lower left) shows almost the same PLE spectra at 77 K (λ_{em} = 420 nm), and at 295 K (λ_{em} = 410 nm), also reminiscent of the PLE spectra of complex **19**. The PL emission is also red-shifted, consistent with the suppression of non-radiative pathways.

In DCM solution, both the complexes show notable changes compared to the solid-state behavior. For the NHC-AuCl complex **19** in solution (Figure 57, upper right), the PLE spectrum (λ_{em} = 515 nm) at 77 K shows multiple excitation features, whereas the 295 K spectrum (λ_{em} = 410 nm) appears smoother and less structured. The PL spectrum at 77 K (λ_{ex} = 350 nm) is broader and red-shifted compared to that at 295 K, suggesting solvent effects and temperature dependent excited state relaxation. The NHC-AuBr complex **20** in DCM (Figure 57, lower right) also displays structured PLE spectrum at 77 K (λ_{em} = 525 nm), in contrast to the spectrum at 295 K (λ_{em} = 430 nm), which has more bands. The corresponding

PL spectrum at low temperature (λ_{ex} = 355 nm) shows enhanced vibronic features and red-shifted emission compared to the higher temperature measurements (λ_{ex} = 370 nm).

The excited states of complexes **19** and **20** decay with a lifetime of around 6 µs at 295 K and 77 K both in DCM solution and the solid state, indicating phosphorescence behavior.

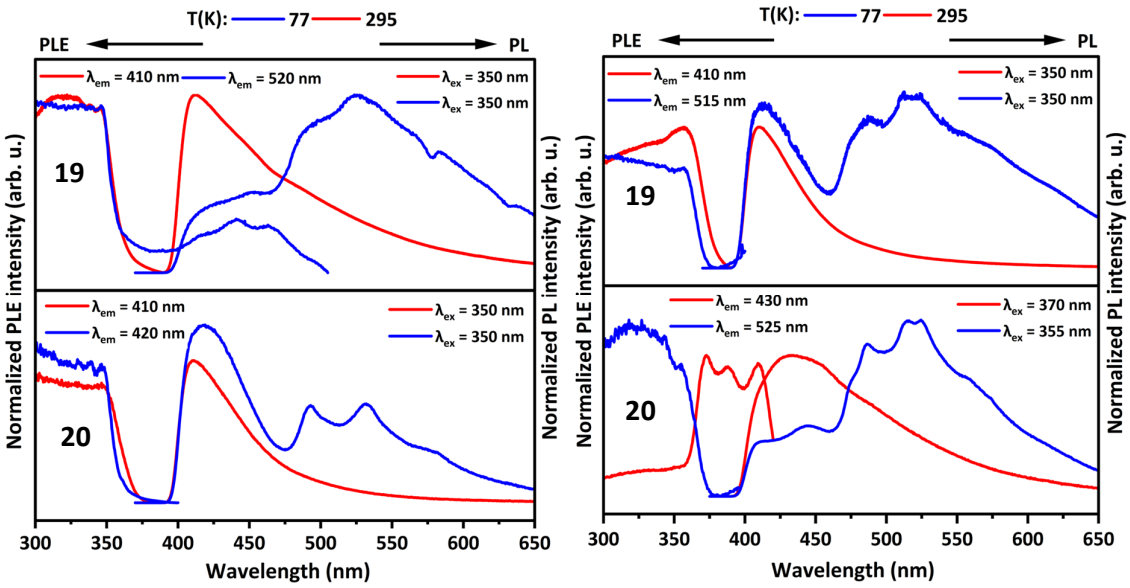

Figure 57: Normalized photoluminescence excitation (PLE) and emission (PL) spectra of solid (left) and DCM solutions (right) of complexes **19** and **20** at 295 K and at 77 K. PLE and PL spectra were recorded at the depicted wavelengths (λ_{em} and λ_{ex}).

For the NHC-AuC_6F_5 complex **21** in the solid state (Figure 58, upper left), the PLE spectra (λ_{em} = 490 nm at 77 K and λ_{em} = 445 nm at 295 K) exhibit pronounced structured features at low temperature, suggesting a more rigid environment and suppressed vibrational broadening. At 77 K, the PL spectrum (λ_{ex} = 355 nm) shows a red-shift and enhanced vibronic structure compared to the emission at 295 K (λ_{ex} = 376 nm), which is broader and less resolved. These observations indicate that non-radiative decay processes are significantly reduced at low temperatures, leading to more efficient emission.[375]

The solid state NHC-AuMes complex **22** (Figure 58, lower left) also displays strong temperature dependence. The PLE spectra (λ_{em} = 585 nm at 77 K and λ_{em} = 565 nm at 295 K) reveal sharper excitation features at 77 K. Similarly, the PL emission (λ_{ex} = 450 nm at 77 K and λ_{ex} = 465 nm at 295 K) shifts towards longer wavelengths and becomes more structured upon cooling. The

spectral broadening and blue-shift at 295 K are characteristic of increased non-radiative relaxation decays.

In solution, the complexes display distinct behaviors compared to their solid state counterparts. For the NHC-AuC_6F_5 complex **21** in DCM (Figure 58, upper right), the PLE spectra (λ_{em} = 425 nm at 77 K and λ_{em} = 450 nm at 295 K) again show sharper features at low temperature, whereas the spectra are smoother and less resolved at 295 K. The PL spectra recorded at 77 K (λ_{ex} = 365 nm) are red-shifted and exhibit vibronic progression, in contrast to the broad emission observed at 295 K (λ_{ex} = 386 nm), reflecting temperature-dependent excited-state dynamics and solvent relaxation.

Similarly, the photoluminescence properties of the NHC-AuMes complex **22** in DCM (Figure 58, lower right) show a pronounced temperature dependence. At 77 K, the PLE spectra (λ_{em} = 512 nm) are highly structured, and the PL spectra (λ_{ex} = 355 nm) display strong vibronic coupling, with red-shifted and multiple emissions relative to the spectrum at 295 K (λ_{ex} = 365 nm and λ_{em} = 420 nm). The shift and resolution enhancement at lower temperatures suggest suppression of dynamic solvent effects and vibrational relaxation pathways.[375]

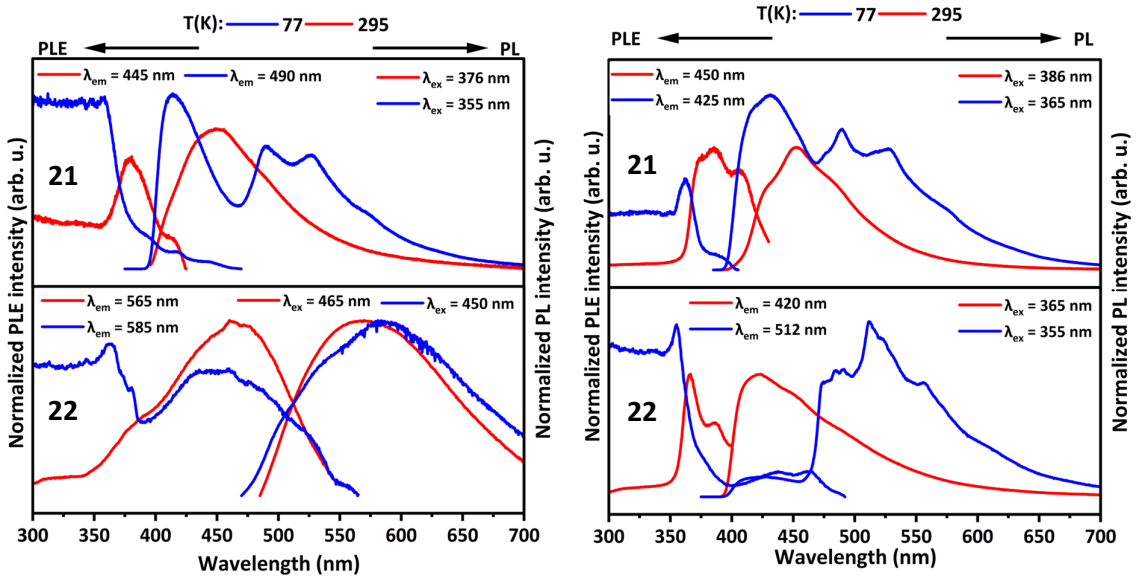

Figure 58: Normalized photoluminescence excitation (PLE) and emission (PL) spectra of solid (left) and DCM solutions (right) of complexes **21** and **22** at 295 K and at 77 K. PLE and PL spectra were recorded at the depicted wavelengths (λ_{em} and λ_{ex}).

The excited states of complex **21** decay with a lifetime of 5 µs at 295 K and 7 µs at 77 K in the solid state, indicating phosphorescence behavior. While it has a lifetime of 6 µs in the DCM solution both at 295 K and 77 K. Whereas excited states of complex **22** decay with a lifetime of 6 µs at 295 K and 8 µs at 77 K in the solid state and it has a lifetime of 6 µs in the DCM solution both at 295 K and 77 K.

The cationic Au(I) complex **23** was also luminescent in nature and was studied for its photophysical properties. In the solid state (Figure 59, left), the PLE spectra (λ_{em} = 420 nm at 77 K and λ_{em} = 425 nm at 295 K) show sharper and more structured features at low temperature, indicative of reduced thermal motion and vibrational broadening. Notably, the low-temperature PL spectrum (λ_{ex} = 350 nm) displays multi emission, red-shifted spectrum extending well into the green region (~500 nm), with clear vibronic progression. In contrast, the emission at 295 K (λ_{ex} = 350 nm) is significantly blue-shifted, suggesting that non-radiative relaxation pathways dominate at ambient conditions, leading to broader and less structured emission.

In DCM solution (Figure 59, right), a similar trend is observed. The PLE spectra recorded at 77 K (λ_{em} = 515 nm) are markedly more structured than at 295 K (λ_{em} = 425 nm), where the excitation features appear broadened. The PL spectrum at 77 K (λ_{ex} = 355 nm) reveals intense, structured emission centered around 515 nm. In contrast, at 295 K (λ_{ex} = 370 nm), the PL is considerably blue-shifted and broad, with diminished intensity.

Overall, the bis(NHC)-Au complex displays typical temperature-dependent luminescence behavior: sharper, red-shifted, and more intense emission at 77 K due to reduced non-radiative processes and better structural rigidity.

The excited states of complex **23** decay with a lifetime of 6 µs at 295 K and 77 K both in DCM solution and the solid state, indicating phosphorescence behavior.

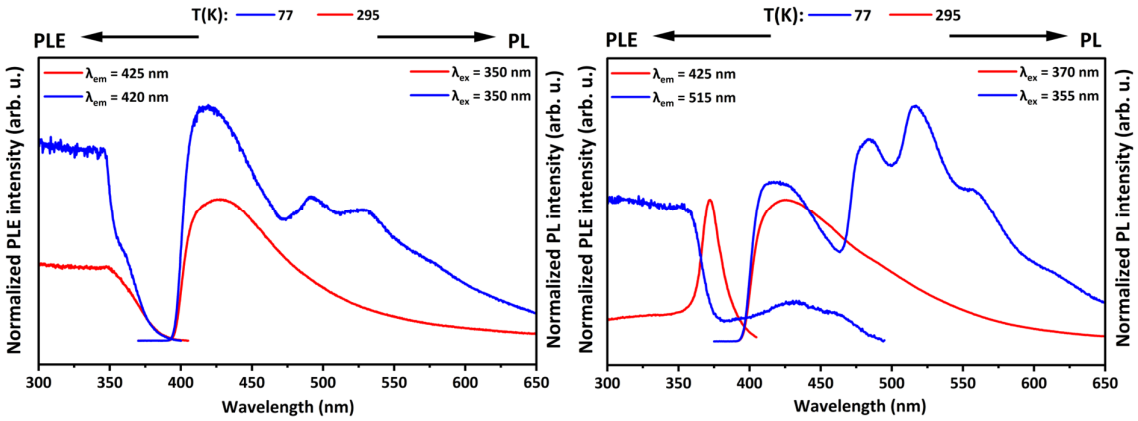

Figure 59: Normalized photoluminescence excitation (PLE) and emission (PL) spectra of solid (left) and DCM solution (right) of complex **23** at 295 K and at 77 K. PLE and PL spectra were recorded at the depicted wavelengths (λ_{em} and λ_{ex}).

The NHC-AuC≡CPh complex **24** was observed to be luminescent both in solid state and in DCM solution at 77 K as well as at 295 K. In the solid state (Figure 60, left), the compound exhibits moderate photoluminescence at 295 K, which is significantly enhanced and structured at 77 K. The PLE spectrum monitored at λ_{em} = 495 nm at 77 K reveal an excitation band at 360 nm that is more defined and intense as compared to at 295 K. Correspondingly, the PL spectra at λ_{ex} = 405 (295 K) and 360 nm (77 K) show stronger and more structured emission at 77 K, suggesting the suppression of vibrational relaxation pathways.

In DCM solution (Figure 60, right), the emission profile changes drastically. At 295 K, the PL spectrum is weak and featureless, but at 77 K, there is a marked increase in intensity with vibronic resolution and a maximum at 515 nm. The emergence of this red-shifted emission band at low temperature points to the activation of a lower-lying excited state that becomes radiatively accessible when thermal deactivation is minimized. PLE spectrum in solution (λ_{em} = 515 nm) also reflect multiple excitation bands at 77 K, suggesting a more complex excited-state landscape in solution, possibly involving equilibrium between locally excited and charge-transfer states.

The excited states of complex **24** decay with a lifetime of 6 µs both at 295 K and 77 K in the solid state, indicating phosphorescence behavior. While it has a lifetime of 6 µs at 295 K and 9 µs at 77 K in the DCM solution.

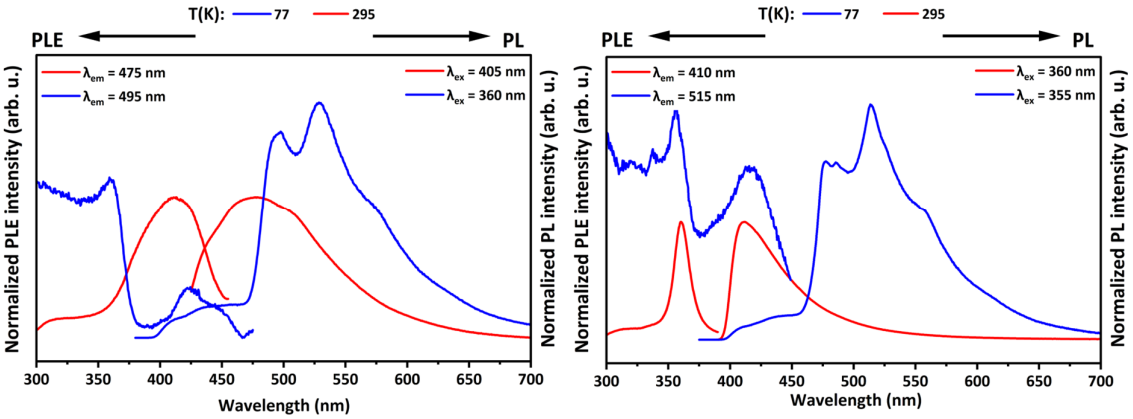

Figure 60: Normalized photoluminescence excitation (PLE) and emission (PL) spectra of solid (left) and DCM solution (right) of complex **24** at 295 K and at 77 K. PLE and PL spectra were recorded at the depicted wavelengths (λ_{em} and λ_{ex}).

The bimetallic Au(I) complex **25** was also found to be luminescent and its photophysical properties were consequently studied. In the solid state (Figure 61, left), the complex exhibits dual emission bands centered at approximately 410 nm and 600 nm (λ_{ex} = 325 nm). The emission at 410 nm is prominent at 295 K, whereas the low-energy emission at 600 nm becomes significantly more intense at 77 K. The corresponding PLE spectrum monitored at λ_{em} = 415 nm (295 K) shows only one band while at λ_{em} = 600 nm (77 K) emission reveal different excitation profiles, indicating the presence of multiple emissive states. The enhancement of the 600 nm emission at 77 K suggests phosphorescence from a triplet state, likely stabilized by aurophilic interactions in the solid state, which are known to increase at lower temperatures. This is consistent with previously reported behavior in gold(I) complexes with close Au···Au contacts.[251]

In contrast, the DCM solution spectrum (Figure 61, right) displays a single structured emission in the blue-green region (centered at 485-500 nm), with only minor temperature dependence and higher intensity at lower temperature. The excitation spectra monitored at λ_{em} = 485 nm (295 K) shows a maximum around 380 nm and excitation at λ_{em} = 500 nm (77 K) results in a maximum around 325 nm.

These observations highlight the role of intramolecular interactions and the environment, solid state or solution, on the photophysical behavior of gold(I) complexes.

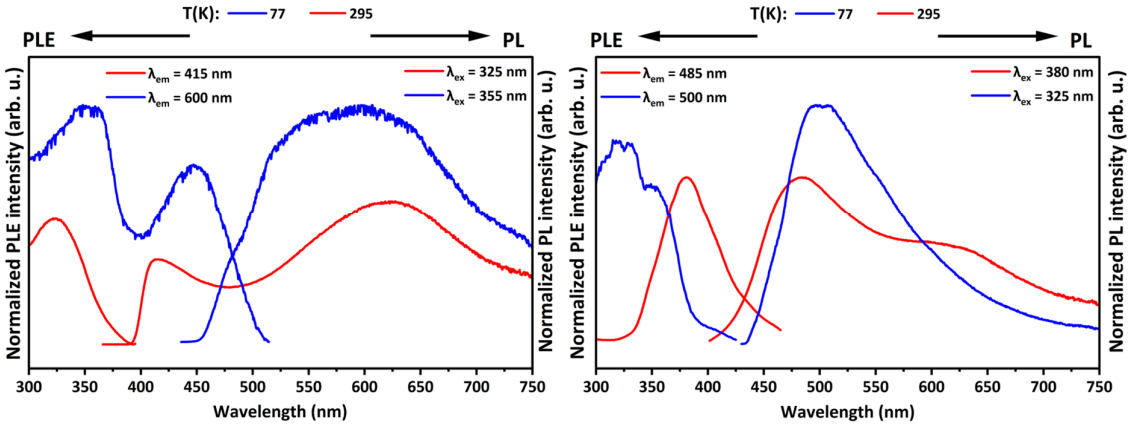

Figure 61: Normalized photoluminescence excitation (PLE) and emission (PL) spectra of solid (left) and DCM solution (right) of complex **25** at 295 K and at 77 K. PLE and PL spectra were recorded at the depicted wavelengths (λ_{em} and λ_{ex}).

The excited states of complex **25** decay with a lifetime of 6 µs at 295 K and 14 µs at 77 K in the solid state, indicating phosphorescence behavior. While it has a lifetime of 6 µs in the DCM solution at 295 K and is prolonged to 201 and 1160 µs at 77 K.

3.4 Syntheses and photophysical properties of coumarin substituted NHC-transition metal complexes

3.4.1 Introduction

Following the groundbreaking work independently reported by Öfele[181] and Wanzlick[182] in 1968, which marked the discovery of the first metal–NHC complexes, a major advancement came with Arduengo *et al.*, who successfully isolated the first stable NHC ligand, 1,3-bis(adamantyl)imidazol-2-ylidene (IAd).[183] This distinctive class of carbenes, with a carbene center embedded within a nitrogen-containing heterocycle, has significantly influenced various areas of chemistry.[317,376-380] Today, NHCs serve as crucial ligands for a broad spectrum of main group elements, transition metals, and *f*-block compounds, finding extensive applications particularly in both homogeneous and heterogeneous catalysis.[378,380]

In 1995, Robert H. Grubbs reported the synthesis of a ruthenium-based olefin metathesis catalyst coordinated by tricyclohexylphosphine, known as the first-generation Grubbs catalyst.[381-382] Subsequently, in 1999, Grubbs introduced a second-generation catalyst that replaced one of the phosphine ligands with an NHC, based on 1,3-bis(mesityl)-dihydroimidazole (Figure 62). This modification led to considerable enhancements in both catalytic performance and stability. The new complex also exhibited superior resistance to moisture and air, which significantly broadened its applicability under more practical reaction conditions.[199] The success of this catalyst contributed to a sharp rise in interest surrounding NHCs as ligands for transition metal complexes.

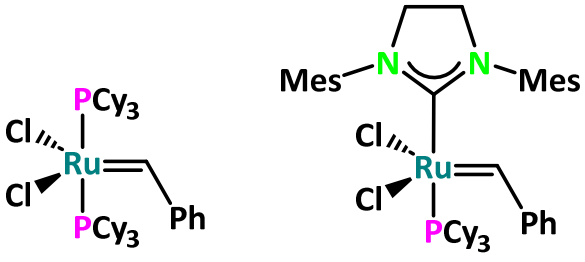

Grubbs I **Grubbs II**

Figure 62: First- and second-generation Grubbs catalysts. [199,381-382]

Following Grubb's pioneering work, numerous other well-known catalysts incorporating NHC ligands were developed for similar applications. These included the Hoveyda–Grubbs catalysts, featuring a chelating isopropoxybenzylidene ligand for enhanced stability and reusability,[383-384] and third-generation Grubbs catalysts, optimized for further activity and functional group tolerance.[385-386] Collectively, these advancements established NHCs as powerful alternatives to phosphines in homogeneous catalysis. NHC ligands quickly gained widespread popularity in coordination chemistry due to their unique and advantageous properties. Compared to phosphines, NHCs are stronger *σ*-donors and weaker *π*-acceptors, are thermally and oxidatively stable, resistant to decomposition in the presence of air and moisture and exhibit highly tunable steric and electronic properties. These features also make them particularly suitable for catalysis in aqueous media.[313,317]

Over time, NHCs have been successfully employed in the synthesis of a wide array of transition metal complexes, particularly with late transition metals such as Ni, Ru, Rh, Pd, Ir or Pt. Metal complexes of differently substituted NHCs offer a plethora of applications, for instance for their catalytic activity or photophysical properties.[387-392] In 2018, Castarlenas *et al.* reported the synthesis of rhodium(I) complexes bearing an NHC ligand functionalized with a coumarin moiety. One of the resulting Rh(I) complexes was found to adopt a pentacoordinated geometry, (Figure 63a where M = Rh, L = COD, Cl).[393]

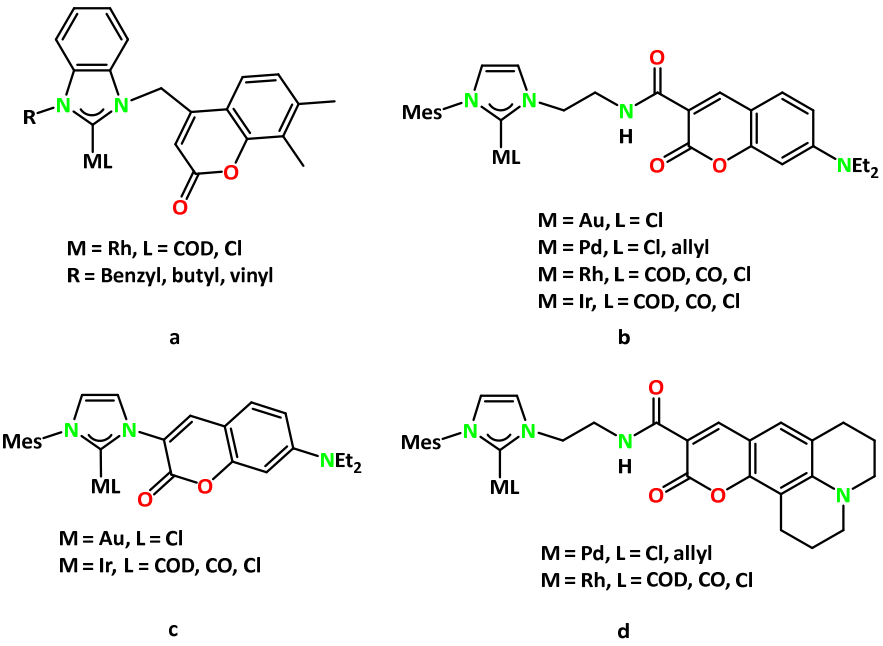

Figure 63: Examples of different types of coumarin substituents on NHC-transition metal complexes.

In the same year Plenio and coworkers conducted a systematic study on NHC ligands modified with various coumarin functionalities and their respective transition metal complexes (Figure 63b-d).[394] Using the ligand shown in Figure 63b, they synthesized a diverse set of complexes, including one each with Au(I) and Ru(II), two with Pd(II), two with Rh(II), and two with Ir(II). With the coumarin-functionalized ligand depicted in Figure 63c, only three metal complexes were successfully obtained, one with Au(I) and two with Ir(I). Finally, using the ligand illustrated in Figure 63d, they reported the synthesis of one Rh(I) and two Pd(II) complexes. Each of these complexes was analyzed to explore their photophysical behavior.

Here, a new series of metal complexes incorporating a 7-methoxy-4-methylene coumarin-functionalized NHC ligand is reported. The transition metals utilized in these studies include Rh(I), Ir(I), Pt(II), Pd(II), and Ru(II). These complexes were characterized and subsequently examined for their photophysical properties.

3.4.2 Syntheses and characterization of NHC-transition metal complexes

Following a similar procedure as for the Au(I) complexes (**19-23**), transition metal complexes were also synthesized. For the synthesis of the Rh(I) complex **27**, the reaction of the imidazolium salt **18** was performed with half an equivalent of Ag_2O in DCM for 16 hours, and the resulting reaction mixture was filtered into a flask containing $[Rh(cod)Cl]_2$ (Scheme 20). After stirring the reaction mixture for additional 16 hours, it was filtered and crystals suitable for SC-XRD analysis were obtained from the mixture of DCM and *n*-pentane.

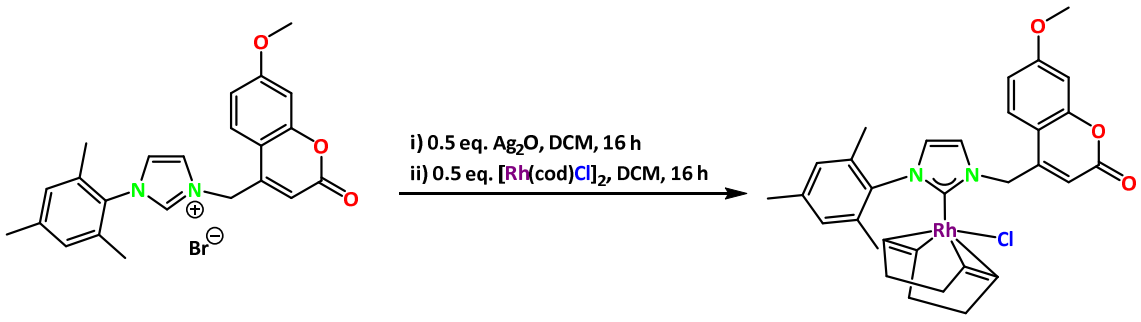

18 27

Scheme 20: Synthesis of NHC-Rh(I) complex **27**.

From the structural analysis it is evident that the Rh(I) center is coordinated by an NHC unit and a 1,5-cyclooctadiene (cod) unit and additionally bonded to a chloride (Figure 64). This coordination environment is consistent with previously reported Rh(I)-carbene

complexes.[393,395] The Rh–C bond length was determined to be 2.055(3) Å which is similar to Rh–C bond distance of 2.034(2) Å in NHC-Rh(I) complex depicted in Figure 63a.[393] The Rh-Cl bond length was found to be 2.399(6) Å which was similar to the reported in literature i.e. 2.394(5) Å.[393,395-396] The C–Rh–Cl angle was observed to be 88.6(7)° which is close to the right angle and slightly larger than the reported value of 87.8(5)° in a similar complex.[393] Interestingly, the Rh(I) center is not perfectly aligned with the NHC ligand but exhibits a slight tilt to one side. This deviation is reflected in the bond angles, where the N2–C–Rh bond angle measures 122.7(2)°, while the N1–C–Rh bond angle is slightly larger at 133.4(2)°.

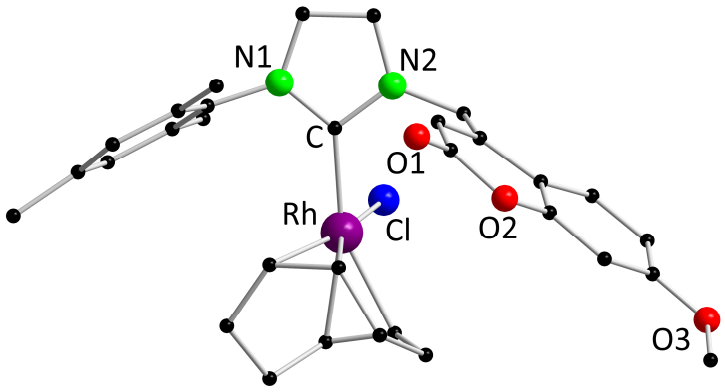

Figure 64: Molecular structure of **27** in the solid state. Hydrogen atoms and non-coordinating solvent molecules are omitted for clarity. Selected bond distances (Å) and angles (°): Rh–C 2.056(3), Rh–Cl 2.399(7), C–N1 1.367(4), C–N2 1.359(4); C–Rh–Cl 88.6(8), N1–C–Rh 133.2(2), N2–C–Rh 122.7(2).

The complex **27** was further analyzed using NMR spectroscopy. In the ^{1}H NMR spectrum, three distinct singlets at δ = 1.90, 2.38 and 2.46 ppm, each integrating to three protons, were observed for the methyl substituents on the mesityl group. Additionally, a singlet at δ = 3.92 ppm was observed for the coumarin methoxy group. Furthermore, signals for the cod moiety were also evident in the aliphatic region of the spectrum. In the aromatic region, the pattern of signals was comparable to those seen in analogous Au(I) complexes, however, a slight downfield shift was noted, suggesting a subtle difference in the electronic environment. In the ^{13}C{^{1}H} NMR spectrum, a characteristic doublet for the carbenic carbon was observed at δ = 185.0 ppm with a splitting caused by coupling to the Rh(I) ion ($^{1}J_{CRh}$ = 51.9 Hz) which is identical to the one reported in literature with same coupling constant at δ = 185.0 ppm.[393]

To obtain an analogous Ir(I) complex, a reaction was performed following the same procedure as for complex **27**. However, instead of employing a Rh(I) precursor, [Ir(cod)Cl]$_2$ was utilized

as an iridium(I) metal precursor (Scheme 21). The resulting NHC-Ir(I) complex **28** was successfully obtained and subsequently crystallized from a mixture of DCM and *n*-pentane, yielding crystals suitable for further structural analysis.

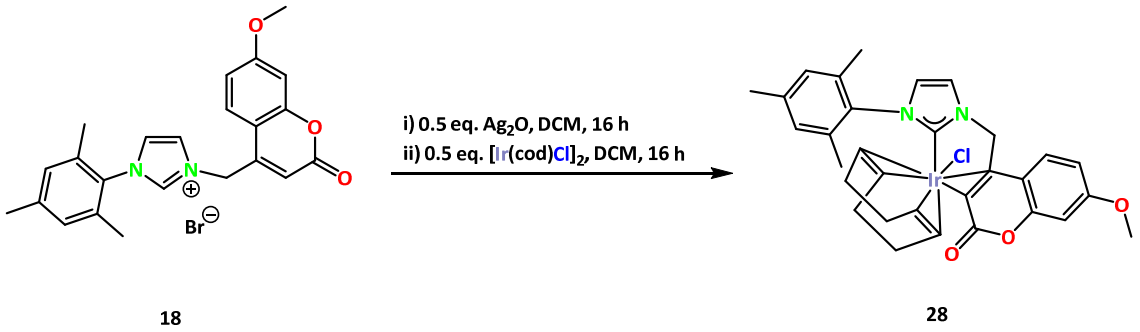

18 28

Scheme 21: Synthesis of NHC-Ir(I) complex **28**.

From the SC-XRD analysis of complex **28**, it is evident that the Ir(I) center is coordinated by the NHC ligand, cod and additionally bonded to a chloride, resembling the coordination pattern observed in the NHC-Rh(I) complex **27** (Figure 65). In addition to these ligands, a distinctive feature of this complex is the interaction of the Ir(I) center with the double bond of the coumarin functionality through π-donation. This additional coordination significantly influences the overall geometry of the complex, causing noticeable deviations in bond angles compared to previously reported structures. The Ir–C1 bond length, representing the Ir(I)-NHC interaction, was determined to be 2.041(5) Å which aligns well with previously reported value of 2.006(2) Å in a similar NHC-Ir(I) complex.[397-399] The Ir–Cl bond length was found to be 2.533(1) Å slightly longer than the bond distance for an Ir(I)-chloride interaction of 2.375(4) Å in a similar NHC-Ir(I)complex.[397] The measured Ir–C2 and Ir–C3 bond distances, corresponding to the interaction between the Ir(I) center and the coumarin's double bond, were found to be 2.156(6) Å and 2.167(6) Å, respectively. The C1–Ir–Cl bond angle was observed to be 81.1(2)° which deviates by approximately 9° from the right angle and is about 7° smaller compared to the complex **27**. This bond angle is also 9° smaller than the reported value of 90.3(5)° for a similar NHC-Ir(I) complex.[397] The Ir(I) center seemed to be bended towards the coumarin group due to the π-interactions and the measured bond angles spanned by N1–C1–Ir and N2–C1–Ir were found to be 141.9(4)° and 114.5(4)°, respectively, strongly deviating from the respective angles in complex **27**. Overall, the structural analysis highlights

how the π type interaction of the coumarin double bond with the Ir(I) center influences the geometry of the complex, leading to noticeable distortions compared to complex **27**.

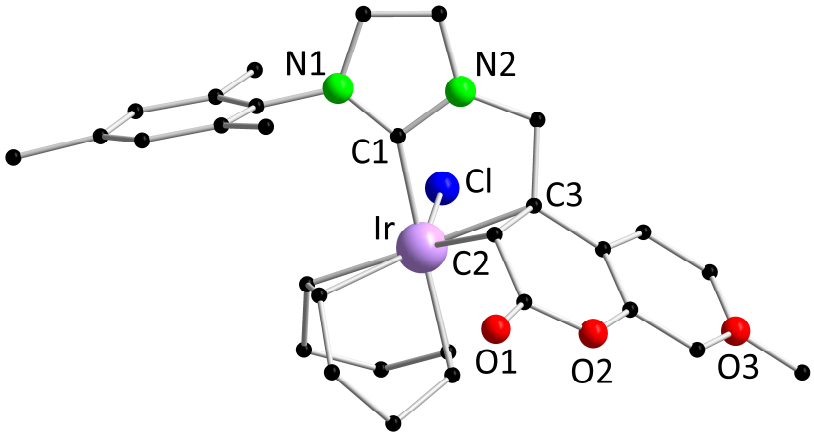

Figure 65: Molecular structure of **28** in the solid state. Hydrogen atoms and non-coordinating solvent molecules are omitted for clarity. Selected bond distances (Å) and angles (°): Ir–C1 2.0441(6), Ir–Cl 2.533(1), C1–N1 1.352(7), C2–N2 1.352(7), Ir–C2 2.156(6), Ir–C3 2.167(6); C1–Ir–Cl 81.1(2), N1–C1–Ir 141.9(4), N2–C1–Ir 114.5(4).

As a next step towards the synthesis of NHC-transition metal complexes, the imidazolium salt **18** was subjected to metalation with half an equivalent of Ag_2O in DCM for *in situ* NHC generation. The reaction mixture was further treated with half an equivalent of platinum(II) chloride ($PtCl_2$) to obtain an NHC-coordinated Pt(II) complex (Scheme 22). After workup, crystals suitable for SC-XRD analysis were obtained from a concentrated solution of complex **29** in DCM.

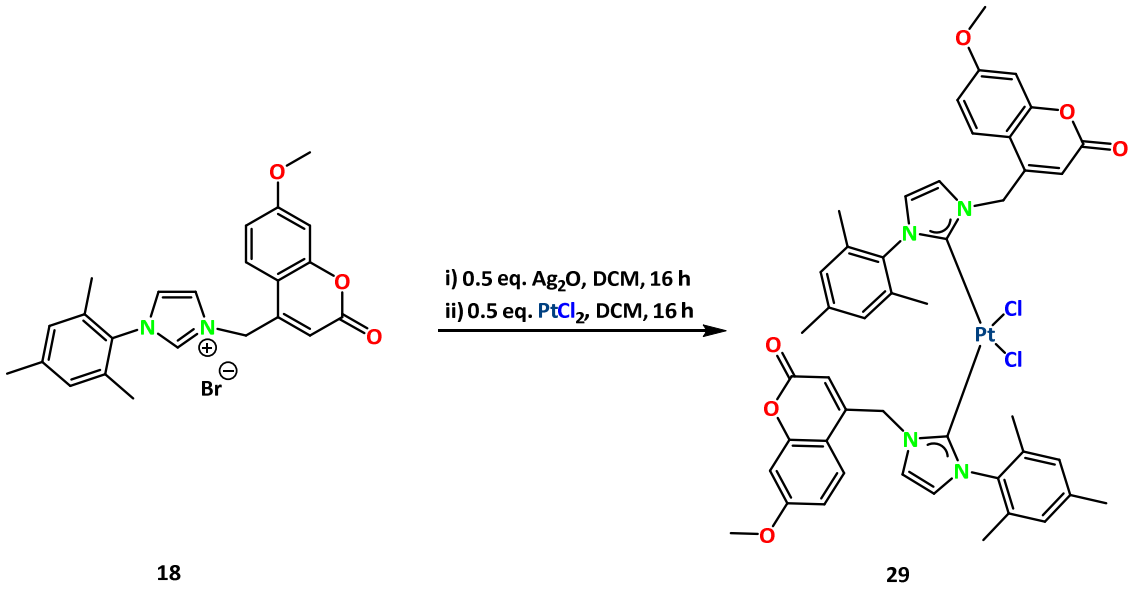

18 29

Scheme 22: Synthesis of NHC-Pt(II) complex **29**.

A comprehensive structural analysis of complex **29** provided insights into the coordination environment and geometric arrangement of the Pt(II) center (Figure 66). The Pt(II) ion is coordinated by two NHC ligands and two chlorides. The Pt–C1 and Pt–C2 bond distances were determined to be 1.952(5) Å which are slightly shorter compared to a plethora of similar NHC-Pt(II) complexes falling in the range 1.969-2.016 Å.[400] The Pt–Cl1 and Pt–Cl2 bond lengths were found to be 2.373(1) Å which are consistent with previously reported values.[401] The Pt(II) center adopts a square planar geometry which is a characteristic feature of d^8-configured transition metal complexes.[373] The C1–Pt–C2 bond angle was determined to be 91.6(3)° indicating that the ring planes of the two NHC ligands are positioned nearly perpendicular to each other and this bond angle is slightly lesser than those of similar complexes falling in the range 93.7-96.4°.[400] The two chlorides almost form a right angle with each other with a Cl1–Pt–Cl2 bond angle of 89.9(6)°. The C1–Pt–Cl1 bond angle was found to be 90.0(2)°, which aligns with the expected values for a near-perfect square planar geometry.

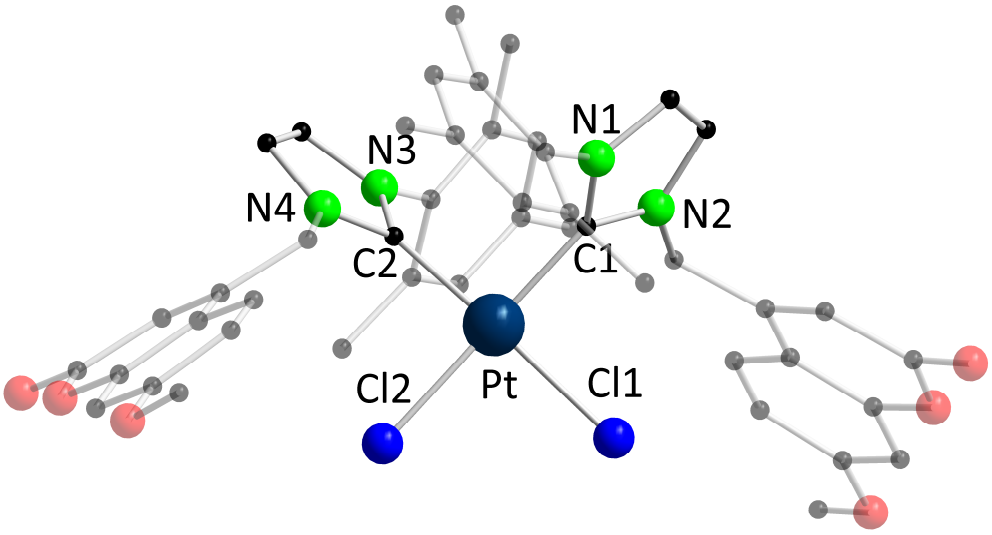

Figure 66: Molecular structure of **29** in the solid state. Hydrogen atoms and non-coordinating solvent molecules are omitted for clarity. Selected bond distances (Å) and angles (°): Pt–C1 1.952(5), Pt–C2 1.952(5), Pt–Cl1 2.373(1), Pt–Cl2 2.373(1); C1–Pt–C2 91.6(3), Cl1–Pt–Cl2 89.9(6), C1–Pt–Cl1 90.0(2), C1–Pt–Cl2 170.7(1).

Due to the low solubility of complex **29** in common deuterated solvents, a high-quality NMR spectrum could not be obtained. Nonetheless, in the $^{13}C\{^{1}H\}$ NMR spectrum of complex **29**, a doublet at δ = 191.2 ppm, with $^{1}J_{CPt}$ = 59.4 Hz, was observed for the carbenic carbon of the NHC coordinating to the Pt(II) center.

In a similar manner as for the previous complexes, after treating the imidazolium salt **18** with half an equivalent of Ag_2O, the reaction was performed with half an equivalent of the allylpalladium(II) chloride dimer ($[(\eta^3\text{-}C_3H_5)PdCl]_2$) for 16 hours (Scheme 23). Crystals suitable for the SC-XRD analysis were obtained from a concentrated solution of complex **30** in DCM.

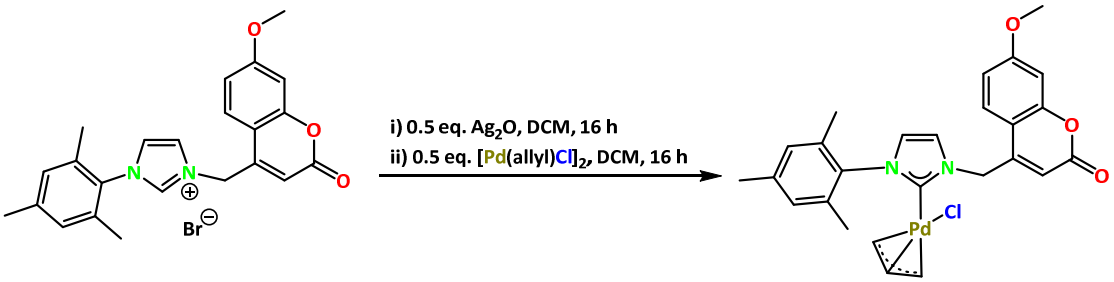

18 30

Scheme 23: Synthesis of NHC-Pd(II) complex **30**.

Complex **30** crystallized in the monoclinic space group $P2_1/n$, and its structural parameters exhibit a high degree of similarity to those observed in analogous complexes discussed in earlier sections (Figure 67). The analysis revealed that the Pd–C1 bond length was 2.039(4) Å which is in agreement to the ones reported values of 2.040(11) Å for palladium-carbene interactions.[402] The Pd–Cl bond distance was measured to be 2.382(1) Å which is also similar to the ones reported in the literature (2.370(5) Å).[402] The palladium ion is also coordinated by a η^3-allyl ligand, and the average distance from the metal center to the allyl carbon atoms was found to be approximately 2.15 Å which was also the case in similar reported complexes.[402] The C1–Pd–Cl bond angle was determined to be 92.7(1)°, indicating a nearly orthogonal arrangement between the carbene ligand and the chloride ion at the metal center. Furthermore, the bond angle spanned by C1–Pd–C4 was found to be 170.3(2) °.

Complex **30** was additionally characterized by NMR spectroscopy. In the ^{1}H NMR spectrum, three well-defined singlets were seen at δ = 2.08, 2.24 and 2.33 ppm, each integrating to three protons, for the methyl substituents on the mesityl group of the NHC ligand. Additionally, a distinct singlet was observed at δ = 3.88 ppm corresponding to the coumarin methoxy group.

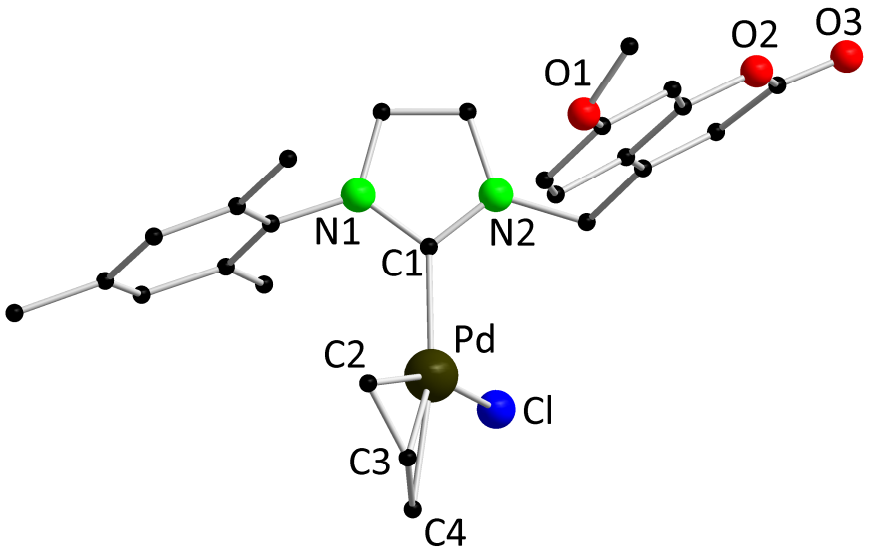

Figure 67: Molecular structure of **30** in the solid state. Hydrogen atoms and non-coordinating solvent molecules are omitted for clarity. Selected bond distances (Å) and angles (°): Pd–C1 2.039(4), Pd–C2 2.109(6), Pd–C3 2.105(6), Pd–C4 2.180(6), Pd–Cl 2.382(1); C1–Pd–Cl 92.7(1), C1–Pd–C4 170.3(2).

The resonances in the aromatic region were also comparable to the ones structurally related complexes discussed earlier (complexes **27-29**). Furthermore, due to the coordination of the

allyl ligand to the Pd(II) center, additional resonances were observed in the aliphatic region of the spectrum. The resonances at δ = 2.99, 4.09 and 4.88 ppm integrating to two, two and one protons, respectively, were assigned to the allyl ligand. Furthermore, a resonance at δ = 184.2 ppm in the $^{13}C\{^{1}H\}$ NMR spectrum for carbenic carbon also confirmed the complex formation and was close to the value of δ = 185.7 ppm reported for similar complexes.[402]

To further demonstrate the versatility of the NHC ligand, the synthesis of a Ru complex was targeted. After performing the carbene activation reaction of the imidazolium salt **18** with half an equivalent of Ag_2O, the reaction mixture was treated with half an equivalent of the (*p*-cymene)ruthenium(II) dichloride dimer ($[Ru(p\text{-cymene})Cl_2]_2$) to obtain the NHC-Ru(II) complex **31** as the product (Scheme 24). Crystals suitable for SC-XRD analysis were obtained by slow diffusion of *n*-pentane to a concentrated DCM solution of complex **31**.

The structural analysis of complex **31** revealed that the Rh(II) center is coordinated by the NHC and a *p*-cymene group and additionally bonded to two chlorides (Figure 68). The Ru–C bond distance, representing the interaction of Ru(II) with the carbene, was observed to be 2.097(9) Å deviating slightly from the reported bond length of 2.060(4) Å in a similar complex.[403]

18 **31**

Scheme 24: Synthesis of NHC-Ru(II) complex **31**.

The two chlorides were also found to be equidistant from the Ru(II) center with Ru–Cl1 and Ru–Cl2 bond lengths of 2.425(2) Å and 2.430(2) Å which are almost same as the bond lengths of 2.420(1) Å and 2.429(1) Å in a similar complex.[403] The C–Ru–Cl1 and C–Ru–Cl2 bond angles were observed to be 84.0(3)°and 92.1(2)°, deviating slightly from the right angle. Both the

chlorides are bonded to the Ru(II) center at nearly a right angle with Cl1–Ru–Cl2 bond angle of 84.7(8)° comparable to the similar complex.[403]

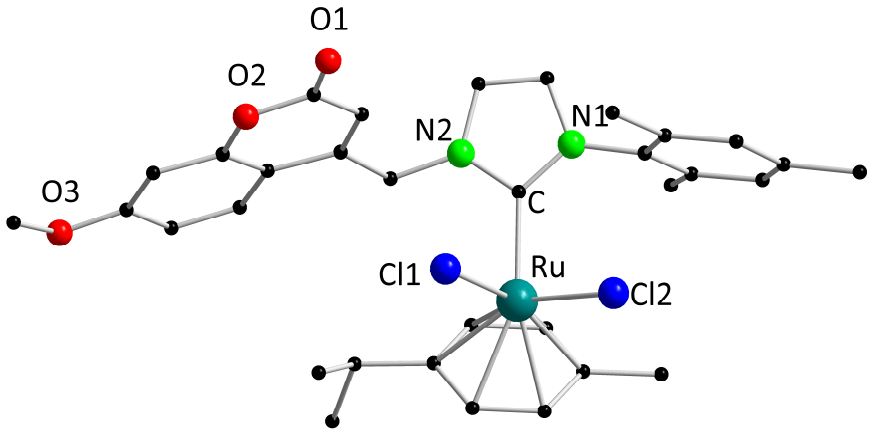

Figure 68: Molecular structure of **31** in the solid state. Hydrogen atoms and non-coordinating solvent molecules are omitted for clarity. Selected bond distances (Å) and angles (°): Ru–C 2.097(9), Ru–Cl1 2.425(2), Ru–Cl2 2.430(2); C–Ru–Cl 1 84.0(3), C–Ru–Cl2 92.1(2), Cl1–Ru–Cl2 84.7(8).

Furthermore, complex **31** was thoroughly characterized by NMR studies. In the ^{1}H NMR spectrum, the methyl substituents on the mesityl group were observed at δ = 2.20 and 2.38 ppm as singlet with an integration ratio of six and three protons, respectively. In addition, a doublet at δ = 0.99 ppm and a singlet at δ = 1.74 ppm were also seen, corresponding to six and three protons, respectively, for the methyl groups of the *p*-cymene moiety coordinating to the Ru(II) center. Additional resonances attributed to the aromatic protons of the *p*-cymene ring were present in the aromatic region of the spectrum. In the ^{13}C{^{1}H} NMR spectrum, a resonance at δ = 174.7 ppm was observed for the carbenic carbon of the NHC ligand, confirming the successful complex formation and was found to be close to the reported resonance of δ = 173.6 ppm for a similar complex.[404]

3.4.3 Photophysical properties

The NHC-Ir(I) complex (**28**) and the NHC-Ru(II) complex (**31**) were found to be luminescent in the solid state and in DCM solution only at 77 K, whereas the NHC-Pt(II) complex (**29**) and the NHC-Pd(II) complex (**30**) were found to be luminescent in the solid state and in DCM solution both at 295 K and at 77 K.

Investigation of the photophysical behavior of the complexes **28** and **31**, both in the solid state and in DCM solution at 77 K, showed that these two complexes exhibit distinctly different PL profiles, which are influenced by the nature of the metal center and the phase.

In the PLE spectrum of the NHC-Ir(I) complex (**28**), a well-defined maximum is observed at 470 nm (λ_{em} = 535) (Figure 69, upper left). Upon excitation at λ_{ex} =470 nm, dual emission appears with bands around 535 nm and 625 nm. The heavy-atom effect of Ir(I) promotes efficient intersystem crossing (ISC), enabling the population of triplet states and giving rise to strong phosphorescence.[405] In DCM solution at 77 K, the Ir(I) complex shows green phosphorescence, with emission centered at around 540 nm when excited at λ_{ex} = 430 nm (Figure 69, upper right). The spectral profile remains similar to the solid state data, though slight broadening occurred due to solvation effects.

In contrast, the emission behavior of the NHC–Ru(II) complex (**31**) differs significantly. In the solid state, upon excitation at λ_{ex} = 310 nm, the Ru(II) complex emits in the blue region at around 415 nm with a broad band (Figure 69, lower left). Unlike the Ir(I) complex, the Ru(II) analogue does not show longer-wavelength emission, which can be attributed to the lower spin–orbit coupling of Ru(II), resulting in inefficient ISC and the predominance of singlet-state emission.[406-407] In DCM solution (77 K), the Ru(II) complex retains this blue emission at 415 nm, excited at λ_{ex} = 330 nm (Figure 69, lower right).

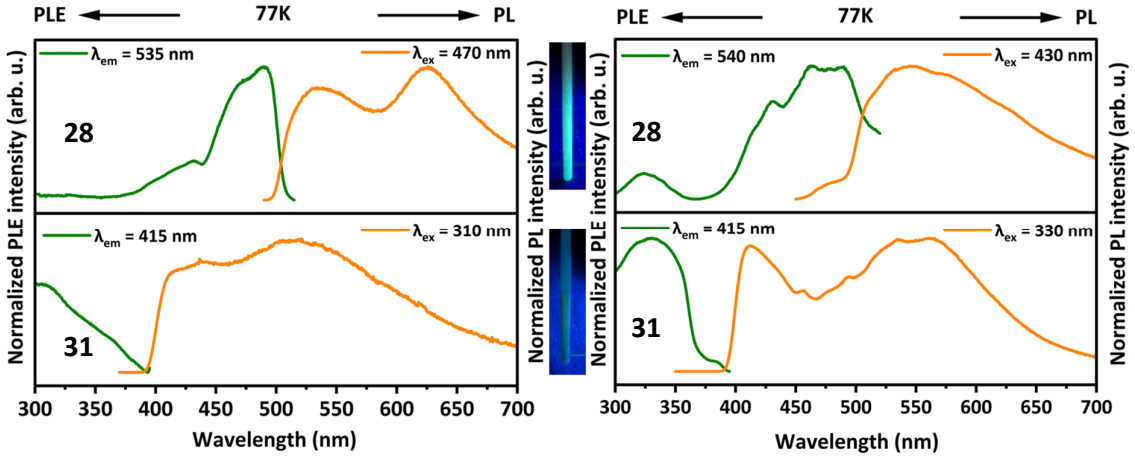

Figure 69: Normalized photoluminescence excitation (PLE) and emission (PL) spectra of solid (left) and DCM solutions (right) of the complexes **28** (top) and **31** (bottom) at 77 K. Photographs of complexes **28** (top) and **31** (bottom) in DCM solutions under UV illumination (λ = 365 nm) at 77 K. PLE and PL spectra were recorded at the depicted wavelengths (λ_{em} and λ_{ex}).

Additionally, a broad band is also seen around 550 nm. The lack of significant spectral shifts between solid and solution states suggests an excited state structure with minimal solvent dependent reorganization.[408-409]

The excited states of complex **28** decay with a lifetime of 8 µs and 11 µs at 77 K in the solid state and in DCM solution, respectively, indicating phosphorescence behavior. Whereas excited states of complex **31** decay with a lifetime of 6 µs at 77 K both in the solid state and in DCM solution.

The photophysical properties of the NHC complexes of Pt(II) (**29**) and Pd(II) (**30**) were investigated using PL and PLE spectroscopy in both the solid state and DCM solution at 295 K and 77 K. The results reveal temperature and environment-dependent emission behavior influenced by the nature of the metal center and the molecular packing.

The PL spectrum of the NHC-Pt(II) complex (**29**) in the solid-state exhibits broad and structured emission centered at 600 nm (295 K) when excited at λ_{ex} = 340 nm and red-shifted to 615 nm at 77 K after excitation at λ_{ex} = 345 nm (Figure 70, upper left). At 77 K, the emission intensity is significantly enhanced and the vibronic features become more pronounced, indicating suppression of non-radiative decay pathways. The PLE spectra (at λ_{em} = 600 nm and 615 nm) show strong excitation bands in the 320-400 nm range, which intensify at 77 K. The temperature-dependent changes in the PLE profiles reflect increased population of emissive triplet states due to thermal deactivation being minimized at low temperature.[410-411]

The NHC-Pd(II) complex (**30**) in the solid state exhibits PL emission centered at 435 nm (77 K) when excited at λ_{ex} = 365 nm and is red-shifted to about 515 nm (295 K) after excitation at λ_{ex} = 440 nm (Figure 70, lower left). The emission is noticeably weaker compared to the Pt(II) analogue, consistent with the lower spin-orbit coupling efficiency of Pd(II), which limits ISC to the triplet state. However, at 77 K, emission intensity increases markedly due to less quenching by thermally assisted relaxation. PLE spectra recorded at λ_{em} = 435 nm and 515 nm reveal broad excitation profiles with maxima in the range 350–400 nm.

In DCM solution, the Pt(II) complex (**29**) shows blue-shifted PL emission around 530 nm at 77 K and 420 nm at 295 K, relative to the solid state (Figure 70, upper right). The emission at 77 K is structured and significantly more intense, suggesting that solvent molecules help reduce non-radiative quenching and promote stabilization of triplet emissive states.[412-413] PLE

spectra observed at λ_{em} = 420 nm and 530 nm display broad and intense excitation bands in the range 320-400 nm. Notably, the excitation profile shifts slightly depending on the emission wavelength, implying multiple emissive states in solution.

The Pd(II) complex (**30**) in DCM exhibits weak PL emission at 425 nm at 295 K when excited at λ_{ex} = 360 nm, with considerable enhancement at 77 K (Figure 70, lower right). PLE spectra measured at λ_{em} = 425 nm reveal strong absorption in the 340-370 nm region, suggesting that ligand-centered π–π* transitions dominate the excitation process. The increased PLE intensity at 77 K is in line with enhanced radiative decay and reduced vibrational relaxation losses.[414]

The excited states of complex **29** decay with a lifetime of 20 µs and 82 µs at 295 K, and 120 µs and 591 µs at 77 K in the solid state, indicating phosphorescence behavior. While it has a lifetime of 6 µs at 295 K, and 7 µs and 126 µs at 77 K in the DCM solution. Whereas excited states of complex **30** decay with a lifetime of 6 µs at 295 K and 77 K both in the solid state and DCM solution.

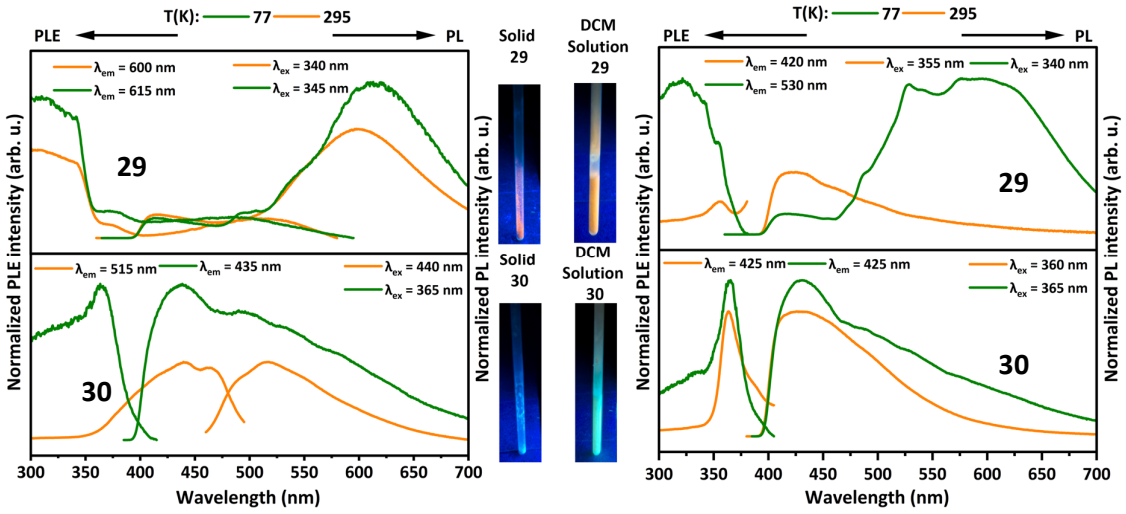

Figure 70: Normalized photoluminescence excitation (PLE) and emission (PL) spectra of solid (left) and DCM solutions (right) of the complexes **29** (top) and **30** (bottom) at 295 K and 77 K. Photographs of solid samples and DCM solutions (center) of the complexes under UV illumination (λ = 365 nm) at 77 K. PLE and PL spectra were recorded at the depicted wavelengths (λ_{em} and λ_{ex}).

3.5 Thioamidinate zinc and lanthanide complexes

3.5.1 Introduction

Thioamides are a versatile class of organic molecules, notable for their distinctive chemical, physical, and biological properties, which significantly differ from those of their oxygen-containing counterparts, the oxoamides.[415-416] This difference arises primarily from displacement of an oxygen by a sulfur atom, resulting in a thiocarbonyl group (C=S). One of the defining features of thioamides is the pronounced resonance stabilization within the thioamide functional group which stems from the donation of the nitrogen's nonbonding electron pair into the π-system of the C=S bond, effectively delocalizing electron density across the framework. The extent of this resonance is further elevated by the highly polarizable nature of the sulfur atom, which is significantly larger and more flexible in electron distribution compared to oxygen.[417] Unlike many other thiocarbonyl containing compounds, which are often known for being unstable, volatile, or foul-smelling, thioamides stand out due to a combination of favourable physical and chemical attributes. They exhibit high thermal and chemical stability, tend to crystallize readily, and are free from the unpleasant odours typically associated with sulfur containing organic substances.[418-422]

The sulfur, owing to its relatively large atomic size and high polarizability, is considered a soft donor, so thioamidinates are categorized as soft ligands. Thus, they are well suited for binding to soft metal centers, especially late transition metals.[171-172] Numerous studies have demonstrated the successful synthesis and characterization of metal complexes incorporating thioamidinate ligands, including complexes with Fe(II), Ru(II), Rh(I), Ir(I), Pd(II), Cu(II) and Hg(II), further emphasizing the broad compatibility and versatility of this ligand class.[206]

In the domain of zinc chemistry, notable advances have also been made involving soft donor ligands structurally analogous to thioamidinates. In 1991, O'Brien *et al.* reported the syntheses of Zn(II) complexes with diethylselenocarbamate ligands, which were subsequently used in chemical vapour deposition (CVD). In their approach, the *N*,*N*'-diethylselenocarbamate ligand was initially prepared as the diethylammonium salt *via* the reaction of carbon diselenide (CSe_2) with diethylamine and further reaction was performed with $ZnSO_4$ to obtain bis(diethylselenocarbamato) zinc(II) complexes (Figure 71a).[423-424] The same group, in 1996, reported similar bis(dialkyldithiocarbamates) of zinc(II) complexes with sulfur. They used $Zn(OH)_2$, a suitable amine and CS_2 as the precursors for these complexes (Figure 71b).[425] In

2019, Johnson and group have shown the synthesis of twelve Zn(II) thioureide complexes by the direct reaction of thiourea proligands with either [$ZnMe_2$] or [$Zn\{N(SiMe_3)_2\}_2$]. These newly formed complexes were explored for their application in the deposition of zinc sulfide thin films using CVD technique (Figure 71c).[426] Recently in 2024, the same group reported a series of Zn(II) thioamidinate complexes by the reaction of suitable thioamidinate ligand with either [$ZnMe_2$] or [$Zn\{N(SiMe_3)_2\}_2$] and used them in aerosol-assisted chemical vapour deposition (AACVD) (Figure 71d).[427]

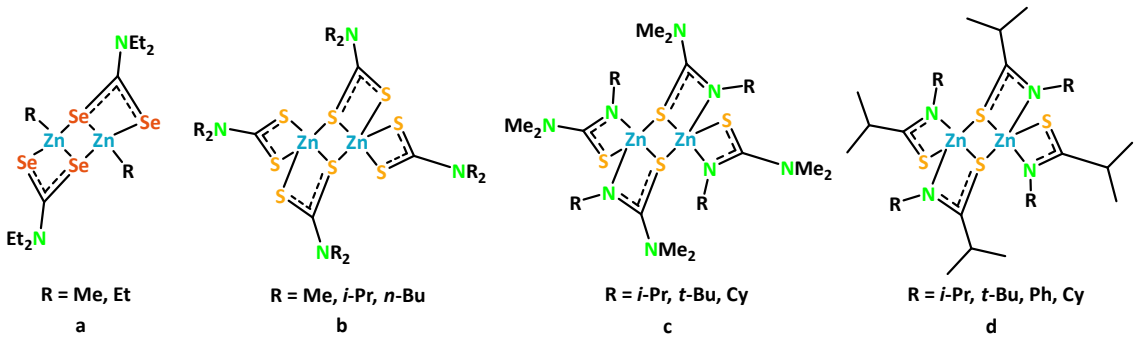

Figure 71: Examples of dimeric Zn(II) complexes with different S and Se containing ligands.

Here, the synthesis thioamidinate ligand with phenyl and *t*-Bu substituents on the carbon backbone and nitrogen, was targeted. Further, it was used for complexation of Zn(II) starting from various precursors. The obtained complexes were found to be luminescent and studied for their photophysical properties.

3.5.2 Syntheses and characterization of Zn(II) complexes

As a primary step towards the synthesis of the desired thioamidinate ligand, the reaction of *t*-butylisothiocyanate was performed with phenyl magnesium bromide to obtain the magnesium salt of the targeted thioamidinate ligand (Scheme 25). After the removal of THF *in vacuo* and addition of DCM, the reaction mixture was hydrolyzed with water. The protonated thioamidinate was extracted from the DCM layer by solvent extraction.

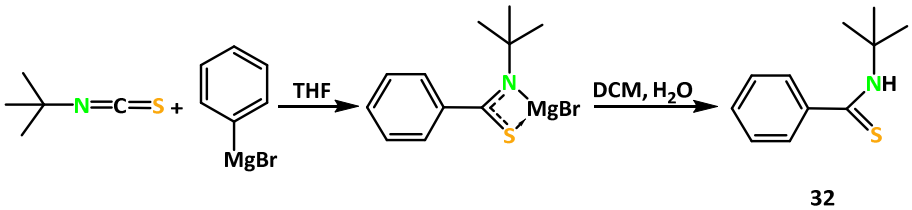

Scheme 25: Synthesis of thioamidinate ligand **32**.

Crystals suitable for SC-XRD measurements were obtained from a concentrated solution of **32** in THF. The compound crystallized in the monoclinic space group $P2_1/c$. The ligand has two coordination sites, the nitrogen and the sulfur centers. The thioamidinate ligand has a lower symmetry than the related amidinate ligands. Replacement of one of the nitrogen centres by sulfur results in the S-C1 bond length being elongated compared to the analogous bond in an amidinate species. In detail, the S-C1 bond (1.679(1) Å) is approximately 25 % longer than the N-C1 bond (1.328(2) Å). The S–C1–N bond angle was measured to be 126.5(1)°.

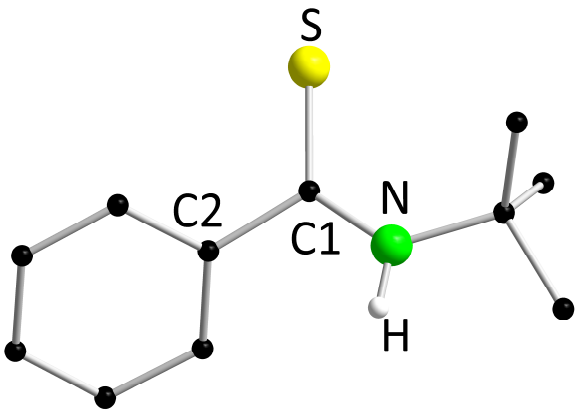

Figure 72: Molecular structure of **32** in the solid state. Hydrogen atoms (except N-H proton) and non-coordinating solvent molecules are omitted for clarity. Selected bond distances (Å) and angles (°): S–C1 1.679(1), N–C1 1.328(2), C1–C2 1.497(2); S–C1–N 126.5(1).

The ligand **32** was also characterized by NMR spectroscopy. A singlet at δ = 1.66 ppm was obtained for the *t*-Bu group on nitrogen. In the aromatic region of the spectrum, two multiplets at δ = 7.37 and 7.65 ppm were observed for the phenyl ring. In addition to other resonances in the $^{13}C\{^1H\}$ NMR, a characteristic resonance at δ = 198.9 ppm was observed for the thioamide carbon atom.

To investigate the complexation abilities of ligand **32**, it was treated with tetramethylethylenediamine-coordinated dimethylzinc ([$ZnMe_2$(TMEDA)]) in THF for 16 hours at ambient temperature (Scheme 26). After completion of the reaction, the solvent was removed under reduced pressure, and the reaction mixture was extracted with toluene. The desired complex **33** was isolated as an off-white solid. Crystals of complex **33** suitable for SC-XRD analysis were obtained from a concentrated THF solution.

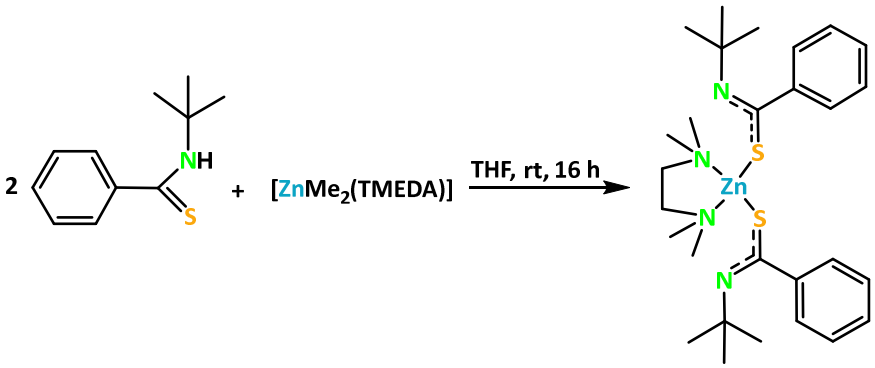

32 **33**

Scheme 26: Reaction of thioamidinate ligand **32** with [$ZnMe_2$(TMEDA)].

The structural analysis revealed that the Zn(II) center was selectively coordinated by two sulfur atoms from two thioamidinate units while the nitrogen atoms within the ligand framework did not coordinate to the Zn(II) center. Furthermore, it was observed that the TMEDA molecule, which was initially coordinated to the Zn(II) center, remained intact throughout the course of the reaction and was not displaced or removed by the ligand during the transformation.

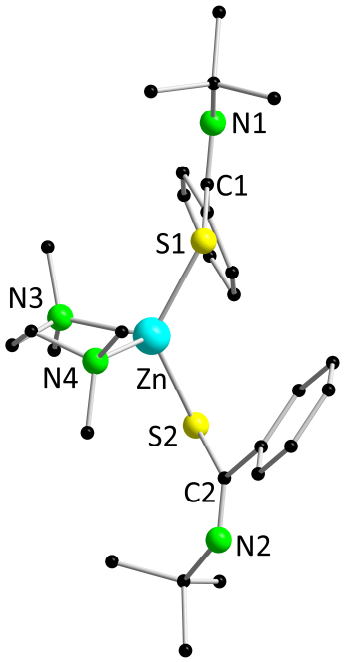

Figure 73: Molecular structure of **33** in the solid state. Hydrogen atoms and non-coordinating solvents are omitted for clarity. Selected bond distances (Å) and angles (°): Zn–S1 2.300(9), Zn–S2 2.291(8), Zn–N3 2.144(3), Zn–N4 2.139(2); S1–Zn–S2 127.6(3).

The Zn–S1 and Zn–S2 bond distances, for the Zn(II) and ligand interaction, were measured to be 2.300(9) Å and 2.291(8) Å, respectively. The Zn–N3 and Zn–N4 bond lengths corresponding to the Zn(II)-TMEDA coordination, were observed to be 2.144(3) Å and 2.139(2) Å, respectively. The S1–Zn–S2 bond angle formed by two ligand units on the metal center was found to be 127.6(3)°.

The complex **33** was also analyzed by NMR studies. In the ^{1}H NMR spectrum a singlet corresponding to the 18 protons of *t*-Bu groups was observed at δ = 1.21 ppm. Additionally, the resonances of the TMEDA protons were observed at δ = 1.55 and 2.39 ppm, integrating to twelve and four protons, respectively. In the aromatic region of the spectrum, resonances corresponding to the ten protons of the phenyl rings were observed. Furthermore, in the ^{13}C{^{1}H} NMR spectrum, a characteristic resonance at δ = 198.8 ppm was observed for the thioamide -*C*(=S)- carbon.

To further study the reactivity of ligand **32** towards different Zn(II) precursors, the reaction of two equivalents of **32** was performed with one equivalent of diphenyl zinc ([$ZnPh_2$]) in THF for 16 hours (Scheme 27). Similarly to the synthetic procedure towards complex **33**, THF was removed under reduced pressure, and the resulting solid extracted with toluene. Single crystals of complex **34** were obtained from a concentrated THF solution.

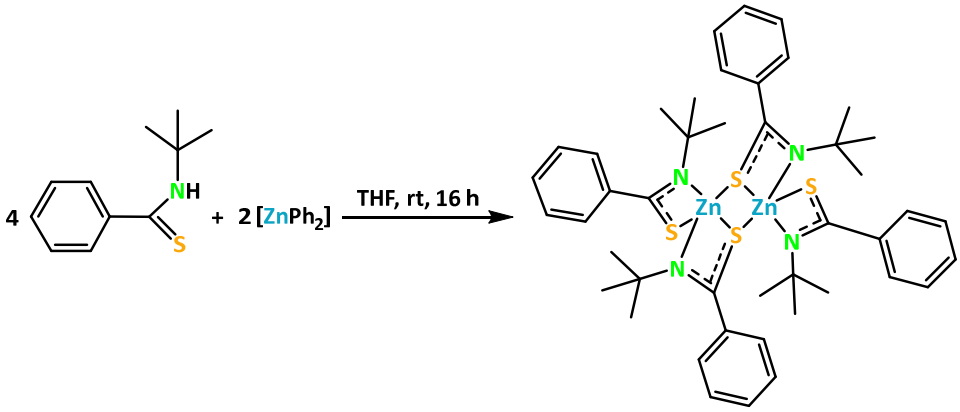

32 **34**

Scheme 27: Reaction of thioamidinate ligand **32** with [$ZnPh_2$].

From the structural analysis of complex **34**, it was evident that it contains two Zn(II) centers and four thioamidinate units (Figure 74). Given that the thioamidinate ligand is monoanionic, each Zn(II) center is coordinated by two thioamidinates. Additionally, one of the sulfur atoms

from each ligand acts in a bridging coordination mode, linking two Zn(II) centers, resulting in a dimeric structure (Figure 74, top). Consequently, each Zn(II) is coordinated by two nitrogen atoms and three sulfur atoms from the thioamidinate ligand, leading to a unique coordination environment. The central core of the complex, where Zn(II) units are present, adopts a structural arrangement resembling a chair-like conformation. Within this core, a Zn_2S_2 unit marks the fundamental framework of the complex (Figure 74, bottom).

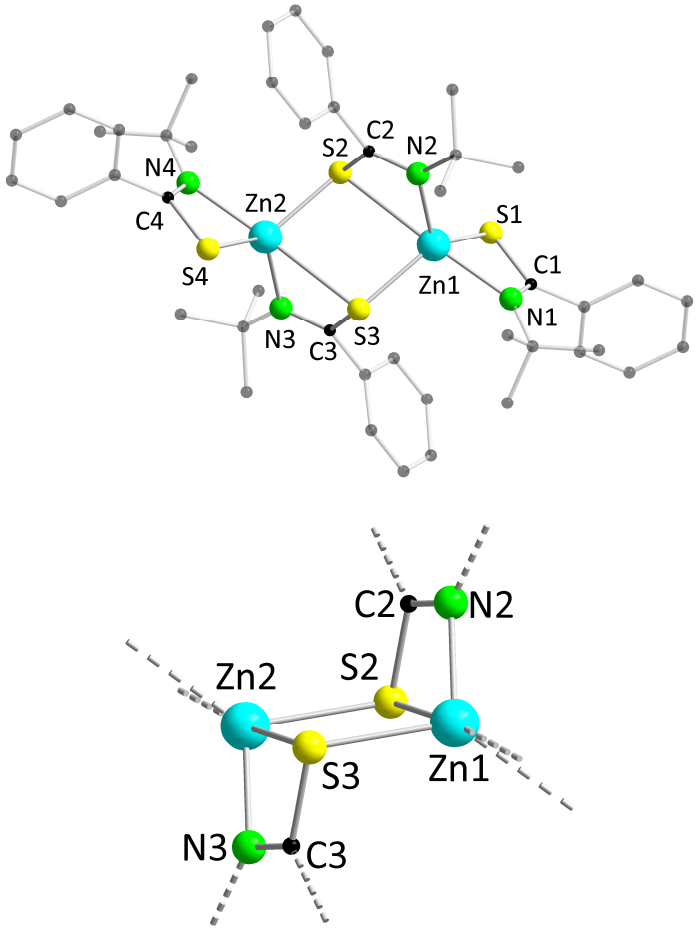

Figure 74: Molecular structure of **34** in the solid state (top) and the central part of the complex with a chair form (bottom). Hydrogen atoms and non-coordinating solvent molecules are omitted for clarity. Selected bond distances (Å) and angles (°): Zn1–S1 2.340(4), Zn1–S2 2.811(4), Zn1–S3 2.368(4), Zn1–N1 2.172(1), Zn1–N2 2.062(1); S1–Zn–S2 98.9(1), N1–Zn–N2 124.4(5).

The observed Zn1–N1 and Zn1–N2 bond lengths were 2.172(1) Å and 2.062(1) Å, respectively, close to the bond lengths of 2.156(2) Å and 2.027(1) Å reported for a similar Zn(II) thioamidinate complex.[427] A slight difference between these two bond lengths was observed, which can be attributed to the structural differences between the two thioamidinate ligands.

One of these ligands coordinates to a single Zn(II) center, while the other serves as a bridging unit, connecting both Zn(II) centers simultaneously. Similarly, the Zn(II) center interacts with three distinct sulfur atoms in different coordination modes. The first sulfur atom originates from a ligand that is solely attached to a single Zn(II) center, resulting in a Zn1–S1 bond length of 2.340(4) Å which is almost same (2.341(5) Å) as that reported for a similar complex.[427] The second sulfur atom belongs to a ligand that not only coordinates to the same Zn(II) center but also extends its coordination to the second Zn(II) ion, leading to a longer Zn1–S2 bond length of 2.811(4) Å and same trend was observed for a similar complex with a bond length of 2.892(1) Å.[427] The third sulfur atom is a part of another ligand that is primarily coordinated to the second Zn(II) center, forming a Zn1–S3 bond with a measured length of 2.368(4) Å which is close to the value of 2.349(5) Å observed for a similar complex.[427] Furthermore, the bond angle spanned by S1–Zn1–S2 , which is formed by the coordination of two ligand units, was measured to be 98.9(1)°. The four membered ring formed by the Zn_2S_2 unit is completely planar with a Zn1–S2–Zn2–S3 torsional angle of 0°.

In the ^{1}H NMR spectrum, a singlet at δ = 1.22 ppm was observed for the *t*-Bu groups and the resonances of the phenyl protons were obtained in the aromatic region in the range δ = 7.26 to 7.38 ppm. In addition to other carbon atoms, a characteristic resonance in the $^{13}C\{^1H\}$ NMR spectrum was observed at δ = 194.7 ppm for the thioamide carbon atom in the thioamidinate backbone.

Furthermore, the reaction of ligand **32** was performed with the previously reported Zn(II) complex aminotroponiminato bis(trimethylsilyl)amidozinc [{ATI(*i*-Pr)$_2$}ZnN(TMS)$_2$],[428] in 1:1 ratio in THF, resulting in the heteroleptic complex **35** as the product (Scheme 28).

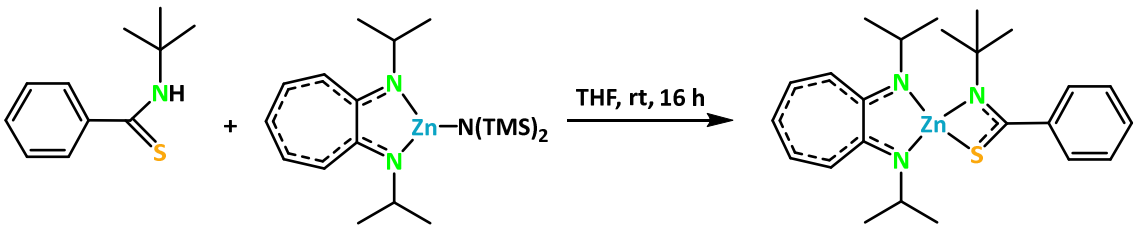

32 **35**

Scheme 28: Reaction of thioamidinate ligand **32** with [{ATI(*i*-Pr)$_2$}ZnN(TMS)$_2$].

Crystals suitable for SC-XRD analysis were obtained from the concentrated solution of **35** in toluene. From the structural analysis, it was evident that the Zn(II) center is coordinated by two nitrogen atoms of the ATI ligand and one nitrogen and one sulfur of the thioamidinate ligand (Figure 75). The Zn–N1, Zn–N2 and Zn–N3 bond lengths were observed to be 2.047(2) Å, 1.964(2) Å and 1.973(2) Å, respectively, indicating that the distance is shorter for the ATI-Zn interaction compared to the thioamidinate-Zn interaction. Additionally, the Zn–S bond length was measured to be 2.392(7) Å, which is in close agreement with the respective distances within complexes **33** and **34**.

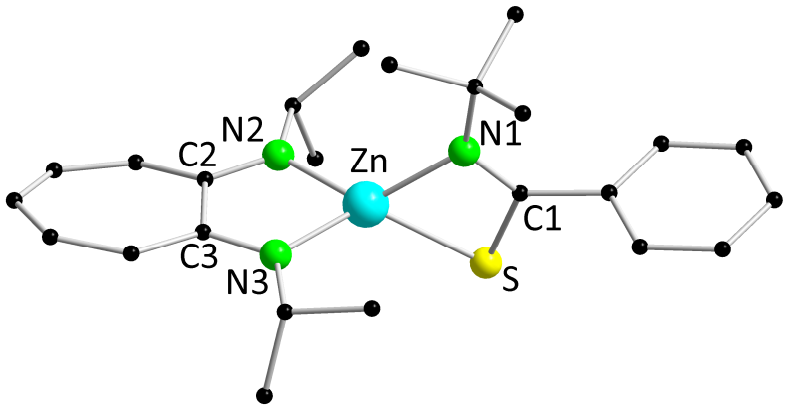

Figure 75: Molecular structure of **35** in the solid state. Hydrogen atoms and non-coordinating solvent molecules are omitted for clarity. Selected bond distances (Å) and angles (°): Zn–S 2.392(7), Zn–N1 2.047(2), Zn–N2 1.964(2), Zn–N3 1.973(2); S–Zn–N1 70.7(6), N2–Zn–N3 83.1(8), S–Zn–N3 129.6(6).

The complex **35** was additionally characterized by NMR spectroscopy. In the ^{1}H NMR spectrum, a singlet at δ = 1.11 ppm was obtained for the *t*-Bu groups on the thioamidinate nitrogen. Moreover, resonances at δ = 1.49 and 4.11 ppm, corresponding to twelve and two protons, respectively, were observed for the *i*-Pr substituents on ATI. Other resonances in the aromatic region of the spectrum were also in agreement with the structure observed. In the ^{13}C{^{1}H} NMR spectrum, a characteristic resonance at δ = 194.3 ppm was observed for the thioamide carbon atom.

3.5.3 Syntheses and characterization of Sm(III) and Y(III) complexes

Furthermore, to explore the applicability of the thioamidinate ligand in lanthanides, the reaction of ligand **32** was performed with samarium tris{bis(trimethylsilyl)amide} [(Sm(BTSA)$_3$)] in 3:1 molar ratio in THF solvent for 16 hours (Scheme 29). The product **36** was

filtered in toluene and the crystals suitable for SC-XRD analysis were obtained from the concentrated toluene solution.

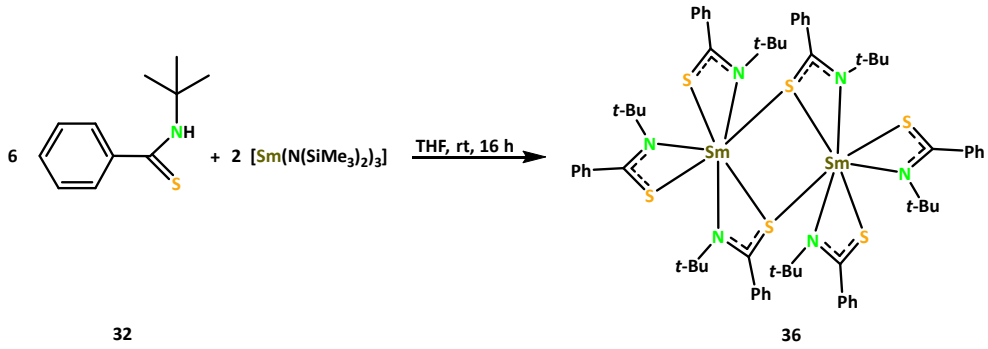

Scheme 29: Synthesis of the Sm(III) complex **36**.

From the structural analysis of complex **36**, it was evident that it exists in the form of a dimer with two Sm(III) centers and six ligand units in the structure (Figure 76). Each Sm(III) is coordinated by three thioamidinate ligands and one additional coordination is observed from one sulfur atom from another Sm(III) center, which is in the bridging coordination mode. The Sm–N bond lengths are found to be in the range 2.515–2.536 Å and Sm–S bond distances are averaged to ~2.785 Å, except for the bridging sulfur atom. The bond lengths for the bridging sulphur centers are found to be Sm2–S3 2.854(1) Å and Sm2–S6 3.003(1) Å, which are longer due to coordination to two Sm(III) centers.

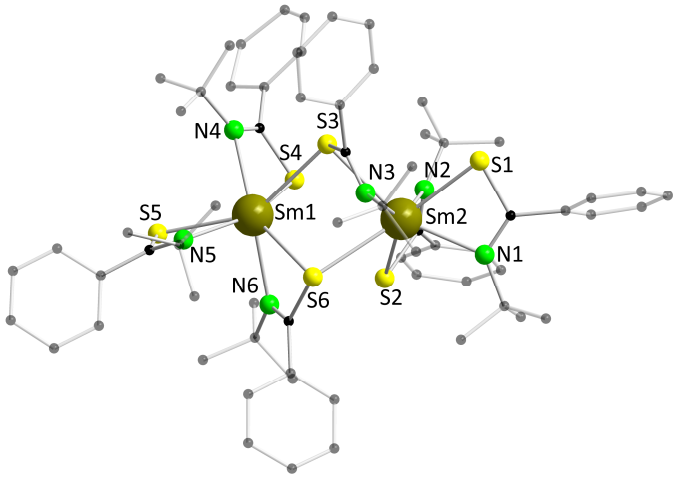

Figure 76: Molecular structure of **36** in the solid state. Hydrogen atoms and non-coordinating solvent molecules are omitted for clarity. Selected bond distances (Å) and angles (°): Sm2–S1 2.795(2), Sm2–S2 2.778(2), Sm2–S3 2.854(1), Sm2–S6 3.003(13), Sm2–N1 2.536(5), Sm2–N2 2.515(5), Sm2–N3 2.527(4); S6–Sm1–S3 77.7(4).

Complex **36** was also characterized by ^{1}H NMR and a resonance at δ = 1.66 ppm was observed for *t*-Bu groups of the ligand. Additionally, in $^{13}C\{^{1}H\}$ NMR spectrum, a characteristic resonance at δ = 199.0 ppm was obtained for the thioamide carbon atom in the ligand backbone.

Inspired from the complex **36**, a similar reaction using [Y(BTSA)$_3$] and ligand **32** in 1:3 ratio was performed in THF for 16 hours (Scheme 30). The reaction mixture was filtered in toluene and the crystals were obtained from a concentrated toluene solution.

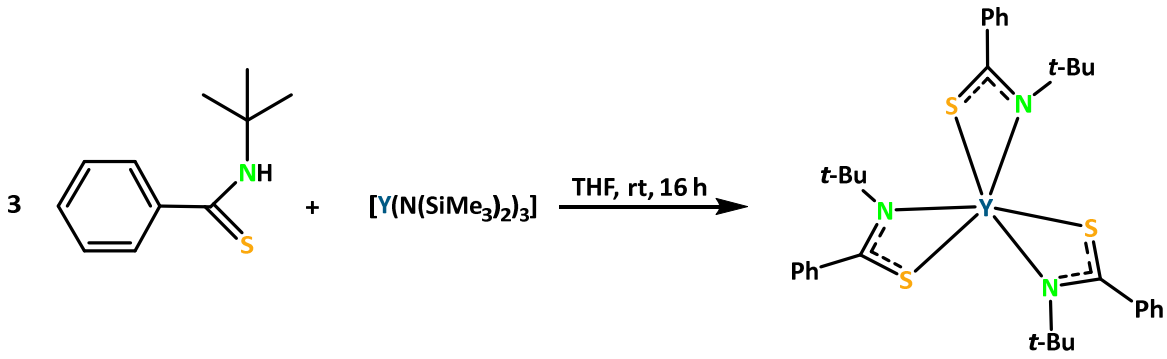

32 **37**

Scheme 30: Synthesis of Y(III) complex **37**.

The structural analysis of complex **37** revealed that it exists as a monomer with one Y(III) center coordinated with three units of thioamidinate ligand and Y(III) has a distorted octahedral geometry. (Figure 77) The Y–S1 and Y–N1 bond distances were observed to be 2.724(10) Å and 2.371(3) Å, respectively, which are in a close agreement with the reported values.[429-430]

Additionally, complex **37** was characterized by NMR spectroscopy. A singlet resonance in ^{1}H NMR spectrum was obtained at δ = 1.33 ppm for *t*-Bu group of the ligand. Moreover, a characteristic resonance at δ = 195.3 ppm was observed in $^{13}C\{^{1}H\}$ NMR spectrum for the thioamide carbon atom in the ligand backbone.

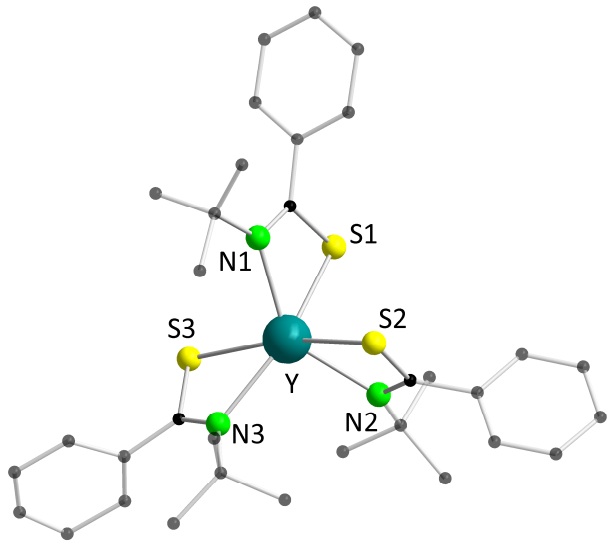

Figure 77: Molecular structure of **37** in the solid state. Hydrogen atoms and non-coordinating solvent molecules are omitted for clarity. Selected bond distances (Å) and angles (°): Y–S1 2.719(10), Y–S2 2.704(1), Y–S3 2.724(1), Y–N1 2.349(3), Y–N2 2.439(3), Y–N3 2.372(3); N1–Y–S1 61.8(8), N2–Y–S2 61.3(8), N3–Y–S3 61.9(8).

3.5.4 Photophysical studies

Complexes **33** and **34** were found to be luminescent in both the solid state and in DCM solution at 77 K with a bluish-green emission. Studies on the photophysical properties of thioamidinate Zn(II) complexes have not been reported in the literature to date.

Photoluminescence spectra were recorded at 77 K to probe the emissive properties of these complexes in both solid state and in DCM solution. For complex **33** in the solid state (Figure 78, upper left), the PLE spectrum shows two maxima at 375 nm and 455 nm (λ_{em} = 525 nm), respectively, indicating the optimal wavelengths for exciting the emissive state, while the PL spectrum shows a broad emission maximum at 525 nm (λ_{ex} = 375 nm). In DCM solution of complex **33** (Figure 78, upper right), the PLE spectrum shifts slightly to 370 nm (λ_{ex} = 500 nm), and the PL spectrum shows emission at 500 nm (λ_{em} = 370 nm). The slight blue-shift in both excitation and emission in solution may result from solvent interactions reducing intermolecular packing effects, leading to a higher energy emissive state.[431-432]

For the dimeric Zn(II) complex (**34**) in the solid state (Figure 78, lower left), the PLE spectrum shows a maximum at 375 nm (λ_{em} = 525 nm), with the corresponding PL spectrum showing emission maximum at 525 nm. The similarity in excitation and emission wavelengths to

complex **33** suggests that the thioamidinate ligand dominates the photophysical behavior, with the Zn–S–Zn bridging in the dimer contributing to a stable emissive state in the solid phase. In DCM solution of complex **34** (Figure 78, lower right), the PLE spectrum shifts to 360 nm, and the PL spectrum shows an emission maximum at 510 nm. The more pronounced blue-shift in both PLE and PL spectra in solution indicates that the dimeric structure may partially dissociate, or experience reduced intermolecular interactions in DCM, altering the electronic environment and resulting in a higher-energy excited state.[433-434]

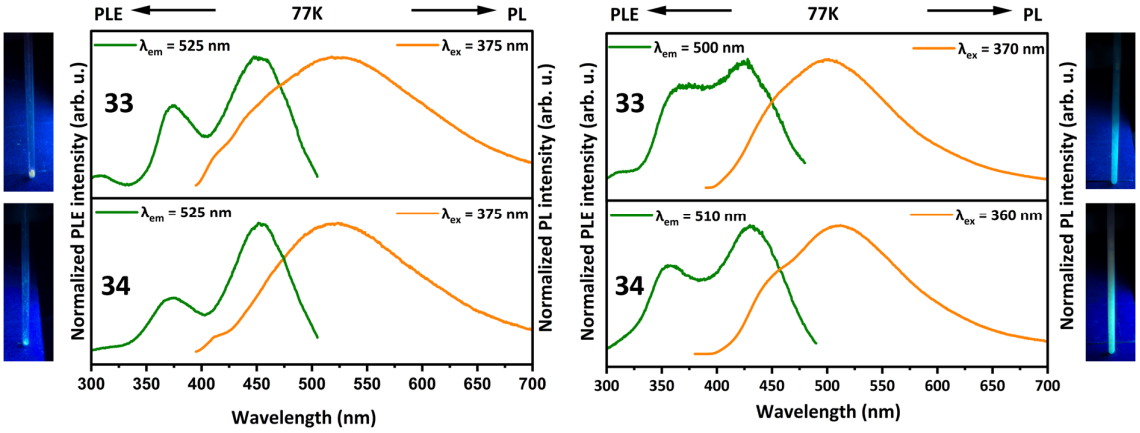

Figure 78: Normalized photoluminescence excitation (PLE) and emission (PL) spectra of solid samples (left) and DCM solutions (right) of the complexes **33** and **34** at 77 K. Photographs of solid samples (left) and DCM solutions (right) of the complexes under UV illumination (λ = 365 nm) at 77 K. PLE and PL spectra were recorded at the depicted wavelengths (λ_{em} and λ_{ex}).

The excited states of complex **33** and **34** decay with a lifetime of 6 µs at 77 K both in the solid state and DCM solution, indicating phosphorescence behavior.

The PL and PLE properties of complex **35** were investigated in both the solid state and DCM solution at 77 K and 295 K. In the solid state (Figure 79, left), the PLE spectrum at 77 K peaks at 440 nm (λ_{em} = 510 nm), with the corresponding PL spectrum showing an emission at 510 nm (λ_{ex} = 440 nm). At 295 K, the PLE spectrum shifts to 410 nm (λ_{em} = 510 nm), and the PL spectrum remains almost the same with a maximum at 510 nm (λ_{ex} = 440 nm). Moreover, the intensity of the spectrum decreases when increasing the temperature to 295 K which might be attributed to the non-radiative decays at higher temperature. [435]

In DCM solution (Figure 79, right), the PLE spectrum at 77 K shows a maximum at 365 nm (λ_{em} = 495 nm), with the PL spectrum showing emission at 495 nm (λ_{ex} = 365 nm). At 295 K,

the PLE maxima shifts to 400 nm (λ_{em} = 510 nm), and the PL spectrum maximum blue-shifted to 495 nm (λ_{ex} = 365 nm), though the emission intensity is slightly reduced. The blue-shift in solution compared to the solid state, along with the temperature effects, suggests that solvent coordination and molecular dynamics influence the electronic structure, potentially disrupting the ligand centered transitions.[436-437]

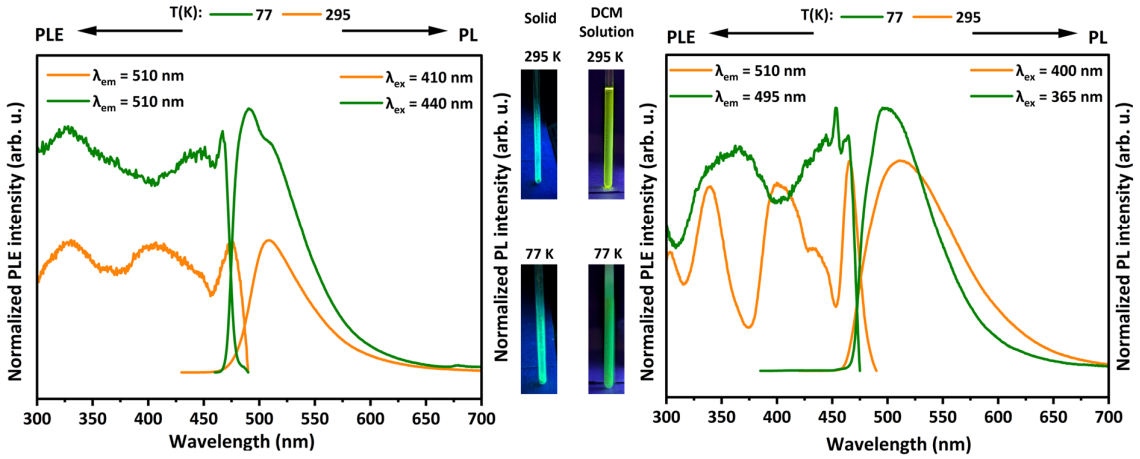

Figure 79: Normalized photoluminescence excitation (PLE) and emission (PL) spectra of complex **35** in solid state (left) and in DCM solution (right) at 295 K and 77 K. Photographs of solid and DCM solution (center) of the complex **35** under UV illumination (λ = 365 nm) at 295 K and at 77 K. PLE and PL spectra were recorded at the depicted wavelengths (λ_{em} and λ_{ex}).

The excited states of complex **35** decay with a lifetime of 6 µs at 295 K and 8 µs at 77 K in the solid state, indicating phosphorescence behavior. While it has a lifetime of 8 µs at 295 K and 6 µs at 77 K in the DCM solution.

4. Experimental section

4.1 General methods

All air- and moisture-sensitive manipulations were performed under dry N_2 or Ar atmosphere using standard Schlenk techniques or in an argon-filled *MBraun* glovebox, unless otherwise stated. Et_2O, *n*-pentane and toluene were dried using an *MBraun* solvent purification system (SPS-800) and degassed. THF was distilled under nitrogen from potassium benzophenone ketyl before storage over $LiAlH_4$. DCM and acetonitrile were dried by refluxing over P_2O_5 and CaH_2, respectively, and distilled under nitrogen atmosphere. Acetone was refluxed over $MgSO_4$ and distilled under nitrogen atmosphere. THF-d_8 was dried over Na-K alloy and degassed by freeze-pump-thaw cycles. $CDCl_3$ and CD_2Cl_2 were dried over P_2O_5, distilled and stored over 4 Å molecular sieves.

Elemental analyses were carried out with an *Elementar* vario MICRO cube.

NMR spectra were recorded on *Bruker* spectrometers (*Avance Neo* 300 MHz, *Avance* 400 MHz or *Avance Neo* 400 MHz). Chemical shifts are referenced internally using signals of the residual protio solvent (^1H) or the solvent ($^{13}C\{^1H\}$) and are reported relative to tetramethylsilane (^1H, $^{13}C\{^1H\}$), or externally relative to H_3PO_4 ($^{31}P\{^1H\}$).

All NMR spectra were measured at 298 K, unless otherwise specified. The multiplicity of the signals is indicated as s = singlet, d = doublet, dd = doublet of doublets, t = triplet, q = quartet, m = multiplet and br = broad. Assignments were determined on the basis of unambiguous chemical shifts, coupling patterns and ^{13}C-DEPT experiments or 2D correlations (^1H-^1H COSY, ^1H-^{13}C HMQC and ^1H-^{13}C HMBC).

Infrared (IR) spectra were recorded in the region 4000–400 cm^{-1} on a *Bruker Tensor* 37 FTIR spectrometer equipped with an ambient temperature DLaTGS detector, a diamond attenuated total reflection (ATR) unit and a nitrogen-flushed chamber. In terms of their relative intensity, the signals were classified into different categories (vs = very strong, s = strong, m = medium, w = weak, and sh = shoulder).

UV-Vis spectra were recorded on a *Varian Cary* 50 spectrophotometer.

ESI mass spectra were recorded on an *LTQ Orbitrap XL* Q Exactive mass spectrometer (Thermo Fisher Scientific, San Jose, CA, USA) equipped with a HESI II probe.

4.2 Syntheses and analytical data

4.2.1 [{$Ph_2PC{\equiv}CC(NDipp)_2$}Li(thf)$_3$] (1):

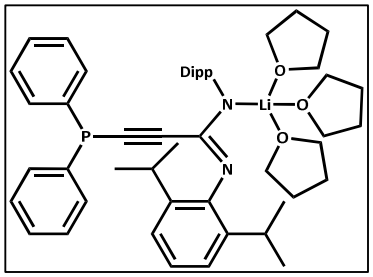

$Ph_2PC{\equiv}CH$ (1.00 g, 4.76 mmol, 1.00 eq.) was dissolved in 30 mL of THF in a Schlenk flask and cooled to -78 °C under N_2 atmosphere. 3.27 mL of a 1.6 M *n*-butyllithium (*n*-BuLi) solution in *n*-hexane (335 mg, 5.23 mmol, 1.10 eq.) was added to it dropwise. The reaction mixture was stirred for 15 minutes at -78 °C and for 20 minutes at ambient temperature. The reaction mixture was cooled again to -78 °C and bis(2,6-diisopropylphenyl)carbodiimide (1.72 g, 4.76 mmol, 1.00 eq.) solution in 15 mL THF, was added dropwise. The reaction mixture was stirred for 30 minutes at -78 °C and for an additional hour after warming up to ambient temperature. The solution was then concentrated to 10 mL and stored overnight at -30 °C to obtain colorless crystals of the desired product. The mother liquor was decanted off and subsequently dried under vacuum. Yield: 2.30 g (64 %).

Anal. calcd for $C_{47}H_{60}LiN_2O_2P$ (722.92 g/mol): C, 77.05; H, 8.62; N, 3.52 %. Found: C, 76.66; H, 7.94; N, 3.78 %.

^{1}H NMR (400 MHz, 298 K, C_6D_6): δ(ppm) 7.27 (d, J = 6.7 Hz, 4H, CH^{Ph}), 7.21 (dd, J = 8.7, 6.1 Hz, 2H, CH^{Ph}), 7.08–6.98 (m, 10H, CH^{Ph}), 3.78 (hept, J = 7.0 Hz, 4H, CH(CH_3)$_2$), 3.61–3.50 (m, 12H, OCH_2), 1.45–1.34 (m, 24H, CH_3), 1.29 (d, J = 7.0 Hz, 12H, CH_2).

^{31}P{^{1}H} NMR (162 MHz, 298 K, C_6D_6): δ(ppm) -33.6 (s).

^{13}C{^{1}H} NMR (100 MHz, 298 K, C_6D_6): δ(ppm) 155.2 (CCN$_2$), 148.6 (1-Ar-C^{Dipp}), 143.7 (2,6-Ar-C^{Dipp}), 135.2 (d, $^1J_{CP}$ = 36.7 Hz, 1-Ar-C^{Ph}), 132.7 (d, $^2J_{CP}$ = 19.8 Hz, 2,6-Ar-CH^{Ph}), 128.7 (d, $^3J_{CP}$ = 15.4 Hz, 3,5-Ar-CH^{Ph}), 128.5 (4-Ar-CH^{Ph}), 123.3 (3,5-Ar-CH^{Dipp}), 123.1 (4-Ar-CH^{Dipp}), 68.2 (OCH$_2$), 28.5 (CH), 25.5 (OCH$_2$), 25.8 (CH$_3$), 24.3 (CH$_3$).

IR (ATR): $\tilde{\nu}$(cm^{-1}) 3054 (w), 3016 (w), 2958 (s), 2928 (m), 2883 (m), 2865 (m), 2362 (w), 2338 (w), 2165 (w), 1614 (m), 1585 (w), 1486 (vs), 1434 (s), 1394 (w), 1378 (w), 1315 (m), 1242 (m), 1205 (w), 1186 (w), 1158 (w), 1096 (w), 1044 (s), 999 (w), 963 (w), 935 (w), 915 (w), 887 (w), 831 (w), 797 (w), 772 (w), 749 (w), 739 (s), 692 (s), 572 (w), 507 (w), 471 (w), 438 (w), 425 (w).

4.2.2 [{$Ph_2PC{\equiv}CC(NDipp)_2\}_2Cu_2$] (2):

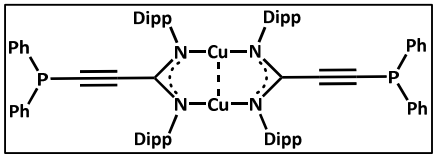

Compound **1** (100 mg, 125.8 µmol, 1.00 eq.) and copper(I) chloride (12.5 mg, 125.8 µmol, 1.00 eq.) were dissolved in 15 mL of THF and stirred at ambient temperature overnight. The solvent was removed under reduced pressure and was filtered in DCM through a 0.22 µm PTFE membrane filter. Removal of the volatiles under vacuum afforded a bright yellow solid. Yield: 90 mg (56 %).

HRMS (ESI): *m/z* Calcd for $C_{78}H_{88}Cu_2N_4P_2$: 1268.5071 [M]; found: 1268.5018.

Anal. calcd for $C_{78}H_{88}Cu_2N_4P_2$ (1270.63 g/mol): C, 73.73; H, 6.98; N, 4.41 %. Found: C, 73.60; H, 7.04; N, 4.50 %.

^{1}H NMR (400 MHz, 298 K, $CDCl_3$): δ(ppm) 7.21–7.17 (m, 4H, C*H*^{Ph}), 7.10–7.04 (m, 10H, C*H*^{Ph}), 6.99–6.98 (m, 10H, C*H*^{Ph}), 6.73–6.68 (m, 8H, C*H*^{Ph}), 3.47 (hept, *J* = 7.0 Hz, 8H, C*H*$(CH_3)_2$), 1.14 (d, *J* = 6.8 Hz, 24H, CH_3), 1.06 (d, *J* = 7.0 Hz, 24H, CH_3).

^{31}P{^{1}H} NMR (162 MHz, 298 K, $CDCl_3$): δ(ppm) 19.9 (s).

^{13}C{^{1}H} NMR (100 MHz, 298 K, C_6D_6): δ(ppm) 159.0 (C*C*N_2), 143.8 (1-Ar-*C*^{Dipp}), 142.3 (2,6-Ar-*C*^{Dipp}), 132.6 (d, $^1J_{CP}$ = 20.17 Hz, 1-Ar-*C*^{Ph}), 131.2 (d, $^2J_{CP}$ = 12.5 Hz, 2,6-Ar-*C*H^{Ph}), 128.8 (d, $^3J_{CP}$ = 7.7 Hz, 3,5-Ar-*C*H^{Ph}), 126.2 (4-Ar-*C*H^{Ph}), 125.8 (3,5-Ar-*C*H^{Dipp}), 123.6 (4-Ar-*C*H^{Dipp}), 100.2 (d, $^1J_{CP}$ = 98.7 Hz, C≡*C*P), 92.1 (*C*≡CP), 28.9 (*C*H), 24.1 (*C*H_3), 23.6 (*C*H_3).

IR (ATR): $\tilde{\nu}$(cm^{-1}) 3057 (w), 2956 (vs), 2923 (sh), 2864 (w), 2326 (w), 2362 (w), 1586 (w), 1502 (vs), 1462 (sh), 1436 (m), 1392 (w), 1359, 1321 (m), 1255 (w), 1214 (w), 1182 (w), 1099 (w), 1057 (w), 1042 (w), 974 (w), 933 (w), 798 (w), 783 (w), 744 (m), 690 (m), 625 (w), 509 (w), 487 (w), 463 (w), 426 (w).

4.2.3 [{$Ph_2PC{\equiv}CC(NDipp)_2\}_2Au_2$] (3):

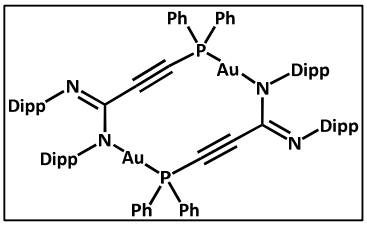

Pathway I: Compound **1** (100 mg, 125.8 µmol, 1.00 eq.) and chloro(tetrahydrothiophene)gold(I) ([Au(tht)Cl]) (40.3 mg, 125.8 µmol, 1.00 eq.) were dissolved in 15 mL of THF and stirred at ambient temperature overnight. Then solvent was evaporated under reduced pressure and the solid was dissolved in 10 mL of DCM and was filtered through a 0.22 µm PTFE membrane filter. The volatiles were evaporated to obtain a light yellow colored solid. Single crystals suitable for X-ray structure determination were obtained from a concentrated solution in THF. Yield: 119 mg (77 %).

Pathway II: [{$HC{\equiv}CC(NDipp)_2\}_2Au_2$] (**4**) (100 mg, 85.5 µmol, 1.00 eq.) was dissolved in 15 mL of THF and cooled to -78 °C under N_2 atmosphere. 112 µL of a 1.6 M *n*-butyllithium solution in *n*-hexane (11.5 mg, 180 µmol, 2.10 eq.) were added to it dropwise. The reaction mixture was stirred for 30 minutes at -78 °C and for 30 minutes at ambient temperature. Then, it was again cooled to -78 °C and 31.6 µL of chlorodiphenylphosphine (37.7 mg, 171 µmol, 2.00eq.) was added to it slowly. The reaction mixture was stirred for 30 minutes at -78 °C and overnight after warming up to ambient temperature. The solvent was evaporated using vacuum and the solid was extracted using 20 mL of DCM. The extracted solution was filtered through a 0.22 µm PTFE membrane filter. and dried completely under vacuum. Yield: 87 mg (67 %).

HRMS (ESI): *m/z* calcd for $C_{78}H_{89}Au_2N_4P_2$: 1537.5888 $[M+H]^+$; found: 1537.5804.

Anal. calcd for $C_{78}H_{88}Au_2N_4P_2$ (1537.47 g/mol): C, 60.94; H, 5.77; N, 3.64 %. Found: C, 61.26; H, 5.18; N, 3.17 %.

^{1}H NMR (400 MHz, 298 K, $CDCl_3$): δ(ppm) 7.55–7.51 (m, 4H, CH^{Ph}), 7.4 2–7.36 (m, 8H, CH^{Ph}), 7.33–7.28 (m, 8H, CH^{Ph}), 7.26–7.25 (m, 6H, CH^{Ph}), 7.12–7.09 (m, 6H, CH^{Ph}), 3.71 (hept, *J* = 6.7 Hz, 4H, C$H(CH_3)_2$), 3.21 (hept, *J* = 6.7 Hz, 4H, C$H(CH_3)_2$), 1.42 (d, *J* = 7.0 Hz, 12H, CH_3), 1.40 (d, *J* = 6.8 Hz, 12H, CH_3), 1.11 (d, *J* = 6.8 Hz, 12H, CH_3), 1.01 (d, *J* = 6.8 Hz, 12H, CH_3).

^{31}P{^{1}H} NMR (162 MHz, 298 K, $CDCl_3$): δ(ppm) 2.1 (s).

^{13}C{^{1}H} NMR (100 MHz, 298 K, $CDCl_3$): δ(ppm) 148.9 (1-Ar-C^{Dipp}), 147.5 (1-Ar-C^{Dipp}), 144.3 (2,6-Ar-C^{Dipp}), 142.3 (2,6-Ar-C^{Dipp}), 140.4 (Ar-C^{Ph}), 133.8 (d, $^1J_{CP}$ = 15.8 Hz, 1-Ar-C^{Ph}), 132.0 (d, $^3J_{CP}$ = 2.9 Hz, 3,5-Ar-CH^{Ph}), 129.2 (d, $^2J_{CP}$ = 13.2 Hz, 2,6-Ar-CH^{Ph}), 128.2 (4-Ar-CH^{Ph}), 127.5 (CCN_2),

125.9 (3,5-Ar-*C*H^{Dipp}), 123.5 (3,5-Ar-*C*H^{Dipp}), 122.7 (4-Ar-*C*H^{Dipp}), 122.1 (4-Ar-*C*H^{Dipp}), 105.0 (d, $^{1}J_{CP}$ = 15.8 Hz, C≡*C*P), 90.3 (*C*≡CP), 27.9 (*C*H), 27.8 (*C*H), 26.7 (*C*H$_3$), 24.4 (*C*H$_3$), 23.9 (*C*H$_3$), 22.9 (*C*H$_3$).

IR (ATR): $\tilde{\nu}$(cm^{-1}) 3056 (w), 2958 (vs), 2925 (sh), 2865 (m), 2167 (w), 1616 (w), 1588, 1548 (vs), 1512 (w), 1460 (w), 1436 (s), 1378 (w), 1358 (m), 1315 (m), 1243 (w), 1180 (w), 1102 (m), 1057 (w), 1000 (w), 934 (w), 830 (w), 803 (w), 776 (w), 749 (w), 725 (m), 688 (w), 658 (m), 620 (w), 567 (w), 535 (w), 492 (w), 420 (w).

4.2.4 [{(AuCl)Ph$_2$PC≡CC(NDipp)$_2$}$_2$Cu$_2$] (5):

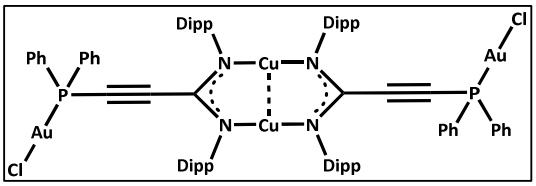

Pathway I: Compound **2** (50 mg, 39.4 µmol, 1.00 eq.) and [Au(tht)Cl] (25.2 mg, 78.8 µmol, 2.00 eq.) were taken in a Schlenk flask and dissolved in 15 mL of THF. The reaction mixture was stirred overnight at ambient temperature and the solvent subsequently evaporated under reduced pressure. The resulting solid was filtered in DCM through a 0.22 µm PTFE membrane filter. The solvent was evaporated by vacuum and a bright yellow colored solid was obtained. The solid was then washed with *n*-pentane. Single crystals suitable for X-ray structure determination were obtained from a concentrated THF solution. Yield: 41 mg (60 %).

Pathway II: Compound **3** (50 mg, 32.5 µmol, 1.00 eq.) and copper(I) chloride (6.4 mg, 65 µmol, 2.00 eq.) were taken in a Schlenk flask and dissolved in 15 mL of THF. The reaction mixture was stirred overnight at ambient temperature and was dried under vacuum afterwards. The obtained solid was dissolved in DCM and filtered through a 0.22 µm PTFE membrane filter. The solvent was evaporated under reduced pressure and a bright yellow colored solid was obtained. The solid was then washed with *n*-pentane. Single crystals suitable for X-ray structure determination were obtained from a concentrated THF solution. Yield: 35 mg (62 %).

Pathway III: Compound **1** (100 mg, 125.8 µmol, 1.00 eq.), [Au(tht)Cl] (40.3 mg, 125.8 µmol, 1.00 eq.), and copper(I) chloride (12.5 mg, 125.8 µmol, 1.00 eq.) were taken in a Schlenk flask and dissolved in 15 mL of THF. The reaction mixture was stirred overnight at ambient temperature and evaporated under reduced pressure. The solid was redissolved in DCM and filtered through a 0.22 µm PTFE membrane filter. The solvent was evaporated under reduced pressure and a bright yellow colored solid was obtained. The solid was then washed with

n-pentane. Single crystals suitable for X-ray structure determination were obtained from a concentrated THF solution. Yield: 157 mg (65 %).

HRMS (ESI): *m/z* calcd for $C_{78}H_{88}Au_2Cl_2Cu_2N_4P_2$: 1732.3779 [M]; found: 1732.3630.

Anal. calcd for $C_{78}H_{88}Au_2Cl_2Cu_2N_4P_2$ (1735.46 g/mol): C, 53.98; H, 5.11; N, 3.23 %. Found: C, 53.03; H, 5.12; N, 2.97 %.

^{1}H NMR (400 MHz, 298 K, $CDCl_3$): δ(ppm) 7.51–7.46 (m, 4H, C*H*^{Ph}), 7.35–7.28 (m, 12H, C*H*^{Ph}), 7.16 (d, *J* = 7.7 Hz, 8H, C*H*^{Ph}), 6.99 (ddd, *J* = 15.2, 8.3, 1.3 Hz, 8H, C*H*^{Ph}), 3.48 (hept, *J* = 6.8 Hz, 8H, C*H*$(CH_3)_2$), 1.25 (d, *J* = 6.8 Hz, 24H, C*H*$_3$), 1.13 (d, *J* = 6.8 Hz, 24H, C*H*$_3$).

^{31}P{^{1}H} NMR (162 MHz, 298 K, $CDCl_3$): δ(ppm) 2.1 (s).

^{13}C{^{1}H} NMR (100 MHz, 298 K, $CDCl_3$): δ(ppm) 157.6 (C*C*N_2), 143.7 (1-Ar-*C*^{Dipp}), 142.1 (2,6-Ar-*C*^{Dipp}), 133.1 (d, $^1J_{CP}$ = 15.8 Hz, 1-Ar-*C*^{Ph}), 132.3 (d, $^3J_{CP}$ = 2.9 Hz, 3,5-Ar-*C*H^{Ph}), 129.3 (d, $^2J_{CP}$ = 13.2 Hz, 2,6-Ar-*C*H^{Ph}), 127.0 (4-Ar-*C*H^{Ph}), 126.3 (3,5-Ar-*C*H^{Dipp}), 123.9 (4-Ar-*C*H^{Dipp}), 100.9 (d, $^2J_{CP}$ = 16.6 Hz, *C*≡CP), 87.5 (d, $^1J_{CP}$ = 105.3 Hz, C≡*C*P), 28.6 (*C*H), 24.2 (*C*H$_3$), 23.9 (*C*H$_3$).

IR (ATR): $\tilde{\nu}$(cm^{-1}) 3058 (w), 2958 (vs), 2925 (sh), 2865 (m), 2362 (w), 2326 (w), 2181 (w), 2169 (w), 1613 (w), 1581 (w), 1511 (vs), 1460 (m), 1437 (s), 1382 (w), 1361 (w), 1320 (m), 1254 (w), 1212 (w), 1180 (w), 1102 (m), 1057 (w), 1043 (w), 998 (w), 973 (w), 934 (w), 801 (w), 784 (w), 747 (m), 715 (w), 688 (m), 632 (w), 534 (w), 490 (m), 429 (w).

4.2.5 [{(AuC_6F_5)Ph_2PC≡CC(NDipp)$_2$}$_2$$Cu_2$] (6):

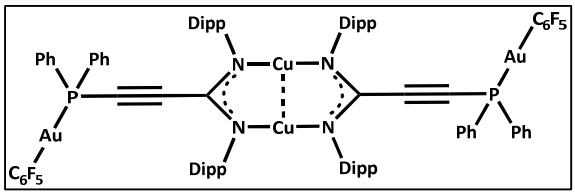

Pathway I: Compound **2** (50 mg, 39.4 µmol, 1.00 eq.) and [Au(tht)C_6F_5] (35.6 mg, 78.8 µmol, 2.00 eq.) were taken in a Schlenk flask and were dissolved in 15 mL of THF. The reaction mixture was stirred overnight at ambient temperature and the solvent was subsequently evaporated under reduced pressure. The resulting solid was filtered in DCM through a 0.22 µm PTFE membrane filter. The solvent was evaporated under reduced pressure and a bright yellow colored solid was obtained. The solid was then washed with *n*-pentane. Single crystals suitable for X-ray structure determination were obtained from a concentrated DCM solution. Yield: 64 mg (66 %).

Pathway II: Compound **1** (100 mg, 125.8 µmol, 1.00 eq.), [Au(tht)C_6F_5] (56.8 mg, 125.8µmol, 1.00 eq.) and copper(I) chloride (12.5 mg, 125.8µmol, 1.00 eq.) were taken in a Schlenk flask and dissolved in 15 mL THF. The reaction mixture was stirred overnight at ambient temperature and the solvent subsequently evaporated under reduced pressure. The solid was again dissolved in DCM and filtered through a 0.22 µm PTFE membrane filter. The solvent was evaporated under vacuum and a bright yellow colored solid was obtained. The solid was then washed with *n*-pentane. Single crystals suitable for X-ray structure determination were obtained from a concentrated DCM solution. Yield: 190 mg (75 %).

HRMS (ESI): *m/z* calcd for $C_{90}H_{88}Au_2Cu_2F_{10}N_4P_2$: 1996.4242 [M]; found: 1996.4052.

^{1}H NMR (400 MHz, 298 K, $CDCl_3$): δ(ppm) 7.43–7.37 (m, 4H, CH^{Ph}), 7.28 (d, *J* = 2.8 Hz, 4H, CH^{Ph}), 7.24 (d, *J* = 2.9 Hz, 4H, CH^{Ph}), 7.11 (dd, *J* = 8.6, 6.7 Hz, 4H, CH^{Ph}), 7.04–6.93 (m, 16H, CH^{Ph}), 3.42 (hept, *J* = 6.8Hz, 8H, C$H(CH_3)_2$), 1.15 (d, *J* = 6.8 Hz, 24H, CH_3), 1.06 (d, *J* = 6.8 Hz, 24H, CH_3).

^{31}P{^{1}H} NMR (162 MHz, 298 K, $CDCl_3$): δ(ppm) 15.1 (s).

^{13}C{^{1}H} NMR (100 MHz, 298 K, $CDCl_3$): δ(ppm) 157.6 (C*C*N_2), 143.7 (1-Ar-*C*^{Dipp}), 142.2 (2,6-Ar-*C*^{Dipp}), 133.3 (d, $^1J_{CP}$ = 15.8 Hz, 1-Ar-*C*^{Ph}), 131.9 (d, $^3J_{CP}$ = 2.9 Hz, 3,5-Ar-*C*H^{Ph}), 129.3 (d, $^2J_{CP}$ = 12.5 Hz, Ar-*C*H^{Ph}), 127.4 (4-Ar-*C*H^{Ph}), 126.2 (3,5-Ar-*C*H^{Dipp}), 123.7 (4-Ar-*C*H^{Dipp}), 101.0 (d, $^2J_{CP}$ = 14.3 Hz, *C*≡CP), 88.5 (d, $^1J_{CP}$ = 92.4 Hz, C≡*C*P), 28.6 (*C*H), 24.1 (*C*H_3), 23.8 (*C*H_3).

No signals for the C_6F_5 group were observed.

^{19}F{^{1}H} NMR (377 MHz, 298 K, $CDCl_3$): δ(ppm) -115.7 – −115.9 (m, *o*-*F*), -158.0 (t, *J* = 19.9 Hz, *p*-*F*), -162.2 – -162.5 (m, *m*-*F*).

IR (ATR): $\tilde{\nu}$(cm^{-1}) 3057 (w), 2957 (vs), 2925 (sh), 2865 (m), 2324 (w), 2171 (w), 1808 (w), 1635 (w), 1588 (w), 1503 (vs), 1455 (s), 1437 (s), 1390 (w), 1358 (m), 1319 (m), 1255 (w), 1213 (w), 1181 (w), 1102 (w), 1061 (m), 1000 (w), 975 (w), 955 (w), 935 (s), 785 (m), 753 (w), 743 (m), 715 (w), 688 (m), 628 (w), 526 (w), 487 (w), 429 (w).

4.2.6 [{(AuBr)Ph_2PC≡CC(NDipp)$_2$}$_2$$Cu_2$] (7):

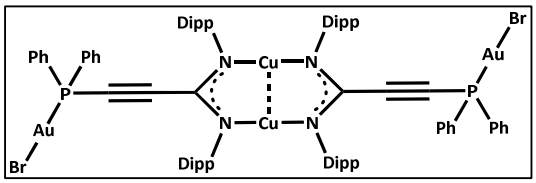

Pathway I: Compound **3** (50 mg, 32.5 µmol, 1.00 eq.) and copper(I) bromide (9.3 mg, 65 µmol, 2.00 eq.) were taken in a Schlenk flask and dissolved in 15 mL of THF. The reaction mixture was stirred overnight at ambient temperature and the solvent was evaporated under reduced pressure afterwards. The obtained solid was dissolved in DCM and filtered through a 0.22 µm PTFE membrane filter. The solvent was evaporated under vacuum and a bright yellow colored solid was obtained. The solid was then washed with *n*-pentane. Single crystals suitable for X-ray structure determination were obtained from a concentrated DCM solution. Yield: 34 mg (57 %).

Pathway II: Compound **1** (100 mg, 125.8 µmol, 1.00 eq.), [Au(tht)Cl] (40.3 mg, 125.8 µmol, 1.00 eq.) and copper(I) bromide (18.1 mg, 125.8 µmol, 1.00 eq.) were taken in a Schlenk flask and dissolved in 15 mL of THF. The reaction mixture was stirred overnight at ambient temperature and the solvent subsequently evaporated under reduced pressure. The solid was redissolved in DCM and filtered through a 0.22 µm PTFE membrane filter. The solvent was evaporated under reduced pressure and a bright yellow colored solid was obtained. The solid was then washed with *n*-pentane. Single crystals suitable for X-ray structure determination were obtained from a concentrated DCM solution. Yield: 162 mg (70 %).

HRMS (ESI): *m/z* calcd for $C_{78}H_{88}Au_2Br_2Cu_2N_4P_2$: 1820.2769 [M]; found: 1820.2576.

Anal. calcd for $C_{78}H_{88}Au_2Br_2Cu_2N_4P_2$ (1824.37 g/mol): C, 51.35; H, 4.86; N, 3.07 %. Found: C, 51.30; H, 4.74; N, 2.95 %.

^{1}H NMR (400 MHz, 298 K, $CDCl_3$): δ(ppm) 7.43–7.37 (m, 4H, C*H*^{Ph}), 7.26–7.17 (m, 12H, C*H*^{Ph}), 7.08 (d, *J* = 7.5 Hz, 8H, C*H*^{Ph}), 6.91 (ddd, 15.0, 8.3, 1.3 Hz, 8H, C*H*^{Ph}), 3.40 (hept, *J* = 6.8 Hz, 8H, C*H*(CH_3)$_2$), 1.17 (d, *J* = 6.8 Hz, 24H, C*H*$_3$), 1.05 (d, *J* = 6.8 Hz, 24H, C*H*$_3$).

^{31}P{^{1}H} NMR (162 MHz, 298 K, $CDCl_3$): δ(ppm) 4.3 (s).

^{13}C{^{1}H} NMR (100 MHz, 298 K, $CDCl_3$): δ(ppm) 157.6 (C*C*N$_2$), 143.7 (1-Ar-*C*^{Dipp}), 142.1 (2,6-Ar-*C*^{Dipp}), 133.1 (d, $^1J_{CP}$ = 15.8 Hz, 1-Ar-*C*^{Ph}), 132.2 (d, $^3J_{CP}$ = 2.9 Hz, 3,5-Ar-*C*H^{Ph}), 129.3 (d, $^2J_{CP}$ = 13.2 Hz, 2,6-Ar-*C*H^{Ph}), 127.2 (4-Ar-*C*H^{Ph}), 126.5 (3,5-Ar-*C*H^{Dipp}), 123.9 (4-Ar-*C*H^{Dipp}), 100.9 (d, $^2J_{CP}$ = 16.1 Hz, *C*≡CP), 87.5 (d, $^1J_{CP}$ = 103.4 Hz, C≡*C*P), 28.6 (*C*H), 24.2 (*C*H$_3$), 24.0 (*C*H$_3$).

IR (ATR): $\tilde{\nu}$(cm^{-1}) 3057 (w), 2958 (vs), 2924 (sh), 2864 (m), 2362 (w), 2335 (w), 2177 (w), 1597 (w), 1577 (w), 1509 (vs), 1459 (m), 1436 (s), 1383 (w), 1361 (w), 1320 (m), 1254 (w), 1211 (w), 1179 (w), 1101 (m), 1057 (w), 1043 (w), 971 (w), 933 (w), 801 (w), 783 (w), 747 (m), 688 (m), 630 (w), 530 (m), 489 (w), 430 (w).

4.2.7 [{(AuI)Ph$_2$PC≡CC(NDipp)$_2$}$_2$Cu$_2$] (8):

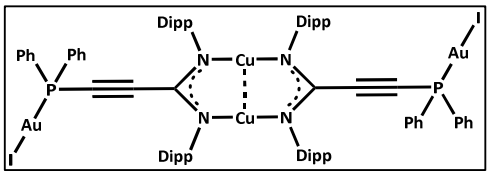

Pathway I: Compound **3** (50 mg, 32.5 µmol, 1.00 eq.) and copper(I) iodide (12.4 mg, 65 µmol, 2.00 eq.) were taken in a Schlenk flask and dissolved in 15 mL of THF. The reaction mixture was stirred overnight at ambient temperature and the solvent subsequently was evaporated under vacuum. Subsequently, the obtained solid was dissolved in DCM and filtered through a 0.22 µm PTFE membrane filter. The solvent was evaporated under reduced pressure and a bright yellow colored solid was obtained. The solid was then washed with *n*-pentane. Single crystals suitable for X-ray structure determination were obtained from a concentrated DCM solution. Yield: 40 mg (64 %).

Pathway II: Compound **1** (100 mg, 125.8 µmol, 1.00 eq.), [Au(tht)Cl] (40.3 mg, 125.8 µmol, 1.00 eq.), and copper(I) iodide (23.9 mg, 125.8 µmol, 1.00 eq.) were taken in a Schlenk flask and dissolved in 15 mL THF. The reaction mixture was stirred overnight at ambient temperature and volatiles were removed under reduced pressure. The solid was dissolved in DCM and filtered through a 0.22 µm PTFE membrane filter. The solvent was evaporated under reduced pressure and a bright yellow colored solid was obtained. The solid was then washed with *n*-pentane. Single crystals suitable for X-ray structure determination were obtained from a concentrated DCM solution. Yield: 176 mg (73 %).

HRMS (ESI): *m/z* calcd for $C_{78}H_{88}Au_2I_2Cu_2N_4P_2$: 1916.2491 [M]; found: 1916.2322.

Anal. calcd for $C_{78}H_{88}Au_2I_2Cu_2N_4P_2$ (1918.37 g/mol): C, 48.84; H, 4.62; N, 2.92 %. Found: C, 48.77; H, 4.61; N, 2.75 %.

^{1}H NMR (400 MHz, 298 K, $CDCl_3$): δ(ppm) 7.54–7.46 (m, 4H, C*H*^{Ph}), 7.37–7.26 (m, 12H, C*H*^{Ph}), 7.17 (d, *J* = 7.5 Hz, 8H, C*H*^{Ph}), 7.01 (ddd, *J* = 15.0, 8.4, 1.3 Hz, 8H, C*H*^{Ph}), 3.50 (hept, *J* = 6.8 Hz, 8H, C*H*(CH$_3$)$_2$), 1.26 (d, *J* = 6.8 Hz, 24H, C*H*$_3$), 1.15 (d, *J* = 6.8 Hz, 24H, C*H*$_3$).

^{31}P{^{1}H} NMR (162 MHz, 298 K, $CDCl_3$): δ(ppm) 8.5 (s).

$^{13}C\{^{1}H\}$ NMR (100 MHz, 298 K, $CDCl_3$): δ(ppm) 157.5 (CCN_2), 143.6 (1-Ar-C^{Dipp}), 142.1 (2,6-Ar-C^{Dipp}), 133.0 (d, $^{1}J_{CP}$ = 16.1 Hz, 1-Ar-C^{Ph}), 132.1 (d, $^{3}J_{CP}$ = 2.6 Hz, 3,5-Ar-CH^{Ph}), 129.3 (d, $^{2}J_{CP}$ = 12.8 Hz, 2,6-Ar-CH^{Ph}), 127.5 (4-Ar-CH^{Ph}), 126.5 (3,5-Ar-CH^{Dipp}), 124.0 (4-Ar-CH^{Dipp}), 100.9 (d, $^{2}J_{CP}$ = 15.0 Hz, C≡CP), 87.8 (d, $^{1}J_{CP}$ = 99.4 Hz, C≡CP), 28.6 (CH), 24.2 (CH_3), 24.1 (CH_3).

IR (ATR): $\tilde{\nu}$(cm^{-1}) 3058 (w), 2959 (vs), 2926 (sh), 2866 (m), 2362 (w), 2326 (w), 2170 (w), 1586 (w), 1504 (vs), 1460 (m), 1435 (s), 1374 (m), 1360 (w), 1318 (m), 1253 (w), 1211 (w), 1179 (w), 1159 (w), 1102 (m), 1059 (w), 1043 (w), 1028 (w), 999 (w), 970 (w), 936 (w), 919 (w), 801 (w), 786 (w), 756 (w), 743 (m), 688 (m), 627 (w), 522 (m), 490 (w), 470 (w), 438 (w).

4.2.8 [{(AuMes)Ph_2PC≡CC(NDipp)$_2$}$_2$$Cu_2$] (9):

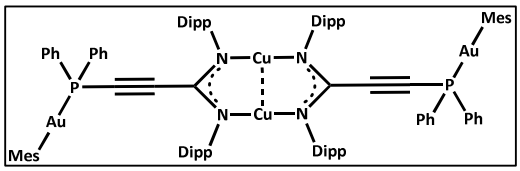

Pathway I: Compound **3** (50 mg, 32.5 µmol, 1.00 eq.) and copper(I) mesityl (11.9 mg, 65 µmol, 2.00 eq.) were taken in a Schlenk flask and dissolved in 20 mL of THF. The reaction mixture was stirred overnight at ambient temperature and subsequently dried under reduced pressure. Then, DCM was added to the solid and filtered through a 0.22 µm PTFE membrane filter. The solvent was evaporated under reduced pressure and a bright yellow colored solid was obtained. The solid was then washed with *n*-pentane. Single crystals suitable for X-ray structure determination were obtained from a concentrated DCM solution. Yield: 41 mg (61 %).

Pathway II: Compound **1** (100 mg, 125.8 µmol, 1.00 eq.), [Au(tht)Cl] (40.3 mg, 125.8µmol, 1.00 eq.), and copper(I) mesityl (23.0 mg, 125.8 µmol, 1.00 eq.) were taken in a Schlenk flask and dissolved in 15 mL THF. The reaction mixture was stirred overnight at ambient temperature and volatiles were removed under reduced pressure. Then, the solid was dissolved in DCM and filtered through a 0.22 µm PTFE membrane filter. The solvent was evaporated under reduced pressure and bright yellow colored solid was obtained. The solid was then washed with *n*-pentane. Single crystals suitable for X-ray structure determination were obtained from a concentrated DCM solution. Yield: 174 mg (73 %).

HRMS (ESI): *m/z* calcd for $C_{96}H_{110}Au_2Cu_2N_4P_2$: 1900.6123 [M]; found: 1900.6025.

Anal. calcd for $C_{96}H_{110}Au_2Cu_2N_4P_2$ (1902.94 g/mol): C, 60.59; H, 5.83; N, 2.94 %. Found: C, 60.92; H, 5.80; N, 2.80 %.

^{1}H NMR (400 MHz, 298 K, $CDCl_3$): δ(ppm) 7.36–7.32 (m, 4H, C*H*^{Ph}), 7.23–7.18 (m, 8H, C*H*^{Ph}), 7.09–7.05 (m, 4H, C*H*^{Ph}), 7.03–6.93 (m, 16H, C*H*^{Ph}), 6.86 (br, 4H, C*H*^{Ph}), 3.44 (hept, *J* = 6.8 Hz, 8H, C*H*$(CH_3)_2$), 2.42 (s, 12H, *o*-CH_3), 2.24 (s, 6H, *p*-CH_3), 1.13 (d, *J* = 6.8 Hz, 24H, CH_3), 1.07(d, *J* = 6.8 Hz, 24H, CH_3).

^{31}P{^{1}H} NMR (162 MHz, 298 K, $CDCl_3$): δ(ppm) 18.8 (s).

^{13}C{^{1}H} NMR (100 MHz, 298 K, $CDCl_3$): δ(ppm) 157.6 (C*C*N_2), 143.5 (1-Ar-*C*^{Dipp}), 142.2 (2,6-Ar-*C*^{Dipp}), 133.1 (d, $^{1}J_{CP}$ = 15.4 Hz, 1-Ar-*C*^{Ph}), 131.1 (d, $^{3}J_{CP}$ = 2.6 Hz, 3,5-Ar-*C*H^{Ph}), 129.1 (d, $^{2}J_{CP}$ = 11.7 Hz, 2,6-Ar-*C*H^{Ph}), 129.0 (Ar-*C*H^{Ph}), 126.2 (Ar-*C*H^{Ph}), 126.3 (Ar-*C*H^{Ph}), 125.9 (3,5-Ar-*C*H^{Dipp}), 123.5 (4-Ar-*C*H^{Dipp}), 100.1 (d, $^{2}J_{CP}$ = 10.6 Hz, *C*≡CP), 90.16 (d, $^{1}J_{CP}$ = 77.4 Hz, C≡*C*P), 28.6 (Dipp-*C*H), 27.0 (Mes-*C*H_3), 24.0 (Dipp-*C*H_3), 23.8 (Dipp-*C*H_3), 21.2 (Mes-*C*H_3).

IR (ATR): $\tilde{\nu}$(cm^{-1}) 3059 (w), 3014 (w), 2956 (vs), 2924 (sh), 2864 (m), 2363 (w), 2330 (w), 2172 (w), 1587 (w), 1506 (vs), 1460 (m), 1437 (m), 1384 (w), 1319 (m), 1253 (w), 1212 (w), 1180 (w), 1100 (m), 1035 (w), 971 (w), 930 (w), 844 (w), 787 (w), 748 (m), 689 (m), 629 (w), 587 (w), 520 (m), 486 (w), 430 (w).

4.2.9 [{(Rh(cod)Cl)Ph$_2$PC≡CC(NDipp)$_2$}$_2$Cu$_2$] (10):

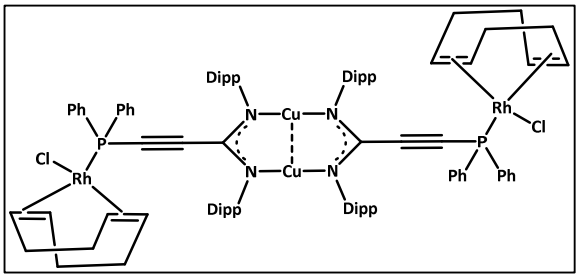

Pathway I: Copper(I) amidinate complex (**2**), [Ph$_2$PC≡CC(NDipp)$_2$}$_2$Cu$_2$] (100 mg, 78.7 µmol, 1.00 eq.) and chloro(1,5-cyclooctadiene)rhodium(I) dimer (38.8 mg, 78.7 µmol, 1.00 eq.) were taken in a Schlenk flask and dissolved in 10 mL of THF. The reaction mixture was stirred overnight at ambient temperature and was evaporated under reduced pressure. The resulting solid was filtered in DCM through a 0.22 µm PTFE membrane filter. The solvent was subsequently evaporated under reduced pressure and a yellow colored solid was obtained. The solid was then washed with *n*-pentane. Single crystals suitable for X-ray structure determination were obtained from layering *n*-pentane on a concentrated THF solution. Yield: 110 mg (79 %).

Pathway II: The lithium salt of the amidinate ligand [Ph$_2$PC≡CC(NDipp)$_2$}Li(thf)$_3$](**1**) (50 mg, 62.9 µmol, 1.00 eq.), chloro(1,5-cyclooctadiene)rhodium(I) dimer (15.5 mg, 31.5 µmol, 0.50 eq.), and copper(I) chloride (6.2 mg, 62.9 µmol, 1.00 eq.) were taken in a Schlenk flask and dissolved in 10 mL of THF. The reaction mixture was stirred overnight at ambient temperature

and evaporated under reduced pressure. The solid was redissolved in DCM and filtered through a 0.22 µm PTFE membrane filter. The solvent was subsequently evaporated under reduced pressure and a bright yellow colored solid was obtained. Yield: 93 mg (84 %).

HRMS (ESI): *m/z* calcd for $C_{94}H_{117}Cl_2Cu_2N_4P_2Rh_2$: 1768.5017 [M+5H]; found: 1768.4891.

Anal. calcd for $C_{94}H_{112}Cl_2Cu_2N_4P_2Rh_2$ (1763.71 g/mol): C, 64.01; H, 6.40; N, 3.18 %. Found: C, 63.67; H, 6.40; N, 2.88 %.

^{1}H NMR (400 MHz, 298 K, $CDCl_3$): δ(ppm) 7.30–7.27 (m, 4H, C*H*^{Ph}), 7.21–7.19 (m, 4H, C*H*^{Ph}), 7.18–7.13 (m, 12H, C*H*^{Ph}), 7.09–7.06 (m, 4H, C*H*^{Ph}), 6.94 (d, *J* = 7.6 Hz, 8H, C*H*^{Ph}), 3.28 (hept, *J* = 7.0 Hz, 8H, C*H*$(CH_3)_2$), 2.75 (br, 8H, COD-C*H*), 2.26–2.18 (m, 4H, COD-CH_2), 2.15–2.06 (m, 4H, COD-CH_2), 1.98–1.93 (m, 4H, COD-CH_2), 1.85–1.78 (m, 4H, COD-CH_2), 0.99 (d, *J* = 6.8 Hz, 24H, CH_3), 0.92 (d, *J* = 7.0 Hz, 24H, CH_3).

^{31}P{^{1}H} NMR (162 MHz, 298 K, $CDCl_3$): δ(ppm) 12.3 (d, *J* = 158.5 Hz).

^{13}C{^{1}H} NMR (100 MHz, 298 K, $CDCl_3$): δ(ppm) 156.0 (C*C*N_2), 142.8 (1-Ar-*C*^{Dipp}), 141.9, (2,6-Ar-*C*^{Dipp}), 133.9 (d, $^1J_{CP}$ = 13.6 Hz, 1-Ar-*C*^{Ph}), 130.3 (d, $^3J_{CP}$ = 2.6 Hz, 3,5-Ar-*C*H^{Ph}), 129.5 (4-Ar-*C*H^{Ph}), 128.5 (d, $^2J_{CP}$ = 11.4 Hz, 2,6-Ar-*C*H^{Ph}), 125.7 (3,5-Ar-*C*H^{Dipp}), 123.4 (4-Ar-*C*H^{Dipp}), 97.9 (d, $^2J_{CP}$ = 5.1 Hz, *C*≡CP), 88.1 (d, $^1J_{CP}$ = 59.8 Hz, C≡*C*P), 72.2 (d, J_{CRh} = 13.6 Hz, COD-*C*H), 33.4 (d, J_{CRh} = 3.3 Hz, COD-*C*H_2), 28.7 (*C*H), 23.6 (*C*H_3), 22.8 (*C*H_3).

IR (ATR): $\tilde{\nu}$(cm^{-1}) 3107 (w), 3055 (w), 3027 (w), 3003 (w), 2955 (vs), 2916 (sh), 2867 (s), 2830 (m), 2250 (w), 2209 (w), 2053 (w), 2006 (w), 1950 (w), 1585 (w), 1500 (vs), 1434 (s), 1386 (sh), 1359 (m), 1321 (s), 1255 (m), 1215 (w), 1181 (w), 1158 (w), 1096 (m), 1059 (w), 1043 (w), 1028 (w), 999 (w), 968 (m), 933 (w), 866 (w), 844 (w), 797 (w), 783 (m), 748 (s), 689 (s), 621 (w), 607 (w), 585 (w), 520 (s), 491 (m), 464 (w), 430 (w).

4.2.10 [{(Ir(cod)Cl)Ph$_2$PC≡CC(NDipp)$_2$}$_2$Cu$_2$] (11):

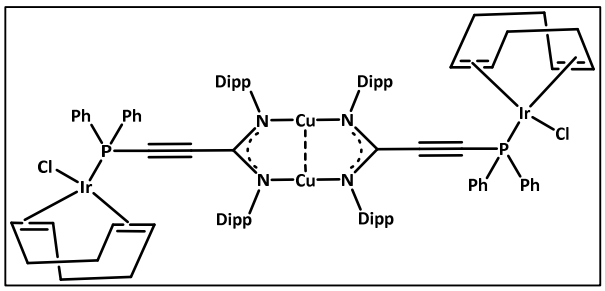

Pathway I: Complex (**2**) (100 mg, 78.7 µmol, 1.00 eq.) and chloro(1,5-cyclooctadiene)iridium(I) dimer (52.8 mg, 78.7 µmol, 1.00 eq.) were taken in a Schlenk flask and dissolved in 10 mL of THF. The reaction mixture was stirred

overnight at ambient temperature and was evaporated under reduced pressure. The resulting solid was filtered in DCM through a 0.22 µm PTFE membrane filter. The solvent was subsequently evaporated under reduced pressure and an amber colored solid was obtained. The solid was then washed with *n*-pentane. Single crystals suitable for X-ray structure determination were obtained from layering *n*-pentane on a concentrated THF solution. Yield: 115 mg (75 %).

Pathway II: The compound **1** (50 mg, 62.9 µmol, 1.00 eq.), chloro(1,5-cyclooctadiene)iridium(I) dimer (21.1 mg, 31.5 µmol, 0.50 eq.), and copper(I) chloride (6.2 mg, 62.9 µmol, 1.00 eq.) were taken in a Schlenk flask and dissolved in 10 mL of THF. The reaction mixture was stirred overnight at ambient temperature and evaporated under reduced pressure. The solid was redissolved in DCM and filtered through a 0.22 µm PTFE membrane filter. The solvent was subsequently evaporated under reduced pressure and a bright yellow colored solid was obtained. Yield: 101 mg (82 %).

HRMS (ESI): *m/z* calcd for $C_{94}H_{114}Cl_2Cu_2N_4P_2Rh_2$: 1941.5751 [M+2H]; found: 1941.5475.

Anal. calcd for $C_{94}H_{112}Cl_2Cu_2N_4P_2Ir_2$ (1942.33 g/mol): C, 58.13; H, 5.81; N, 2.88 %. Found: C, 58.28; H, 5.93; N, 2.61 %.

^{1}H NMR (400 MHz, 298 K, $CDCl_3$): δ(ppm) 7.30–7.27 (m, 4H, C*H*^{Ph}), 7.18–7.14 (m, 12H, C*H*^{Ph}), 7.12–7.10 (m, 4H, C*H*^{Ph}), 7.09–7.06 (m, 4H, C*H*^{Ph}), 6.95 (d, *J* = 7.7 Hz, 8 H, C*H*^{Ph}), 3.32 (hept, *J* = 7.0 Hz, 8H, C*H*$(CH_3)_2$), 2.33 (br, 4H, COD-C*H*), 2.06–1.96 (m, 4H, COD-CH_2), 1.53–1.50 (m, 4H, COD-CH_2), 1.00 (d, *J* = 6.8 Hz, 24H, CH_3), 0.94 (d, *J* = 7.0 Hz, 24H, CH_3).

^{31}P{^{1}H} NMR (162 MHz, 298 K, $CDCl_3$): δ(ppm) 4.1 (s).

^{13}C{^{1}H} NMR (100 MHz, 298 K, $CDCl_3$): δ(ppm) 156.0 (C*C*N_2), 142.8 (1-Ar-*C*^{Dipp}), 141.9, (2,6-Ar-*C*^{Dipp}), 133.9 (d, $^1J_{CP}$ = 13.2 Hz, 1-Ar-*C*^{Ph}), 130.5 (d, $^3J_{CP}$ = 2.6 Hz, 3,5-Ar-*C*H^{Ph}), 129.5 (4-Ar-*C*H^{Ph}), 128.5 (d, $^2J_{CP}$ = 11.4 Hz, 2,6-Ar-*C*H^{Ph}), 125.7 (3,5-Ar-*C*H^{Dipp}), 123.4 (4-Ar-*C*H^{Dipp}), 95.9 (d, $^2J_{CP}$ = 15.0 Hz, *C*≡CP), 86.0 (d, $^1J_{CP}$ = 74.1 Hz, C≡*C*P), 55.4 (COD-*C*H), 33.9 (COD-*C*H_2), 28.7 (*C*H), 23.6(*C*H_3), 22.8 (*C*H_3).

IR (ATR): $\tilde{\nu}$(cm^{-1}) 3138 (w), 3053 (w), 3030 (w), 3007 (w), 2956 (vs), 2916 (sh), 2867 (m), 2832 (m), 2314 (w), 2249 (w), 2231 (w), 2168 (w), 1586 (w), 1500 (vs), 1478 (sh), 1434 (s), 1386 (m), 1359 (m), 1321 (s), 1254 (m), 1214 (m), 1181 (m), 1158 (w), 1097 (m), 1059 (w),

1043 (w), 1020 (w), 999 (w), 970 (m), 933 (w), 907 (w), 885 (w), 870 (w), 843 (w), 797 (w), 783 (m), 747 (s), 690 (s), 622 (w), 608 (w), 586 (w), 534 (s), 512 (m), 494 (m), 466 (m), 442 (m), 425 (w).

4.2.11 $[Ph_2PC{\equiv}CC(NDipp)(NHDipp)]_2$ (14):

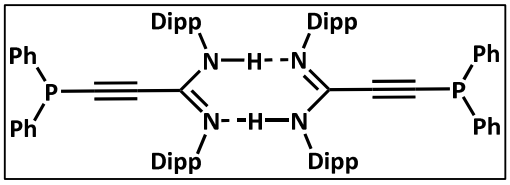

The compound **1** (100 mg, 125.8 µmol) was dissolved in 10 mL DCM, hydrolyzed with 10 mL water and stirred for 2 hours. The organic phase was extracted 3 times with DCM (3 X 10 mL) and dried over Na_2SO_4. The solvent was evaporated under reduced pressure and an off-white colored solid was obtained. Single crystals suitable for X-ray structure determination were obtained from layering *n*-pentane on a concentrated THF solution. Yield: 66 mg (92 %).

Anal. calcd for $C_{39}H_{45}N_2P$ (572.77 g/mol): C, 81.78; H, 7.92; N, 4.89 %. Found: C, 82.02; H, 7.79; N, 4.82 %.

^{1}H NMR (400 MHz, 298 K, $CDCl_3$): δ(ppm) 7.24–7.15 (m, 3H, Ar-C*H*^{Ph}), 7.15–7.08 (m, 5H, Ar-C*H*^{Ph}), 7.05 (d, *J* = 7.3 Hz, 5H, Ar-C*H*^{Ph}), 6.77 (s, 3H, Ar-C*H*^{Ph}), 3.28 (bs, 4H, -C*H*$(CH_3)_2$), 1.00 (d, *J* = 44.9 Hz, 24H, -C*H*$_3$).

^{31}P{^{1}H} NMR (162 MHz, 298 K, $CDCl_3$): δ(ppm) -33.6 (s).

^{13}C{^{1}H} NMR (100 MHz, 298 K, $CDCl_3$): δ(ppm) 147.8 (C*C*N_2), 146.9 (1-Ar-*C*^{Dipp}), 144.1 (2,6-Ar-*C*^{Dipp}), 133.4 (1-Ar-*C*^{Ph}), 132.3 (d, J_{CP} = 19.8 Hz, 2,6-Ar-*C*H^{Ph}), 128.9 (d, J_{CP} = 30.1 Hz, 3,5-Ar-*C*H^{Ph}), 128.6 (d, J_{CP} = 7.4 Hz, 4-Ar-*C*H^{Ph}), 125.8 (3,5-Ar-*C*H^{Dipp}), 123.2 (4-Ar-*C*H^{Dipp}), 98.2 (C≡*C*P), 95.1 (*C*≡CP), 28.5 (*C*H), 24.1 (*C*H$_3$), 23.3 (*C*H$_3$).

IR (ATR): $\tilde{\nu}$(cm^{-1}) 3193 (w), 3140 (w), 3069 (w), 3055 (w), 3024 (w), 3015 (w), 2957 (vs), 2925 (m), 2864 (s), 2157 (w), 1613 (vs), 1584 (s), 1477 (w), 1456 (m), 1435 (s), 1373 (s), 1360 (s), 1319 (s), 1242 (m), 1207 (w), 1186 (m), 1156 (w), 1156 (w), 1096 (m), 1057 (w), 1042 (w), 1025 (w), 998 (w), 958 (w), 934 (w), 870 (w), 831 (m), 796 (w), 776 (w), 745 (s), 738 (s), 691 (s), 673 (w), 505 (m), 469 (w), 446 (w), 408 (w).

4.2.12 [(Rh(cod)Cl)Ph_2PC≡CC(NDipp)(NHDipp)]$_2$ (15):

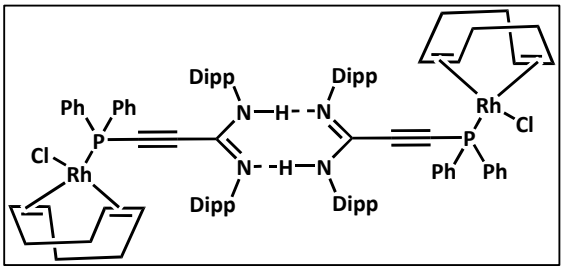

Pathway I: The compound **1** (100 mg, 125.8 µmol, 1.00 eq.) and chloro(1,5-cyclooctadiene) rhodium(I) dimer (31.1 mg, 62.9 µmol, 0.50 eq.), were taken in a Schlenk flask and dissolved in 10 mL of THF. The reaction mixture was stirred overnight at ambient temperature and evaporated under reduced pressure to obtain the complex [{(Rh(cod)Cl)Ph_2PC≡CC(NDipp)$_2$}Li(thf)$_3$] (**12**) *in situ*. The solid was redissolved in DCM and hydrolyzed with 10 mL of water. The organic phase was extracted three times with DCM (3 X 10 mL) and dried over Na_2SO_4. It was filtered and the solvent was evaporated under reduced pressure and a bright yellow colored solid was obtained. Single crystals suitable for X-ray structure determination were obtained from layering *n*-pentane on a concentrated THF solution. Yield: 78 mg (86 %).

Pathway II: The ligand **14** (50 mg, 87.3 µmol, 2.00 eq.) and chloro(1,5-cyclooctadiene)rhodium(I) dimer (21.5 mg, 43.6 µmol, 1.00 eq.) were taken in a Schlenk flask and dissolved in 10 mL of THF. The reaction mixture was stirred overnight at ambient temperature and was subsequently evaporated under reduced pressure. The resulting solid was filtered in DCM through a 0.22 µm PTFE membrane filter. The solvent was evaporated under reduced pressure and a bright yellow colored solid was obtained. The solid was then washed with *n*-pentane. Yield: 57 mg (80 %).

HRMS (ESI): *m/z* calcd for $C_{47}H_{58}ClN_2PRh$: 819.3076 [M+H]; found: 819.3051.

Anal. calcd for $C_{47}H_{57}ClN_2PRh$ (819.32 g/mol): C, 68.90; H, 7.01; N, 3.42 %. Found: C, 68.49; H, 7.04; N, 2.96 %.

^{1}H NMR (400 MHz, 298 K, $CDCl_3$): δ(ppm) 7.56–7.51 (m, 2H, C*H*^{Ph}), 7.35–7.29 (m, 2H, C*H*^{Ph}), 7.22–7.17 (m, 6H, C*H*^{Ph}), 7.14–7.10 (m, 2H, C*H*^{Ph}), 7.05 (d, *J* = 7.8 Hz, 4H, C*H*^{Ph}), 3.31 (br, 1H, N*H*), 3.07 (hept, *J* = 7.0 Hz, 4H, C*H*$(CH_3)_2$), 2.93–2.69 (m, 4H, COD-C*H*), 2.21–1.84 (m, 8H, COD-CH_2), 0.97 (d, *J* = 6.7 Hz, 12H, CH_3), 0.93 (d, *J* = 7.1 Hz, 12H, CH_3).

^{31}P{^{1}H} NMR (162 MHz, 298 K, $CDCl_3$): δ(ppm) 12.2 (d, *J* = 158.0 Hz).

^{13}C{^{1}H} NMR (100 MHz, 298 K, $CDCl_3$): δ(ppm) 147.6 (C*C*N_2), 144.8 (1-Ar-*C*^{Dipp}), 143.6, (2,6-Ar-*C*^{Dipp}), 134.1 (d, $^1J_{CP}$ = 13.7 Hz, 1-Ar-*C*^{Ph}), 130.5 (4-Ar-*C*H^{Ph}), 129.5 (d, $^3J_{CP}$ = 50.8 Hz, 3,5-Ar-*C*H^{Ph})

128.5 (d, $^{2}J_{CP}$ = 10.7 Hz, 2,6-Ar-*C*H^{Ph}), 126.3 (3,5-Ar-*C*H^{Dipp}), 123.5 (4-Ar-*C*H^{Dipp}), 95.6 (*C*≡CP), 86.4 (d, $^{1}J_{CP}$ = 58.0 Hz, C≡*C*P), 72.3 (d, $^{1}J_{CRh}$ = 13.7 Hz, COD-*C*H), 33.3 (COD-*C*H$_2$), 28.5 (*C*H), 23.6(*C*H$_3$), 23.0 (*C*H$_3$).

IR (ATR): $\tilde{\nu}$(cm^{-1}) 3184 (w), 3124 (w), 3054 (m), 2958 (vs), 2920 (sh), 2866 (s), 2832 (s), 2323 (sh), 2293 (w), 2215 (w), 2165 (w), 1608 (vs), 1583 (vs), 1459 (s), 1435 (vs), 1360 (vs), 1319 (s), 1253 (m), 1241 (m), 1220 (w), 1205 (m), 1184 (m), 1158 (w), 1095 (s), 1044 (w), 1000 (w), 965 (w), 948 (m), 935 (w), 861 (m), 827 (w), 796 (w), 778 (m), 744 (s), 690 (s), 600 (w), 559 (w), 521 (s), 507 (), 479 (m), 431 (w), 417 (w).

4.2.13 [(Ir(cod)Cl)Ph$_2$PC≡CC(NDipp)(NHDipp)]$_2$ (16):

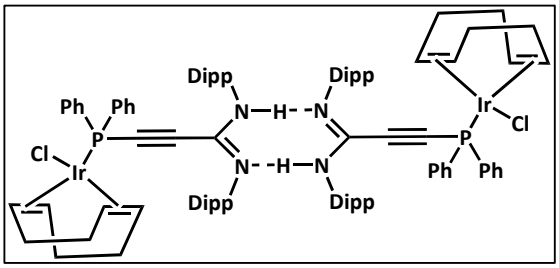

Pathway I: The compound **1** (100 mg, 125.8 µmol, 1.00 eq.) and chloro(1,5-cyclooctadiene)iridium(I) dimer (42.2 mg, 62.9 µmol, 0.50 eq.), were taken in a Schlenk flask and dissolved in 10 mL of THF. The reaction mixture was stirred overnight at ambient temperature and subsequently evaporated under reduced pressure to obtain the complex [{(Ir(cod)Cl)Ph$_2$PC≡CC(NDipp)$_2$}Li(thf)$_3$] (**13***) in situ*. The solid was redissolved in DCM and hydrolyzed with 10 mL water. The organic phase was extracted three times with DCM (3 X 10 mL) and dried over Na_2SO_4. It was filtered and the solvent was evaporated under reduced pressure and an amber colored solid was obtained. Single crystals suitable for X-ray structure determination were obtained from layering *n*-pentane on a concentrated THF solution. Yield: 84 mg (73 %).

Pathway II: The ligand (**14**) (50 mg, 87.3 µmol, 2.00 eq.) and chloro(1,5-cyclooctadiene)iridium(I) dimer (29.3 mg, 43.6 µmol, 1.00 eq.) were taken in a Schlenk flask and dissolved in 10 mL of THF. The reaction mixture was stirred overnight at ambient temperature and was subsequently evaporated under reduced pressure. The resulting solid was filtered in DCM through a 0.22 µm PTFE membrane filter. The solvent was evaporated under reduced pressure and an amber colored solid was obtained. The solid was then washed with *n*-pentane. Yield: 62 mg (78 %).

HRMS (ESI): *m/z* calcd for $C_{47}H_{58}ClN_2PIr$: 909.3650 [M+H]; found: 909.3598.

Anal. calcd for $C_{47}H_{57}ClN_2PIr$ (908.63 g/mol): C, 62.13; H, 6.32; N, 3.08 %. Found: C, 62.47; H, 6.28; N, 2.94 %.

^{1}H NMR (400 MHz, 298 K, $CDCl_3$): δ(ppm) 7.55–7.40 (m, 2H, C*H*^{Ph}), 7.37–7.31 (m, 2H, C*H*^{Ph}), 7.22–7.18 (m, 6H, C*H*^{Ph}), 7.14–7.12 (m, 2H, C*H*^{Ph}), 7.07 (d, *J* = 7.1 Hz, 4H, C*H*^{Ph}), 3.44 (br, 1H, N*H*), 3.14–3.06 (br m, 4H, C*H*$(CH_3)_2$), 2.37–2.17 (m, 4H, COD-C*H*), 1.96–1.80 (m, 4H, COD-CH_2), 1.63–1.62 (m, 4H, COD-CH_2) 1.03 (d, *J* = 6.7 Hz, 12H, CH_3), 0.97 (d, *J* = 6.6 Hz, 12H, CH_3).

^{31}P{^{1}H} NMR (162 MHz, 298 K, $CDCl_3$): δ(ppm) 4.1 (s).

^{13}C{^{1}H} NMR (100 MHz, 298 K, $CDCl_3$): δ(ppm) 147.7 (C*C*N_2), 144.7 (1-Ar-*C*^{Dipp}), 143.7, (2,6-Ar-*C*^{Dipp}), 134.1 (d, $^1J_{CP}$ = 13.7 Hz, 1-Ar-*C*^{Ph}), 131.0 (d, $^3J_{CP}$ = 12.2 Hz, 3,5-Ar-*C*H^{Ph}), 130.6 (4-Ar-*C*H^{Ph}), 128.6 (d, $^2J_{CP}$ = 12.2 Hz, 2,6-Ar-*C*H^{Ph}), 126.3 (3,5-Ar-*C*H^{Dipp}), 123.5 (4-Ar-*C*H^{Dipp}), 96.3 (d, $^2J_{CP}$ = 15.3 Hz, *C*≡CP), 84.3 (d, $^1J_{CP}$ = 73.2 Hz, C≡*C*P), 55.6 (COD-*C*H), 33.8 (COD-*C*H_2), 28.6 (*C*H), 23.6(*C*H_3), 23.1 (*C*H_3).

IR (ATR): $\tilde{\nu}$(cm^{-1}) 3252 (w), 3186 (w), 3123 (w), 3053 (w), 2957 (vs), 2922 (sh), 2866 (s), 2832 (sh), 2300 (w), 2240 (w), 2167 (w), 2059 (w), 1608 (vs), 1582 (s), 1459 (m), 1435 (s), 1359 (s), 1319 (m), 1240 (w), 1205 (w), 1183 (m), 1158 (w), 1096 (m), 1057 (w), 1044 (w), 998 (w), 971 (w), 947 (w), 907 (w), 859 (w), 827 (w), 797 (w), 777 (w), 745 (s), 691 (s), 599 (w), 560 (w), 533 (m), 508 (m), 480 (w), 455 (w), 438 (w), 417 (w).

4.2.14 [Coum-Mes-Im][Br] (18):

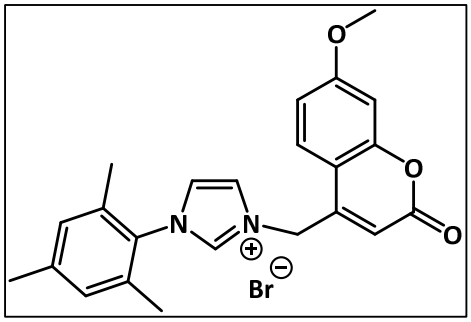

The mesityl imidazole (1.0 g, 5.37 mmol, 1.00 eq.) and 4-brommethyl-7-methoxycumarin (1.4 g, 5.37 mmol, 1eq.) were taken in a Schlenk flask and ~30-40 mL of acetonitrile was added to it. The reaction mixture was cloudy and became clear after it was heated to 140 °C. It was refluxed for 16 hours and the solvent was removed *in vacuo* after the reaction was completed. The obtained solid was washed three times with diethyl ether (3 X 15 mL) and dried completely under vacuum. The imidazolium salt (**18**) was obtained as a colorless solid. Yield: 2.1 g (86 %).

HRMS (ESI): *m/z* calcd for $[C_{23}H_{23}N_2O_3]^+$: 375.1703 $[M]^+$; found: 375.1695.

Anal. calcd for $C_{23}H_{23}N_2O_3Br$ (455.35 g/mol): C, 60.67; H, 5.09; N, 6.15 %. Found: C, 60.56; H, 5.07; N, 6.19 %.

^{1}H NMR (400 MHz, 298 K, $CDCl_3$): δ(ppm) 10.67 (s, 1H, N-C*H*=N), 8.02 (d, *J* = 8.9 Hz, 1H, -C*H*^{Coumarin}), 7.93 (t, *J* = 1.8 Hz, 1H, -C*H*^{Coumarin}), 7.21 (t, *J* = 1.8 Hz, 1H, -C*H*^{Coumarin}), 6.99 (s, 2H, Ar-C*H*^{Mes}), 6.89 (dd, *J* = 8.9, 2.6 Hz, 1H,-C*H*^{Imidazole}), 6.77 (d, *J* = 2.6 Hz, 1H, -C*H*^{Imidazole}), 6.45 (s, 2H, -CH_2^{Coumarin}), 6.15 (s, 1H, -C*H*^{Coumarin}), 3.85 (s, 3H, -OCH_3^{Coumarin}), 2.33 (s, 3H, -CH_3^{Mes}), 2.07 (s, 6H, -CH_3^{Mes}).

^{13}C{^{1}H} NMR (100 MHz, 298 K, $CDCl_3$): δ(ppm) 163.6 (-*C*=O^{Coumarin}), 160.3 (Ar-*C*^{Coumarin}), 155.7 (Ar-*C*^{Coumarin}), 148.1 (Ar-*C*^{Coumarin}), 141.8 (Ar-*C*^{Mes}), 139.0 (N-*C*H=N), 134.2 (Ar-*C*^{Coumarin}),130.6 (Ar-*C*^{Mes}), 130.1 (Ar-*C*^{Mes}), 126.2 (Ar-*C*H^{Mes}), 123.7 (-*C*H^{Imidazole}), 123.5 (-*C*H^{Imidazole}), 113.0 (Ar-*C*H^{Coumarin}), 112.3 (Ar-*C*H^{Coumarin}), 110.3 (Ar-*C*^{Coumarin}), 101.8 (Ar-*C*H^{Coumarin}), 56.1 (-O*C*H$_3$^{Coumarin}), 50.00 (-*C*H$_2$^{Coumarin}), 21.2 (-*C*H$_3$^{Mes}), 17.9 (-*C*H$_3$^{Mes}).

IR (ATR): $\tilde{\nu}$(cm^{-1}) 3145 (w), 3116 (w), 3081 (w), 3016 (vs), 2943 (sh), 2843 (w), 2011 (w), 1996 (w), 1752 (sh), 1709 (vs), 1606 (vs), 1552 (s), 1512 (w), 1486 (w), 1463 (w), 1443 (m), 1405 (w), 1385 (vs), 1350 (m), 1287 (vs), 1261 (s), 1206 (vs), 1166 (m), 1148 (s), 1130 (m), 1054 (s), 1019 (m), 990 (m), 951 (w), 937 (w), 872 (m), 856 (m), 846 (m), 824 (m), 798 (m), 769 (w), 742 (w), 694 (w), 668 (m), 638 (m), 594 (w), 578 (w), 554 (w), 523 (w), 489 (w), 456 (w), 441 (w).

4.2.15 [Coum-Mes-NHC-AuCl] (19):

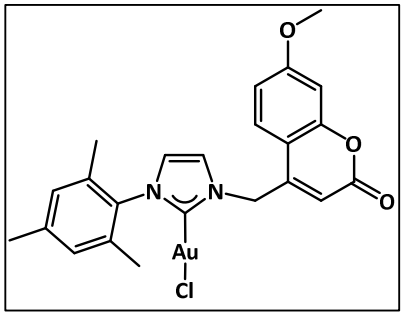

The imidazolium salt (**18**) (100 mg, 219.6 µmol, 1 eq.) and Ag_2O (25.5 mg, 109.8 µmol, 0.50 eq.) were suspended in 20 mL of DCM and stirred for 16 hours under exclusion of light. The resulting reaction mixture was filtered through a 0.22 µm PTFE membrane filter into a Schlenk flask containing solid [Au(tht)Cl] (70.4 mg, 219.6 µmol, 1.00 eq.) and stirred for additional 16 hours. The precipitates formed were filtered off again to remove AgCl and the solvent was removed under reduced pressure. The residue was washed three times with 10 mL of *n*-pentane and the product was obtained as an off-white colored solid. Crystals suitable for SC-XRD analysis were obtained by slow diffusion of *n*-pentane to a concentrated DCM solution. Yield: 122 mg (91 %).

Anal. calcd for $C_{23}H_{22}N_2O_3AuCl$ (606.87 g/mol): C, 45.52; H, 3.65; N, 4.62 %. Found: C, 44.86; H, 3.65; N, 4.40 %.

^{1}H NMR (400 MHz, 298 K, $CDCl_3$): δ(ppm) 7.61 (d, J = 8.4 Hz, 1H, -C$H^{Coumarin}$), 7.18 (d, J = 2.9 Hz, 1H, -C$H^{Coumarin}$), 7.03–6.97 (m, 3H, -C$H^{Imidazole}$ and -C$H^{Coumarin}$), 6.93–6.85 (m, 2H, -CH^{Mes}), 5.81 (t, J = 1.3 Hz, 1H, -C$H^{Coumarin}$), 5.68 (d, J = 1.5 Hz, 2H, -C$H_2^{Coumarin}$), 3.90 (s, 3H, -OC$H_3^{Coumarin}$), 2.34 (s, 3H, -CH_3^{Mes}), 2.06 (s, 6H, -CH_3^{Mes}).

^{13}C{^{1}H} NMR (100 MHz, 298 K, $CDCl_3$): δ(ppm) 174.3 (N-*C*-N), 163.6 (-*C*=O^{Coumarin}), 160.3 (Ar-*C*^{Coumarin}), 155.8 (Ar-*C*^{Coumarin}), 149.0 (Ar-*C*^{Coumarin}), 140.3 (Ar-*C*^{Mes}), 134.7 (Ar-*C*^{Mes}), 134.4 (Ar-*C*^{Mes}), 129.7 (Ar-*C*H^{Mes}), 124.7 (-*C*H^{Imidazole}), 123.6 (-*C*H^{Imidazole}), 121.0 (Ar-*C*^{Coumarin}), 113.1 (Ar-*C*H^{Coumarin}), 111.2 (Ar-*C*H^{Coumarin}), 110.5 (Ar-*C*^{Coumarin}), 101.7 (Ar-*C*H^{Coumarin}), 56.1 (-O*C*H$_3^{Coumarin}$), 51.5 (-*C*H$_2^{Coumarin}$), 21.3 (-*C*H$_3^{Mes}$), 18.0 (-*C*H$_3^{Mes}$).

IR (ATR): $\tilde{\nu}$(cm^{-1}) 3175 (w), 3136 (w), 3100 (w), 3068 (w), 3014 (w), 2979 (w), 2951 (w), 2919 (w), 2845 (w), 1984 (w), 1951 (w), 1714 (vs), 1608 (vs), 1561 (sh), 1513 (w), 1487 (w), 1452 (m), 1439 (m), 1421 (w), 1395 (m), 1346 (m), 1321 (m), 1278 (vs), 1254 (w), 1206 (s), 1150 (w), 1133 (vs), 1055 (w), 1032 (m), 1020 (m), 984 (m), 887 (w), 846 (s), 812 (m), 786 (w), 736 (m), 704 (w), 691 (m), 640 (w), 589 (w), 578 (w), 559 (w), 483 (m), 448 (w).

4.2.16 [Coum-Mes-NHC-AuBr] (20):

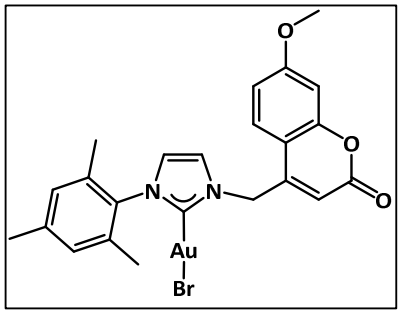

The imidazolium salt (**18**) (100 mg, 219.6 µmol, 1.00 eq.) and Ag_2O (25.5 mg, 109.8 µmol, 0.50 eq.) were suspended in 20 mL of DCM and stirred for 16 hours under exclusion of light. The resulting reaction mixture was filtered through a 0.22 µm PTFE membrane filter into a Schlenk flask containing solid [Au(tht)Br] (99.5 mg, 219.6 µmol, 1.00 eq.) and stirred for additional 16 hours. The precipitates formed were filtered off again to remove AgCl and the solvent was removed under reduced pressure. The residue was washed three times with 10 mL of *n*-pentane and the product was obtained as an off-white colored solid. Crystals suitable for SC-XRD analysis were obtained from the concentrated DCM solution. Yield: 128 mg (89 %).

Anal. calcd for $C_{23}H_{22}N_2O_3AuBr$ (651.31 g/mol): C, 42.41; H, 3.40; N, 4.30 %. Found: C, 40.94; H, 3.39; N, 3.93 %.

^{1}H NMR (400 MHz, 298 K, $CDCl_3$): δ(ppm) 7.61 (d, *J* = 8.9 Hz, 1H, -C*H*^{Coumarin}), 7.22 (d, *J* = 2.0 Hz, 1H, -C*H*^{Coumarin}), 6.98 (m, 3H, -C*H*^{Imidazole} and -C*H*^{Coumarin}), 6.92–6.78 (m, 2H, -C*H*^{Mes}), 5.79 (s, 1H, -C*H*^{Coumarin}), 5.68 (s, 2H, -C$H_2^{Coumarin}$), 3.87 (s, 3H, -OC$H_3^{Coumarin}$), 2.32 (s, 3H, -CH_3^{Mes}), 2.05 (s, 6H, -CH_3^{Mes}).

^{13}C{^{1}H} NMR (100 MHz, 298 K, $CDCl_3$): δ(ppm) 177.5 (N-*C*-N), 163.5 (-*C*=O^{Coumarin}), 160.3 (Ar-*C*^{Coumarin}), 155.7 (Ar-*C*^{Coumarin}), 149.1 (Ar-*C*^{Coumarin}), 140.1 (Ar-*C*^{Mes}), 134.7 (Ar-*C*^{Mes}), 134.3 (Ar-*C*^{Mes}), 129.7 (Ar-*C*H^{Mes}), 124.8 (-*C*H^{Imidazole}), 123.4 (-*C*H^{Imidazole}), 121.1 (Ar-*C*^{Coumarin}), 113.0 (Ar-*C*H^{Coumarin}), 111.1 (Ar-*C*H^{Coumarin}), 110.5 (Ar-*C*^{Coumarin}), 101.6 (Ar-*C*H^{Coumarin}), 56.0 (-O*C*H$_3^{Coumarin}$), 51.3 (-*C*H$_2^{Coumarin}$), 21.2 (-*C*H$_3^{Mes}$), 18.1 (-*C*H$_3^{Mes}$).

IR (ATR): $\tilde{\nu}$ (cm^{-1}) 3161 (w),3122 (w), 3104 (w), 3055 (w), 3039 (w), 2932 (w), 2916 (w), 2836 (w), 2178 (w), 2093 (w), 2082 (w), 2051 (w), 1725 (vs), 1615 (vs), 1569 (sh), 1554 (m), 1514 (w), 1488 (m), 1449 (m), 1428 (sh), 1395 (s), 1348 (w), 1321 (m), 1293 (vs), 1247 (s), 1206 (m), 1146 (vs), 1056 (w), 1035 (m), 1017 (m), 987 (w), 966 (w), 936 (w), 890 (m), 861 (m), 842 (s), 803 (w), 783 (w), 761 (m), 744 (w), 692 (w), 643 (m), 588 (w), 570 (m), 536 (w), 485 (w), 456 (w).

4.2.17 [Coum-Mes-NHC-AuC_6F_5] (21):

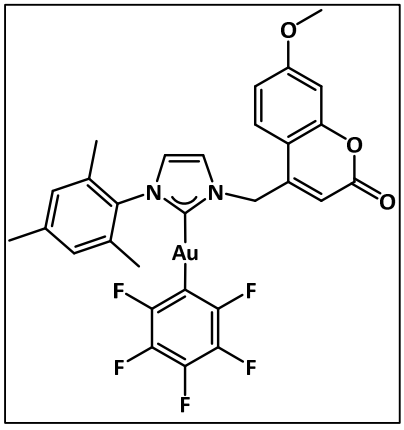

The imidazolium salt (**18**) (100 mg, 219.6 µmol, 1.00 eq.) and Ag_2O (25.5 mg, 109.8 µmol, 0.50 eq.) were suspended in 20 mL of DCM and stirred for 16 hours under exclusion of light. The resulting reaction mixture was filtered through a 0.22 µm PTFE membrane filter into a Schlenk flask containing solid [Au(tht)C_6F_5] (99.3 mg, 219.6 µmol, 1.00 eq.) and stirred for additional 16 hours. The precipitates formed were filtered off again to remove AgCl and the solvent was removed under reduced pressure. The residue was washed three times with 10 mL of *n*-pentane and the product was obtained as an off-white colored solid. Crystals suitable for SC-XRD analysis were obtained by the diffusion of *n*-pentane to a concentrated DCM solution. Yield: 130 mg (80 %).

Anal. calcd for $C_{29}H_{22}N_2O_3AuF_5$ (738.46 g/mol): C, 47.17; H, 3.00; N, 3.79 %. Found: C, 47.96; H, 3.86; N, 3.81 %.

^{1}H NMR (400 MHz, 298 K, $CDCl_3$): δ(ppm) 7.82 (d, J = 8.9 Hz, 1H, -C$H^{Coumarin}$), 7.24 (d, J = 2.0 Hz, 1H, -C$H^{Coumarin}$), 7.02 (d, J = 1.8 Hz, 1H, -C$H^{Coumarin}$), 7.00 (s, 2H, -C$H^{Imidazole}$), 6.92–6.79 (m, 2H, -CH^{Mes}), 5.97 (s, 1H, -C$H^{Coumarin}$), 5.71 (s, 2H, -C$H_2^{Coumarin}$), 3.87 (s, 3H, -OC$H_3^{Coumarin}$), 2.33 (s, 3H, -CH_3^{Mes}), 2.10 (s, 6H, -CH_3^{Mes}).

^{19}F{^{1}H} NMR (377 MHz, 298 K, $CDCl_3$): δ(ppm) -116.31 (d, J = 20.6 Hz), -159.81 (t, J = 20.0 Hz), -163.13 (t, J = 20.0 Hz).

^{13}C{^{1}H} NMR (100 MHz, 298 K, $CDCl_3$): δ(ppm) 191.0 (N-*C*-N), 163.5 (-*C*=O^{Coumarin}), 160.5 (Ar-*C*^{Coumarin}), 155.8 (Ar-*C*^{Coumarin}), 150.3 (d, J = 27.5 Hz, -C_6F_5), 149.3 (Ar-*C*^{Coumarin}), 148.0 (dd, J = 23.7, 11.4 Hz, -C_6F_5), 139.9 (Ar-*C*^{Mes}), 138.2 (dd, J = 32.0, 12.2 Hz, -C_6F_5), 135.7 (dd, J = 30.5, 12.2 Hz, -C_6F_5), 134.7 (Ar-*C*^{Mes}), 134.6 (Ar-*C*^{Mes}), 129.5 (Ar-*C*H^{Mes}), 125.0 (-*C*H^{Imidazole}), 123.6 (-*C*H^{Imidazole}), 120.9 (Ar-*C*^{Coumarin}), 113.0 (Ar-*C*H^{Coumarin}), 111.7 (Ar-*C*H^{Coumarin}), 110.6 (Ar-*C*^{Coumarin}), 101.5 (Ar-*C*H^{Coumarin}), 56.0 (-O*C*H$_3^{Coumarin}$), 51.1 (-*C*H$_2^{Coumarin}$), 21.2 (-*C*H$_3^{Mes}$), 18.0 (-*C*H$_3^{Mes}$).

IR (ATR): $\tilde{\nu}$(cm^{-1}) 3167 (w), 3135 (w), 3073 (w), 2976 (sh), 2922 (m), 2853 (w), 1697 (vs), 1607 (vs), 1559 (sh), 1501 (vs), 1451 (vs), 1436 (sh), 1399 (s), 1348 (s), 1326 (m), 1285 (s), 1267 (m), 1253 (s), 1225 (w), 1205 (s), 1160 (m), 1134 (s), 1058 (s), 1037 (m), 1020 (m), 992 (m), 969 (w), 948 (vs), 901 (w), 866 (m), 841 (s), 813 (w), 793 (m), 747 (m), 696 (w), 640 (w), 605 (w), 582 (w), 566 (w), 484 (w), 452 (w).

4.2.18 [Coum-Mes-NHC-AuMes] (22):

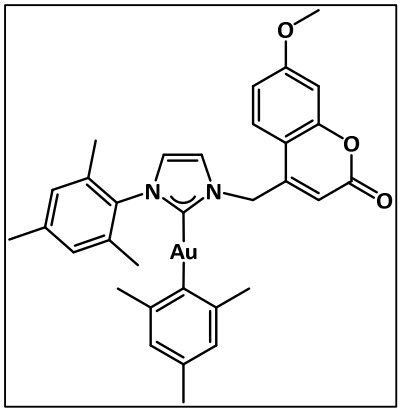

The imidazolium salt (**18**) (100 mg, 219.6 µmol, 1.00 eq.) and Ag_2O (25.5 mg, 109.8 µmol, 0.50 eq.) were suspended in 20 mL of DCM and stirred for 16 hours under exclusion of light. The resulting reaction mixture was filtered through a 0.22 µm PTFE membrane filter into a Schlenk flask containing solid mesityl gold(I) (69.4 mg, 219.6 µmol, 1.00 eq.) and stirred for additional 16 hours. The precipitates formed were filtered off again to remove AgCl and the solvent was removed under reduced pressure. The residue was washed three times with 10 mL of *n*-pentane and the product was obtained as an off-white colored solid. The crystals suitable for SC-XRD analysis were obtained from the concentrated DCM solution. Yield: 109 mg (72 %).

Anal. calcd for $C_{32}H_{33}N_2O_3Au$ (690.59 g/mol): C, 55.66; H, 4.82; N, 4.06 %. Found: C, 55.85; H, 4.86; N, 4.18 %.

^{1}H NMR (400 MHz, 298 K, $CDCl_3$): δ(ppm) 7.96 (d, *J* = 9.5 Hz, 1H, -C*H*^{Coumarin}), 7.14 (d, *J* = 1.8 Hz, 1H, -C*H*^{Coumarin}), 7.00–6.95 (m, 1H, -C*H*^{Coumarin}), 6.96 (d, *J* = 1.9 Hz, 1H, -C*H*^{Imidazole}), 6.95–6.87 (m, 1H, -C*H*^{Imidazole}), 6.88–6.81 (m, 2H, -C*H*^{Mes}), 6.75–6.70 (m, 2H, -C*H*^{Mes}), 6.05 (s, 1H, -C*H*^{Coumarin}), 5.74 (d, *J* = 1.0 Hz, 2H, -C*H*$_2^{Coumarin}$), 3.88 (s, 3H, -OC*H*$_3^{Coumarin}$), 2.33 (s, 3H, -C*H*$_3^{Mes}$), 2.17 (s, 6H, -C*H*$_3^{Mes}$), 2.15 (s, 3H, -C*H*$_3^{Mes}$), 2.08 (s, 6H, -C*H*$_3^{Mes}$).

^{13}C{^{1}H} NMR (100 MHz, 298 K, $CDCl_3$): δ(ppm) 198.7 (N-*C*-N), 163.4 (-*C*=O^{Coumarin}), 160.6 (Ar-*C*^{Coumarin}), 155.9 (Ar-*C*^{Coumarin}), 149.6 (Ar-*C*^{Coumarin}), 146.8 (Ar-*C*^{Mes}), 140.0 (Ar-*C*^{Mes}), 139.6 (Ar-*C*^{Mes}), 135.1 (Ar-*C*^{Mes}), 134.8 (Ar-*C*^{Mes}), 134.3 (Ar-*C*^{Mes}), 129.3 (Ar-*C*H^{Mes}), 126.0 (Ar-*C*H^{Mes}), 125.4 (-*C*H^{Imidazole}), 122.9 (-*C*H^{Imidazole}), 120.2 (Ar-*C*^{Coumarin}), 112.9 (Ar-*C*H^{Coumarin}), 112.2 (Ar-*C*H^{Coumarin}), 110.9 (Ar-*C*^{Coumarin}), 101.5 (Ar-*C*H^{Coumarin}), 56.0 (-O*C*H$_3^{Coumarin}$), 51.0 (-*C*H$_2^{Coumarin}$), 26.3 (-*C*H$_3^{Mes}$), 21.2 (-*C*H$_3^{Mes}$), 21.1 (-*C*H$_3^{Mes}$), 18.0 (-*C*H$_3^{Mes}$), 17.8 (-*C*H$_3^{Mes}$).

IR (ATR): $\tilde{\nu}$(cm^{-1}) 3171 (w), 3154 (w), 3122 (w), 3082 (w), 3006 (w), 2978 (w), 2961 (w), 2941 (w), 2917 (w), 2844 (w), 2577 (w), 2325 (w), 2238 (w), 2164 (w), 2126 (w), 2051 (w), 2012 (w), 1720 (vs), 1611 (vs), 1556 (s), 1515 (w), 1489 (w), 1430 (s), 1391 (w), 1346 (w), 1326 (m), 1290 (vs), 1266 (sh), 1246 (m), 1205 (m), 1146 (vs), 1091 (w), 1054 (w), 1035 (m), 1019 (m), 987 (w), 969 (w), 936 (w), 890 (w), 864 (sh), 848 (s), 809 (w), 781 (w), 744 (m), 715 (w), 701 (w), 696 (w), 639 (w), 587 (w), 569 (w), 541 (w), 485 (w), 452 (w).

4.2.19 [(Coum-Mes-NHC)$_2$Au][OTf] (23):

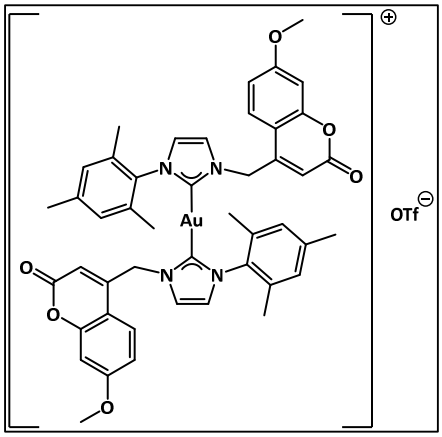

The imidazolium salt (**18**) (100 mg, 219.6 µmol, 1.00 eq.) and Ag_2O (25.5 mg, 109.8 µmol, 0.50 eq.) were suspended in 20 mL of DCM and stirred for 16 hours under exclusion of light. The resulting reaction mixture was filtered through a 0.22 µm PTFE membrane filter into a Schlenk flask containing solid mesityl gold(I) (69.4 mg, 219.6 µmol, 1.00 eq.) and stirred for additional 16 hours. The precipitates formed were filtered off again to remove AgCl and the solvent was removed under reduced pressure. The residue was washed three times with 10 mL of *n*-pentane and the product was obtained as an off-white

colored solid. Crystals suitable for SC-XRD analysis were obtained from the concentrated DCM solution. Yield: 152 mg (63 %).

HRMS (ESI): *m/z* calcd for $[C_{46}H_{44}AuN_4O_6]^+$: 945.2921 $[M]^+$; found: 945.2876.

Anal. calcd for $C_{47}H_{44}N_4O_9AuF_3S$ (1094.91 g/mol): C, 51.56; H, 4.05; N, 5.12 %. Found: C, 49.96; H, 4.07; N, 5.01 %.

^{1}H NMR (400 MHz, 298 K, $CDCl_3$): δ(ppm) 7.67 (d, *J* = 8.8 Hz, 2H, -C*H*^{Coumarin}), 7.30 (d, *J* = 1.8 Hz, 2H, -C*H*^{Coumarin}), 6.90 (d, *J* = 2.0 Hz, 2H, -C*H*^{Coumarin}), 6.83 (dd, *J* = 8.9, 2.6 Hz, 2H, -C*H*^{Imidazole}), 6.79 (d, *J* = 2.4 Hz, 2H, -C*H*^{Imidazole}), 6.77 (s, 4H, -C*H*^{Mes}), 5.60 (s, 4H, -C*H*$_2{}^{Coumarin}$), 5.36 (s, 2H, -C*H*^{Coumarin}), 3.90 (s, 6H, -OC*H*$_3{}^{Coumarin}$), 2.33 (s, 6H, -C*H*$_3{}^{Mes}$), 1.71 (s, 12H, -C*H*$_3{}^{Mes}$).

^{19}F{^{1}H} NMR (377 MHz, 298 K, $CDCl_3$): δ(ppm) -78.2 (s).

^{13}C{^{1}H} NMR (100 MHz, 298 K, $CDCl_3$): δ(ppm) 186.1 (N-*C*-N), 163.4 (-*C*=O^{Coumarin}), 160.3 (Ar-*C*^{Coumarin}), 155.2 (Ar-*C*^{Coumarin}), 150.8 (Ar-*C*^{Coumarin}), 140.0 (Ar-*C*^{Mes}), 134.7 (Ar-*C*^{Mes}), 134.2 (Ar-*C*^{Mes}), 129.3 (Ar-*C*H^{Mes}), 125.6 (-*C*H^{Imidazole}), 123.1 (-*C*H^{Imidazole}), 123.0 (Ar-*C*^{Coumarin}), 112.6 (Ar-*C*H^{Coumarin}), 110.5 (Ar-*C*H^{Coumarin}), 109.2 (Ar-*C*^{Coumarin}), 101.5 (Ar-*C*H^{Coumarin}), 56.0 (-O*C*H$_3{}^{Coumarin}$), 51.0 (-*C*H$_2{}^{Coumarin}$), 21.2 (-*C*H$_3{}^{Mes}$), 17.6 (-*C*H$_3{}^{Mes}$).

IR (ATR): $\tilde{\nu}$(cm^{-1}) 3162 (w), 3135 (w), 3018 (w), 2961 (w), 2938 (w), 2915 (w), 2852 (w), 1725 (vs), 1609 (vs), 1559 (m), 1513 (w), 1489 (m), 1456 (m), 1441 (m), 1402 (m), 1380 (w), 1348 (m), 1331 (m), 1273 (vs), 1251 (vs), 1222 (s), 1203 (s), 1150 (vs), 1130 (vs), 1059 (w), 1028 (vs), 984 (m), 889 (w), 858 (w), 840 (m), 831 (m), 812 (w), 784 (w), 758 (w), 746 (m), 699 (m), 635 (s), 572 (w), 516 (w), 483 (w), 454 (w).

4.2.20 [Coum-Mes-NHC-Au-CCPh] (24):

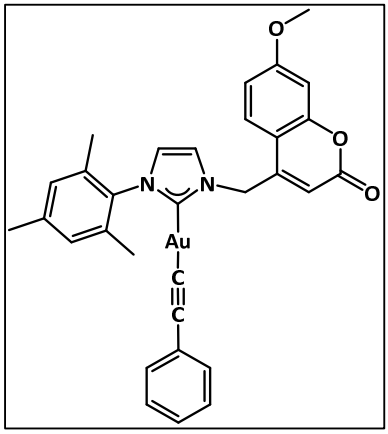

The NHC-AuCl complex (**19**) (100 mg, 164.8 µmol, 1.00 eq.), K_2CO_3 (34.2 mg, 247.2 µmol, 1.50 eq.) and phenyl acetylene (18.1 µL, 164.8 µmol, 1.00 eq.) were taken in a Schlenk flask and 15 mL of DCM was added to the mixture. The reaction mixture was stirred for 16 hours under exclusion of light. The resulting reaction mixture was filtered through a 0.22 µm PTFE membrane filter and the solvent was removed under reduced pressure. The residue was washed with 10 mL of

n-pentane and the product was obtained as an off-white colored solid. The crystals suitable for SC-XRD analysis were obtained from the concentrated DCM solution. Yield: 74 mg (64 %).

Anal. calcd for $C_{31}H_{27}N_2O_3Au$ (672.53 g/mol): C, 55.36; H, 4.05; N, 4.17 %. Found: C, 56.92; H, 4.81; N, 4.68 %.

^{1}H NMR (400 MHz, 298 K, $CDCl_3$): δ(ppm) 7.63 (d, J = 9.0 Hz, 1H, -C$H^{Coumarin}$), 7.37 (dd, J = 8.2, 1.6 Hz, 2H, -CH^{Ph}), 7.23–7.06 (m, 3H, -C$H^{Coumarin}$ and -C$H^{Imidazole}$), 6.97 (dd, J = 10.3, 1.6 Hz, 3H, -CH^{Ph}), 6.89 (dd, J = 8.6, 2.0 Hz, 3H, -CH^{Mes} and -C$H^{Coumarin}$), 5.82 (m, 1H, -C$H^{Coumarin}$), 5.71 (d, J = 25.9 Hz, 2H, -C$H_2^{Coumarin}$), 3.89 (s, 3H, -OC$H_3^{Coumarin}$), 2.34 (s, 3H, -CH_3^{Mes}), 2.06 (s, 6H, -CH_3^{Mes}).

^{13}C{^{1}H} NMR (100 MHz, 298 K, $CDCl_3$): δ(ppm) 190.1 (N-*C*-N), 163.6 (-*C*=O^{Coumarin}), 160.4 (Ar-*C*^{Coumarin}), 155.8 (Ar-*C*^{Coumarin}), 149.3 (Ar-*C*^{Coumarin}), 140.0 (Ar-*C*^{Mes}), 134.8 (Ar-*C*^{Mes}), 134.4 (Ar-*C*^{Mes}), 132.4 (Ar-*C*H^{Ph}), 129.8 (Ar-*C*H^{Mes}), 127.9 (Ar-*C*H^{Ph}), 126.5 (Ar-*C*H^{Ph}), 125.4 (Ar-*C*H^{Ph}), 124.7 (-*C*H^{Imidazole}), 123.6 (-*C*H^{Imidazole}), 120.9 (Ar-*C*^{Coumarin}), 113.2 (Ar-*C*H^{Coumarin}), 113.1 (Ar-*C*H^{Coumarin}), 111.2 (Ar-*C*^{Coumarin}), 105.1 (*C*≡C), 101.7 (C≡*C*), 101.6 (Ar-*C*H^{Coumarin}), 56.0 (-O*C*H$_3^{Coumarin}$), 51.3 (-*C*H$_2^{Coumarin}$), 21.3 (-*C*H$_3^{Mes}$), 18.0 (-*C*H$_3^{Mes}$).

IR (ATR): $\tilde{\nu}$(cm^{-1}) 3213 (w), 3161 (w), 3131 (w), 3048 (w), 2939 (w), 2918 (w), 2852 (w), 2843 (w), 2167 (w), 2113 (w), 2095 (w), 2053 (w), 2020 (w), 1993 (w), 1950 (w), 1716 (vs), 1609 (vs), 1558 (m), 1514 (m), 1485 (m), 1441 (m), 1397 (m), 1347 (m), 1327 (m), 1283 (s), 1264 (m), 1249 (m), 1205 (s), 1147 (m), 1133 (s), 1094 (w), 1054 (w), 1034 (m), 1020 (m), 986 (m), 969 (w), 935 (w), 917 (w), 892 (w), 853 (m), 839 (s), 807 (w), 783 (w), 762 (m), 744 (w), 732 (m), 694 (m), 646 (w), 636 (w), 587 (w), 564 (w), 531 (w), 485 (w), 449 (w).

4.2.21 [Coum-Mes-NHC-Au]$_2$ (25):

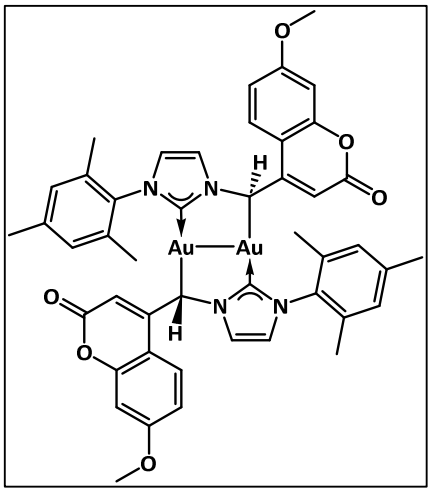

The NHC-AuCl complex (**19**) (100 mg, 164.8 µmol, 1.00 eq.) and KO*t*-Bu (20.3 mg, 181.3 µmol, 1.10 eq.) were taken in a Schlenk flask and dissolved in 20 mL of THF. The reaction mixture was stirred for 16 hours and the solvent was removed under reduced pressure. Then, 20 mL of DCM was added to the solid residue and filtered through a 0.22 µm PTFE membrane filter. The solvent was removed again under reduced pressure and a dark-yellow colored solid was obtained. The crystals suitable for SC-XRD analysis were obtained from the concentrated DCM solution. Yield: 71 mg (75 %).

Anal. calcd for $C_{46}H_{42}N_4O_6Au_2$ (1140.80 g/mol): C, 48.43; H, 3.71; N, 4.91 %. Found: C, 47.96; H, 3.97; N, 4.76 %.

^{1}H NMR (400 MHz, 298 K, $CDCl_3$): δ(ppm) 7.58 (d, J = 9.0 Hz, 2H, -C*H*^{Coumarin}), 6.98 (s, 2H, -C*H*^{Coumarin}), 6.94 (d, J = 1.8 Hz, 2H, -C*H*^{Imidazole}), 6.90 (d, J = 1.8 Hz, 2H, -C*H*^{Imidazole}), 6.76 (d, J = 2.6 Hz, 2H, -C*H*^{Mes}), 6.52 (s, 2H, -C*H*^{Mes}), 6.47 (dd, J = 8.9, 2.7 Hz, 2H, -C*H*^{Coumarin}), 5.27 (s, 2H, -C*H*^{Coumarin}), 5.05 (s, 2H, -C*H*^{Coumarin}), 3.92 (s, 6H, -OC*H*$_3^{Coumarin}$), 2.36 (s, 6H, -C*H*$_3^{Mes}$), 2.14 (s, 6H, -C*H*$_3^{Mes}$), 1.60 (s, 6H, -C*H*$_3^{Mes}$).

^{13}C{^{1}H} NMR (100 MHz, 298 K, $CDCl_3$): δ(ppm) 185.6 (N-*C*-N), 162.5 (-*C*=O^{Coumarin}), 161.8 (Ar-*C*^{Coumarin}), 154.6 (Ar-*C*^{Coumarin}), 138.8 (Ar-*C*^{Mes}), 135.3 (Ar-*C*^{Mes}), 135.1 (Ar-*C*^{Mes}), 129.2 (Ar-*C*^{Coumarin}), 128.9 (Ar-*C*H^{Mes}), 126.0 (-*C*H^{Imidazole}), 125.1 (-*C*H^{Imidazole}), 121.4 (Ar-*C*^{Coumarin}), 112.1 (Ar-*C*H^{Coumarin}), 111.4 (Ar-*C*H^{Coumarin}), 99.9 (Ar-*C*H^{Coumarin}), 98.8 (Ar-*C*H^{Coumarin}), 62.6 (-O*C*H$_3^{Coumarin}$), 55.7 (-*C*H^{Coumarin}), 21.2 (-*C*H$_3^{Mes}$), 18.3 (-*C*H$_3^{Mes}$), 17.9 (-*C*H$_3^{Mes}$).

IR (ATR): $\tilde{\nu}$(cm^{-1}) 3171 (w), 3154 (w), 3122 (w), 3082 (w), 3006 (w), 2978 (w), 2961 (w), 2941 (sh), 2917 (m), 2844 (w), 2611 (w), 2577 (w), 2325 (w), 2238 (w), 2164 (w), 2126 (w), 2051 (w), 2012 (w), 1720 (vs), 1611 (vs), 1556 (s), 1515 (w), 1489 (m), 1430 (s), 1391 (m), 1346 (sh), 1326 (m), 1290 (vs), 1266 (sh), 1246 (s), 1205 (s), 1146 (vs), 1091 (w), 1054 (w), 1035 (m), 1019 (m), 987 (w), 969 (w), 936 (w), 890 (w), 864 (sh), 848 (s), 809 (w), 781 (w), 744 (m), 715 (w), 701 (w), 696 (w), 639 (w), 587 (w), 569 (w), 541 (w), 485 (w), 452 (w).

4.2.22 [(Coum-Mes-NHC)$_2$AuI$_2$][I$_3$] (26):

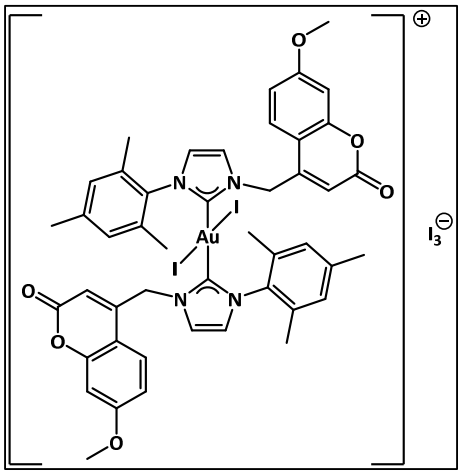

The NHC-AuCl complex (**19**) (100 mg, 164.8 µmol, 1.00 eq.) and iodine (I_2) (62.7 mg, 247.2 µmol, 1.50 eq.) were taken in a Schlenk flask and dissolved in 15 mL of DCM. The reaction mixture was stirred for 16 hours and filtered through a 0.22 µm PTFE membrane filter. The solvent was removed under reduced pressure and a dark-brown colored solid was obtained. The crystals suitable for SC-XRD analysis were obtained from the concentrated DCM solution. Yield: 92 mg (71 %).

HRMS (ESI): *m/z* calcd for $[C_{46}H_{44}AuI_2N_4O_6]^+$: 1199.1010 $[M]^+$; found: 1199.0890.

^{1}H NMR (400 MHz, 298 K, $CDCl_3$): δ(ppm) 7.61 (d, *J* = 8.9 Hz, 1H, -C*H*^{Coumarin}), 7.35 (s, 1H, -C*H*^{Coumarin}), 7.19 (s, 1H, -C*H*^{Coumarin}), 6.99 (s, 2H, -C*H*^{Mes}), 6.92 (dd, *J* = 8.8, 2.6 Hz, 1H, -C*H*^{Imidazole}), 6.86 (d, *J* = 2.4 Hz, 1H, -C*H*^{Imidazole}), 6.10 (bs, 1H, -C*H*^{Coumarin}), 5.67 (s, 2H, -C*H*$_2^{Coumarin}$), 3.90 (s, 3H, -OC*H*$_3^{Coumarin}$), 2.35 (s, 3H, -C*H*$_3^{Mes}$), 2.27 (bs, 6H, -C*H*$_3^{Mes}$).

^{13}C{^{1}H} NMR (100 MHz, 298 K, $CDCl_3$): δ(ppm) 163.7 (-*C*=O^{Coumarin}), 160.1 (Ar-*C*^{Coumarin}), 155.9 (Ar-*C*^{Coumarin}), 147.3 (Ar-*C*^{Coumarin}), 141.2 (Ar-*C*^{Coumarin}), 135.0 (Ar-*C*H^{Mes}), 131.7 (Ar-*C*H^{Mes}), 130.2 (Ar-*C*H^{Mes}), 125.2 (-*C*H^{Imidazole}), 124.7 (-*C*H^{Imidazole}), 113.2 (Ar-*C*H^{Coumarin}), 110.4 (Ar-*C*^{Coumarin}), 101.8 (Ar-*C*H^{Coumarin}), 56.1 (-O*C*H$_3^{Coumarin}$), 52.6 (-*C*H$_2^{Coumarin}$), 30.8 (-*C*H$_3^{Mes}$), 21.3 (-*C*H$_3^{Mes}$).

No signal for the carbenic carbon was observed in the spectrum.

IR (ATR): $\tilde{\nu}$(cm^{-1}) 3215 (w), 3194 (w), 3154 (w), 3113 (w), 3089 (w), 3034 (w), 3005 (w), 2962 (sh), 2921 (m), 2852 (w), 2730 (w), 1708 (vs), 1612 (vs), 1553 (s), 1512 (w), 1482 (w), 1459 (m), 1430 (m), 1398 (m), 1379 (sh), 1349 (w), 1322 (w), 1295 (vs), 1265 (sh), 1251 (m), 1205 (m), 1151 (vs), 1055 (w), 1037 (w), 1019 (m), 987 (w), 968 (w), 933 (w), 897 (w), 877 (w), 856 (sh), 843 (s), 811 (w), 784 (w), 764 (m), 743 (w), 701 (m), 651 (w), 640 (w), 586 (w), 571 (w), 537 (w), 484 (w), 450 (w).

4.2.23 [Coum-Mes-NHC-Rh(cod)Cl] (27):

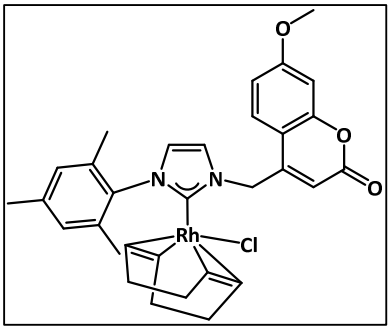

The imidazolium salt (**18**) (100 mg, 219.6 µmol, 1.00 eq.) and Ag_2O (25.5 mg, 109.8 µmol, 0.50 eq.) were suspended in 20 mL of DCM and stirred for 16 hours under exclusion of light. The resulting reaction mixture was filtered through a 0.22 µm PTFE membrane filter into a Schlenk flask containing solid chloro(1,5-cyclooctadiene)rhodium(I) dimer (54.1 mg, 109.8 µmol, 0.50 eq.) and stirred for additional 16 hours. The precipitates formed were filtered off again to remove AgCl and the solvent was removed under reduced pressure. The residue was washed three times with 10 mL of *n*-pentane and the product was obtained as an off-white colored solid. The crystals suitable for SC-XRD analysis were from the mixture of DCM and *n*-pentane. Yield: 113 mg (83 %).

Anal. calcd for $C_{31}H_{34}N_2O_3RhCl$ (620.98 g/mol): C, 59.96; H, 5.52; N, 4.51 %. Found: C, 60.14; H, 5.80; N, 4.47 %.

^{1}H NMR (400 MHz, 298 K, $CDCl_3$): δ(ppm) 7.88 (d, *J* = 8.8 Hz, 1H, -C*H*^{Coumarin}), 7.25 (dd, *J* = 17.6, 1.5 Hz, 1H, -C*H*^{Coumarin}), 7.12 (d, *J* = 1.9 Hz, 2H, -C*H*^{Imidazole}), 6.97 (dd, *J* = 8.8, 2.6 Hz, 1H, -C*H*^{Coumarin}), 6.94 (s, 1H, -C*H*^{Coumarin}), 6.89 (dd, *J* = 10.4, 2.2 Hz, 2H, -C*H*^{Mes}), 5.77–5.75 (m, 1 H, -C$H_2^{Coumarin}$), 5.34 (dd, *J* = 17.7, 1.7 Hz, 1H, -C$H_2^{Coumarin}$), 4.85–4.70 (m, 2H, -CH_2^{COD}), 3.92 (s, 3H, -OC$H_3^{Coumarin}$), 3.32–3.22 (m, 1H, -C*H*^{COD}), 3.00–2.97 (m, 1H, -C*H*^{COD}), 2.46 (s, 3H, -CH_3^{Mes}), 2.38 (s, 3H, -CH_3^{Mes}), 1.90 (s, 3H, -CH_3^{Mes}), 1.79–1.60 (m, 4H, -CH_2^{COD}), 1.58–1.36 (m, 4H, -CH_2^{COD}).

^{13}C{^{1}H} NMR (100 MHz, 298 K, $CDCl_3$): δ(ppm) 185.0 (d, $^1J_{CRh}$ = 51.9 Hz, N-*C*-N), 163.5 (-*C*=O^{Coumarin}), 161.0 (Ar-*C*^{Coumarin}), 155.6 (Ar-*C*^{Coumarin}), 152.8 (Ar-*C*^{Coumarin}), 139.2 (Ar-*C*^{Mes}), 137.0 (Ar-*C*^{Mes}), 135.9 (Ar-*C*^{Mes}), 134.4 (Ar-*C*^{Mes}), 129.8 (Ar-*C*H^{Mes}), 125.5 (Ar-*C*H^{Coumarin}), 124.1 (-*C*H^{Imidazole}), 122.0 (Ar-*C*^{Coumarin}), 112.9 (Ar-*C*H^{Coumarin}), 111.3 (Ar-*C*H^{Coumarin}), 109.7 (Ar-*C*^{Coumarin}), 101.5 (Ar-*C*H^{Coumarin}), 98.5 (d, *J* = 7.6 Hz, -*C*H^{COD}), 97.8 (d, *J* = 6.1 Hz, -*C*H^{COD}), 69.6 (d, $^1J_{CRh}$ = 15.3 Hz, -*C*H^{COD}), 68.8 (d, $^1J_{CRh}$ = 13.7 Hz), -*C*H^{COD}), 56.0 (-OC$H_3^{Coumarin}$), 51.5 (-*C*$H_2^{Coumarin}$), 33.7 (-*C*H_2^{COD}), 31.8 (-*C*H_2^{COD}), 28.9 (-*C*H_2^{COD}), 28.0 (-*C*H_2^{COD}), 21.2 (-*C*H_3^{Mes}), 19.8 (-*C*H_3^{Mes}), 18.1 (-*C*H_3^{Mes}).

IR (ATR): $\tilde{\nu}$(cm^{-1}) 3146 (w), 3118 (w), 3081 (w), 3065 (w), 3007 (w), 2983 (w), 2935 (m), 2910 (m), 2873 (m), 2829 (w), 2645 (), 2628 (w), 2580 (w), 2545 (w), 2075 (w), 2052 (w),

2005 (w), 1949 (w), 1722 (vs), 1608 (vs), 1554 (sh), 1512 (w), 1484 (w), 1465 (w), 1432 (w), 1397 (m), 1386 (m), 1345 (w), 1328 (m), 1280 (s), 1264 (sh), 1243 (w), 1207 (m), 1150 (m), 1131 (s), 1099 (w), 1044 (w), 1033 (w), 1020 (m), 985 (w), 961 (w), 889 (w), 851 (s), 812 (w), 794 (w), 780 (w), 756 (w), 744 (w), 706 (w), 637 (w), 589 (w), 561 (w), 480 (w), 449 (w).

4.2.24 [Coum-Mes-NHC-Ir(cod)Cl] (28):

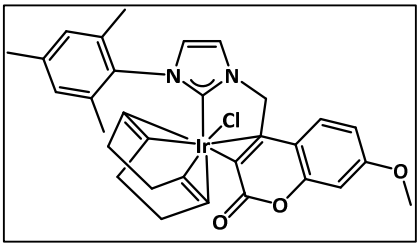

The imidazolium salt (**18**) (100 mg, 219.6 µmol, 1.00 eq.) and Ag_2O (25.5 mg, 109.8 µmol, 0.50 eq.) were suspended in 20 mL of DCM and stirred for 16 hours under exclusion of light. The resulting reaction mixture was filtered through a 0.22 µm PTFE membrane filter into a Schlenk flask containing solid chloro(1,5-cyclooctadiene)iridium(I) dimer (73.8 mg, 109.8 µmol, 0.50 eq.) and stirred for additional 16 hours. The precipitates formed were filtered off again to remove AgCl and the solvent was removed under reduced pressure. The residue was washed three times with 10 mL of *n*-pentane and the product was obtained as an off-white colored solid. The crystals suitable for SC-XRD analysis were from the mixture of DCM and *n*-pentane. Yield: 121 mg (78 %).

Anal. calcd for $C_{31}H_{34}N_2O_3IrCl$ (710.29 g/mol): C, 52.42; H, 4.83; N, 3.94 %. Found: C, 52.87; H, 4.88; N, 3.38 %.

^{1}H NMR (400 MHz, 298 K, $CDCl_3$): δ(ppm) No clear observations from the spectrum.

^{13}C{^{1}H} NMR (100 MHz, 298 K, $CDCl_3$): δ(ppm) No clear observations from the spectrum.

IR (ATR): $\tilde{\nu}$(cm^{-1}) 3174 (w), 3142 (w), 3111 (w), 3070 (w), 3048 (w), 3009 (w), 2950 (m), 2916 (m), 2876 (m), 2831 (m), 2759 (w), 2656 (w), 2584 (w), 2458 (w), 2324 (w), 2285 (w), 2250 (w), 2209 (w), 2165 (), 2143 (w), 2112 (w), 1727 (vs), 1618 (s), 1579 (m), 1507 (s), 1490 (w), 1455 (w), 1440 (w), 1425 (w), 1402 (w), 1382 (w), 1353 (w), 1334 (w), 1304 (m), 1278 (m), 1243 (m), 1215 (m),1190 (w), 1173 (m), 1156 (s), 1134 (vs), 1120 (s), 1045 (m), 1024 (m), 996 (m), 969 (w), 926 (w), 858 (m), 836 (m), 815 (w), 787 (m), 734 (w), 695 (w), 636 (w), 604 (m), 590 (w), 551 (w), 487 (w), 461 (w).

4.2.25 [(Coum-Mes-NHC)$_2$PtCl$_2$] (29):

The imidazolium salt (**18**) (100 mg, 219.6 µmol, 1.00 eq.) and Ag_2O (25.5 mg, 109.8 µmol, 0.50 eq.) were suspended in 20 mL of DCM and stirred for 16 hours under exclusion of light.

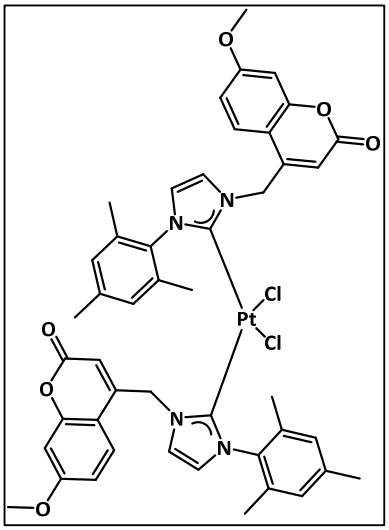

The resulting reaction mixture was filtered through a 0.22 µm PTFE membrane filter into a Schlenk flask containing solid platinum(II) dichloride ($PtCl_2$) (29.2 mg, 109.8 µmol, 0.50 eq.) and stirred for additional 16 hours. The precipitates formed were filtered off again to remove AgCl and the solvent was removed under reduced pressure. The residue was washed three times with 10 mL of *n*-pentane and the product was obtained as an off-white colored solid. The crystals suitable for SC-XRD analysis were from the mixture of DCM and *n*-pentane. Yield: 78 mg (70 %).

Anal. calcd for $C_{46}H_{44}N_4O_6PtCl_2$ (1014.86 g/mol): C, 54.44; H, 4.37; N, 5.52 %. Found: C, 54.35; H, 5.23; N, 3.33 %.

^{1}H NMR (400 MHz, 298 K, $CDCl_3$): δ(ppm) Due to low solubility, interpretable NMR could not be obtained.

^{13}C{^{1}H} NMR (100 MHz, 298 K, $CDCl_3$): δ(ppm) Due to low solubility, interpretable NMR could not be obtained.

IR (ATR): $\tilde{\nu}$(cm^{-1}) 3201 (w), 3162 (w), 3134 (w), 3109 (w), 3085 (w), 3052 (w), 3024 (w), 3004 (w), 2940 (w), 2918 (w), 2840 (w), 2812 (w), 2175 (w), 2125 (w), 2086 (w), 2038 (w), 2011 (w), 1983 (w), 1718 (vs), 1610 (vs), 1556 (m), 1512 (m), 1486 (m), 1441 (m), 1395 (m), 1346 (m), 1326 (m), 1282 (s), 1265 (m), 1246 (m), 1206 (m), 1146 (s), 1133 (s), 1052 (m), 1033 (m), 1021 (m), 988 (m), 968 (w), 934 (w), 891 (w), 837 (m), 811 (w), 784 (w), 742 (w), 717 (m), 668 (w), 637 (w), 576 (w), 537 (w), 486 (w), 450 (w).

4.2.26 [Coum-Mes-NHC-Pd(allyl)Cl] (30):

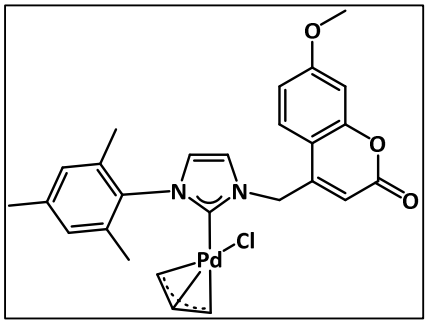

The imidazolium salt (**18**) (100 mg, 219.6 µmol, 1.00 eq.) and Ag_2O (25.5 mg, 109.8 µmol, 0.50 eq.) were suspended in 20 mL of DCM and stirred for 16 hours under exclusion of light. The resulting reaction mixture was filtered through a 0.22 µm PTFE membrane filter into a Schlenk flask containing solid allylpalladium(II) chloride dimer ([(η^3-C_3H_5)PdCl]$_2$) (40.2 mg, 109.8 µmol, 0.50 eq.) and stirred for additional 16 hours.

The precipitates formed were filtered off again to remove AgCl and the solvent was removed under reduced pressure. The residue was washed three times with 10 mL of *n*-pentane and the product was obtained as an off-white colored solid. The crystals suitable for SC-XRD analysis were from the mixture of DCM and *n*-pentane. Yield: 95 mg (78 %).

Anal. calcd for $C_{26}H_{27}N_2O_3PdCl$ (557.38 g/mol): C, 56.03; H, 4.88; N, 5.03 %. Found: C, 56.26; H, 5.12; N, 5.04 %.

^{1}H NMR (400 MHz, 298 K, $CDCl_3$): δ(ppm) 7.69 (d, *J* = 8.8 Hz, 1H, -C*H*^{Coumarin}), 7.17 (d, *J* = 1.9 Hz, 1H, -C*H*^{Coumarin}), 7.02 (d, *J* = 1.8 Hz, 1H, -C*H*^{Coumarin}), 6.96 (d, *J* = 11.8 Hz, 2H, -C*H*^{Mes}), 6.88 (dd, *J* = 8.8, 2.5 Hz, 1H, -C*H*^{Imidazole}), 6.84 (d, *J* = 2.4 Hz, 1H, -C*H*^{Imidazole}), 6.12 (d, *J* = 17.4 Hz, 1H, -C*H*^{Coumarin}), 5.76 (d, *J* = 15.6 Hz, 2H, -C*H*$_2^{Coumarin}$), 4.88 (bs, 1H, -C*H*^{Allyl}), 4.09 (dd, *J* = 22.9, 6.6 Hz, 2H, -C*H*$_2^{Allyl}$), 3.88 (s, 3H, -OC*H*$_3^{Coumarin}$), 2.99 (dd, *J* = 28.2, 12.4 Hz, 2H, -C*H*$_2^{Allyl}$), 2.33 (s, 3H, -C*H*$_3^{Mes}$), 2.24 (s, 3H, -C*H*$_3^{Mes}$), 2.08 (s, 3H, -C*H*$_3^{Mes}$).

^{13}C{^{1}H} NMR (100 MHz, 298 K, $CDCl_3$): δ(ppm) 184.2 (N-*C*-N), 163.3 (-*C*=O^{Coumarin}), 160.9 (Ar-*C*^{Coumarin}), 155.6 (Ar-*C*^{Coumarin}), 151.4 (Ar-*C*^{Coumarin}), 139.4 (Ar-*C*^{Mes}), 136.2 (Ar-*C*^{Mes}), 135.1 (Ar-*C*^{Mes}), 129.4 (Ar-*C*H^{Mes}), 125.4 (-*C*H^{Imidazole}), 123.2 (-*C*H^{Imidazole}), 122.2 (Ar-*C*^{Coumarin}), 112.8 (Ar-*C*H^{Coumarin}), 111.00 (Ar-*C*H^{Coumarin}), 110.1 (Ar-*C*^{Coumarin}), 101.4 (Ar-*C*H^{Coumarin}), 73.2 (-*C*H^{Allyl}), 56.0 (-O*C*H$_3^{Coumarin}$), 53.3 (-*C*H$_2^{Coumarin}$), 51.1 (-*C*H$_2^{Allyl}$), 49.9 (-*C*H$_2^{Allyl}$), 21.2 (-*C*H$_3^{Mes}$), 18.7 (-*C*H$_3^{Mes}$), 18.3 (-*C*H$_3^{Mes}$).

IR (ATR): $\tilde{\nu}$(cm^{-1}) 3128 (w), 3089 (w), 3052 (w), 3019 (w), 3006 (w), 2968 (w), 2954 (w), 2920 (m), 2855 (w), 2804 (w), 2758 (w), 2228 (w), 2213 (w), 2184 (w), 2169 (w), 2045 (w), 2008 (w), 1996 (w), 1948 (w), 1896 (w), 1834 (w), 1724 (vs), 1611 (vs), 1557 (m), 1510 (w), 1490 (m), 1437 (m), 1397 (s), 1346 (w), 1325 (m), 1289 (s), 1265 (m), 1237 (m), 1206, 1147 (vs), 1133 (sh), 1051 (w), 1031 (m), 1019 (w), 986 (w), 966 (w), 934 (w), 888 (s), 858 (w), 844 (w), 782 (w), 767 (w), 745 (w), 735 (w), 694 (w), 641 (w), 587 (w), 568 (w), 537 (w), 486 (w), 452 (w).

4.2.27 [Coum-Mes-NHC-Ru(*p*-cymene)Cl_2] (31):

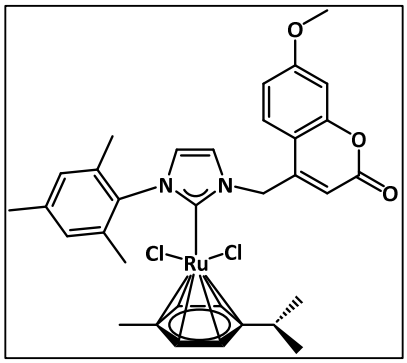

The imidazolium salt (**18**) (100 mg, 219.6 µmol, 1.00 eq.) and Ag_2O (25.5 mg, 109.8 µmol, 0.50 eq.) were suspended in 20 mL of DCM and stirred for 16 hours under exclusion of light. The resulting reaction mixture was filtered through a 0.22 µm PTFE membrane filter into a Schlenk flask containing solid (*p*-cymene)ruthenium(II) dichloride dimer ([Ru(*p*-cymene)Cl_2]$_2$) (67.2 mg, 109.8 µmol, 0.50 eq.) and stirred for additional 16 hours. The precipitates formed were filtered off again to remove AgCl and the solvent was removed under reduced pressure. The residue was washed three times with 10 mL of *n*-pentane and the product was obtained as an off-white colored solid. The crystals suitable for SC-XRD analysis were from the mixture of DCM and *n*-pentane. Yield: 118 mg (79 %).

Anal. calcd for $C_{33}H_{36}N_2O_3RuCl_2$ (680.63 g/mol): C, 58.23; H, 5.33; N, 4.12 %. Found: C, 58.67; H, 5.27; N, 3.74 %.

^{1}H NMR (400 MHz, 298 K, $CDCl_3$): δ(ppm) 7.61 (d, *J* = 8.8 Hz, 1H, -C*H*^{Coumarin}), 7.08 (dd, *J* = 10.1, 2.3 Hz, 1H, -C*H*^{Coumarin}), 7.05 (s, 2H, -C*H*^{Imidazole}), 6.98 (bs, 1H, -C*H*^{Coumarin}), 6.90 (d, *J* = 1.9 Hz, 1H, -C*H*^{Coumarin}), 6.84 (dd, *J* = 8.8, 2.5 Hz, 1H, -C*H*^{Mes}), 6.81 (d, *J* = 2.5 Hz, 1H, -C*H*^{Mes}), 6.08 (bs, 1H, -C$H_2^{Coumarin}$), 5.69 (s, 1H, -C$H_2^{Coumarin}$), 5.15 (d, *J* = 6.3 Hz, 2H, Ar-C*H*$^{p\text{-cymene}}$), 4.89 (d, *J* = 6.1 Hz, 2H, Ar-C*H*$^{p\text{-cymene}}$), 3.86 (s, 3H, -OC$H_3^{Coumarin}$), 2.50 (hept, *J* = 6.9 Hz, 1H, -C$H_3^{p\text{-cymene}}$), 2.38 (s, 3H, -CH_3^{Mes}), 2.20 (s, 6H, -CH_3^{Mes}), 1.74 (s, 3H, -C$H_3^{p\text{-cymene}}$), 0.99 (d, *J* = 7.0 Hz, 6H, -C$H_3^{p\text{-cymene}}$).

^{13}C{^{1}H} NMR (100 MHz, 298 K, $CDCl_3$): δ(ppm) 174.7 (N-*C*-N), 163.1 (-*C*=O^{Coumarin}), 161.4 (Ar-*C*^{Coumarin}), 155.3 (Ar-*C*^{Coumarin}), 149.2 (Ar-*C*^{Coumarin}), 140.0 (Ar-*C*^{Mes}), 137.9 (Ar-*C*^{Mes}), 136.7 (Ar-*C*^{Mes}), 134.4 (Ar-*C*^{Mes}), 129.3 (Ar-*C*^{Mes}), 125.6 (-*C*H^{Imidazole}), 124.7 (-*C*H^{Imidazole}), 123.0 (Ar-*C*^{Coumarin}), 112.7 (Ar-*C*H^{Coumarin}), 111.1 (Ar-*C*H^{Coumarin}), 108.7 (Ar-*C*^{Coumarin}), 105.5 (Ar-*C*H$^{p\text{-cymene}}$), 101.1 (Ar-*C*H^{Coumarin}), 93.8 (Ar-*C*H$^{p\text{-cymene}}$), 88.2 (Ar-*C*H$^{p\text{-cymene}}$), 85.0 (Ar-*C*H$^{p\text{-cymene}}$), 55.9 (-O*C*H$_3^{Coumarin}$), 53.6 (-*C*H$_2^{Coumarin}$), 30.5 (-*C*H$^{p\text{-cymene}}$), 22.3 (-*C*H$_3^{p\text{-cymene}}$), 21.3 (-*C*H$_3^{Mes}$), 19.1 (-*C*H$_3^{Mes}$), 18.0 (-*C*H$_3^{p\text{-cymene}}$), 17.9 (-*C*H$_3^{p\text{-cymene}}$).

IR (ATR): $\tilde{\nu}$(cm^{-1}) 3132 (w), 3086 (w), 3063 (w), 3046 (w), 3014 (w), 2992 (w), 2958 (w), 2916 (w), 2866 (w), 2840 (w), 2734 (w), 2659 (w), 2602 (w), 2188 (w), 2141 (w), 2105 (w), 2066 (w), 2066 (w), 2050 (w), 2019 (w), 1994 (w), 1983 (w), 1716 (vs), 1611 (vs), 1585 (m), 1559 (w), 1508 (m), 1487 (w), 1453 (m), 1427 (w), 1390 (m), 1375 (w), 1352 (m), 1325 (w), 1304 (w), 1281 (s), 1263 (s), 1242 (m), 1208 (m), 1193 (m), 1159 (m), 1133 (s), 1089 (w), 1041 (m), 1028 (w), 1002 (w), 985 (w), 964 (w), 928 (w), 893 (w), 839 (s), 795 (w), 752 (w), 728 (w), 695 (s), 675 (w), 637 (w), 597 (w), 570 (w), 530 (w), 485 (w), 459 (w).

4.2.28 [L^{Ph}thioamide] (32):

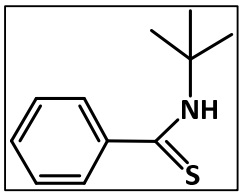

The *t*-butyl isothiocyanate (2.0 g, 17.36 mmol, 1.00 eq.) was dissolved in 25 mL THF and cooled to -78 °C. To the cooled solution, 3.0 M phenyl magnesiumbromide solution in diethyl ether (5.79 mL, 17.36mmol, 1.00 eq.) was added dropwise and stirred for 30 minutes. The reaction mixture was allowed to warm to ambient temperature and subsequently stirred overnight. The solvent was removed under reduced pressure and 25 mL of DCM was added to the resulting solid. The reaction mixture was hydrolyzed with 10 mL of water and the product was extracted three times with DCM. The organic phase was dried over $MgSO_4$ and after the removal of the solvent, the product was obtained as a pastel yellow solid. Yield: 2.87 g (85 %).

Anal. calcd for $C_{11}H_{15}NS$ (193.31 g/mol): C, 68.35; H, 7.82; N, 7.25; S 16.58 %. Found: C, 69.28; H, 7.36; N, 7.00; S, 16.12%.

^{1}H NMR (400 MHz, 298 K, $CDCl_3$): δ(ppm) 7.65 (m, 2H, -C*H*^{Ph}), 7.37 (m, 3H, -C*H*^{Ph}), 1.66 (s, 9H, -C$H_3^{t\text{-Bu}}$).

^{13}C{^{1}H} NMR (100 MHz, 298 K, $CDCl_3$): δ(ppm) 198.9 (-*C*(=S)-), 144.8 (Ar-*C*^{Ph}), 130.6 (Ar-*C*H^{Ph}), 128.5 (Ar-*C*H^{Ph}), 126.4 (Ar-*C*H^{Ph}), 56.2 (-*C*$(CH_3)_3$), 27.8 (-*C*$H_3^{t\text{-Bu}}$).

IR (ATR): $\tilde{\nu}$(cm^{-1}) 3326 (w), 3250 (vs), 3091 (w), 3078 (w), 3058 (m), 3043 (w), 3025 (m), 2996 (w), 2962 (s), 2918 (s), 2883 (m), 2735 (w), 2580 (w), 2440 (w), 2386 (w), 2049 (w), 2018 (w), 1953 (w), 1892 (w), 1804 (w), 1769, 1597 (w), 1578 (w), 1525 (vs), 1485 (s), 1476 (s), 1445 (vs), 1399 (s), 1385 (s), 1360 (vs), 1316 (w), 1286 (w), 1262 (s), 1211 (s), 1179 (m), 1076 (w), 1047 (w), 1028 (w), 1000 (vs), 963 (w), 921 (m), 881 (w), 838 (w), 775 (m), 753 (s), 717 (m), 690 (s), 677 (s), 633 (m), 622 (m), 609 (m), 516 (w), 455 (w).

4.2.29 [(L^{Ph}thioamidinate)$_2$Zn(TMEDA)] (33):

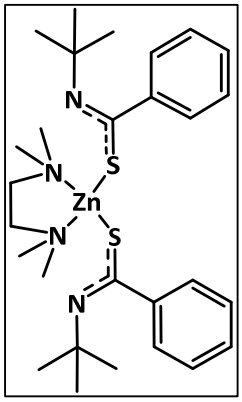

The ligand **32** (100 mg, 517.3 µmol, 1.00 eq.) and [$ZnMe_2$(TMEDA)] (54.7 mg, 258.7 µmol, 0.50 eq.) were dissolved in 10 mL of THF and stirred for 16 hours at ambient temperature. Thereafter, the solvent was removed under reduced pressure, and the resulting residue extracted with toluene. After removal of the solvent, the product was isolated as an off-white solid. The crystals suitable for SC-XRD analysis were obtained form a concentrated THF solution. Yield: 112 mg (77 %).

Anal. calcd for $C_{28}H_{44}N_4S_2Zn$ (566.19 g/mol): C, 59.40; H, 7.83; N, 9.90; S, 11.32 %. Found: C, 58.64; H, 7.68; N, 8.77; S, 11.05 %.

^{1}H NMR (400 MHz, 298 K, $CDCl_3$): δ(ppm) 7.98–7.90 (m, 3H, -C*H*^{Ph}), 7.34–7.31 (m, 5H, -C*H*^{Ph}), 7.30–7.26 (m, 2H, -C*H*^{Ph}), 2.39 (s, 4H, -C*H*$_2^{TMEDA}$), 1.55 (s, 12H, -C*H*$_3^{TMEDA}$), 1.21 (s, 18H, -C*H*$_3^{t\text{-Bu}}$).

^{13}C{^{1}H} NMR (100 MHz, 298 K, $CDCl_3$): δ(ppm) 198.8 (-*C*(=S)-), 149.0 (Ar-*C*^{Ph}), 130.6 (Ar-*C*H^{Ph}), 128.6 (Ar-*C*H^{Ph}), 128.5 (Ar-*C*H^{Ph}), 128.1 (Ar-*C*H^{Ph}), 127.7 (Ar-*C*H^{Ph}), 126.4 (Ar-*C*H^{Ph}), 125.6 (Ar-*C*H^{Ph}), 57.8 (-*C*H$_2^{TMEDA}$), 57.1 (-*C*H$_2^{TMEDA}$), 31.9 (-*C*H$_3^{t\text{-Bu}}$), 31.4 (-*C*H$_3^{t\text{-Bu}}$), 28.9 (-*C*H$_3^{TMEDA}$), 27.9 (-*C*H$_3^{TMEDA}$) .

IR (ATR): $\tilde{\nu}$(cm^{-1}) 3109 (w), 3076 (w), 3057 (w), 3015 (w), 2989 (m), 2962 (s), 2949 (s), 2916 (m), 2897 (m), 2852 (m), 2805 (w), 2789 (w), 2166 (w), 2144 (w), 2111 (w), 2080 (w), 2059 (w), 2038 (w), 2024 (w), 2003 (w), 1976 (w), 1581 (vs), 1562 (vs), 1464 (s), 1443 (s), 1397 (w), 1381 (m), 1356 (m), 1300 (w), 1285 (m), 1264 (w), 1232 (s), 1209 (s), 1194 (s), 1167 (m), 1123 (w), 1103 (w), 1073 (w), 1059 (w), 1043 (w), 1022 (m), 1004 (m), 951 (m), 940 (s), 920 (s), 909 (vs), 881 (m), 851 (), 797 (m), 770 (m), 751 (s), 696 (s), 649 (w), 636 (m), 620 (m), 583 (w), 489 (w), 469 (w), 438 (w).

4.2.30 [(L^{Ph}thioamidinate)$_4Zn_2$] (34):

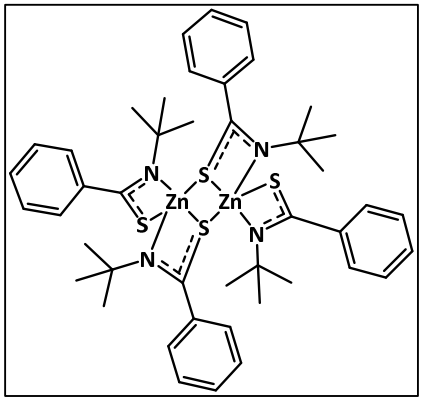

The ligand **32** (100 mg, 517.3 µmol, 1.00 eq.) and [$ZnPh_2$] (56.8 mg, 258.7 µmol, 0.50 eq.) were dissolved in 10 mL of THF and stirred for 16 hours at ambient temperature. Thereafter, the solvent was removed under reduced pressure and the resulting residue extracted with toluene. After removal of the solvent, the product was isolated as an off-white solid. Crystals suitable for SC-XRD analysis were obtained form a concentrated THF solution. Yield: 95 mg (82 %).

Anal. calcd for $C_{44}H_{56}N_4S_4Zn_2$ (899.96 g/mol): C, 58.72; H, 6.27; N, 6.23; S, 14.25 %. Found: C, 58.15; H, 6.19; N, 6.19; S, 14.03 %.

^{1}H NMR (400 MHz, 298 K, $CDCl_3$): δ(ppm) 7.38–7.31 (m, 12H, -C*H*^{Ph}), 7.33–7.26 (m, 8H, -C*H*^{Ph}), 1.22 (s, 36H, -C$H_3^{t\text{-Bu}}$).

^{13}C{^{1}H} NMR (100 MHz, 298 K, $CDCl_3$): δ(ppm) 194.7 (-*C*(=S)-), 140.9 (Ar-*C*^{Ph}), 128.5 (Ar-*C*H^{Ph}), 128.1 (Ar-*C*H^{Ph}), 125.6 (Ar-*C*H^{Ph}), 58.8 (-*C*$(CH_3)_3$), 31.4 (-*C*$H_3^{t\text{-Bu}}$).

IR (ATR): $\tilde{\nu}$(cm^{-1}) 3100 (w), 3058 (w), 3022 (w), 2966 (vs), 2929 (m), 2868 (w), 2822 (w), 2234 (w), 2188 (w), 2164 (w), 2049 (w), 2039 (w), 2023 (w), 1981 (w), 1901 (w), 1890 (m), 1601 (m), 1564 (s), 1534 (vs), 1477 (s), 1462 (m), 1444 (m), 1395 (m), 1364 (m), 1328 (s), 1307 (w), 1236 (s), 1213 (vs), 1158 (w), 1073 (w), 1041 (w), 1030 (w), 997 (w), 974 (s), 917 (m), 878 (w), 825 (w), 802 (w), 771 (s), 755 (s), 723 (vs), 697 (vs), 671 (w), 621 (w), 564 (w), 547 (w), 514 (sh), 498 (m).

4.2.31 [(L^{Ph}thioamidinate)(ATI)Zn] (35):

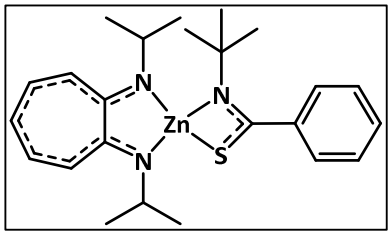

The ligand **32** (100 mg, 517.3 µmol, 1.00 eq.) and aminotroponiminato bis(trimethylsilyl) amidozinc [{ATI(*i*-Pr)$_2$}ZnN(TMS)$_2$] (221.9 mg, 517.3 µmol, 1.00 eq.) were dissolved in 10 mL of THF and stirred for 16 hours at ambient temperature. Thereafter, the solvent was removed under reduced pressure and the resulting residue extracted with toluene. After removal of

the solvent, the product was isolated as a yellow colored solid. The crystals suitable for SC-XRD analysis were obtained form a concentrated toluene solution. Yield: 163 mg (68 %).

Anal. calcd for $C_{24}H_{33}N_3SZn$ (460.99 g/mol): C, 62.53; H, 7.22; N, 9.12; S, 6.95 %. Found: C, 63.96; H, 7.29; N, 8.84; S, 6.28 %.

^{1}H NMR (400 MHz, 298 K, $CDCl_3$): δ(ppm) 7.38–7.32 (m, 2H, -C*H*^{Ph}), 7.32–7.27 (m, 3H, -C*H*^{Ph}), 7.03 (dd, *J* = 11.7, 9.0 Hz, 2H, -C*H*^{ATI}), 6.67 (s, 1H, -C*H*^{ATI}), 6.64 (s, 1H, -C*H*^{ATI}), 6.28 (t, *J* = 9.1 Hz, 1H, -C*H*^{ATI}), 4.11 (hep, *J* = 6.3 Hz, 2H, -C*H*^{ATI}), 1.49 (d, *J* = 21.5 Hz, 12H, -CH_3^{ATI}), 1.11 (s, 9H, -C$H_3^{t\text{-Bu}}$).

^{13}C{^{1}H} NMR (100 MHz, 298 K, $CDCl_3$): δ(ppm) 194.3 (-*C*(=S)-), 159.9 (Ar-*C*H^{ATI}), 142.2 (Ar-*C*^{Ph}), 134.5 (Ar-*C*H^{Ph}), 127.9 (Ar-*C*^{ATI}), 127.8 (Ar-*C*H^{Ph}), 125.7 (Ar-*C*H^{Ph}), 116.3 (Ar-*C*H^{ATI}), 111.7 (Ar-*C*H^{ATI}), 57.9 (-*C*$(CH_3)_3$), 48.6 (-*C*H^{ATI}), 31.9 (-*C*$H_3^{t\text{-Bu}}$), 23.8 (-*C*H_3^{ATI}), 23.6 (-*C*H_3^{ATI}).

IR (ATR): $\tilde{\nu}$(cm^{-1}) 3095 (w), 3078 (w), 3058 (w), 3040 (w), 2994 (w), 2964 (vs), 2924 (m), 2866 (m), 2742 (w), 2660 (w), 2510 (w), 2495 (w), 2469 (w), 2168 (w), 2124 (w), 2051 (w), 2038 (w), 2003 (w), 1986 (w), 1974 (w), 1934 (w), 1906 (w), 1592 (s), 1529 (s), 1501 (vs), 1481 (m), 1469 (s), 1441 (w), 1414 (vs), 1376 (vs), 1362 (s), 1308 (w), 1265 (vs), 1228 (vs), 1216 (s), 1156 (m), 1123 (w), 1069 (m), 1042 (w), 1029 (w), 998 (w), 977 (s), 948 (m), 916 (w), 884 (w), 872 (w), 852 (w), 824 (w), 798 (w), 757 (m), 723 (s), 699 (m), 611 (w), 581 (w), 535 (w), 524 (w), 503 (w), 478 (w), 420 (w).

4.2.32 [(L^{Ph}thioamidinate)$_6$Sm$_2$] (36):

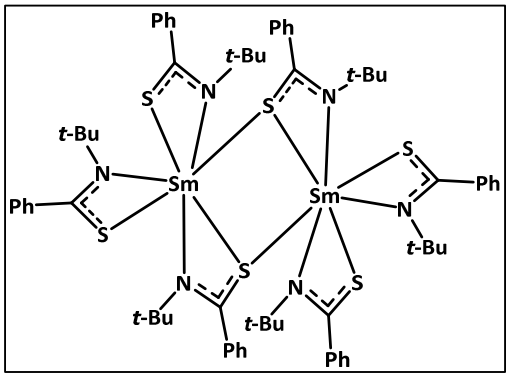

The ligand **32** (100 mg, 517.3 µmol, 3.00 eq.) and samarium tris{bis(trimethylsilyl)amide} [Sm(BTSA)$_3$] (108.9 mg, 172.4 µmol, 1.00 eq.) were dissolved in 10 mL of THF and stirred for 16 hours at ambient temperature. Thereafter, the solvent was removed under reduced pressure and the resulting residue extracted with toluene. After removal of the solvent, the product was isolated as a light yellow solid. The crystals suitable for SC-XRD analysis were obtained form a concentrated toluene solution. Yield: 94 mg (75 %).

Anal. calcd for $C_{66}H_{84}N_6S_6Sm_2$ (1454.52 g/mol): C, 54.50; H, 5.82; N, 5.78; S, 13.22 %. Found: C, 55.63; H, 5.96; N, 5.17; S, 12.92 %.

^{1}H NMR (400 MHz, 298 K, $CDCl_3$): δ(ppm) 7.67–7.64 (m, 10H, -C*H*^{Ph}), 7.42–7.33 (m, 20H, -C*H*^{Ph}), 1.66 (s, 54H, -C$H_3^{t\text{-Bu}}$).

^{13}C{^{1}H} NMR (100 MHz, 298 K, $CDCl_3$): δ(ppm) 199.0 (-*C*(=S)-), 149.5 (Ar-*C*^{Ph}), 130.6 (Ar-*C*H^{Ph}), 128.6 (Ar-*C*H^{Ph}), 126.5 (Ar-*C*H^{Ph}), 58.5 (-*C*$(CH_3)_3$), 27.9 (-*C*$H_3^{t\text{-Bu}}$).

IR (ATR): $\tilde{\nu}$(cm^{-1}) 3453 (w), 3441 (w), 3413 (w), 3388 (w), 3331 (w), 3301 (w), 3251 (w), 3194 (w), 3118 (w), 3076 (w), 3058 (w), 3024 (w), 2964 (vs), 2929 (s), 2867 (s), 2741 (m), 2705 (w), 2197 (w), 2177 (w), 2163 (w), 2119 (w), 2050 (w), 2030 (w), 1982 (w), 1971 (w), 1934 (w), 1888 (w), 1804 (w), 1758 (w), 1681 (w), 1598 (w), 1545 (sh), 1519 (vs), 1476 (vs), 1446 (s), 1397 (m), 1387 (sh), 1361 (vs), 1297 (w), 1263 (m), 1232 (s), 1198 (vs), 1156 (sh), 1071 (w), 1042 (w), 1029 (m), 1001 (m), 971 (s), 962 (s), 911 (w), 882 (w), 841 (w), 766 (m), 749 (m), 718 (s), 696 (s), 633 (w), 609 (w), 562 (w), 511 (w), 480 (w).

4.2.33 [(L^{Ph}thioamidinate)$_3$Y] (37):

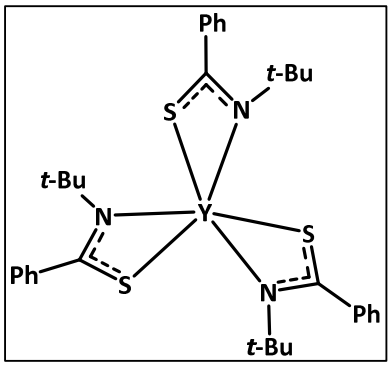

The ligand **32** (100 mg, 517.3 µmol, 3 eq.) and yttrium tris{bis(trimethylsilyl)amide} [Y(BTSA)$_3$] (98.3 mg, 172.4 µmol, 1 eq.) were dissolved in 10 mL of THF and stirred for 16 hours at ambient temperature. Thereafter, the solvent was removed under reduced pressure and the resulting residue extracted with toluene. After removal of the solvent, the product was isolated as light yellow solid. The crystals suitable for SC-XRD analysis were obtained form a concentrated toluene solution. Yield: 90 mg (78 %).

Anal. calcd for $C_{33}H_{42}N_3S_3Y$ (656.81 g/mol): C, 59.53; H, 6.36; N, 6.31; S, 14.45 %. Found: C, 59.28; H, 6.27; N, 5.43; S, 14.86 %.

^{1}H NMR (400 MHz, 298 K, $CDCl_3$): δ(ppm) 7.37–7.28 (m, 10H, -C*H*^{Ph}), 7.26–7.23 (m, 5H, -C*H*^{Ph}), 1.33 (s, 27H, -C$H_3^{t\text{-Bu}}$).

^{13}C{^{1}H} NMR (100 MHz, 298 K, $CDCl_3$): δ(ppm) 195.3 (-*C*(=S)-), 144.5 (Ar-*C*^{Ph}), 128.1 (Ar-*C*H^{Ph}), 126.4 (Ar-*C*H^{Ph}), 125.0 (Ar-*C*H^{Ph}), 59.2 (-*C*$(CH_3)_3$), 31.9 (-*C*$H_3^{t\text{-Bu}}$).

IR (ATR): $\tilde{\nu}$(cm^{-1}) 3384 (w), 3251 (w), 3075 (w), 3058 (w), 3024 (w), 2993 (m), 2965 (s), 2931 (m), 2908 (m), 2864 (m), 2455 (w), 2164 (w), 2118 (w), 2104 (w), 1992 (w), 1906 (w),

1597 (w), 1574 (w), 1524 (vs), 1477 (vs), 1463 (s), 1442 (s), 1396 (m), 1380 (m), 1362 (vs), 1263 (w), 1236 (s), 1199 (vs), 1159 (m), 1072 (m), 1040 (m), 1029 (m), 999 (), 968 (s), 916 (m), 908 (m), 884 (w), 871 (w), 766 (m), 752 (s), 720 (s), 696 (s), 673 (w), 571 (w), 566 (w), 512 (w), 480 (w).

5. Crystal structure measurements

5.1 Data collection and refinement

A suitable crystal was covered in mineral oil (Aldrich) and mounted on a glass fiber. The crystal was transferred directly to the cold stream of a *STOE* IPDS 2 (150 or 200 K) or a *STOE* StadiVari (100, 130, 150, 180 or 210 K) diffractometer. All structures were solved by using the program SHELXS/T[438-439] and Olex2.[440] The remaining non-hydrogen atoms were located from successive difference Fourier map calculations and Olex2. The refinements were carried out by using full-matrix least-squares techniques on F^2 by using the program SHELXL. The H-atoms were introduced into the geometrically calculated positions (SHELXL procedures) unless otherwise stated and refined riding on the corresponding parent atoms. In each case, the locations of the largest peaks in the final difference Fourier map calculations, as well as the magnitude of the residual electron densities, were of no chemical significance. Summary of the crystal data, data collection and refinement for compounds are given in section 5.2.

5.2 Crystal data

5.2.1 [{$Ph_2PC{\equiv}CC(NDipp)_2$}$Li(thf)_3$] (1)

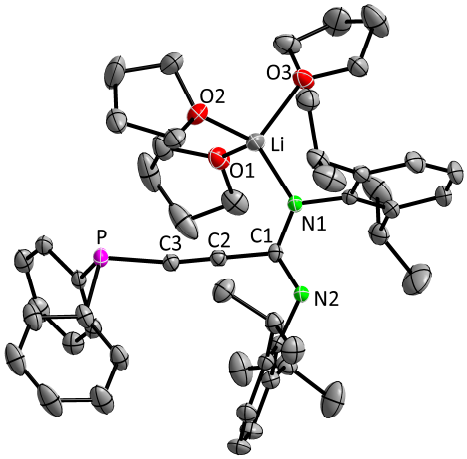

Empirical formula	$C_{51}H_{68}LiN_2O_3P$
Formula weight	794.98
Temperature/K	100
Crystal system	monoclinic
Space group	$P2_1/n$
a/Å	11.8389(2)
b/Å	18.8024(5)
c/Å	20.9064(4)
α/°	
β/°	97.0110(10)
γ/°	
Volume/Å^3	4618.96(17)
Z	4
ρ_{calc}/g/cm^3	1.143
μ/mm^{-1}	0.102
F(000)	1720
Radiation	MoK_α (λ = 0.71073)
2Θ range for data collection/°	3.926 to 57.846
Index ranges	-15 ≤ h ≤ 15, -24 ≤ k ≤ 24, -28 ≤ l ≤ 25
Reflections collected	45200
Independent reflections	10968 [R_{int} = 0.0204, R_{sigma} = 0.0149]
Data/restraints/parameters	10968/948/669
Goodness-of-fit on F^2	1.024
Final R indexes [I>=2σ (I)]	R_1 = 0.0392, wR_2 = 0.1021
Final R indexes [all data]	R_1 = 0.0476, wR_2 = 0.1075
Largest diff. peak/hole / e Å^{-3}	0.48/-0.34

5.2.2 [{$Ph_2PC{\equiv}CC(NDipp)_2\}_2Au_2$] (3)

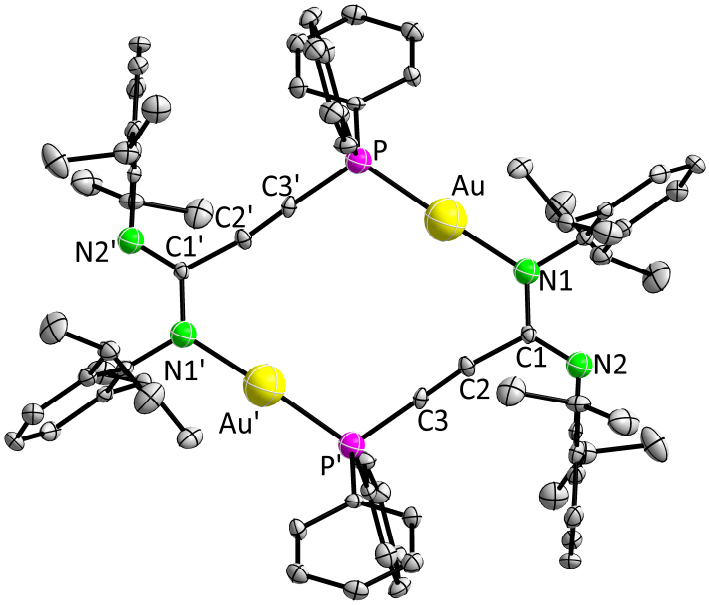

Empirical formula	$C_{90}H_{112}Au_2N_4O_3P_2$
Formula weight	1753.7
Temperature/K	100
Crystal system	monoclinic
Space group	$P2_1/c$
a/Å	11.9591(5)
b/Å	17.3241(8)
c/Å	19.6705(10)
α/°	
β/°	102.312(4)
γ/°	
Volume/Å^3	3981.6(3)
Z	2
ρ_{calc}/g/cm^3	1.463
μ/mm^{-1}	3.772
F(000)	1784
Radiation	MoK_α (λ = 0.71073)
2Θ range for data collection/°	4.204 to 63.596
Index ranges	-17 ≤ h ≤ 16, -25 ≤ k ≤ 25, -26 ≤ l ≤ 26
Reflections collected	56241
Independent reflections	11689 [R_{int} = 0.0402, R_{sigma} = 0.0345]
Data/restraints/parameters	11689/69/486
Goodness-of-fit on F^2	1.057
Final R indexes [I>=2σ (I)]	R_1 = 0.0343, wR_2 = 0.0741
Final R indexes [all data]	R_1 = 0.0533, wR_2 = 0.0927
Largest diff. peak/hole / e Å^{-3}	2.10/-1.01

5.2.3 [{(AuCl)Ph_2PC≡CC(NDipp)$_2$}$_2$$Cu_2$] (5)

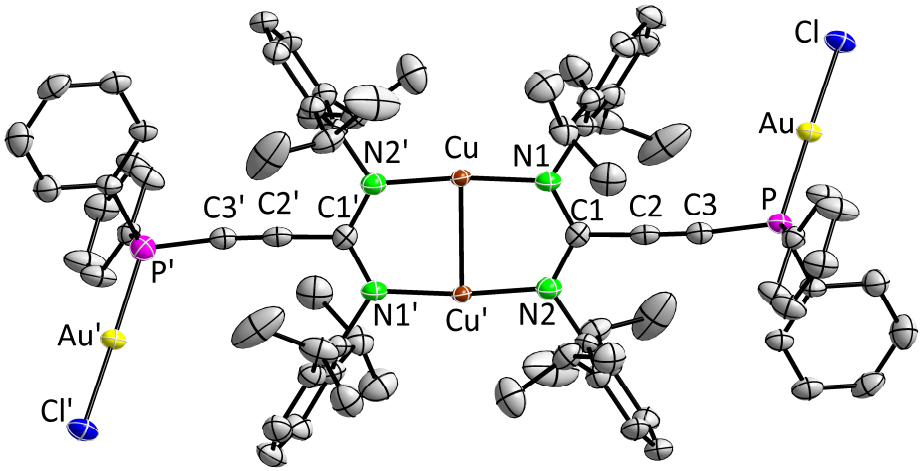

Empirical formula	$C_{84}H_{100}Au_2Cl_{14}Cu_2N_4P_2$
Formula weight	2244.93
Temperature/K	100
Crystal system	monoclinic
Space group	$P2_1/n$
a/Å	15.2796(4)
b/Å	14.2613(3)
c/Å	22.0976(6)
α/°	
β/°	108.539(2)
γ/°	
Volume/Å^3	4565.3(2)
Z	2
ρ_{calc}/g/cm^3	1.633
μ/mm^{-1}	4.152
F(000)	2232
Radiation	MoK_α (λ = 0.71073)
2Θ range for data collection/°	3.454 to 57.852
Index ranges	-13 ≤ h ≤ 20, -18 ≤ k ≤ 18, -30 ≤ l ≤ 26
Reflections collected	34757
Independent reflections	10725 [R_{int} = 0.0383, R_{sigma} = 0.0578]
Data/restraints/parameters	10725/150/553
Goodness-of-fit on F^2	1.069
Final R indexes [I>=2σ (I)]	R_1 = 0.0457, wR_2 = 0.1094
Final R indexes [all data]	R_1 = 0.0734, wR_2 = 0.1164
Largest diff. peak/hole / e Å^{-3}	1.02/-1.02

5.2.4 [{(AuC$_6$F$_5$)Ph$_2$PC≡CC(NDipp)$_2$}$_2$Cu$_2$] (6)

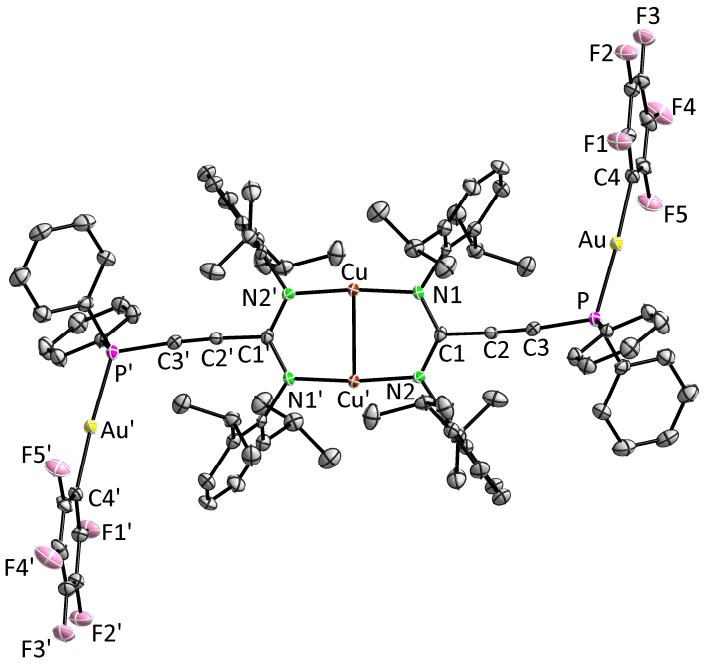

Empirical formula	$C_{94}H_{96}Au_2Cl_8Cu_2F_{10}N_4P_2$
Formula weight	2338.3
Temperature/K	110
Crystal system	monoclinic
Space group	$P2_1/c$
a/Å	15.9662(7)
b/Å	16.1637(6)
c/Å	19.2750(9)
α/°	
β/°	107.022(4)
γ/°	
Volume/Å^3	4756.4(4)
Z	2
ρ_{calc}/g/cm^3	1.633
μ/mm^{-1}	3.841
F(000)	2320
Radiation	MoK$_\alpha$ (λ = 0.71073)
2Θ range for data collection/°	3.352 to 62.64
Index ranges	-23 ≤ h ≤ 23, -21 ≤ k ≤ 23, -27 ≤ l ≤ 27
Reflections collected	38872
Independent reflections	13305 [R_{int} = 0.0338, R_{sigma} = 0.0529]
Data/restraints/parameters	13305/0/558
Goodness-of-fit on F^2	1.031
Final R indexes [I>=2σ (I)]	R_1 = 0.0376, wR_2 = 0.0759
Final R indexes [all data]	R_1 = 0.0679, wR_2 = 0.0868
Largest diff. peak/hole / e Å^{-3}	1.20/-0.80

5.2.5 [{(AuBr)Ph_2PC≡CC(NDipp)$_2$}$_2$$Cu_2$] (7)

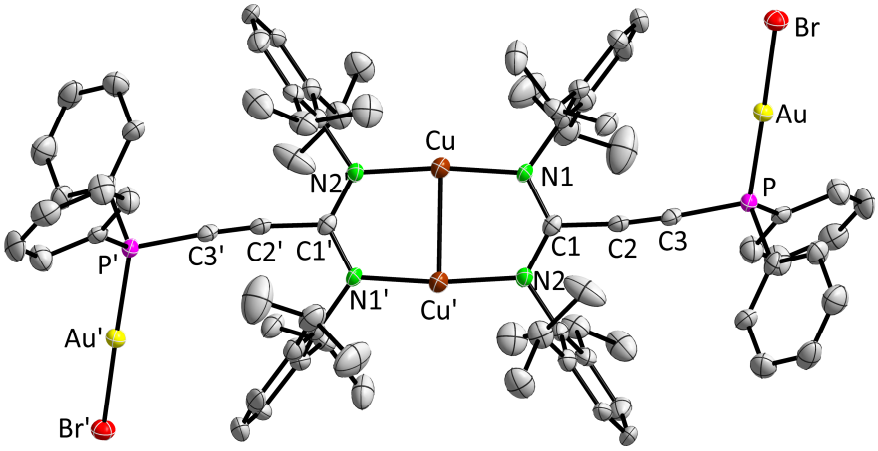

Empirical formula	$C_{82}H_{92}Au_2Br_2Cl_{12}Cu_2N_4P_2$
Formula weight	2301.76
Temperature/K	100
Crystal system	monoclinic
Space group	$P2_1/n$
a/Å	13.8145(5)
b/Å	13.5491(8)
c/Å	24.6139(9)
α/°	
β/°	102.118(3)
γ/°	
Volume/Å^3	4504.4(4)
Z	2
ρ_{calc}/g/cm^3	1.697
μ/mm^{-1}	5.035
F(000)	2264
Radiation	MoK_α (λ = 0.71073)
2Θ range for data collection/°	5.822 to 50.5
Index ranges	-15 ≤ h ≤ 16, -16 ≤ k ≤ 15, -29 ≤ l ≤ 20
Reflections collected	26703
Independent reflections	8133 [R_{int} = 0.0563, R_{sigma} = 0.0891]
Data/restraints/parameters	8133/110/487
Goodness-of-fit on F^2	0.944
Final R indexes [I>=2σ (I)]	R_1 = 0.0421, wR_2 = 0.0884
Final R indexes [all data]	R_1 = 0.0765, wR_2 = 0.0944
Largest diff. peak/hole / e Å^{-3}	1.41/-1.87

5.2.6 [{(AuI)Ph_2PC≡CC(NDipp)$_2$}$_2$$Cu_2$] (8)

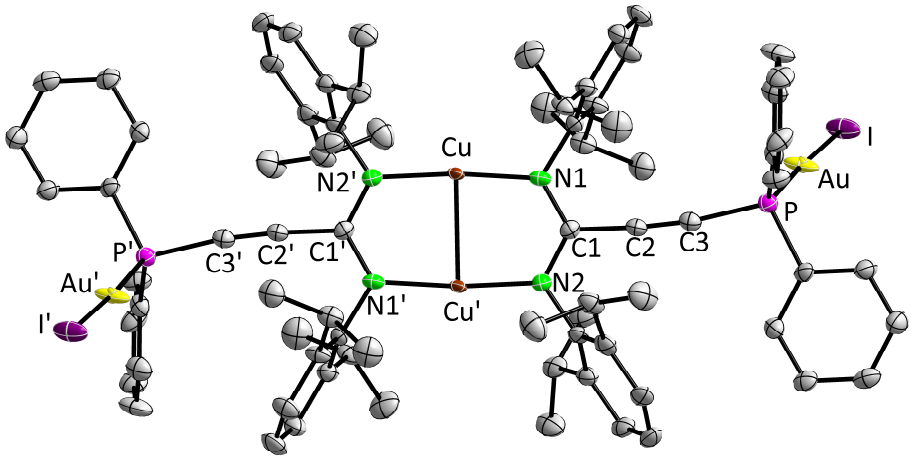

Empirical formula	$C_{86}H_{104}Au_2Cu_2I_2N_4O_2P_2$
Formula weight	2062.48
Temperature/K	100
Crystal system	monoclinic
Space group	$P2_1/n$
a/Å	13.2984(4)
b/Å	24.0130(11)
c/Å	13.3873(5)
α/°	
β/°	103.945(3)
γ/°	
Volume/Å^3	4149.0(3)
Z	2
ρ_{calc}/g/cm^3	1.651
μ/mm^{-1}	4.861
F(000)	2032
Radiation	MoK_α (λ = 0.71073)
2Θ range for data collection/°	3.564 to 57.892
Index ranges	-18 ≤ h ≤ 16, -26 ≤ k ≤ 31, -17 ≤ l ≤ 17
Reflections collected	24324
Independent reflections	9364 [R_{int} = 0.0322, R_{sigma} = 0.0605]
Data/restraints/parameters	9364/258/481
Goodness-of-fit on F^2	0.952
Final R indexes [I>=2σ (I)]	R_1 = 0.0323, wR_2 = 0.0627
Final R indexes [all data]	R_1 = 0.0523, wR_2 = 0.0652
Largest diff. peak/hole / e Å^{-3}	1.38/-1.09

5.2.7 [{(AuMes)$Ph_2PC{\equiv}CC(NDipp)_2\}_2Cu_2$] (9)

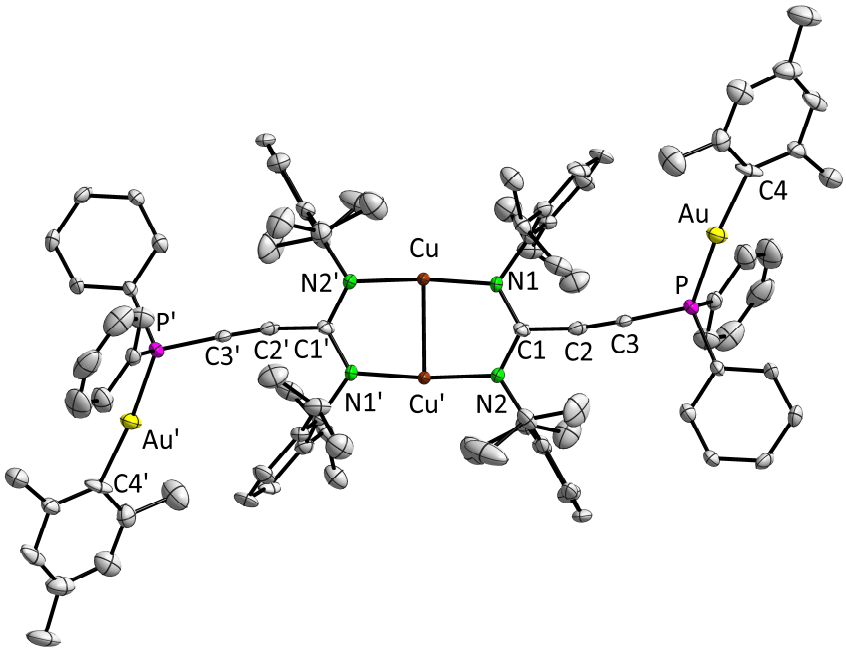

Empirical formula	$C_{96}H_{110}Au_2Cu_2N_4P_2$
Formula weight	1902.83
Temperature/K	100
Crystal system	triclinic
Space group	$P\bar{1}$
a/Å	10.4565(4)
b/Å	11.3634(4)
c/Å	18.6003(7)
α/°	87.597(3)
β/°	81.717(3)
γ/°	78.425(3)
Volume/Å^3	2142.39(14)
Z	1
ρ_{calc}/g/cm^3	1.475
μ/mm^{-1}	3.988
F(000)	960
Radiation	MoK_α (λ = 0.71073)
2*Θ* range for data collection/°	3.658 to 58.216
Index ranges	-14 ≤ h ≤ 13, -14 ≤ k ≤ 15, -24 ≤ l ≤ 24
Reflections collected	23208
Independent reflections	9893 [R_{int} = 0.0282, R_{sigma} = 0.0456]
Data/restraints/parameters	9893/259/505
Goodness-of-fit on F^2	1.025
Final *R* indexes [*I*>=2*σ* (*I*)]	R_1 = 0.0361, wR_2 = 0.0787
Final *R* indexes [all data]	R_1 = 0.0571, wR_2 = 0.0847
Largest diff. peak/hole / e Å^{-3}	1.44/-0.77

5.2.8 [{(Rh(cod)Cl)$Ph_2PC{\equiv}CC(NDipp)_2\}_2Cu_2$] (10)

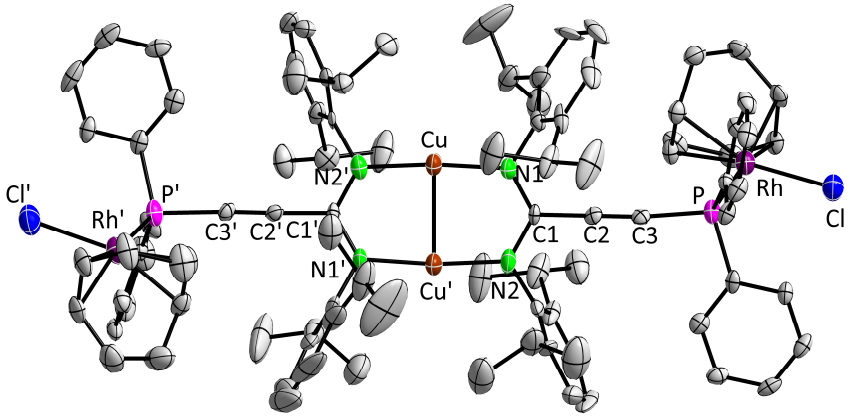

Empirical formula	$C_{188}H_{224}Cl_4Cu_4N_8P_4Rh_4$
Formula weight	3527.22
Temperature/K	110
Crystal system	triclinic
Space group	$P\bar{1}$
a/Å	13.6481(5)
b/Å	16.6555(6)
c/Å	19.1914(6)
α/°	101.518(3)
β/°	94.964(3)
γ/°	94.822(3)
Volume/Å^3	4235.6(3)
Z	1
ρ_{calc}/g/cm^3	1.383
μ/mm^{-1}	1.027
F(000)	1832
Radiation	MoK_α (λ = 0.71073)
2Θ range for data collection/°	3.65 to 60.284
Index ranges	-17 ≤ h ≤ 18, -22 ≤ k ≤ 22, -25 ≤ l ≤ 26
Reflections collected	60720
Independent reflections	20613 [R_{int} = 0.1823, R_{sigma} = 0.1792]
Data/restraints/parameters	20613/0/971
Goodness-of-fit on F^2	1.025
Final R indexes [I>=2σ (I)]	R_1 = 0.0720, wR_2 = 0.1485
Final R indexes [all data]	R_1 = 0.1707, wR_2 = 0.1893
Largest diff. peak/hole / e Å^{-3}	1.64/-0.98

5.2.9 [{(Ir(cod)Cl)Ph_2PC≡CC(NDipp)$_2$}$_2$$Cu_2$] (11)

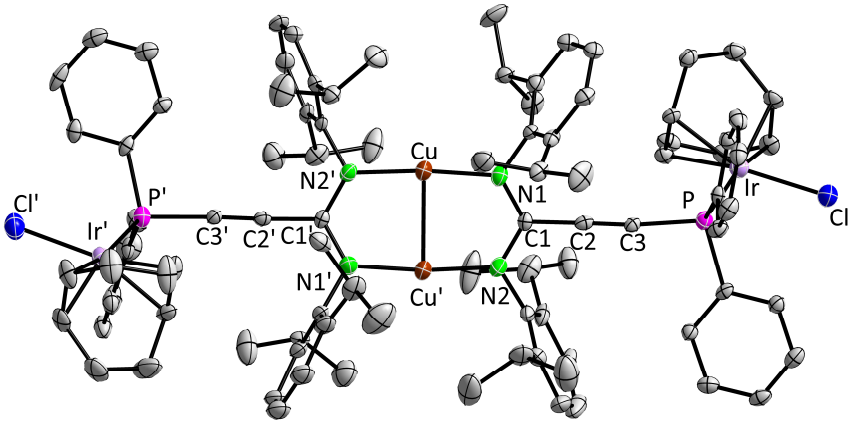

Empirical formula	$C_{94}H_{112}Cl_2Cu_2Ir_2N_4P_2$
Formula weight	1942.19
Temperature/K	100
Crystal system	triclinic
Space group	$P\bar{1}$
a/Å	13.6121(6)
b/Å	16.6709(9)
c/Å	19.1993(9)
α/°	101.291(4)
β/°	95.052(4)
γ/°	94.882(4)
Volume/Å^3	4232.5(4)
Z	2
ρ_{calc}/g/cm^3	1.524
μ/mm^{-1}	3.779
F(000)	1960
Radiation	MoK_α (*λ* = 0.71073)
2*Θ* range for data collection/°	3.528 to 60.502
Index ranges	-18 ≤ h ≤ 18, -21 ≤ k ≤ 23, -25 ≤ l ≤ 25
Reflections collected	45825
Independent reflections	20236 [R_{int} = 0.0319, R_{sigma} = 0.0545]
Data/restraints/parameters	20236/794/1197
Goodness-of-fit on F^2	0.952
Final *R* indexes [*I*>=2*σ* (*I*)]	R_1 = 0.0338, wR_2 = 0.0754
Final *R* indexes [all data]	R_1 = 0.0565, wR_2 = 0.0819
Largest diff. peak/hole / e Å^{-3}	1.56/-1.82

5.2.10 $[Ph_2PC{\equiv}CC(NDipp)(NHDipp)]_2$ (14)

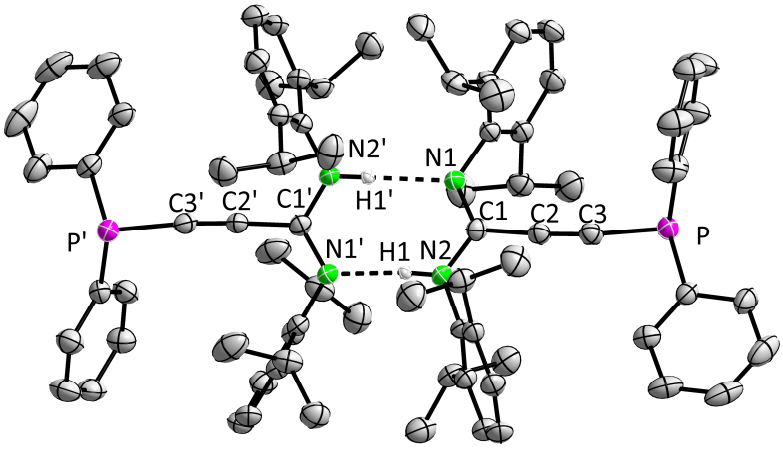

Empirical formula	$C_{78}H_{90}N_4P_2O_{0.5}$
Formula weight	1153.47
Temperature/K	100
Crystal system	triclinic
Space group	$P\bar{1}$
a/Å	12.068(5)
b/Å	15.389(7)
c/Å	19.298(4)
α/°	97.31(3)
β/°	91.50(3)
γ/°	111.74(3)
Volume/Å^3	3291(2)
Z	2
ρ_{calc}/g/cm^3	1.164
μ/mm^{-1}	0.114
F(000)	1240
Radiation	MoK_α (λ = 0.71073)
2Θ range for data collection/°	3.83 to 64.59
Index ranges	-15 ≤ h ≤ 17, -22 ≤ k ≤ 20, -26 ≤ l ≤ 28
Reflections collected	55598
Independent reflections	18021 [R_{int} = 0.1569, R_{sigma} = 0.1046]
Data/restraints/parameters	18021/0/773
Goodness-of-fit on F^2	1.087
Final R indexes [I>=2σ (I)]	R_1 = 0.0781, wR_2 = 0.2034
Final R indexes [all data]	R_1 = 0.1209, wR_2 = 0.2582
Largest diff. peak/hole / e Å^{-3}	1.93/-0.91

5.2.11 [(Rh(cod)Cl)Ph$_2$PC≡CC(NDipp)(NHDipp)]$_2$ (15)

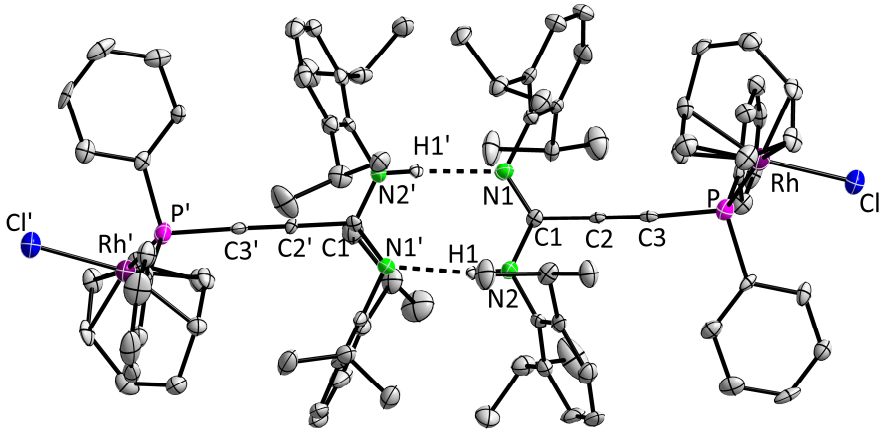

Empirical formula	$C_{94}H_{114}Cl_2N_4P_2Rh_2$
Formula weight	1638.55
Temperature/K	100
Crystal system	triclinic
Space group	$P\bar{1}$
a/Å	13.6866(9)
b/Å	16.0711(11)
c/Å	19.4579(11)
α/°	101.646(5)
β/°	97.221(5)
γ/°	97.164(5)
Volume/Å^3	4108.7(5)
Z	2
ρ_{calc}/g/cm^3	1.324
μ/mm^{-1}	0.554
F(000)	1720
Radiation	MoK_α (λ = 0.71073)
2*Θ* range for data collection/°	3.748 to 50.498
Index ranges	-16 ≤ h ≤ 16, -18 ≤ k ≤ 19, -23 ≤ l ≤ 23
Reflections collected	42439
Independent reflections	14835 [R_{int} = 0.0829, R_{sigma} = 0.1088]
Data/restraints/parameters	14835/0/953
Goodness-of-fit on F^2	1.075
Final *R* indexes [I>=2σ (I)]	R_1 = 0.0655, wR_2 = 0.1305
Final *R* indexes [all data]	R_1 = 0.1337, wR_2 = 0.1660
Largest diff. peak/hole / e Å^{-3}	1.10/-0.98

5.2.12 [(Ir(cod)Cl)Ph$_2$PC≡CC(NDipp)(NHDipp)]$_2$ (16)

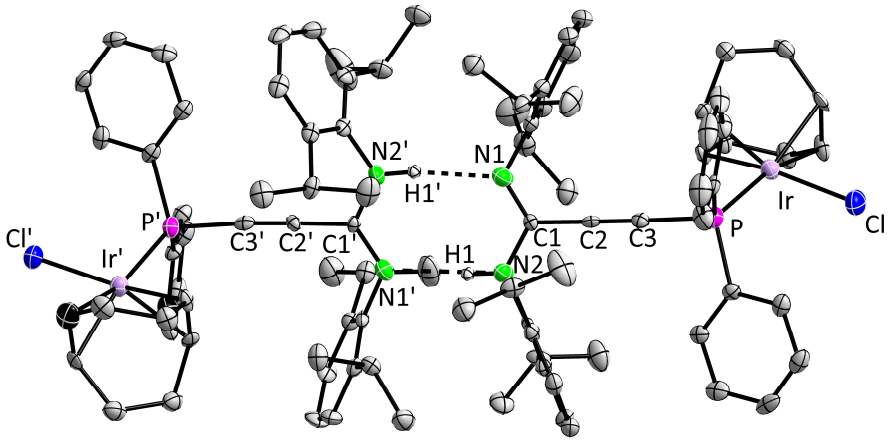

Empirical formula	$C_{94}H_{114}Cl_2Ir_2N_4P_2$
Formula weight	1817.13
Temperature/K	110
Crystal system	triclinic
Space group	$P\bar{1}$
a/Å	13.7286(5)
b/Å	16.0585(7)
c/Å	19.4711(8)
α/°	101.415(4)
β/°	97.240(3)
γ/°	97.113(3)
Volume/Å^3	4125.0(3)
Z	2
ρ_{calc}/g/cm^3	1.463
μ/mm^{-1}	3.375
F(000)	1848
Radiation	MoK$_\alpha$ (λ = 0.71073)
2*Θ* range for data collection/°	3.98 to 60.606
Index ranges	-18 ≤ h ≤ 19, -22 ≤ k ≤ 22, -26 ≤ l ≤ 27
Reflections collected	49948
Independent reflections	20183 [R_{int} = 0.0481, R_{sigma} = 0.0787]
Data/restraints/parameters	20183/0/953
Goodness-of-fit on F^2	1.031
Final *R* indexes [*I*>=2*σ* (*I*)]	R_1 = 0.0447, wR_2 = 0.0798
Final *R* indexes [all data]	R_1 = 0.0937, wR_2 = 0.0958
Largest diff. peak/hole / e Å^{-3}	1.15/-1.84

5.2.13 [Coum-Mes-NHC-AuCl] (19)

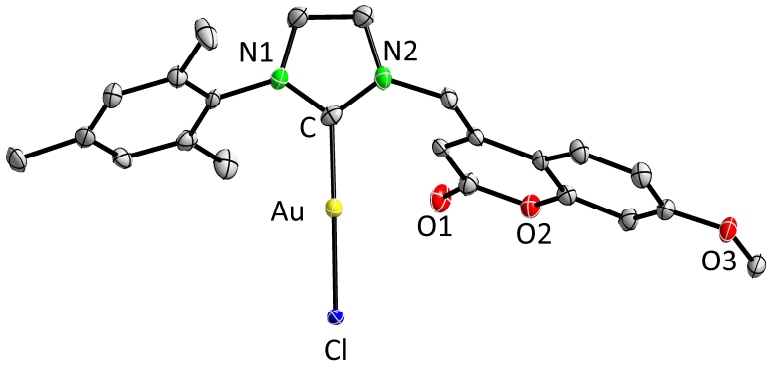

Empirical formula	$C_{23}H_{22}AuClN_2O_3$
Formula weight	606.84
Temperature/K	110
Crystal system	monoclinic
Space group	$P2_1/n$
a/Å	11.8966(13)
b/Å	15.1329(12)
c/Å	12.4023(13)
α/°	
β/°	108.695(8)
γ/°	
Volume/Å^3	2115.0(4)
Z	4
ρ_{calc}/g/cm^3	1.906
μ/mm^{-1}	7.11
F(000)	1176
Radiation	MoK_α (λ = 0.71073)
2Θ range for data collection/°	4.13 to 59.758
Index ranges	-16 ≤ h ≤ 15, -19 ≤ k ≤ 19, -15 ≤ l ≤ 17
Reflections collected	12129
Independent reflections	4968 [R_{int} = 0.0242, R_{sigma} = 0.0300]
Data/restraints/parameters	4968/0/275
Goodness-of-fit on F^2	1.114
Final R indexes [I>=2σ (I)]	R_1 = 0.0319, wR_2 = 0.0843
Final R indexes [all data]	R_1 = 0.0419, wR_2 = 0.0988
Largest diff. peak/hole / e Å^{-3}	2.01/-1.81

5.2.14 [Coum-Mes-NHC-AuBr] (20)

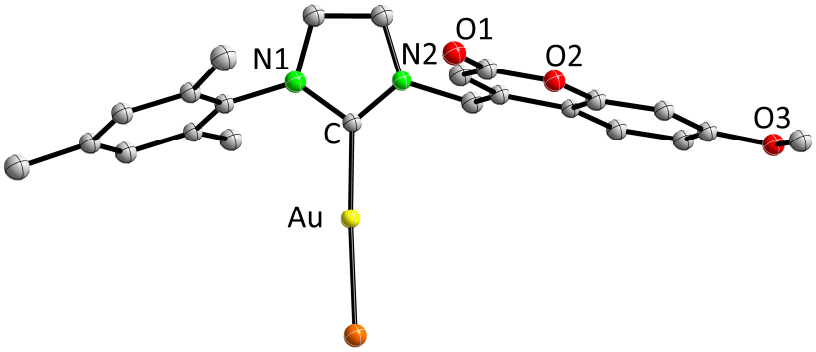

Empirical formula	$C_{54}H_{60}Au_{1.94}Br_2N_4O_8$
Formula weight	1440.9
Temperature/K	100
Crystal system	triclinic
Space group	$P\bar{1}$
a/Å	9.5702(9)
b/Å	12.2887(10)
c/Å	12.4469(11)
α/°	74.599(7)
β/°	68.487(7)
γ/°	76.418(7)
Volume/Å^3	1297.4(2)
Z	1
ρ_{calc}/g/cm^3	1.844
μ/mm^{-1}	7.16
F(000)	702
Radiation	MoK_α (λ = 0.71073)
2Θ range for data collection/°	4.85 to 60.13
Index ranges	-13 ≤ h ≤ 13, -16 ≤ k ≤ 17, -16 ≤ l ≤ 16
Reflections collected	16203
Independent reflections	6183 [R_{int} = 0.1155, R_{sigma} = 0.0861]
Data/restraints/parameters	6183/0/328
Goodness-of-fit on F^2	1.037
Final R indexes [I>=2σ (I)]	R_1 = 0.0566, wR_2 = 0.1427
Final R indexes [all data]	R_1 = 0.0649, wR_2 = 0.1467
Largest diff. peak/hole / e Å^{-3}	2.35/-3.50

5.2.15 [Coum-Mes-NHC-AuMes] (22)

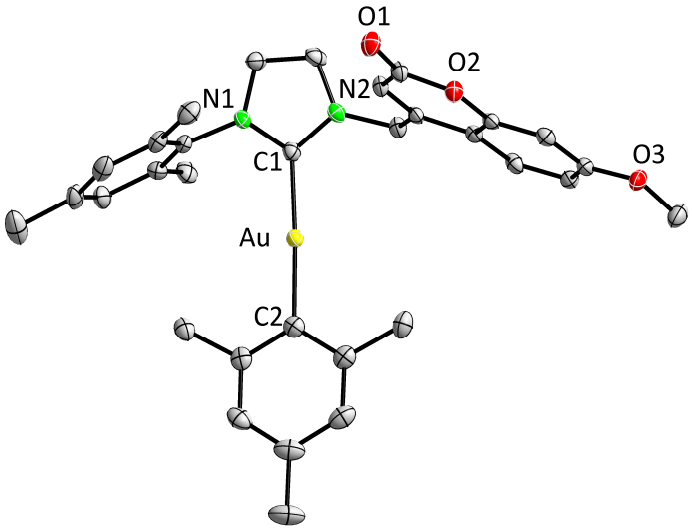

Empirical formula	$C_{32}H_{33}AuN_2O_3$
Formula weight	690.57
Temperature/K	100
Crystal system	monoclinic
Space group	$P2_1/c$
a/Å	12.2781(4)
b/Å	11.5105(6)
c/Å	19.5943(7)
α/°	
β/°	96.424(3)
γ/°	
Volume/Å^3	2751.8(2)
Z	4
ρ_{calc}/g/cm^3	1.667
μ/mm^{-1}	5.382
F(000)	1368
Radiation	MoK_α (λ = 0.71073)
2Θ range for data collection/°	4.866 to 57.598
Index ranges	-12 ≤ h ≤ 16, -13 ≤ k ≤ 14, -22 ≤ l ≤ 24
Reflections collected	15351
Independent reflections	6356 [R_{int} = 0.0218, R_{sigma} = 0.0309]
Data/restraints/parameters	6356/0/350
Goodness-of-fit on F^2	1.001
Final R indexes [I>=2σ (I)]	R_1 = 0.0226, wR_2 = 0.0525
Final R indexes [all data]	R_1 = 0.0323, wR_2 = 0.0544
Largest diff. peak/hole / e Å^{-3}	0.55/-0.70

5.2.16 [(Coum-Mes-NHC)$_2$Au][OTf] (23)

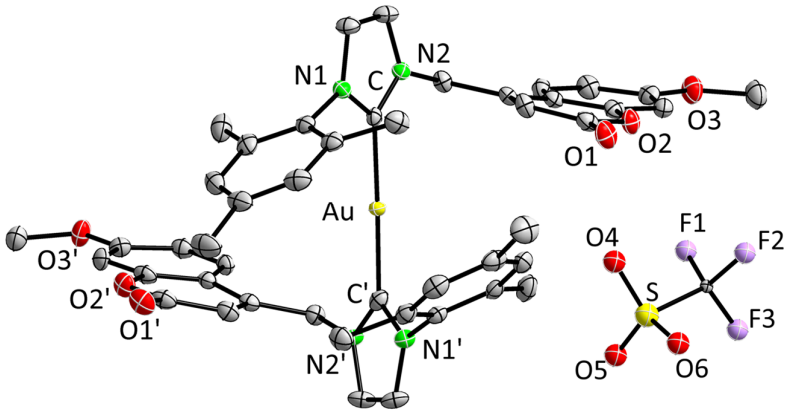

Empirical formula	$C_{47}H_{44}AuF_3N_4O_9S$
Formula weight	1094.89
Temperature/K	100
Crystal system	orthorhombic
Space group	$P2_12_12_1$
a/Å	14.2250(2)
b/Å	24.3811(2)
c/Å	26.0498(3)
α/°	
β/°	
γ/°	
Volume/Å^3	9034.62(18)
Z	8
ρ_{calc}/g/cm^3	1.61
μ/mm^{-1}	3.376
F(000)	4384
Radiation	MoK_α (λ = 0.71073)
2Θ range for data collection/°	4.24 to 58.012
Index ranges	-18 ≤ h ≤ 18, -31 ≤ k ≤ 31, -34 ≤ l ≤ 34
Reflections collected	98146
Independent reflections	21882 [R_{int} = 0.0178, R_{sigma} = 0.0208]
Data/restraints/parameters	21882/0/1187
Goodness-of-fit on F^2	0.997
Final R indexes [I>=2σ (I)]	R_1 = 0.0183, wR_2 = 0.0388
Final R indexes [all data]	R_1 = 0.0212, wR_2 = 0.0396
Largest diff. peak/hole / e Å^{-3}	1.48/-0.58

5.2.17 [Coum-Mes-NHC-Au]$_2$

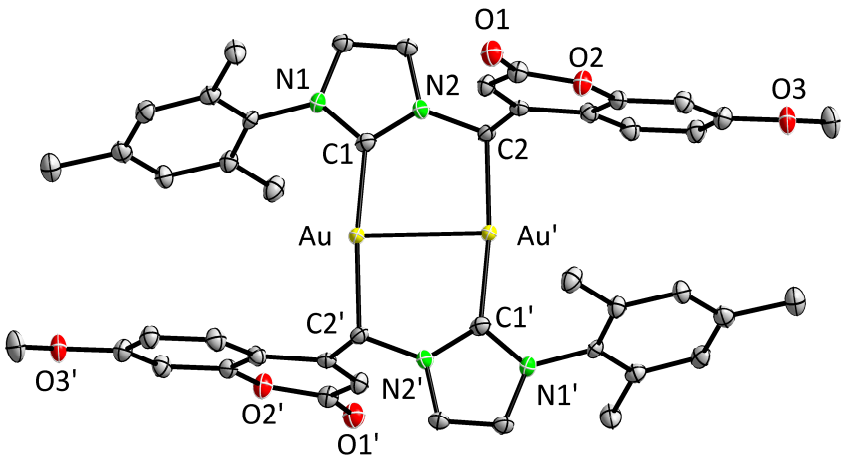

Empirical formula	$C_{46}H_{42}Au_2N_4O_6$
Formula weight	1140.77
Temperature/K	100
Crystal system	triclinic
Space group	$P\bar{1}$
a/Å	9.8161(4)
b/Å	10.8227(4)
c/Å	11.2490(5)
α/°	108.338(3)
β/°	100.858(3)
γ/°	110.558(3)
Volume/Å^3	1000.28(8)
Z	1
ρ_{calc}/g/cm^3	1.894
μ/mm^{-1}	7.381
F(000)	552
Radiation	MoK_α (λ = 0.71073)
2*Θ* range for data collection/°	4.416 to 62.592
Index ranges	-14 ≤ h ≤ 12, -14 ≤ k ≤ 15, -15 ≤ l ≤ 16
Reflections collected	15363
Independent reflections	5501 [R_{int} = 0.0647, R_{sigma} = 0.0482]
Data/restraints/parameters	5501/0/266
Goodness-of-fit on F^2	0.652
Final *R* indexes [*I*>=2*σ* (*I*)]	R_1 = 0.0278, wR_2 = 0.0769
Final *R* indexes [all data]	R_1 = 0.0309, wR_2 = 0.0797
Largest diff. peak/hole / e Å^{-3}	1.83/-2.52

5.2.18 [(Coum-Mes-NHC)$_2$AuI$_2$][I$_3$] (26)

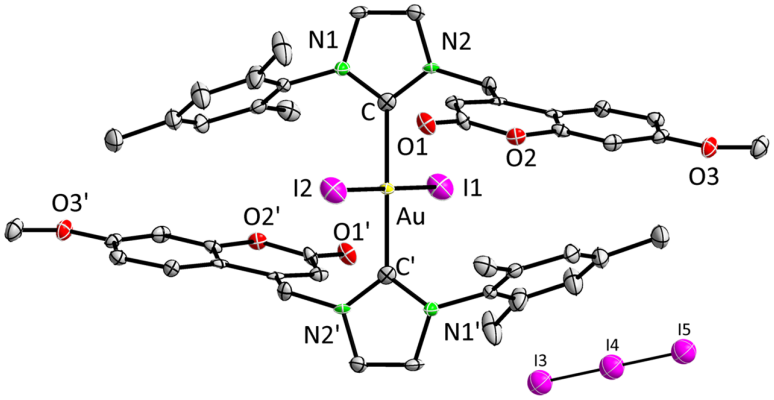

Empirical formula	$C_{46}H_{44}AuI_5N_4O_6$
Formula weight	1580.32
Temperature/K	100
Crystal system	triclinic
Space group	$P\bar{1}$
a/Å	7.2017(3)
b/Å	13.2206(5)
c/Å	13.5389(5)
α/°	67.901(3)
β/°	83.553(3)
γ/°	82.856(3)
Volume/Å^3	1182.07(8)
Z	1
ρ_{calc}/g/cm^3	2.22
μ/mm^{-1}	6.428
F(000)	740
Radiation	MoK_α (λ = 0.71073)
2Θ range for data collection/°	5.454 to 50.994
Index ranges	-8 ≤ h ≤ 8, -16 ≤ k ≤ 16, -16 ≤ l ≤ 16
Reflections collected	14679
Independent reflections	17035 [R_{int} = 0.0246, R_{sigma} = 0.0307]
Data/restraints/parameters	17035/0/287
Goodness-of-fit on F^2	1.125
Final R indexes [I>=2σ (I)]	R_1 = 0.0532, wR_2 = 0.1771
Final R indexes [all data]	R_1 = 0.0621, wR_2 = 0.1817
Largest diff. peak/hole / e Å^{-3}	2.10/-4.74

5.2.19 [Coum-Mes-NHC-Rh(cod)Cl] (27)

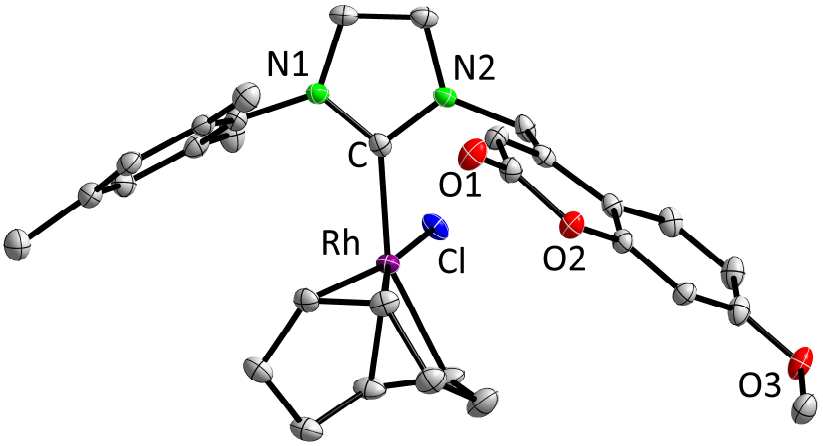

Empirical formula	$C_{31}H_{34}ClN_2O_3Rh$
Formula weight	620.96
Temperature/K	100
Crystal system	monoclinic
Space group	$P2_1/c$
a/Å	14.5012(4)
b/Å	17.9487(6)
c/Å	11.2961(3)
α/°	
β/°	111.572(2)
γ/°	
Volume/Å^3	2734.18(14)
Z	4
ρ_{calc}/g/cm^3	1.508
μ/mm^{-1}	0.758
F(000)	1280
Radiation	MoK_α (λ = 0.71073)
2Θ range for data collection/°	4.492 to 60.426
Index ranges	-19 ≤ h ≤ 20, -25 ≤ k ≤ 23, -15 ≤ l ≤ 15
Reflections collected	21634
Independent reflections	7189 [R_{int} = 0.0772, R_{sigma} = 0.0644]
Data/restraints/parameters	7189/0/347
Goodness-of-fit on F^2	1.019
Final R indexes [I>=2σ (I)]	R_1 = 0.0389, wR_2 = 0.0837
Final R indexes [all data]	R_1 = 0.0648, wR_2 = 0.0925
Largest diff. peak/hole / e Å^{-3}	0.61/-1.05

5.2.20 [Coum-Mes-NHC-Ir(cod)Cl] (28)

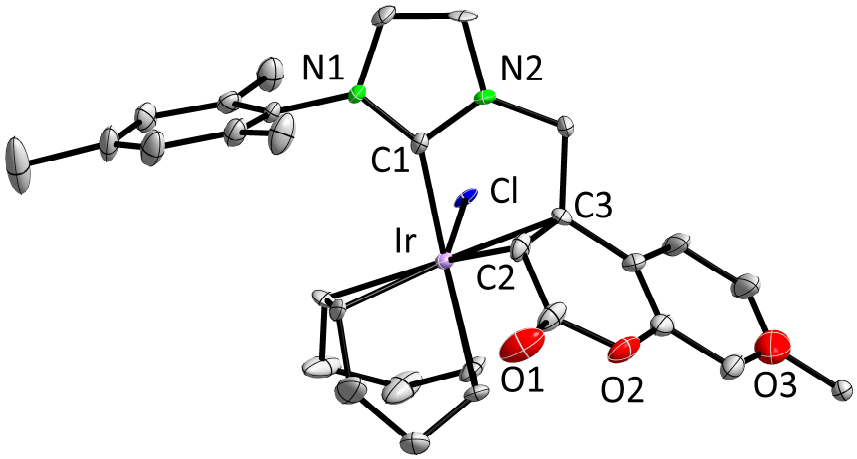

Empirical formula	$C_{31}H_{31}ClIrN_2O_3$
Formula weight	710.77
Temperature/K	100
Crystal system	triclinic
Space group	$P\bar{1}$
a/Å	9.8019(4)
b/Å	11.6309(5)
c/Å	12.5550(5)
α/°	84.823(3)
β/°	72.497(3)
γ/°	86.366(3)
Volume/Å^3	1358.50(10)
Z	2
ρ_{calc}/g/cm^3	1.738
μ/mm^{-1}	5.058
F(000)	701
Radiation	MoK_α (λ = 0.71073)
2Θ range for data collection/°	4.672 to 51.996
Index ranges	-12 ≤ h ≤ 11, -14 ≤ k ≤ 14, -15 ≤ l ≤ 15
Reflections collected	13220
Independent reflections	14652 [R_{int} = 0.0284, R_{sigma} = 0.0387]
Data/restraints/parameters	14652/0/357
Goodness-of-fit on F^2	1.015
Final R indexes [I>=2σ (I)]	R_1 = 0.0316, wR_2 = 0.0803
Final R indexes [all data]	R_1 = 0.0372, wR_2 = 0.0817
Largest diff. peak/hole / e Å^{-3}	2.17/-2.24

5.2.21 [(Coum-Mes-NHC)$_2$PtCl$_2$] (29)

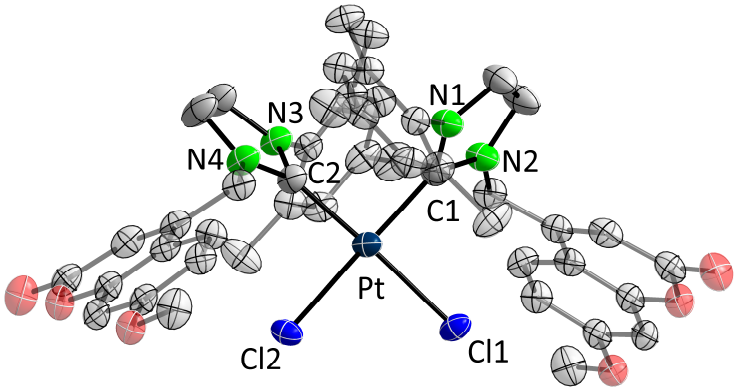

Empirical formula	$C_{46}H_{44}Cl_2N_4O_6Pt$
Formula weight	1014.84
Temperature/K	100
Crystal system	monoclinic
Space group	*C*2/*c*
a/Å	10.8354(3)
b/Å	14.0823(3)
c/Å	27.4733(9)
α/°	
β/°	99.804(3)
γ/°	
Volume/Å^3	4130.9(2)
Z	4
ρ_{calc}/g/cm^3	1.632
μ/mm^{-1}	3.581
F(000)	2032
Radiation	MoK_α (λ = 0.71073)
2*Θ* range for data collection/°	4.788 to 51.998
Index ranges	-13 ≤ h ≤ 13, -17 ≤ k ≤ 16, -33 ≤ l ≤ 31
Reflections collected	12595
Independent reflections	13972 [R_{int} = 0.0212, R_{sigma} = 0.0284]
Data/restraints/parameters	13972/0/271
Goodness-of-fit on F^2	1.088
Final *R* indexes [*I*>=2*σ* (*I*)]	R_1 = 0.0382, wR_2 = 0.0945
Final *R* indexes [all data]	R_1 = 0.0466, wR_2 = 0.0979
Largest diff. peak/hole / e Å^{-3}	2.66/-0.90

5.2.22 [Coum-Mes-NHC-Pd(allyl)Cl] (30)

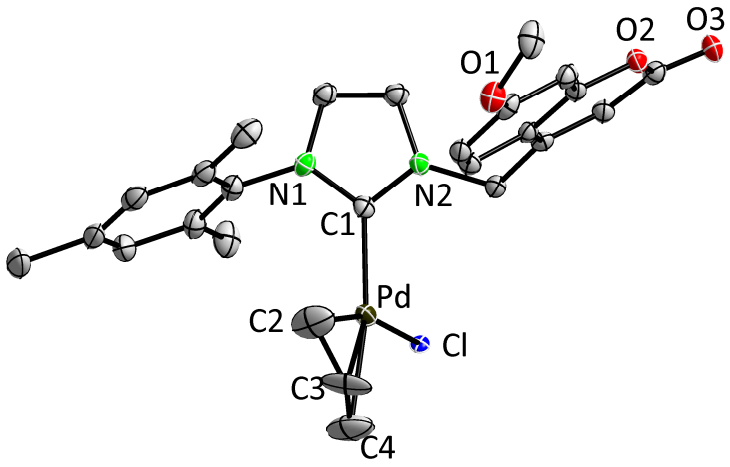

Empirical formula	$C_{27}H_{29}Cl_3N_2O_3Pd$
Formula weight	640.25
Temperature/K	100
Crystal system	monoclinic
Space group	$P2_1/n$
a/Å	11.5031(5)
b/Å	16.5422(7)
c/Å	14.7226(6)
α/°	
β/°	91.998(3)
γ/°	
Volume/Å^3	2799.8(2)
Z	4
ρ_{calc}/g/cm^3	1.519
μ/mm^{-1}	0.98
F(000)	1296
Radiation	MoK_α (λ = 0.71073)
2Θ range for data collection/°	4.314 to 58.908
Index ranges	-15 ≤ h ≤ 9, -22 ≤ k ≤ 22, -19 ≤ l ≤ 20
Reflections collected	23965
Independent reflections	7176 [R_{int} = 0.0669, R_{sigma} = 0.0613]
Data/restraints/parameters	7176/0/329
Goodness-of-fit on F^2	1.084
Final R indexes [I>=2σ (I)]	R_1 = 0.0518, wR_2 = 0.1481
Final R indexes [all data]	R_1 = 0.0741, wR_2 = 0.1584
Largest diff. peak/hole / e Å^{-3}	2.61/-1.11

5.2.23 [Coum-Mes-NHC-Ru(*p*-cymene)Cl_2] (31)

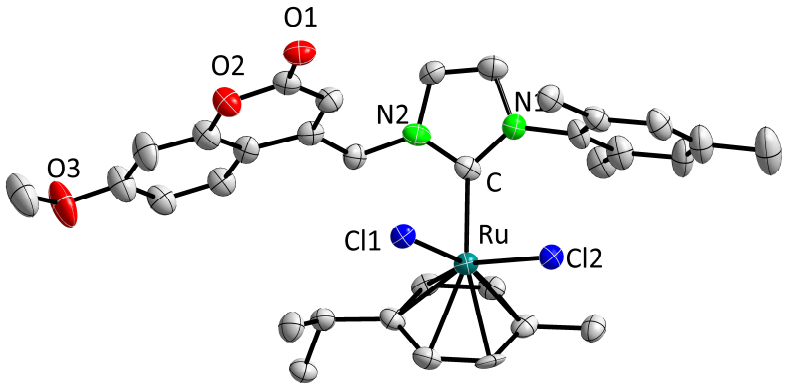

Empirical formula	$C_{33}H_{38}Cl_2N_2O_4Ru$
Formula weight	689.55
Temperature/K	100
Crystal system	monoclinic
Space group	$P2_1/c$
a/Å	9.2430(4)
b/Å	28.9942(17)
c/Å	12.1242(6)
α/°	90
β/°	94.957(4)
γ/°	90
Volume/Å^3	3237.1(3)
Z	4
ρ_{calc}/g/cm^3	1.415
μ/mm^{-1}	0.687
F(000)	1404
Radiation	MoK_α (λ = 0.71073)
2Θ range for data collection/°	5.24 to 51.996
Index ranges	-9 ≤ h ≤ 11, -35 ≤ k ≤ 35, -9 ≤ l ≤ 14
Reflections collected	19895
Independent reflections	6219 [R_{int} = 0.1413, R_{sigma} = 0.1103]
Data/restraints/parameters	6219/0/394
Goodness-of-fit on F^2	1.154
Final R indexes [I>=2σ (I)]	R_1 = 0.0924, wR_2 = 0.2170
Final R indexes [all data]	R_1 = 0.1258, wR_2 = 0.2024
Largest diff. peak/hole / e Å^{-3}	2.32/-0.97

5.2.24 [L^{Ph}thioamide] (32)

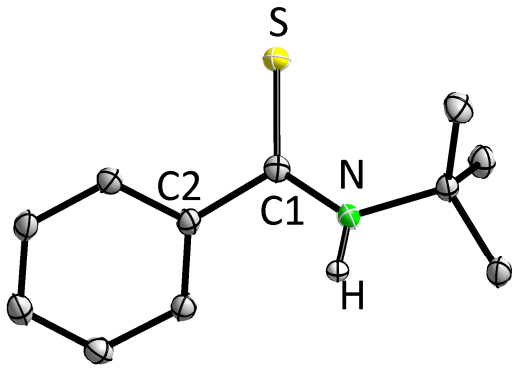

Empirical formula	$C_{44}H_{60}N_4S_4$
Formula weight	773.2
Temperature/K	100
Crystal system	monoclinic
Space group	$P2_1/c$
a/Å	10.7225(7)
b/Å	9.5117(4)
c/Å	11.3986(7)
α/°	
β/°	111.606(5)
γ/°	
Volume/Å^3	1080.85(11)
Z	1
ρ_{calc}/g/cm^3	1.188
μ/mm^{-1}	0.254
F(000)	416
Radiation	MoK_α (λ = 0.71073)
2Θ range for data collection/°	5.756 to 62.48
Index ranges	-14 ≤ h ≤ 15, -13 ≤ k ≤ 13, -14 ≤ l ≤ 16
Reflections collected	9199
Independent reflections	3022 [R_{int} = 0.0756, R_{sigma} = 0.0506]
Data/restraints/parameters	3022/0/121
Goodness-of-fit on F^2	1.068
Final R indexes [I>=2σ (I)]	R_1 = 0.0402, wR_2 = 0.1090
Final R indexes [all data]	R_1 = 0.0493, wR_2 = 0.1135
Largest diff. peak/hole / e Å^{-3}	0.55/-0.32

5.2.25 [(L^{Ph}thioamidinate)$_2$Zn(TMEDA)] (33)

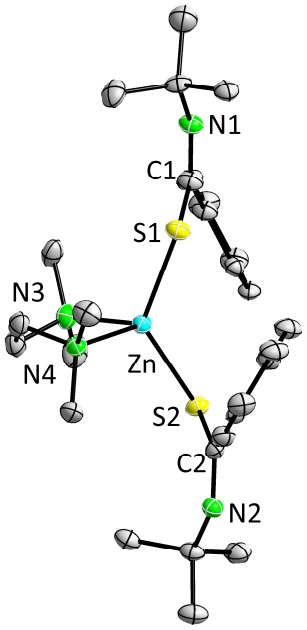

Empirical formula	$C_{32}H_{52}N_4OS_2Zn$
Formula weight	638.26
Temperature/K	110
Crystal system	monoclinic
Space group	*C*2/*c*
a/Å	17.645(3)
b/Å	13.1378(11)
c/Å	29.855(4)
α/°	
β/°	100.967(13)
γ/°	
Volume/Å^3	6794.5(16)
Z	8
ρ_{calc}/g/cm^3	1.248
μ/mm^{-1}	0.875
F(000)	2736
Radiation	MoK_α (λ = 0.71073)
2*Θ* range for data collection/°	3.89 to 58.046
Index ranges	-23 ≤ h ≤ 23, -17 ≤ k ≤ 17, -39 ≤ l ≤ 39
Reflections collected	31923
Independent reflections	8117 [R_{int} = 0.0446, R_{sigma} = 0.0501]
Data/restraints/parameters	8117/18/371
Goodness-of-fit on F^2	0.797
Final *R* indexes [I>=2σ (I)]	R_1 = 0.0471, wR_2 = 0.1138
Final *R* indexes [all data]	R_1 = 0.0776, wR_2 = 0.1360
Largest diff. peak/hole / e Å^{-3}	0.79/-0.62

5.2.26 [(L^{Ph}thioamidinate)$_4Zn_2$] (34)

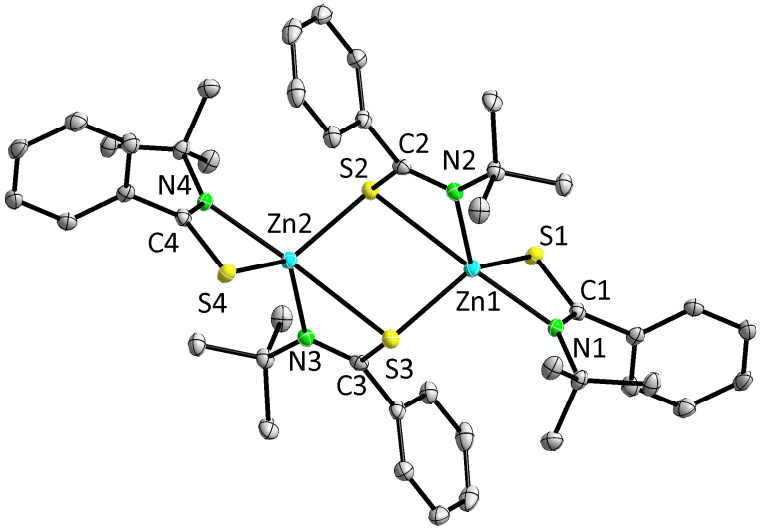

Empirical formula	$C_{44}H_{56}N_4S_4Zn_2$
Formula weight	899.9
Temperature/K	110
Crystal system	monoclinic
Space group	$P2_1/n$
a/Å	12.6567(3)
b/Å	8.2682(3)
c/Å	21.0237(5)
α/°	
β/°	99.315(2)
γ/°	
Volume/Å^3	2171.08(11)
Z	2
ρ_{calc}/g/cm^3	1.377
μ/mm^{-1}	1.333
F(000)	944
Radiation	MoK_α (λ = 0.71073)
2Θ range for data collection/°	3.524 to 57.712
Index ranges	-16 ≤ h ≤ 17, -9 ≤ k ≤ 11, -28 ≤ l ≤ 20
Reflections collected	15650
Independent reflections	5116 [R_{int} = 0.0214, R_{sigma} = 0.0251]
Data/restraints/parameters	5116/0/250
Goodness-of-fit on F^2	1.043
Final R indexes [I>=2σ (I)]	R_1 = 0.0248, wR_2 = 0.0603
Final R indexes [all data]	R_1 = 0.0336, wR_2 = 0.0627
Largest diff. peak/hole / e Å^{-3}	0.41/-0.27

5.2.27 [(L^{Ph}thioamidinate)(ATI)Zn] (35)

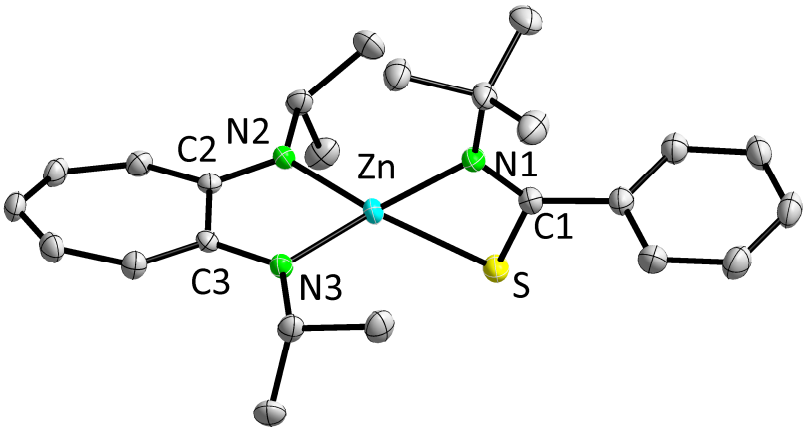

Empirical formula	$C_{24}H_{33}N_3SZn$
Formula weight	460.96
Temperature/K	100
Crystal system	monoclinic
Space group	$P2_1/c$
a/Å	17.6717(19)
b/Å	7.7153(5)
c/Å	17.1339(18)
α/°	
β/°	90.529(9)
γ/°	
Volume/Å^3	2336.0(4)
Z	4
ρ_{calc}/g/cm^3	1.311
μ/mm^{-1}	1.155
F(000)	976
Radiation	MoK$_\alpha$ (λ = 0.71073)
2Θ range for data collection/°	5.304 to 59.768
Index ranges	-24 ≤ h ≤ 22, -8 ≤ k ≤ 10, -22 ≤ l ≤ 24
Reflections collected	15134
Independent reflections	5563 [R_{int} = 0.0886, R_{sigma} = 0.0639]
Data/restraints/parameters	5563/0/269
Goodness-of-fit on F^2	1.057
Final R indexes [I>=2σ (I)]	R_1 = 0.0471, wR_2 = 0.1217
Final R indexes [all data]	R_1 = 0.0649, wR_2 = 0.1309
Largest diff. peak/hole / e Å^{-3}	0.61/-1.01

5.2.28 [(L^{Ph}thioamidinate)$_6Sm_2$] (36)

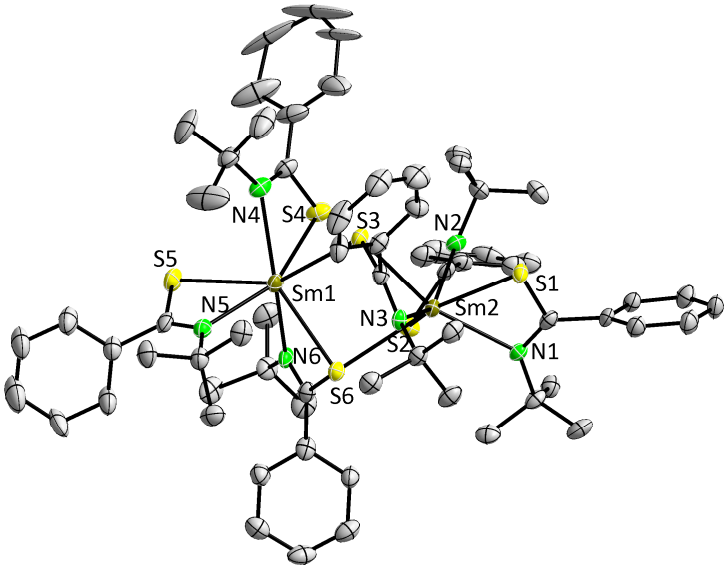

Empirical formula	$C_{140}H_{164}N_{12}S_{12}Sm_4$
Formula weight	3028.99
Temperature/K	100
Crystal system	triclinic
Space group	$P\bar{1}$
a/Å	12.5765(5)
b/Å	13.4189(5)
c/Å	23.5829(11)
α/°	76.702(3)
β/°	78.780(4)
γ/°	69.111(3)
Volume/Å^3	3590.8(3)
Z	1
ρ_{calc}/g/cm^3	1.401
μ/mm^{-1}	1.837
F(000)	1544
Radiation	MoK_α (λ = 0.71073)
2Θ range for data collection/°	4.596 to 56.878
Index ranges	-16 ≤ h ≤ 16, -17 ≤ k ≤ 17, -30 ≤ l ≤ 31
Reflections collected	38496
Independent reflections	16445 [R_{int} = 0.0444, R_{sigma} = 0.0668]
Data/restraints/parameters	16445/0/775
Goodness-of-fit on F^2	1.068
Final R indexes [I>=2σ (I)]	R_1 = 0.0414, wR_2 = 0.1275
Final R indexes [all data]	R_1 = 0.0678, wR_2 = 0.1711
Largest diff. peak/hole / e Å^{-3}	1.92/-2.47

5.2.29 [(L^{Ph}thioamidinate)$_3$Y] (37)

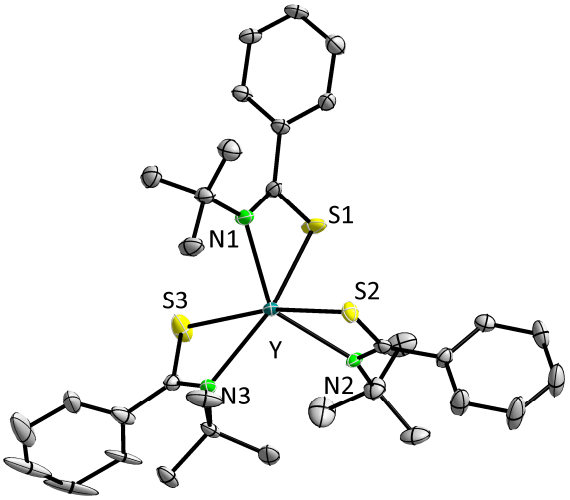

Empirical formula	$C_{33}H_{42}N_3S_3Y$
Formula weight	665.78
Temperature/K	100
Crystal system	monoclinic
Space group	$P2_1/n$
a/Å	15.1945(11)
b/Å	14.9798(9)
c/Å	16.3865(11)
α/°	
β/°	115.283(5)
γ/°	
Volume/Å^3	3372.5(4)
Z	4
ρ_{calc}/g/cm^3	1.311
μ/mm^{-1}	1.94
F(000)	1392
Radiation	MoK$_\alpha$ (λ = 0.71073)
2Θ range for data collection/°	5.498 to 59.872
Index ranges	-20 ≤ h ≤ 20, -19 ≤ k ≤ 20, -21 ≤ l ≤ 22
Reflections collected	22697
Independent reflections	7893 [R_{int} = 0.1363, R_{sigma} = 0.1075]
Data/restraints/parameters	7893/0/370
Goodness-of-fit on F^2	0.999
Final R indexes [I>=2σ (I)]	R_1 = 0.0616, wR_2 = 0.1514
Final R indexes [all data]	R_1 = 0.0972, wR_2 = 0.1714
Largest diff. peak/hole / e Å^{-3}	0.88/-0.88

6. Summary (Zusammenfassung)

6.1 Summary

The disseration focuses on the synthesis of transiton-metal complexes featuring advanced ligand systems, specifically, a phosphine acetylide functionalized amidinate ligand, a coumarin substituted NHC ligand and a *t*-Bu substituted thioamidinate ligand. The metal ions with d^8 and d^{10} electronic configurations were chosen as they are well known to exhibit interesting optical and catalytic properties. The synthesized metal complexes were characterized using standard analytical tools and investigated for their photophysical properties.

Chapter 3.1 describes the synthesis of a phosphine acetylide funtionalized amidinate ligand (**1**) employed for the synthyesis of monometallic Cu(I) and Au(I) complexes (**2** and **3**) as well as heterobimetallic Cu(I)–Au(I) complexes with various counter ions (**5**-**9**) (Scheme 31). Ligand **1**, featuring two orthogonal donor sites, enabled the synthesis of the heterobimetallic complexes **5**-**9**, either in a stepwise manner or in a more efficient one-pot reaction.

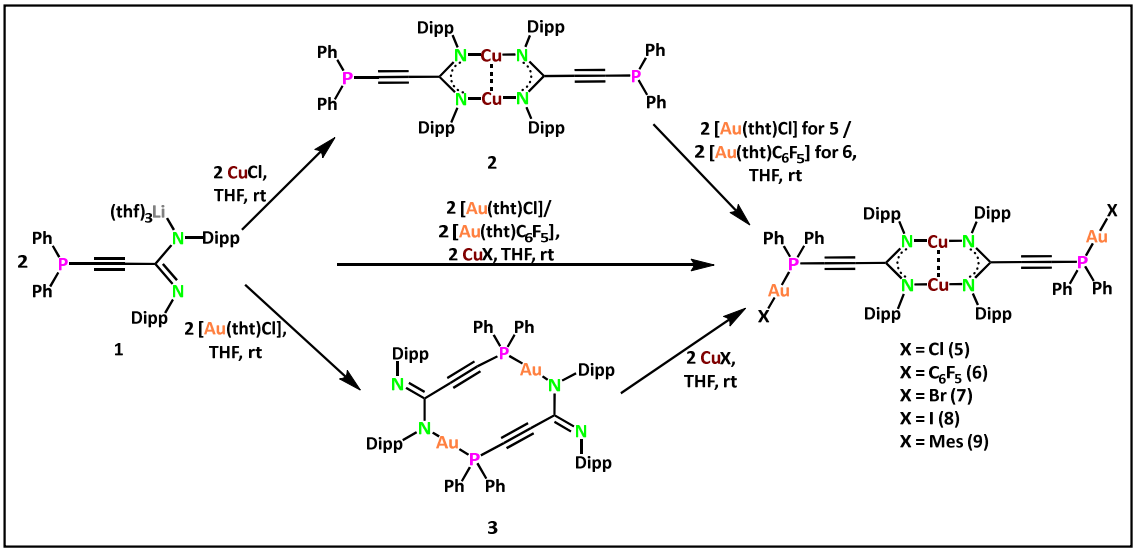

Scheme 31: Synthesis of complexes **2** and **3** from **1** and **5**-**9** in stepwise manner or a one-pot reaction.

Complexes **2** and **5**-**9** were found to be luminescent in the solid state as well as in DCM solution, with both exhibiting yellow luminescence. Complex **2** showed an emission maximum at 500 nm, while complexes **5**-**9** exhibited emission maxima between 550 and 630 nm, respectively. For the complexes **5, 7** and **8**, with less bulky anions at the Au(I) center, the emission maximum was around 550 nm, while for complexes **6** and **9**, with bulky anions at the Au(I) center, the emission maximum was red-shifted to around 630 nm.

Chapter 3.2 describes the synthesis of heterobimetallic Cu(I)–Rh(I) (**10**) and Cu(I)–Ir(I) (**11**) complexes using metalloligand **2** or using ligand **1** in a one-pot reaction (Scheme 32). Ligand **1** was additionally utilized for the synthesis of Rh(I) (**15**) and Ir(I) (**16**) complexes following two pathways. In the first pathway, complexes **12** and **13** were synthesized from compound **1** and hydrolyzed to obtain complexes **15** and **16**. In the second pathway, compound **1** was hydrolyzed to obtain compound **14** which was further converted to complexes **15** and **16**. Remarkably, complex **11** showed catalytic activity for TH reactions of aryl aldehydes. 10 mol% of complex **11** catalyzed the TH reaction delivering yields greater than 70 % of the corresponding hydrogenated alcohols. Complexes **11** and **16** were found to be luminescent in the solid state and in DCM solution at 77 K and further studied for their luminescent properties. Both in the solid state and DCM solution, complexes **11** and **16** exhibited an emission maximum around 580 nm.

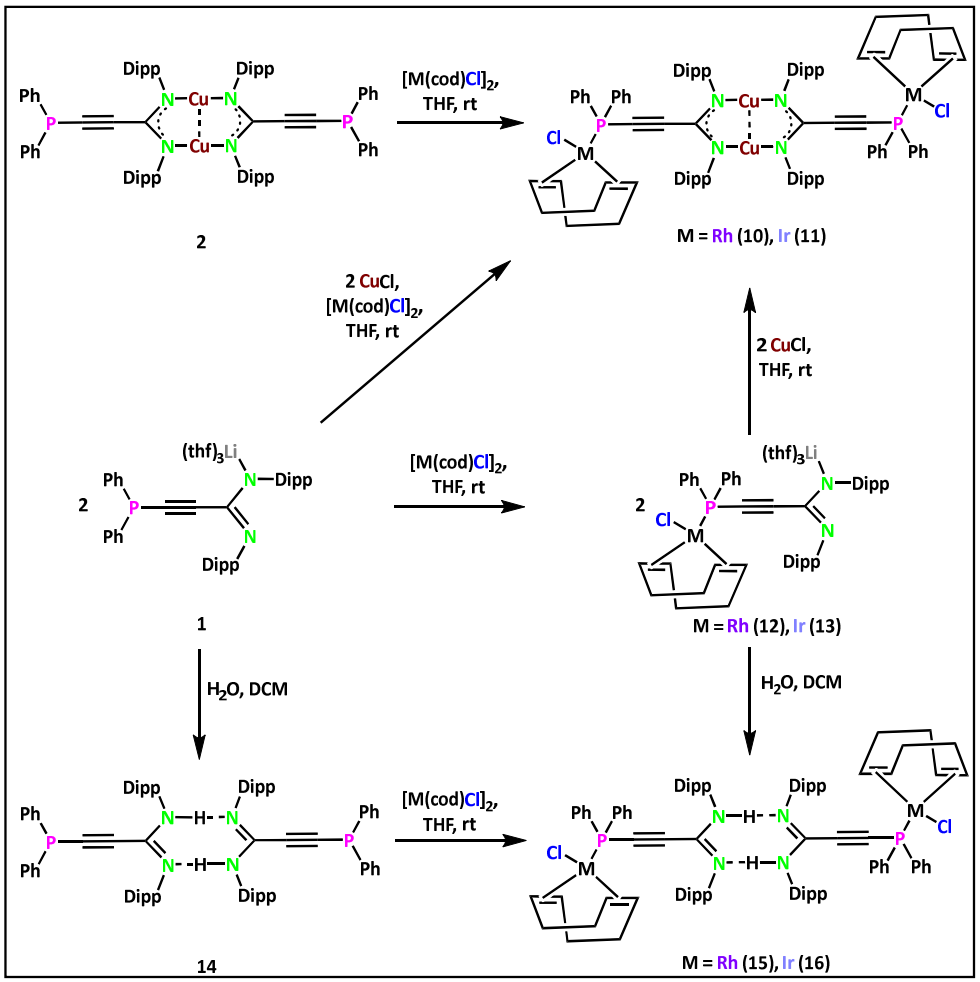

Scheme 32: Synthesis of compounds **10-16.**

Chapter 3.3 describes the synthesis of a coumarin functionalized imidazolium salt (**18**) from mesityl imidazole (Scheme 33). Deprotonation of **18** using Ag_2O enabled the synthesis of various Au(I) carbene complexes with diverse counter anions at the Au(I) center. The resulting complexes **19-22** are neutral with Cl, Br, C_6F_6 and mesityl ligands at the Au(I) center, while complex **23** is cationic with two NHC ligands coordinating the Au(I) center.

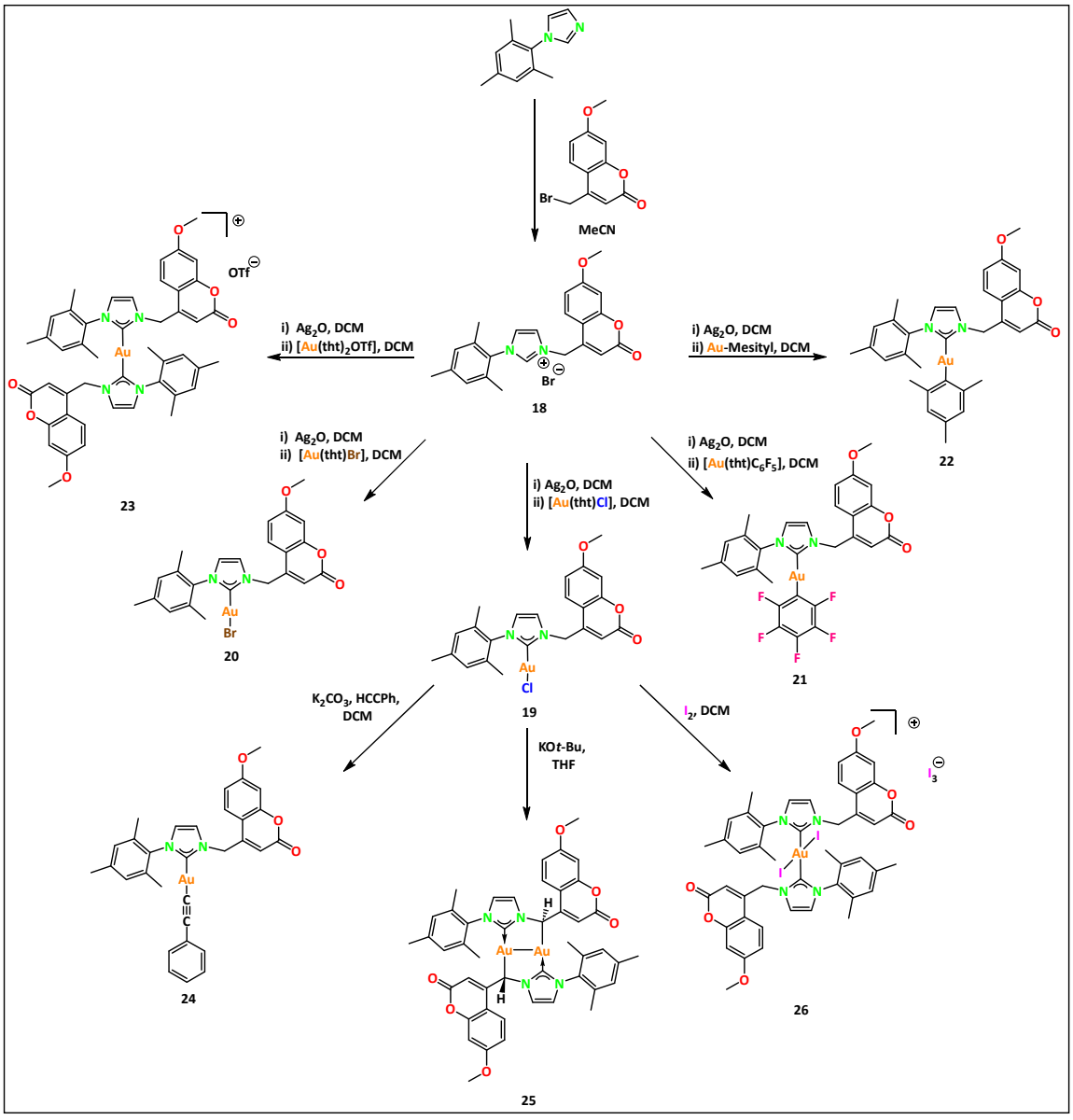

Scheme 33: Synthesis of NHC-gold complexes **19-26**.

Detailed reactivity studies of the NHC-AuCl complex (**19**) resulted in the discovery of the complexes **24-26**. Notably, complex **25** is a bimetallic complex showing aurophilic interactions. To access complex **26**, the Au(I) center was oxidized to Au(III) using iodine as an oxidizing

agent. Complexes **19**-**25** all show luminescent behavior. Importantly, complexes **19-24** were found to be luminescent with a blue-green emission, while complex **25** shows a distinct yellow luminescence due to the aurophilic interactions. In complexes **19-24**, the emission maxima were observed around 420 nm at ambient temperature, while a red-shift was observed at 77 K with the emission maxima located around 520 nm. In complex **25**, the emission maxima were observed around 415 to 600 nm in the solid state and around 485 to 500 nm in DCM solution.

Chapter 3.4 describes the transition metal functionalization of the coumarin-imidazolium salt **18** starting from various transition metal precursors (Scheme 34). After the carbene activation, further reactions were performed with Rh(I), Ir(I), Pt(II), Pd(II), and Ru(II) precursors to obtain the corresponding NHC-transition metal complexes **27-31**.

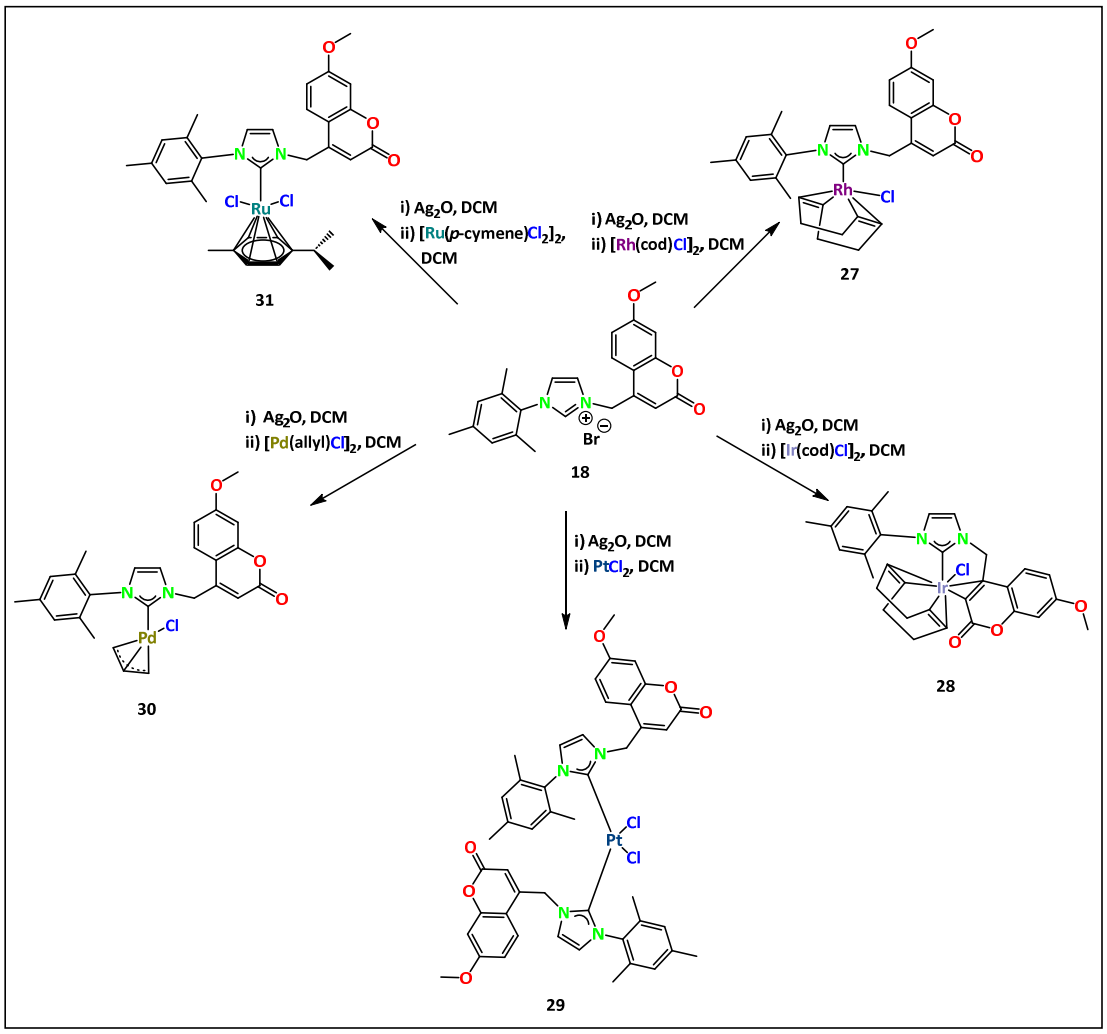

Scheme 34: Synthesis of NHC-transition metal complexes **27-31**.

Complexes **28** and **31** were found to be luminescent in the solid state and in DCM solution at 77 K with emission maxima at 535 and 415 nm, respectively. Complexes **29** and **30** were luminescent in the solid state and in DCM solution, not only at 77 K but also at ambient temperature. Complex **29** exhibits an emission maximum around 600 nm and complex **30** around 430 nm.

The final chapter 3.5 describes the synthesis of a thioamide ligand (**32**) and its utilization for the synthesis of Zn(II) and lanthanide(III) complexes (Scheme 35). Ligand **32** was treated with different Zn(II) precursors to obtain the complexes **33-35**. Additionally, a Sm(III) complex (**36**) and a Y(III) complex (**37**) were synthesized from ligand **32**. Complexes **33** and **34** were observed to be luminescent in the solid state and in DCM solution at 77 K with a blue emission. The emission maxima were observed between 500 and 525 nm for both complexes. The heteroleptic complex **35** was luminescent not only at 77 K but notably also at ambient temperature. Independent of the temperature, the emission maxima were observed between 500 and 510 nm.

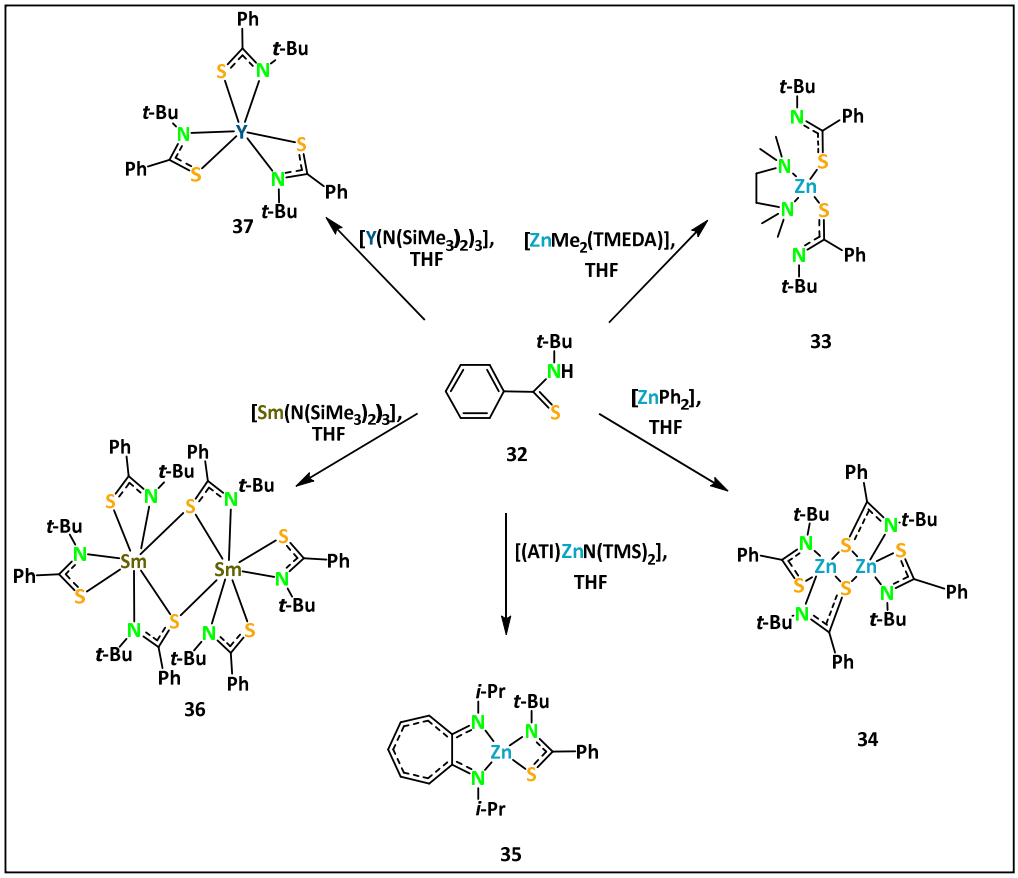

Scheme 35: Synthesis of complexes **33-37** from the thioamidinate ligand **32**.

The thesis significantly broadens the conceptual and synthetic scope of heterobimetallic transition metal complexes by introducing an orthogonal ligand design strategy. Through systematic variation of the metal centers, ligand environments, and counterions, this work demonstrates fine-tuned luminescence ranging from blue to deep red and reveals structure-property relations. Beyond photophysical studies, the work demonstrates the synthetic utility and catalytic activity of the new complexes. Notably, the heterobimetallic Cu–Ir complex **11** exhibited robust catalytic activity in transfer hydrogenation reactions of aryl aldehydes. This catalytic performance shows the potential of such heterobimetallic systems in advanced chemical transformations. The work also extends into the realm of coumarin-functionalized NHC systems, offering a versatile platform for the synthesis of luminescent Au(I) and transition metal-NHC complexes with finely tunable optoelectronic characteristics.

These findings represent more than just a collection of new compounds, they provide a cohesive and strategic framework for designing new molecules that integrate luminescent, catalytic, and coordination properties. In doing so, this thesis does not merely contribute progressive knowledge to the field of organometallic chemistry, it also establishes new pathways for creating responsive molecular architectures with real world potential.

6.2 Zusammenfassung

Die vorliegende Dissertation befasst sich mit der Synthese von Übergangsmetallkomplexen mit fortschrittlichen Ligandensystemen, insbesondere einem Phosphanacetylid-funktionalisierten Amidinatliganden, einem Cumarin-substituierten NHC-Liganden und einem *t*-Bu-substituierten Thioamidinatliganden. Die Metallionen mit den Elektronen-konfigurationen d^8 und d^{10} wurden ausgewählt, da sie bekanntermaßen interessante optische und katalytische Eigenschaften aufweisen. Die synthetisierten Metallkomplexe wurden mit Hilfe von Standard-Analytikmethoden charakterisiert und auf ihre photophysikalischen Eigenschaften hin untersucht.

Kapitel 3.1 beschreibt die Synthese eines Phosphanacetylid-funktionalisierten Amidinatliganden (**1**), der für die Synthese von monometallischen Cu(I)- und Au(I)-Komplexen (**2,3**) sowie heterobimetallischen Cu(I)–Au(I)-Komplexen mit verschiedenen Gegenionen (**5-9**) verwendet wurde (Schema 31). Der Ligand **1**, der zwei orthogonale Donorfunktionalitäten aufweist, ermöglichte die Synthese der heterobimetallischen Komplexe **5-9**, entweder schrittweise oder in einer effizienteren Eintopfreaktion.

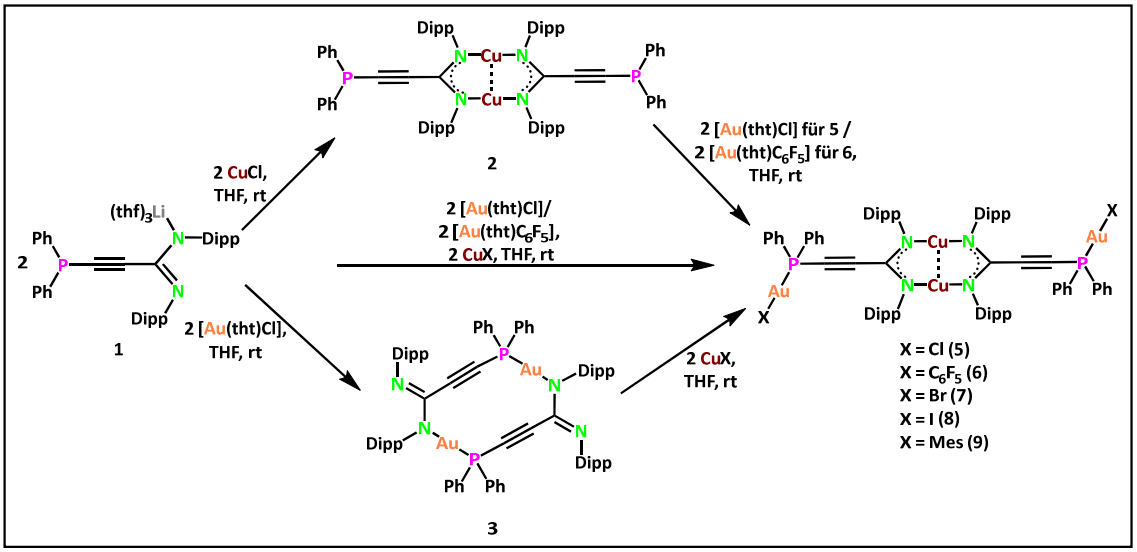

Schema 31: Synthese der Komplexe **5-9** schrittweise und durch Ein-Topf-Reaktion.

Die Komplexe **2** und **5-9** erwiesen sich sowohl im festen Zustand als auch in DCM-Lösung als lumineszierend, wobei beide eine gelbe Lumineszenz aufwiesen. Komplex **2** zeigte ein Emissionsmaximum bei 500 nm, während die Komplexe **5-9** Emissionsmaxima zwischen 550 und 630 nm aufwiesen. Bei den Komplexen **5, 7** und **8** mit weniger sterisch anspruchsvollen

Anionen am Au(I)-Zentrum lag das Emissionsmaximum bei 550 nm, während bei den Komplexen **6** und **9** mit sterisch anspruchsvolleren Anionen am Au(I)-Zentrum das Emissionsmaximum zu etwa 630 nm rotverschoben war.

Kapitel 3.2 beschreibt die Synthese von heterobimetallischen Cu(I)–Rh(I)- (**10**) und Cu(I)–Ir(I)-Komplexen (**11**) unter Verwendung des Metalloliganden **2** oder des Liganden **1** in einer Eintopfreaktion (Schema 32). Ligand **1** wurde außerdem für die Synthese von Rh(I)- (**15**) und Ir(I)-Komplexen (**16**) durch zwei unterschiedliche Syntheserouten verwendet. Auf dem ersten Weg wurden die Komplexe **12** und **13** aus Verbindung **1** synthetisiert und anschließend hydrolysiert, um die Komplexe **15** und **16** zu erhalten. Im zweiten Weg wurde Verbindung **1** zuerst hydrolysiert, um Verbindung **14** zu erhalten, die dann in die Komplexe **15** und **16** umgewandelt wurde.

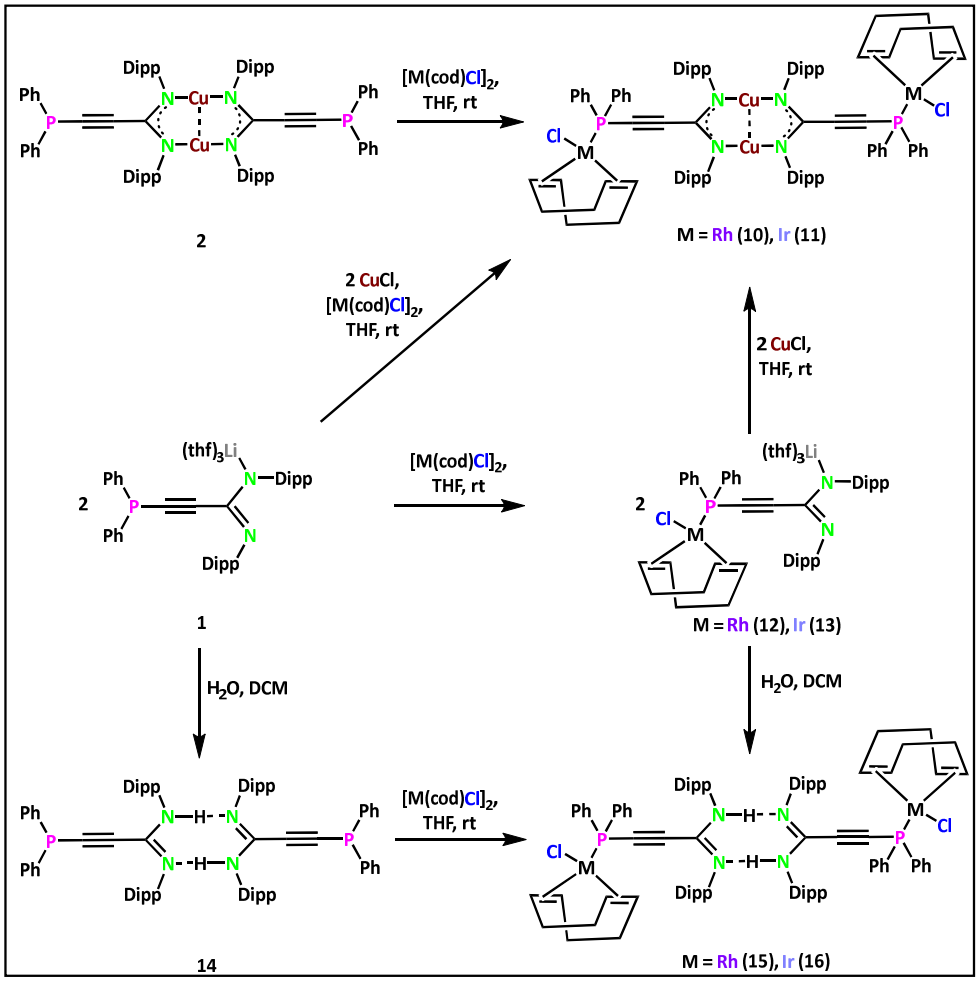

Schema 32: Synthese der Komplexe **10-16**.

Bemerkenswerterweise zeigte der Komplex **11** katalytische Aktivität für TH-Reaktionen von Arylaldehyden. 10 mol% des Komplexes **11** katalysierten die TH-Reaktion und lieferten Ausbeuten von mehr als 70 % der entsprechenden hydrierten Alkohole. Die Komplexe **11** und **16** erwiesen sich im festen Zustand und in DCM-Lösung bei 77 K als lumineszierend und wurden weiter auf ihre lumineszenten Eigenschaften hin untersucht. Sowohl im festen Zustand als auch in DCM-Lösung wiesen die Komplexe **11** und **16** ein Emissionsmaximum bei 580 nm auf.

Kapitel 3.3 beschreibt die Synthese eines Cumarin-Imidazolium-Salzes (**18**) aus Mesitylimidazol (Schema 33). Die Deprotonierung von **18** mit Ag_2O ermöglichte die Synthese verschiedener Au(I)-Carbenkomplexe mit diversen Gegenanionen am Au(I)-Zentrum. Die resultierenden Komplexe **19-22** sind neutral mit Cl, Br, C_6F_6 und Mesityl-Liganden am Au(I)-Zentrum, während Komplex **23** kationisch ist und über zwei an das Au(I)-Zentrum koordinierende NHC-Liganden verfügt. Detaillierte Reaktivitätsstudien des NHC-AuCl-Komplexes (**19**) führten zur Entdeckung der Komplexe **24-26**. Bemerkenswert ist dabei besonders der bimetallische Komplex **25** , der aurophile Wechselwirkungen aufweist. Um Komplex **26** zu erhalten, wurde das Au(I)-Zentrum unter Verwendung von Iod als Oxidationsmittel zu Au(III) oxidiert. Die Komplexe **19-25** zeigen alle Lumineszente Eigenschaften. Die Komplexe **19-24** lumineszieren mit einer blau-grünen Emission, während Komplex **25** aufgrund der aurophilen Wechselwirkungen eine deutlich gelbe Lumineszenz zeigt. Bei den Komplexen **19-24** wurden die Emissionsmaxima bei Umgebungstemperatur um 420 nm beobachtet, während bei 77 K eine Rotverschiebung mit Emissionsmaxima um 520 nm beobachtet wurde. Bei Komplex **25** wurden die Emissionsmaxima zwischen 415 und 600 nm im festen Zustand und zwischen 485 und 500 nm in DCM-Lösung beobachtet.

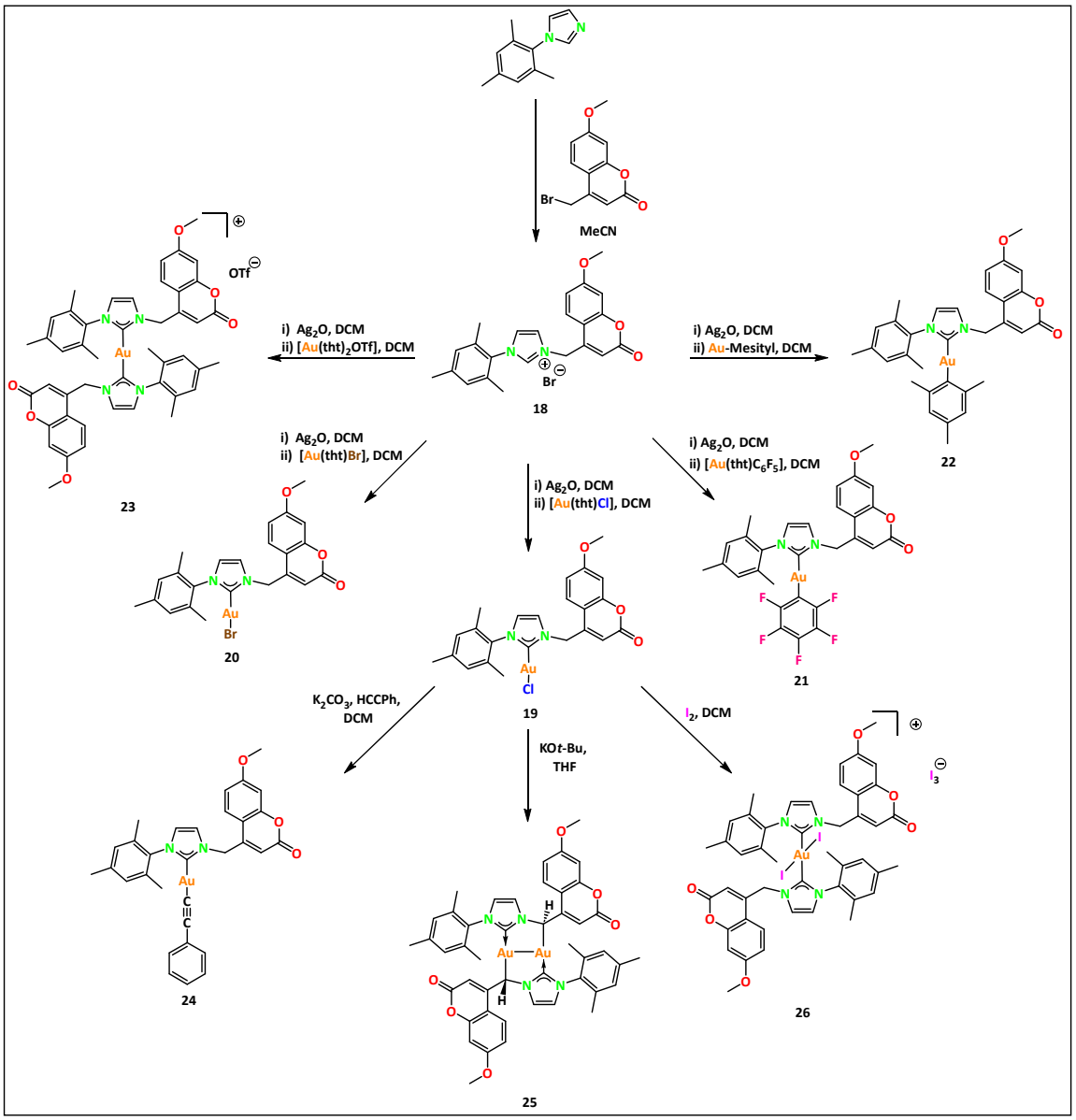

Schema 33: Synthese der NHC-Gold-Komplexe **19-26**.

Kapitel 3.4 beschreibt die Übergangsmetallfunktionalisierung des Cumarin-Imidazoliumsalzes **18** ausgehend von verschiedenen Übergangsmetallvorstufen (Schema 34). Nach erfolgter Carbenaktivierung wurden Reaktionen mit Rh(I)-, Ir(I)-, Pt(II)-, Pd(II)- und Ru(II)-Vorläufern durchgeführt, um die entsprechenden NHC-Komplexe **27-31** zu erhalten. Die Komplexe **28** und **31** erwiesen sich im festen Zustand und in DCM-Lösung bei 77 K als lumineszierend mit Emissionsmaxima bei 535 beziehunsweise 415 nm. Die Komplexe **29** und **30** lumineszierten im festen Zustand und in DCM-Lösung nicht nur bei 77 K, sondern auch bei

Umgebungstemperatur. Komplex **29** weist ein Emissionsmaximum bei 600 nm und Komplex **30** bei 430 nm auf.

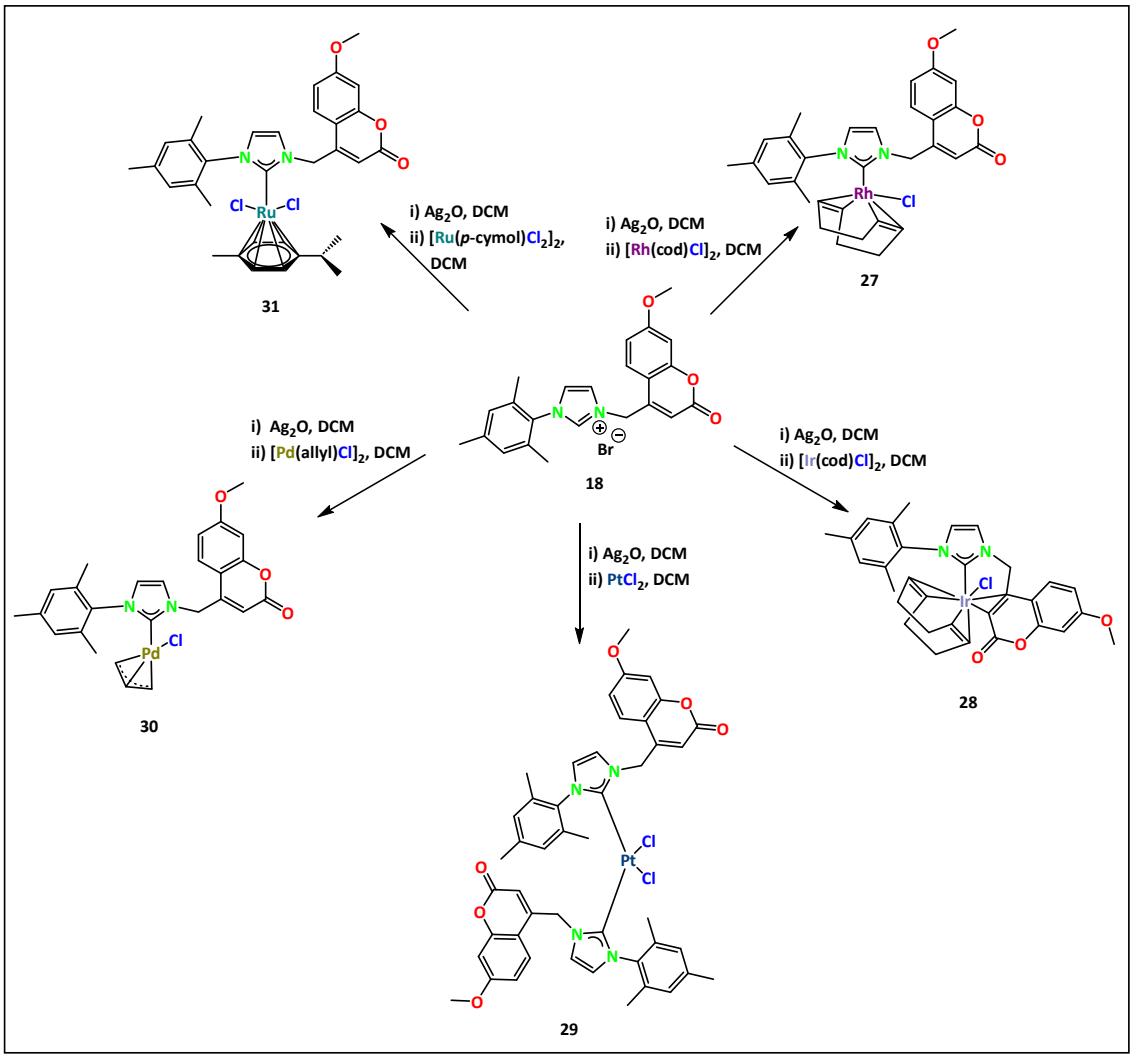

Schema 34: Synthese der NHC-Übergangsmetallkomplexe **27-31**.

Das abschließende Kapitel 3.5 beschreibt die Synthese eines Thioamid-Liganden (**32**) und seine Verwendung für die Synthese von Zn(II)- und Lanthanoid(III)-Komplexen (Schema 35). Der Ligand **32** wurde mit verschiedenen Zn(II)-Vorläufern behandelt, um die Komplexe **33-35** zu erhalten. Außerdem wurden ein Sm(III)-Komplex (**36**) und ein Y(III)-Komplex (**37**) ausgehend von Ligand **32** synthetisiert. Die Komplexe **33** und **34** erwiesen sich im festen Zustand und in DCM-Lösung bei 77 K als blau lumineszierend. Die Emissionsmaxima wurden bei beiden Komplexen zwischen 500 und 525 nm beobachtet. Der heteroleptische Komplex

35 lumineszierte nicht nur bei 77 K, sondern auch bei Umgebungstemperatur. Unabhängig von der Temperatur wurden die Emissionsmaxima zwischen 500 und 510 nm beobachtet.

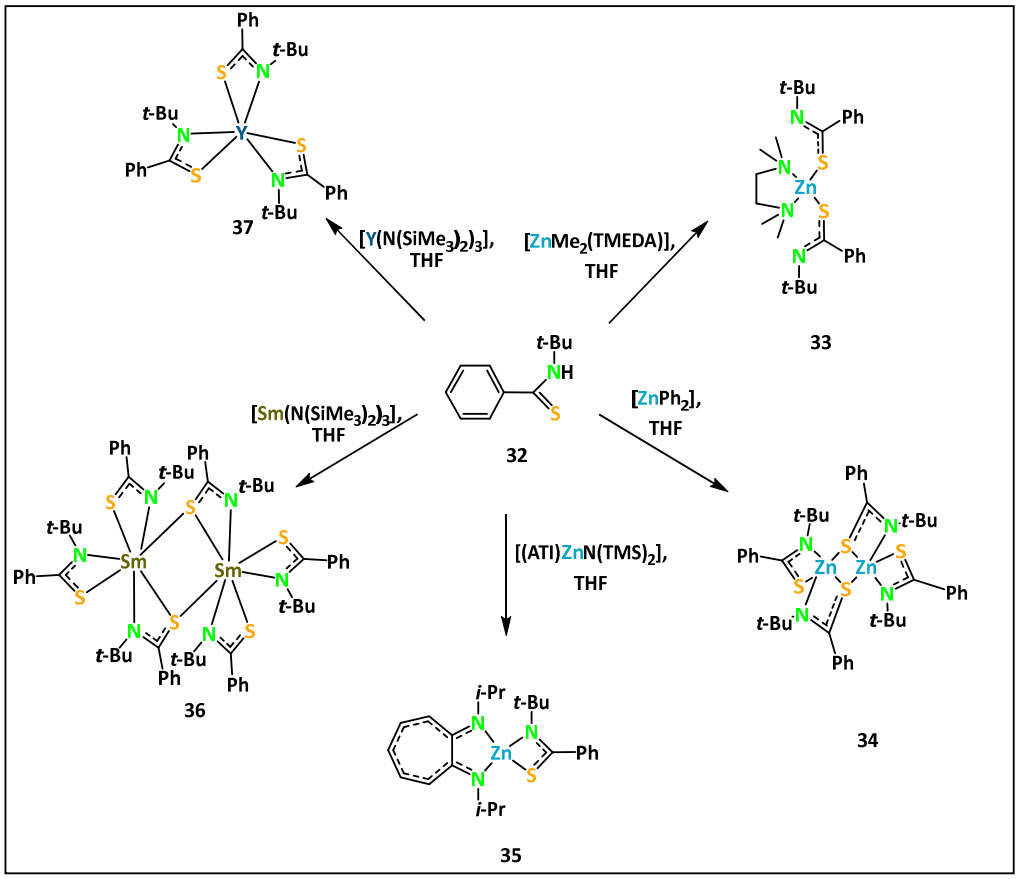

Schema 35: Synthese der Komplexe **33-37** ausgehend vom Thioamidinat-Liganden **32**.

Die Dissertation erweitert den konzeptionellen und synthetischen chemischen Raum der heterobimetallischen Übergangsmetallkomplexe durch die Einführung einer orthogonalen Ligandendesignstrategie. Durch die systematische Variation der Metallzentren, Ligandenumgebungen und Gegenionen konnte in dieser Arbeit eine fein abgestimmte Lumineszenz von Blau bis Tiefrot nachgewiesen und Struktur-Eigenschafts-Beziehungen aufgezeigt werden. Über die photophysikalischen Studien hinaus wurden das synthetische Potenzial und die katalytische Aktivität der neuen Komplexe nachgewiesen. Insbesondere der Cu-Ir-Komplex zeigte eine robuste katalytische Aktivität bei Transferhydrierungsreaktionen von Arylaldehyden. Dies unterstreicht das Potenzial solcher heterobimetallischen Systeme für fortschrittliche chemische Transformationen. Die Arbeit erstreckt sich auch auf den Bereich der Cumarin-funktionalisierten NHC-Systeme, die eine vielseitige Plattform für die Synthese

von lumineszierenden Au(I)- und Übergangsmetall-NHC-Komplexen mit fein abstimmbaren optoelektronischen Eigenschaften bieten.

Diese Ergebnisse stellen mehr als nur eine Sammlung neuer Verbindungen dar, sie bieten einen zusammenhängenden und strategischen Rahmen für die Entwicklung neuer Moleküle, die lumineszierende, katalytische und koordinative Eigenschaften kombinieren. Damit trägt diese Arbeit nicht nur zu fortschrittlichen Erkenntnissen auf dem Gebiet der metallorganischen Chemie bei, sondern eröffnet auch neue Wege zur Schaffung reaktionsfähiger molekularer Architekturen mit praktischem Anwendungspotenzial.

7. References

[1] S. Hong, J.-P. Candelone, C. C. Patterson and C. F. Boutron, *Science* **1996**, *272*, 246-249.
[2] G. M. Ingo, C. Riccucci, F. Faraldi, M. Pascucci, E. Messina, G. Fierro and G. Di Carlo, *Appl. Surf. Sci.* **2017**, *421*, 109-119.
[3] T. Higham, J. Chapman, V. Slavchev, B. Gaydarska, N. Honch, Y. Yordanov and B. Dimitrova, *Antiquity* **2007**, *81*, 640-654.
[4] T. Higham, V. Slavchev, B. Gaydarska and J. Chapman, *Radiocarbon* **2018**, *60*, 493-516.
[5] R. Wenzlhuemer, *Hist. Compass* **2007**, *5*, 1720-1742.
[6] V. S. Dubinin, T. A. Stepanova, S. O. Shkarupa and M. Y. Alekseevich, *J. Phys.: Conf. Ser.* **2021**, *1749*, 012030.
[7] https://markets.businessinsider.com/commodities/copper-price. 23.04.2025.
[8] B. J. Elliott, *Chapter 7 - Copper cable technology — cable*, (Ed. B. J. Elliott), Woodhead Publishing, **2000**, pp. 91-114.
[9] M. J. Schulz, B. Ruff, A. Johnson, K. Vemaganti, W. Li, M. M. Sundaram, G. Hou, A. Krishnaswamy, G. Li, S. Fialkova, S. Yarmolenko, A. Wang, Y. Liu, J. Sullivan, N. Alvarez, V. Shanov and S. Pixley, *Chapter 2 - New Applications and Techniques for Nanotube Superfiber Development*, (Eds.: M. J. Schulz, V. N. Shanov and Z. Yin), William Andrew Publishing, Boston, **2014**, pp. 33-59.
[10] G. P. Shultz, *Chapter 1 - Fundamental Concepts: Transformers*, (Ed. G. P. Shultz), Newnes, Boston, **1989**, pp. 3-22.
[11] D. Zheng, W. Zhang, S. Netsanet Alemu, P. Wang, G. T. Bitew, D. Wei and J. Yue, *Chapter 10 - Communication requirements of microgrids*, (Eds.: D. Zheng, W. Zhang, S. Netsanet Alemu, P. Wang, G. T. Bitew, D. Wei and J. Yue), Academic Press, **2021**, pp. 297-319.
[12] S. Moreno-Leiva, J. Haas, T. Junne, F. Valencia, H. Godin, W. Kracht, W. Nowak and L. Eltrop, *J. Clean. Prod.* **2020**, *246*, 118978.
[13] R. Hamze, J. L. Peltier, D. Sylvinson, M. Jung, J. Cardenas, R. Haiges, M. Soleilhavoup, R. Jazzar, P. I. Djurovich, G. Bertrand and M. E. Thompson, *Science* **2019**, *363*, 601-606.
[14] I. Salah, I. P. Parkin and E. Allan, *RSC Adv.* **2021**, *11*, 18179-18186.
[15] M. Vincent, R. E. Duval, P. Hartemann and M. Engels-Deutsch, *J. Appl. Microbiol.* **2018**, *124*, 1032-1046.
[16] C. Marzano, M. Pellei, F. Tisato and C. Santini, *Anti-Cancer Agents Med. Chem.* **2009**, *9*, 185-211.
[17] J. F. Machado, F. Marques, T. Pinheiro, M. J. Villa de Brito, G. Scalese, L. Pérez-Díaz, L. Otero, J. P. M. António, D. Gambino and T. S. Morais, *ChemMedChem* **2023**, *18*, e202300074.
[18] E. J. Underwood, *Chapter 3 - Copper*, (Ed. E. J. Underwood), Academic Press, **1977**, pp. 56-108.
[19] Z. W. Myint, T. H. Oo, K. Z. Thein, A. M. Tun and H. Saeed, *Ann. Hematol.* **2018**, *97*, 1527-1534.
[20] https://silverprice.org. 24.04.2025.
[21] S. Rout, P. Jana, C. R. Borra and M. A. R. Önal, *Renew. Sustain. Energy Rev.* **2025**, *210*, 115205.
[22] M. Polívková, T. Hubáček, M. Staszek, V. Švorčík and J. Siegel, *Int. J. Mol. Sci.* **2017**, *18*, 419.
[23] J. von Liebig, *London Edinburgh Dublin Philos. Mag. & J. Sci.* **1868**, *35*, 146-147.
[24] https://science.nasa.gov/mission/webb/webbs-mirrors/. 25.04.2025.
[25] C. A. Asiaghi, Gloves for touchscreen use US 8,528,117 B2; **2013**.
[26] C. Graham, *Br. J. Nurs.* **2005**, *14*, S22-S28.

[27] C. O. Enwonwu, *Environ. Res.* **1987**, *42*, 257-274.
[28] M. Hanson and J. Pleva, *Experientia* **1991**, *47*, 9-22.
[29] D. Bensalah, N. Gurbuz, I. Özdemir, R. Gatri, L. Mansour and N. Hamdi, *Bioinorg. Chem. Appl.* **2023**, *2023*, 3066299.
[30] F. Prencipe, A. Zanfardino, M. Di Napoli, F. Rossi, S. D'Errico, G. Piccialli, G. F. Mangiatordi, M. Saviano, L. Ronga, M. Varcamonti and D. Tesauro, *Int. J. Mol. Sci.* **2021**, *22*, 2497.
[31] E. Atalay Çetinkaya, A. Koç, H. Kübra Koç, H. Karabiyik, H. Karabiyik, E. Üstün and İ. Özdemir, *Polyhedron* **2023**, *237*, 116383.
[32] P. M. H. Petter, H. M. Veit and A. M. Bernardes, *Waste Manage.* **2014**, *34*, 475-482.
[33] M. C. Vats and S. K. Singh, *Waste Manage.* **2015**, *45*, 280-288.
[34] M. C. Gimeno, *The Chemistry of Gold*, **2008**, pp. 1-63.
[35] E. Rutherford, *London Edinburgh Dublin Philos. Mag. & J. Sci.* **1911**, *21*, 669-688.
[36] https://www.thorlabs.de/newgrouppage9.cfm?objectgroup_id=744. 24.04.2025.
[37] B. I. Gramatikov, *Optik* **2020**, *207*, 164474.
[38] https://science.nasa.gov/mission/webb/. 24.04.2025.
[39] R. de la Rica and M. M. Stevens, *Nat. Nanotechnol.* **2012**, *7*, 821-824.
[40] D. A. Giljohann, D. S. Seferos, W. L. Daniel, M. D. Massich, P. C. Patel and C. A. Mirkin, *Angew. Chem. Int. Ed.* **2010**, *49*, 3280-3294.
[41] I. Ott, *Coord. Chem. Rev.* **2009**, *253*, 1670-1681.
[42] B. Bertrand and A. Casini, *Dalton Trans.* **2014**, *43*, 4209-4219.
[43] C. I. Yeo, K. K. Ooi and E. R. T. Tiekink, *Molecules* **2018**, *23*, 1410.
[44] F. E. Kühn and A. Schmidt, *Chem. Unserer Zeit* **2017**, *51*, 86-95.
[45] R. V. Parish, B. P. Howe, J. P. Wright, J. Mack, R. G. Pritchard, R. G. Buckley, A. M. Elsome and S. P. Fricker, *Inorg. Chem.* **1996**, *35*, 1659-1666.
[46] T. Zou, C. T. Lum, C.-N. Lok, J.-J. Zhang and C.-M. Che, *Chem. Soc. Rev.* **2015**, *44*, 8786-8801.
[47] C. Roder and M. J. Thomson, *Drugs R&D* **2015**, *15*, 13-20.
[48] N. Tejman-Yarden, Y. Miyamoto, D. Leitsch, J. Santini, A. Debnath, J. Gut, J. H. McKerrow, S. L. Reed and L. Eckmann, *Antimicrob. Agents Chemother.* **2013**, *57*, 2029-2035.
[49] H. Lu, W. Lu, Y. Zhu, C. Wang, L. Shi, X. Li, Z. Wu, G. Wang, W. Dong, C. Tan and M. Liu, *Antibiotics* **2021**, *10*, 26.
[50] C.-Y. Wong, M.-C. Tang, L.-K. Li, M.-Y. Leung, W.-K. Tang, S.-L. Lai, W.-L. Cheung, M. Ng, M.-Y. Chan and V. W.-W. Yam, *Chem. Sci.* **2022**, *13*, 10129-10140.
[51] M.-C. Tang, M.-Y. Chan and V. W.-W. Yam, *Chem. Rev.* **2021**, *121*, 7249-7279.
[52] S. G. Bratsch, *J. Phys. Chem. Ref. Data* **1989**, *18*, 1-21.
[53] F. A. Cotton, G. Wilkinson and P. L. Gaus, *Basic Inorganic Chemistry*, Wiley & Sons, **1995**, p. 856.
[54] H. Schmidbaur and J. L. Cihonski, *Noble Metals (Chemistry)*, (Ed. R. A. Meyers), Academic Press, New York, **2003**, pp. 463-492.
[55] https://www.britannica.com/technology/copper-processing/Copper-nickel. 28.04.2025.
[56] G. W. Watt and J. W. Dawes, *J. Inorg. Nucl. Chem.* **1960**, *14*, 32-34.
[57] K. Hua, F. Xie, S. Ye and M.-T. Zhang, *JACS Au* **2024**, *4*, 4406-4414.
[58] O. V. Mikhailov and D. V. Chachkov, *Inorg. Chem. Commun.* **2019**, *106*, 224-227.
[59] R. A. Jackson, N. J. Evans, D. J. Babula, T. M. Horsley Downie, R. S. C. Charman, S. E. Neale, M. F. Mahon and D. J. Liptrot, *Nat. Commun.* **2025**, *16*, 1101.

[60] D. S. Weinberger, N. Amin Sk, K. C. Mondal, M. Melaimi, G. Bertrand, A. C. Stückl, H. W. Roesky, B. Dittrich, S. Demeshko, B. Schwederski, W. Kaim, P. Jerabek and G. Frenking, *J. Am. Chem. Soc.* **2014**, *136*, 6235-6238.
[61] Y. Liu, S. G. Resch, I. Klawitter, G. E. Cutsail III, S. Demeshko, S. Dechert, F. E. Kühn, S. DeBeer and F. Meyer, *Angew. Chem. Int. Ed.* **2020**, *59*, 5696-5705.
[62] F. H. Jardine, *Copper (I) Complexes*, *Vol. 17*, (Eds.: H. J. Emeléus and A. G. Sharpe), Academic Press, **1975**, pp. 115-163.
[63] D. Kakizoe, M. Nishikawa, Y. Fujii and T. Tsubomura, *Dalton Trans.* **2017**, *46*, 14804-14811.
[64] H. Zhang, B. Yao, L. Zhao, D.-X. Wang, B.-Q. Xu and M.-X. Wang, *J. Am. Chem. Soc.* **2014**, *136*, 6326-6332.
[65] Y. K. Maurya, K. Noda, K. Yamasumi, S. Mori, T. Uchiyama, K. Kamitani, T. Hirai, K. Ninomiya, M. Nishibori, Y. Hori, Y. Shiota, K. Yoshizawa, M. Ishida and H. Furuta, *J. Am. Chem. Soc.* **2018**, *140*, 6883-6892.
[66] W. Harnischmacher and R. Hoppe, *Angew. Chem. Int. Ed.* **1973**, *12*, 582-583.
[67] D. Kissel and R. Hoppe, *Z. Anorg. Allg. Chem.* **1988**, *559*, 40-48.
[68] T. V. Popova and N. V. Aksenova, *Russ. J. Coord. Chem.* **2003**, *29*, 743-765.
[69] G. A. Palyanova, *Geol. Ore Depos.* **2020**, *62*, 383-406.
[70] E. Y. Yazici, E. Yilmaz, F. Ahlatci, O. Celep and H. Deveci, *Hydrometallurgy* **2017**, *174*, 175-183.
[71] A. Williams, *J. Phys.: Condens. Matter* **1989**, *1*, 2569.
[72] F. A. Cotton and G. Wilkinson, *Advanced Inorganic Chemistry*, Wiley & Sons, **1988**, p. 1355.
[73] G. Kleinhans, A. K.-W. Chan, M.-Y. Leung, D. C. Liles, M. A. Fernandes, V. W.-W. Yam, I. Fernández and D. I. Bezuidenhout, *Chem. Eur. J.* **2020**, *26*, 6993-6998.
[74] J. Jimenez, I. Chakraborty, A. M. Del Cid and P. K. Mascharak, *Inorg. Chem.* **2017**, *56*, 4784-4787.
[75] G. A. Broker and E. R. T. Tiekink, *Acta Crystallogr. E: Crystallogr. Commun.* **2007**, *63*, m2368.
[76] W. Levason and M. D. Spicer, *Coord. Chem. Rev.* **1987**, *76*, 45-120.
[77] A. K. Singh, F. S. T. Khan and S. P. Rath, *Angew. Chem. Int. Ed.* **2017**, *56*, 8849-8854.
[78] S. M. Zhmodik, E. V. Airiyants, D. K. Belyanin, B. B. Damdinov, N. S. Karmanov, O. N. Kiseleva, A. V. Kozlov, A. A. Mironov, T. N. Moroz and V. A. Ponomarchuk, *Minerals* **2023**, *13*, 1149.
[79] A. Anand, S. Singh, A. Gantait, A. Srivastava, G. K. Mayachar and M. Kumar, *Minerals* **2022**, *12*, 1345.
[80] V. Murzin, G. Palyanova, T. Mayorova and T. Beliaeva, *Minerals* **2022**, *12*, 765.
[81] G. A. Palyanova, P. S. Zhegunov, T. V. Beliaeva, V. V. Murzin, A. A. Borovikov and N. A. Goryachev, *Minerals* **2023**, *13*, 1019.
[82] J. Chen, Y. Li and C. Zhao, *Comput. Mater. Sci.* **2014**, *88*, 1-6.
[83] L. E. Orgel, *J. Am. Chem. Soc.* **1958**, 4186-4190.
[84] M. N. I. Khan, R. J. Staples, C. King, J. P. Fackler, Jr. and R. E. P. Winpenny, *Inorg. Chem.* **1993**, *32*, 5800-5807.
[85] J. Meiners, J.-S. Herrmann and P. W. Roesky, *Inorg. Chem.* **2007**, *46*, 4599-4604.
[86] A. Straube, P. Coburger, M. R. Ringenberg and E. Hey-Hawkins, *Chem. Eur. J.* **2020**, *26*, 5758-5764.
[87] W. J. Peer and J. J. Lagowski, *J. Am. Chem. Soc.* **1978**, *100*, 6260-6261.
[88] F. Fetzer, N. Pollard, N. C. Michenfelder, M. Strienz, A. N. Unterreiner, A. Z. Clayborne and A. Schnepf, *Angew. Chem. Int. Ed.* **2022**, *61*, e202206019.

[89] M. N. I. Khan, S. Wang and J. P. Fackler, Jr., *Inorg. Chem.* **1989**, *28*, 3579-3588.
[90] D. Himmel and S. Riedel, *Inorg. Chem.* **2007**, *46*, 5338-5342.
[91] G. J. Hutchings, *ACS Cent. Sci.* **2018**, *4*, 1095-1101.
[92] J.-U. Kim, S.-H. Cha, K. Shin, J. Y. Jho and J.-C. Lee, *J. Am. Chem. Soc.* **2005**, *127*, 9962-9963.
[93] X. S. Boon K. Teo, Hong Zhang, *J. Am. Chem. Soc.* **1992**, *114*, 2743-2745.
[94] S. Kenzler and A. Schnepf, *Chem. Sci.* **2021**, *12*, 3116-3129.
[95] T. J. Robilotto, J. Bacsa, T. G. Gray and J. P. Sadighi, *Angew. Chem. Int. Ed.* **2012**, *51*, 12077-12080.
[96] D. S. Weinberger, M. Melaimi, C. E. Moore, A. L. Rheingold, G. Frenking, P. Jerabek and G. Bertrand, *Angew. Chem. Int. Ed.* **2013**, *52*, 8964-8967.
[97] A. J. Blake, J. A. Greig, A. J. Holder, T. I. Hyde, A. Taylor and M. Schröder, *Angew. Chem. Int. Ed.* **1990**, *29*, 197-198.
[98] S. Seidel and K. Seppelt, *Science* **2000**, *290*, 117-118.
[99] S. Preiß, C. Förster, S. Otto, M. Bauer, P. Müller, D. Hinderberger, H. Hashemi Haeri, L. Carella and K. Heinze, *Nat. Chem.* **2017**, *9*, 1249-1255.
[100] W. Lu, H. Hu, Y. Li, R. Ganguly and R. Kinjo, *J. Am. Chem. Soc.* **2016**, *138*, 6650-6661.
[101] J. Hicks, P. Vasko, J. M. Goicoechea and S. Aldridge, *Nature* **2018**, *557*, 92-95.
[102] J. Hicks, A. Mansikkamäki, P. Vasko, J. M. Goicoechea and S. Aldridge, *Nat. Chem.* **2019**, *11*, 237-241.
[103] P. Pyykko, *Chem. Rev.* **1988**, *88*, 563-594.
[104] P. Schwerdtfeger, P. D. W. Boyd, S. Brienne and A. K. Burrell, *Inorg. Chem.* **1992**, *31*, 3411-3422.
[105] A. Einstein, *Ann. Phys.* **1916**, *354*, 769-822.
[106] P. Pyykko and J. P. Desclaux, *Acc. Chem. Res.* **1979**, *12*, 276-281.
[107] O. L. Trinhammer and H. G. Bohr, *Europhys. Lett.* **2019**, *128*, 21001.
[108] H. Schmidbaur, *Gold Bull.* **1990**, *23*, 11-21.
[109] V. W.-W. Yam and E. C.-C. Cheng, *Chem. Soc. Rev.* **2008**, *37*, 1806-1813.
[110] R. T. Sanderson, *Inorg. Chem.* **1986**, *25*, 1856-1858.
[111] S. Löffelsender, P. Schwerdtfeger, S. Grimme and J.-M. Mewes, *J. Am. Chem. Soc.* **2022**, *144*, 485-494.
[112] N. Bartlett, *Gold Bull.* **1998**, *31*, 22-25.
[113] P. Pyykkö, J. Li and N. Runeberg, *Chem. Phys. Lett.* **1994**, *218*, 133-138.
[114] P. G. Huray in *Maxwell's equations*, *Vol.* Wiley : IEEE Press, Hoboken, N.J., **2010**.
[115] L. H. Doerrer, *Dalton Trans.* **2010**, *39*, 3543-3553.
[116] V. R. Naina, F. Krätschmer and P. W. Roesky, *Chem. Commun.* **2022**, *58*, 5332-5346.
[117] H. B. Gray, S. Záliš and A. Vlček, *Coord. Chem. Rev.* **2017**, *345*, 297-317.
[118] E. J. Fernández, A. Laguna and J. M. López-de-Luzuriaga, *Gold Bull.* **2001**, *34*, 14-19.
[119] R. Guajardo Maturana and A. Muñoz-Castro, *Chem. Phys. Lett.* **2016**, *651*, 34-38.
[120] M. Jansen, *Angew. Chem. Int. Ed.* **1987**, *26*, 1098-1110.
[121] S. Sculfort and P. Braunstein, *Chem. Soc. Rev.* **2011**, *40*, 2741-2760.
[122] H. Schmidbaur and A. Schier, *Chem. Soc. Rev.* **2012**, *41*, 370-412.
[123] P. Pyykkö and Y. Zhao, *Angew. Chem. Int. Ed.* **1991**, *30*, 604-605.
[124] F. London, *Trans. Faraday Soc.* **1937**, *33*, 8-26.
[125] J. Li and P. Pyykkö, *Chem. Phys. Lett.* **1992**, *197*, 586-590.
[126] N. Runeberg, M. Schütz and H.-J. Werner, *J. Chem. Phys.* **1999**, *110*, 7210-7215.
[127] H. Schmidbaur and A. Schier, *Chem. Soc. Rev.* **2008**, *37*, 1931-1951.

[128] M. Dahlen, M. Kehry, S. Lebedkin, M. M. Kappes, W. Klopper and P. W. Roesky, *Dalton Trans.* **2021**, *50*, 13412-13420.
[129] H. Schmidbaur and A. Schier, *Angew. Chem. Int. Ed.* **2015**, *54*, 746-784.
[130] A. K. Jassal, *Inorg. Chem. Front.* **2020**, *7*, 3735-3764.
[131] N. V. S. Harisomayajula, B.-H. Wu, D.-Y. Lu, T.-S. Kuo, I.-C. Chen and Y.-C. Tsai, *Angew. Chem. Int. Ed.* **2018**, *57*, 9925-9929.
[132] H. L. Hermann, G. Boche and P. Schwerdtfeger, *Chem. Eur. J.* **2001**, *7*, 5333-5342.
[133] J. R. Lakowicz, *Principles of Fluorescence Spectroscopy* Springer, **2006**, p. 954.
[134] P. Atkins, *Shriver and Atkins' inorganic chemistry*, Oxford University Press, USA, **2010**, p. 824.
[135] J. F. W. Herschel, *Philos. Trans. R. Soc.* **1845**, *135*, 147-153.
[136] M. Swaminathan, *Fluorescence and phosphorescence spectroscopy*, Jenny Stanford Publishing, **2023**, pp. 279-306.
[137] B. P. Straughan and S. Walker, *Fluorescence and Phosphorescence Spectroscopy*, (Eds.: B. P. Straughan and S. Walker), Springer Netherlands, Dordrecht, **1976**, pp. 161-198.
[138] R. Delorme and F. Perrin, *J. Phys. Radium* **1929**, *10*, 177-186.
[139] G. N. Lewis, D. Lipkin and T. T. Magel, *J. Am. Chem. Soc.* **1941**, *63*, 3005-3018.
[140] H. Uoyama, K. Goushi, K. Shizu, H. Nomura and C. Adachi, *Nature* **2012**, *492*, 234-238.
[141] R. Gao, M. S. Kodaimati and D. Yan, *Chem. Soc. Rev.* **2021**, *50*, 5564-5589.
[142] T. Hofbeck, U. Monkowius and H. Yersin, *J. Am. Chem. Soc.* **2015**, *137*, 399-404.
[143] M. J. Leitl, V. A. Krylova, P. I. Djurovich, M. E. Thompson and H. Yersin, *J. Am. Chem. Soc.* **2014**, *136*, 16032-16038.
[144] G. J. P. Britovsek, V. C. Gibson and D. F. Wass, *Angew. Chem. Int. Ed.* **1999**, *38*, 428-447.
[145] R. Kempe, *Angew. Chem. Int. Ed.* **2000**, *39*, 468-493.
[146] F. T. Edelmann, *Chapter 2 - Recent Progress in the Chemistry of Metal Amidinates and Guanidinates: Syntheses, Catalysis and Materials*, *Vol. 61*, (Eds.: A. F. Hill and M. J. Fink), Academic Press, **2013**, pp. 55-374.
[147] F. T. Edelmann, *Chem. Soc. Rev.* **2009**, *38*, 2253-2268.
[148] P. C. Junk and M. L. Cole, *Chem. Commun.* **2007**, 1579-1590.
[149] L. Bourget-Merle, M. F. Lappert and J. R. Severn, *Chem. Rev.* **2002**, *102*, 3031-3066.
[150] P. W. Roesky, *Chem. Soc. Rev.* **2000**, *29*, 335-345.
[151] A. A. Trifonov, *Coord. Chem. Rev.* **2010**, *254*, 1327-1347.
[152] S. Collins, *Coord. Chem. Rev.* **2011**, *255*, 118-138.
[153] B. Goswami and P. W. Roesky, *Inorg. Chem. Front.* **2025**, *12*, 3555-3581.
[154] M. Asay, C. Jones and M. Driess, *Chem. Rev.* **2011**, *111*, 354-396.
[155] F. T. Edelmann, *Coord. Chem. Rev.* **1994**, *137*, 403-481.
[156] M. P. Coles, *Dalton Trans.* **2006**, 985-1001.
[157] S.-i. Ogata, A. Mochizuki, M.-a. Kakimoto and Y. Imai, *Bull. Chem. Soc. Jpn.* **1986**, *59*, 2171-2177.
[158] F. T. Edelmann, *Angew. Chem. Int. Ed.* **1995**, *34*, 2466-2488.
[159] M. P. Coles, D. C. Swenson, R. F. Jordan and V. G. Young, *Organometallics* **1997**, *16*, 5183-5194.
[160] S. Fichter, S. Kaufmann, P. Kaden, T. S. Brunner, T. Stumpf, P. W. Roesky and J. März, *Chem. Eur. J.* **2020**, *26*, 8867-8870.
[161] T. S. Brunner, P. Benndorf, M. T. Gamer, N. Knöfel, K. Gugau and P. W. Roesky, *Organometallics* **2016**, *35*, 3474-3487.

[162] F. T. Edelmann, *Chapter 3 - Advances in the Coordination Chemistry of Amidinate and Guanidinate Ligands*, *Vol. 57*, (Eds.: A. F. Hill and M. J. Fink), Academic Press, **2008**, pp. 183-352.
[163] A. R. Sanger, *Inorg. Nucl. Chem. Lett.* **1973**, *9*, 351-354.
[164] R. T. Boeré, R. T. Oakley and R. W. Reed, *J. Organomet. Chem.* **1987**, *331*, 161-167.
[165] D. Fenske, G. Baum, A. Zinn and K. Dehnicke, *Z. Naturforsch. B* **1990**, *45*, 1273-1278.
[166] T. J. Feuerstein, M. Poß, T. P. Seifert, S. Bestgen, C. Feldmann and P. W. Roesky, *Chem. Commun.* **2017**, *53*, 9012-9015.
[167] S. Kaufmann and P. W. Roesky, *Eur. J. Inorg. Chem.* **2021**, *2021*, 2899-2905.
[168] R. Kretschmer, *Chem. Eur. J.* **2020**, *26*, 2099-2119.
[169] T. W. J.-W. Mao, R.-Q. Liu, Sh.-D. Bai, J.-P. Guo, D.-Sh. Liu, *Mendeleev Commun.* **2013**, *2*, 2.
[170] M. Dahlen, J. Vázquez Quesada, L. Santos Correa, L. Münzfeld, N. Reinfandt, W. Klopper and P. W. Roesky, *ACS Omega* **2022**, *7*, 4683-4693.
[171] R. G. Pearson, *J. Chem. Educ.* **1968**, *45*, 643.
[172] R. G. Pearson, *J. Chem. Educ.* **1968**, *45*, 581.
[173] W.-H. Chan, K.-K. Cheung, T. C. W. Mak and C.-M. Che, *J. Chem. Soc., Dalton Trans.* **1998**, 873-874.
[174] N. Tsukada, O. Tamura and Y. Inoue, *Organometallics* **2002**, *21*, 2521-2528.
[175] M. Dahlen, E. H. Hollesen, M. Kehry, M. T. Gamer, S. Lebedkin, D. Schooss, M. M. Kappes, W. Klopper and P. W. Roesky, *Angew. Chem. Int. Ed.* **2021**, *60*, 23365-23372.
[176] C. Zovko, S. Bestgen, C. Schoo, A. Görner, J. M. Goicoechea and P. W. Roesky, *Chem. Eur. J.* **2020**, *26*, 13191-13202.
[177] V. J. Catalano, J. M. López-de-Luzuriaga, M. Monge, M. E. Olmos and D. Pascual, *Dalton Trans.* **2014**, *43*, 16486-16497.
[178] S. Nayeri, S. Jamali, A. Jamjah and H. Samouei, *Inorg. Chem.* **2019**, *58*, 12122-12131.
[179] J.-B. Dumas and E. M. Peligot, *Ann. Chim. Phys.* **1835**, *58*, 5-74.
[180] H. W. Wanzlick, *Angew. Chem. Int. Ed.* **1962**, *1*, 75-80.
[181] K. Öfele, *J. Organomet. Chem.* **1968**, *12*, P42-P43.
[182] H.-W. Wanzlick and H.-J. Schönherr, *Angew. Chem. Int. Ed.* **1968**, *7*, 141-142.
[183] A. J. Arduengo, III, R. L. Harlow and M. Kline, *J. Am. Chem. Soc.* **1991**, *113*, 361-363.
[184] C. Heinemann and W. Thiel, *Chem. Phys. Lett.* **1994**, *217*, 11-16.
[185] R. Hoffmann, *J. Am. Chem. Soc.* **1968**, *90*, 1475-1485.
[186] D. Bourissou, O. Guerret, F. P. Gabbaï and G. Bertrand, *Chem. Rev.* **2000**, *100*, 39-92.
[187] H. Jacobsen, A. Correa, A. Poater, C. Costabile and L. Cavallo, *Coord. Chem. Rev.* **2009**, *253*, 687-703.
[188] D. Nemcsok, K. Wichmann and G. Frenking, *Organometallics* **2004**, *23*, 3640-3646.
[189] D. J. Nelson and S. P. Nolan, *Chem. Soc. Rev.* **2013**, *42*, 6723-6753.
[190] C. Boehme and G. Frenking, *Organometallics* **1998**, *17*, 5801-5809.
[191] C. A. Tolman, *Chem. Rev.* **1977**, *77*, 313-348.
[192] A. R. Chianese, X. Li, M. C. Janzen, J. W. Faller and R. H. Crabtree, *Organometallics* **2003**, *22*, 1663-1667.
[193] S. Wolf and H. Plenio, *J. Organomet. Chem.* **2009**, *694*, 1487-1492.
[194] D. Cremer and E. Kraka, *Dalton Trans.* **2017**, *46*, 8323-8338.
[195] D. S. Coll, A. B. Vidal, J. A. Rodríguez, E. Ocando-Mavárez, R. Añez and A. Sierraalta, *Inorg. Chim. Acta* **2015**, *436*, 163-168.
[196] R. Kalescky, E. Kraka and D. Cremer, *Inorg. Chem.* **2014**, *53*, 478-495.

[197] H. Clavier and S. P. Nolan, *Chem. Commun.* **2010**, *46*, 841-861.
[198] D. J. Cardin, B. Cetinkaya, M. F. Lappert, L. Manojlović-Muir and K. W. Muir, *J. Chem. Soc. D, Chem. Commun.* **1971**, 400-401.
[199] M. Scholl, S. Ding, C. W. Lee and R. H. Grubbs, *Org. Lett.* **1999**, *1*, 953-956.
[200] E. Peris, *Routes to N-Heterocyclic Carbene Complexes*, (Ed. F. Glorius), Springer Berlin Heidelberg, Berlin, Heidelberg, **2007**, pp. 83-116.
[201] W. A. Herrmann, M. Elison, J. Fischer, C. Köcher and G. R. J. Artus, *Chem. Eur. J.* **1996**, *2*, 772-780.
[202] J. Huang, E. D. Stevens, S. P. Nolan and J. L. Petersen, *J. Am. Chem. Soc.* **1999**, *121*, 2674-2678.
[203] K. Öfele, W. A. Herrmann, D. Mihalios, M. Elison, E. Herdtweck, W. Scherer and J. Mink, *J. Organomet. Chem.* **1993**, *459*, 177-184.
[204] H. M. J. Wang and I. J. B. Lin, *Organometallics* **1998**, *17*, 972-975.
[205] O. Santoro, F. Lazreg, D. B. Cordes, A. M. Z. Slawin and C. S. J. Cazin, *Dalton Trans.* **2016**, *45*, 4970-4973.
[206] K. Okamoto, J. Kuwabara and T. Kanbara, *Thioamide-Based Transition Metal Complexes*, (Ed. T. Murai), Springer Singapore, Singapore, **2019**, pp. 157-191.
[207] J.-M. Bret, P. Castan and J.-P. Laurent, *Transition Met. Chem.* **1983**, *8*, 218-221.
[208] M. H. Habibi, S. Tangestaninejad, A. Fallah-Shojaie, I. Mohammadpoor-Baltork, S. F. Tayyari, G. Emtiazi and R. Hamidimotlagh, *J. Coord. Chem.* **2005**, *58*, 955-962.
[209] A. Ranskiy, N. Didenko and O. Gordienko, *Chem. Chem. Technol.* **2016**, *11*, 11-18.
[210] T. Hamaguchi, K. Ujimoto and I. Ando, *Inorg. Chem.* **2007**, *46*, 10455-10457.
[211] G. Dyson, A. Hamilton, B. Mitchell and G. R. Owen, *Dalton Trans.* **2009**, 6120-6126.
[212] M. N. Xanthopoulou, S. K. Hadjikakou, N. Hadjiliadis, E. R. Milaeva, J. A. Gracheva, V. Y. Tyurin, N. Kourkoumelis, K. C. Christoforidis, A. K. Metsios, S. Karkabounas and K. Charalabopoulos, *Eur. J. Med. Chem.* **2008**, *43*, 327-335.
[213] C. Alagöz, D. J. Brauer and F. Mohr, *J. Organomet. Chem.* **2009**, *694*, 1283-1288.
[214] A. L. Catherall, S. Harris, M. S. Hill, A. L. Johnson and M. F. Mahon, *Cryst. Growth Des.* **2017**, *17*, 5544-5551.
[215] D. Das, S. S. Mohapatra and S. Roy, *Chem. Soc. Rev.* **2015**, *44*, 3666-3690.
[216] B. G. Cooper, J. W. Napoline and C. M. Thomas, *Catal. Rev. - Sci. Eng.* **2012**, *54*, 1-40.
[217] H. Xu, R. Chen, Q. Sun, W. Lai, Q. Su, W. Huang and X. Liu, *Chem. Soc. Rev.* **2014**, *43*, 3259-3302.
[218] N. Desbois, S. Pacquelet, A. Dubois, C. Michelin and C. P. Gros, *Beilstein J. Org. Chem.* **2015**, *11*, 2202-2208.
[219] M. Böhmer, G. Guisado-Barrios, F. Kampert, F. Roelfes, T. T. Y. Tan, E. Peris and F. E. Hahn, *Organometallics* **2019**, *38*, 2120-2131.
[220] W. Zhou in *Synthesis and Catalytic Application of Heterobimetallic Complexes*, *Vol. Doctor of Philosophy* Brandeis University, **2013**.
[221] M. Hardy, N. Struch, F. Topić, G. Schnakenburg, K. Rissanen and A. Lützen, *Inorg. Chem.* **2018**, *57*, 3507-3515.
[222] H.-K. Yip, H.-M. Lin, K.-K. Cheung, C.-M. Che and Y. Wang, *Inorg. Chem.* **1994**, *33*, 1644-1651.
[223] C. Uhlmann, T. J. Feuerstein, T. P. Seifert, A. P. Jung, M. T. Gamer, R. Köppe, S. Lebedkin, M. M. Kappes and P. W. Roesky, *Dalton Trans.* **2022**, *51*, 10357-10360.
[224] H.-K. Yip, H.-M. Lin, Y. Wang and C.-M. Che, *J. Chem. Soc., Dalton Trans.* **1993**, 2939-2944.
[225] V. W.-W. Yam and K. M.-C. Wong, *Chem. Commun.* **2011**, *47*, 11579-11592.

[226] R. G. Pearson, *J. Am. Chem. Soc.* **1963**, *85*, 3533-3539.
[227] V. J. Catalano, M. A. Malwitz and A. O. Etogo, *Inorg. Chem.* **2004**, *43*, 5714-5724.
[228] V. J. Catalano and A. L. Moore, *Inorg. Chem.* **2005**, *44*, 6558-6566.
[229] M. J. Calhorda, C. Ceamanos, O. Crespo, M. C. Gimeno, A. Laguna, C. Larraz, P. D. Vaz and M. D. Villacampa, *Inorg. Chem.* **2010**, *49*, 8255-8269.
[230] C. E. Strasser and V. J. Catalano, *Inorg. Chem.* **2011**, *50*, 11228-11234.
[231] E. Hobbollahi, M. List, B. Hupp, F. Mohr, R. J. F. Berger, A. Steffen and U. Monkowius, *Dalton Trans.* **2017**, *46*, 3438-3442.
[232] C. Kaub, S. Lebedkin, A. Li, S. V. Kruppa, P. H. Strebert, M. M. Kappes, C. Riehn and P. W. Roesky, *Chem. Eur. J.* **2018**, *24*, 6094-6104.
[233] C. Kaub, S. Lebedkin, S. Bestgen, R. Köppe, M. M. Kappes and P. W. Roesky, *Chem. Commun.* **2017**, *53*, 9578-9581.
[234] O. Crespo, E. J. Fernández, M. Gil, M. Concepción Gimeno, P. G. Jones, A. Laguna, J. M. López-de-Luzuriaga and M. Elena Olmos, *J. Chem. Soc., Dalton Trans.* **2002**, 1319-1326.
[235] T. P. Seifert, S. Bestgen, T. J. Feuerstein, S. Lebedkin, F. Krämer, C. Fengler, M. T. Gamer, M. M. Kappes and P. W. Roesky, *Dalton Trans.* **2019**, *48*, 15427-15434.
[236] N. Mirzadeh, S. H. Privér, A. J. Blake, H. Schmidbaur and S. K. Bhargava, *Chem. Rev.* **2020**, *120*, 7551-7591.
[237] S. Raju, H. B. Singh and R. J. Butcher, *Dalton Trans.* **2020**, *49*, 9099-9117.
[238] V. W.-W. Yam, V. K.-M. Au and S. Y.-L. Leung, *Chem. Rev.* **2015**, *115*, 7589-7728.
[239] F. Scherbaum, A. Grohmann, B. Huber, C. Krüger and H. Schmidbaur, *Angew. Chem. Int. Ed.* **1988**, *27*, 1544-1546.
[240] N. V. S. Harisomayajula, S. Makovetskyi and Y.-C. Tsai, *Chem. Eur. J.* **2019**, *25*, 8936-8954.
[241] V. Wing-Wah Yam and E. Chung-Chin Cheng, *Photochemistry and Photophysics of Coordination Compounds: Gold*, (Eds.: V. Balzani and S. Campagna), Springer Berlin Heidelberg, Berlin, Heidelberg, **2007**, pp. 269-309.
[242] S. Bestgen, M. T. Gamer, S. Lebedkin, M. M. Kappes and P. W. Roesky, *Chem. Eur. J.* **2015**, *21*, 601-614.
[243] Z. Li, S. T. Barry and R. G. Gordon, *Inorg. Chem.* **2005**, *44*, 1728-1735.
[244] A. C. Lane, M. V. Vollmer, C. H. Laber, D. Y. Melgarejo, G. M. Chiarella, J. P. Fackler, Jr., X. Yang, G. A. Baker and J. R. Walensky, *Inorg. Chem.* **2014**, *53*, 11357-11366.
[245] A. C. Lane, C. L. Barnes, W. E. Antholine, D. Wang, A. T. Fiedler and J. R. Walensky, *Inorg. Chem.* **2015**, *54*, 8509-8517.
[246] A. Márquez, E. Ávila, C. Urbaneja, E. Álvarez, P. Palma and J. Cámpora, *Inorg. Chem.* **2015**, *54*, 11007-11017.
[247] N. V. S. Harisomayajula, B.-H. Wu, D.-Y. Lu, T.-S. Kuo, I. C. Chen and Y.-C. Tsai, *Angew. Chem. Int. Ed.* **2018**, *57*, 9925-9929.
[248] N. Nebra, C. Lescot, P. Dauban, S. Mallet-Ladeira, B. Martin-Vaca and D. Bourissou, *Eur. J. Org. Chem.* **2013**, *2013*, 984-990.
[249] V. R. Naina, A. K. Singh, P. Rauthe, S. Lebedkin, M. T. Gamer, M. M. Kappes, A.-N. Unterreiner and P. W. Roesky, *Chem. Eur. J.* **2023**, *29*, e202300497.
[250] R. P. Herrera and M. C. Gimeno, *Chem. Rev.* **2021**, *121*, 8311-8363.
[251] T. J. Feuerstein, T. P. Seifert, A. P. Jung, R. Müller, S. Lebedkin, M. M. Kappes and P. W. Roesky, *Chem. Eur. J.* **2020**, *26*, 16676-16682.
[252] M. Dahlen, T. P. Seifert, S. Lebedkin, M. T. Gamer, M. M. Kappes and P. W. Roesky, *Chem. Commun.* **2021**, *57*, 13146-13149.

[253] A. Chakraborty, J. C. Deaton, A. Haefele and F. N. Castellano, *Organometallics* **2013**, *32*, 3819-3829.
[254] V. W.-W. Yam, T.-F. Lai and C.-M. Che, *J. Chem. Soc., Dalton Trans.* **1990**, 3747-3752.
[255] H. Amouri, *Chem. Rev.* **2023**, *123*, 230-270.
[256] A. Ghodbane, N. Saffon, S. Blanc and S. Fery-Forgues, *Dyes Pigm.* **2015**, *113*, 219-226.
[257] H. Yersin, R. Czerwieniec, U. Monkowius, R. Ramazanov, R. Valiev, M. Z. Shafikov, W.-M. Kwok and C. Ma, *Coord. Chem. Rev.* **2023**, *478*, 214975.
[258] Y. Chen, C. Liu and L. Wang, *Tetrahedron* **2019**, *75*, 130686.
[259] J. Ma, J. Schaab, S. Paul, S. R. Forrest, P. I. Djurovich and M. E. Thompson, *J. Am. Chem. Soc.* **2023**, *145*, 20097-20108.
[260] S. K. Langley, C. Le, L. Ungur, B. Moubaraki, B. F. Abrahams, L. F. Chibotaru and K. S. Murray, *Inorg. Chem.* **2015**, *54*, 3631-3642.
[261] J. A. Chipman and J. F. Berry, *Chem. Rev.* **2020**, *120*, 2409-2447.
[262] L. Peña, C. Jiménez, R. Arancibia, A. Angeli and C. T. Supuran, *J. Inorg. Biochem.* **2022**, *232*, 111814.
[263] Shubham, V. R. Naina and P. W. Roesky, *Chem. Eur. J.* **2024**, *30*, e202401696.
[264] V. Ritleng and M. J. Chetcuti, *Chem. Rev.* **2007**, *107*, 797-858.
[265] B. Bertrand, G. Gontard, C. Botuha and M. Salmain, *Eur. J. Inorg. Chem.* **2020**, *2020*, 3370-3377.
[266] A. Hicken, A. J. P. White and M. R. Crimmin, *Dalton Trans.* **2018**, *47*, 10595-10600.
[267] A. Neshat, A. Mahdavi, M. R. Yousefshahi, M. Cheraghi, S. Mohammadi, V. Eigner, M. Kucerakova, M. Dusek, B. Kaboudin and M. R. Halvagar, *J. Organomet. Chem.* **2024**, *1005*, 122972.
[268] S. Srivastava, A. Ali, A. Tyagi and R. Gupta, *Eur. J. Inorg. Chem.* **2014**, *2014*, 2113-2123.
[269] T. P. Seifert, V. R. Naina, T. J. Feuerstein, N. D. Knöfel and P. W. Roesky, *Nanoscale* **2020**, *12*, 20065-20088.
[270] R. Maity, B. S. Birenheide, F. Breher and B. Sarkar, *ChemCatChem* **2021**, *13*, 2337-2370.
[271] A. Majumder, T. Nath Saha, N. Majumder, R. Naskar, K. Pal and R. Maity, *Eur. J. Inorg. Chem.* **2021**, *2021*, 1104-1110.
[272] A. Majumder, R. Naskar, P. Roy, B. Mondal, S. Garai and R. Maity, *Dalton Trans.* **2023**, *52*, 2272-2281.
[273] Z. Fickenscher and E. Hey-Hawkins, *Molecules* **2023**, *28*, 4233.
[274] T. L. Lohr and T. J. Marks, *Nat. Chem.* **2015**, *7*, 477-482.
[275] D. E. Fogg and E. N. dos Santos, *Coord. Chem. Rev.* **2004**, *248*, 2365-2379.
[276] A. Sharma, V. Tiwari, R. Yadav, B. Das, C. Majumder, A. Das, T. Karmakar and S. Kundu, *Organometallics* **2024**, *43*, 3054-3061.
[277] W. Wang, L. Zhao, H. Lv, G. Zhang, C. Xia, F. E. Hahn and F. Li, *Angew. Chem. Int. Ed.* **2016**, *55*, 7665-7670.
[278] S. A. Chala, R. Liu, E. O. Oseghe, S. T. Clausing, C. Kampf, J. Bansmann, A. H. Clark, Y. Zhou, I. Lieberwirth, J. Biskupek, U. Kaiser and C. Streb, *ACS Catal.* **2024**, *14*, 15553-15564.
[279] M. A. Nasseri, Z. Rezazadeh, M. Kazemnejadi and A. Allahresani, *Catal. Lett.* **2021**, *151*, 1049-1067.
[280] F. Han, W. Sun, C. Xia and C. Liu, *Alcohol as a Reagent in Homogeneous Catalysis*, **2017**, pp. 403-447.
[281] S. Bera, L. M. Kabadwal and D. Banerjee, *Chem. Soc. Rev.* **2024**, *53*, 4607-4647.
[282] G. McDonnell and A. D. Russell, *Clin. Microbiol. Rev.* **1999**, *12*, 147-179.

[283] M. Waser, *Asymmetric Organocatalysis in Natural Product Syntheses*, (Ed. M. Waser), Springer Vienna, Vienna, **2012**, pp. 1-5.
[284] N. M. Yoon, *Pure & Appl. Chem.* **1996**, *68*, 843-848.
[285] R. C. Hoye, *J. Chem. Educ.* **1999**, *76*, 33-34.
[286] H.-U. Blaser, F. Spindler and M. Thommen, *Industrial Applications*, **2006**, pp. 1279-1324.
[287] N. Steinfeldt and K. Junge, *2.1 Reduction of Aldehydes*, *Vol. 2017/6*, Georg Thieme Verlag KG, Stuttgart, **2018**.
[288] D. Wang and D. Astruc, *Chem. Rev.* **2015**, *115*, 6621-6686.
[289] T. Ikariya and A. J. Blacker, *Acc. Chem. Res.* **2007**, *40*, 1300-1308.
[290] A. Dubey and E. Khaskin, *ACS Catal.* **2016**, *6*, 3998-4002.
[291] Y. Koto, F. Shibahara and T. Murai, *Chem. Lett.* **2016**, *45*, 1327-1329.
[292] X. Zhang, J. Chen, R. Khan, G. Shen, Z. He, Y. Zhou and B. Fan, *Org. Biomol. Chem.* **2019**, *17*, 10142-10147.
[293] S. Kaufmann, M. Radius, E. Moos, F. Breher and P. W. Roesky, *Organometallics* **2019**, *38*, 1721-1732.
[294] Z. E. Clarke, P. T. Maragh, T. P. Dasgupta, D. G. Gusev, A. J. Lough and K. Abdur-Rashid, *Organometallics* **2006**, *25*, 4113-4117.
[295] X. Gong, H. Zhang and X. Li, *Tetrahedron Lett.* **2011**, *52*, 5596-5600.
[296] V. R. Landaeta, A. D. S.-L. Rosa and R. E. Rodríguez-Lugo, *Inorg. Chim. Acta* **2018**, *470*, 303-311.
[297] X. Quan, S. Kerdphon, B. B. C. Peters, J. Rujirawanich, S. Krajangsri, J. Jongcharoenkamol and P. G. Andersson, *Chem. Eur. J.* **2020**, *26*, 13311-13316.
[298] B. Longato, R. Coppo, G. Pilloni, C. Corvaja, A. Toffoletti and G. Bandoli, *J. Organomet. Chem.* **2001**, *637-639*, 710-718.
[299] H. W. Roesky, K. K. Panday, B. Krebs and M. Dartmann, *J. Chem. Soc., Dalton Trans.* **1984**, 2271-2273.
[300] A. Doddi, D. Bockfeld, T. Bannenberg and M. Tamm, *Chem. Eur. J.* **2020**, *26*, 14878-14887.
[301] S. J. Coles, P. N. Horton, P. Kimber, W. T. Klooster, P. Liu, F. Plasser, M. B. Smith and G. J. Tizzard, *Chem. Commun.* **2022**, *58*, 5598-5601.
[302] R. N. V. K. Deepak and R. Sankararamakrishnan, *Biophys. J.* **2016**, *110*, 1967-1979.
[303] V. K. Rai, M. Nishiura, M. Takimoto and Z. Hou, *J. Mater. Chem. C* **2014**, *2*, 5317-5326.
[304] C. Sahin, A. Goren and C. Varlikli, *J. Organomet. Chem.* **2014**, *772-773*, 68-78.
[305] L. Hua, M. Iwamura, S. Takeuchi and T. Tahara, *Phys. Chem. Chem. Phys.* **2015**, *17*, 2067-2077.
[306] M. Xie, Y. Zhou, H. Zhou, C. Ma, Q. Sun, S.-T. Zhang, Y. Zhang, W. Yang and S. Xue, *Chem. Sci.* **2024**, *15*, 5589-5595.
[307] M. G. Colombo, A. Hauser and H. U. Guedel, *Inorg. Chem.* **1993**, *32*, 3088-3092.
[308] I. Soriano-Díaz, E. Ortí and A. Giussani, *Inorg. Chem.* **2021**, *60*, 13222-13232.
[309] I. Soriano-Díaz, E. Ortí and A. Giussani, *Dalton Trans.* **2023**, *52*, 10437-10447.
[310] S. Dhar, D. K. Rana, S. Singha Roy, S. Roy, S. Bhattacharya and S. C. Bhattacharya, *J. Lumin.* **2012**, *132*, 957-964.
[311] Y. Shi, T. Zhang, X. M. Jiang, G. Xu, C. He and C. Duan, *Nat. Commun.* **2020**, *11*, 5384.
[312] P. de Frémont, N. M. Scott, E. D. Stevens and S. P. Nolan, *Organometallics* **2005**, *24*, 2411-2418.
[313] T. Dröge and F. Glorius, *Angew. Chem. Int. Ed.* **2010**, *49*, 6940-6952.
[314] J. D. Egbert, A. M. Z. Slawin and S. P. Nolan, *Organometallics* **2013**, *32*, 2271-2274.

[315] J. C. Y. Lin, R. T. W. Huang, C. S. Lee, A. Bhattacharyya, W. S. Hwang and I. J. B. Lin, *Chem. Rev.* **2009**, *109*, 3561-3598.
[316] F. Glorius, *N-Heterocyclic Carbenes in Transition Metal Catalysis* Springer, Heidelberg, **2007**, p. 232.
[317] M. N. Hopkinson, C. Richter, M. Schedler and F. Glorius, *Nature* **2014**, *510*, 485-496.
[318] S. Würtemberger-Pietsch, U. Radius and T. B. Marder, *Dalton Trans.* **2016**, *45*, 5880-5895.
[319] L. J. Murphy, K. N. Robertson, J. D. Masuda and J. A. C. Clyburne, *NHC Complexes of Main Group Elements: Novel Structures, Reactivity, and Catalytic Behavior*, **2014**, pp. 427-498.
[320] S. Hameury, P. de Frémont, P.-A. R. Breuil, H. Olivier-Bourbigou and P. Braunstein, *Organometallics* **2015**, *34*, 2183-2201.
[321] D. J. D. Wilson, S. A. Couchman and J. L. Dutton, *Inorg. Chem.* **2012**, *51*, 7657-7668.
[322] O. Kühl, *Chem. Soc. Rev.* **2007**, *36*, 592-607.
[323] A. T. Normand and K. J. Cavell, *Eur. J. Inorg. Chem.* **2008**, *2008*, 2781-2800.
[324] S. Gaillard and J.-L. Renaud, *Dalton Trans.* **2013**, *42*, 7255-7270.
[325] P. L. Chiu and H. M. Lee, *Organometallics* **2005**, *24*, 1692-1702.
[326] P. Nägele, U. Herrlich, F. Rominger and P. Hofmann, *Organometallics* **2013**, *32*, 181-191.
[327] P. Ai, A. A. Danopoulos, P. Braunstein and K. Y. Monakhov, *Chem. Commun.* **2014**, *50*, 103-105.
[328] F. Jean-Baptiste dit Dominique, H. Gornitzka, A. Sournia-Saquet and C. Hemmert, *Dalton Trans.* **2009**, 340-352.
[329] W.-H. Yang, C.-S. Lee, S. Pal, Y.-N. Chen, W.-S. Hwang, I. J. B. Lin and J.-C. Wang, *J. Organomet. Chem.* **2008**, *693*, 3729-3740.
[330] L. Ray, M. M. Shaikh and P. Ghosh, *Dalton Trans.* **2007**, 4546-4555.
[331] S. C. Seitz, F. Rominger and B. F. Straub, *Organometallics* **2013**, *32*, 2427-2434.
[332] C. Fliedel and P. Braunstein, *J. Organomet. Chem.* **2014**, *751*, 286-300.
[333] C. Kiefer, S. Bestgen, M. T. Gamer, M. Kühn, S. Lebedkin, F. Weigend, M. M. Kappes and P. W. Roesky, *Chem. Eur. J.* **2017**, *23*, 1591-1603.
[334] D. Yuan, H. Tang, L. Xiao and H. V. Huynh, *Dalton Trans.* **2011**, *40*, 8788-8795.
[335] A. John and P. Ghosh, *Dalton Trans.* **2010**, *39*, 7183-7206.
[336] C. Kiefer, S. Bestgen, M. T. Gamer, S. Lebedkin, M. M. Kappes and P. W. Roesky, *Dalton Trans.* **2015**, *44*, 13662-13670.
[337] J. Vila, M. Solà, T. Achard, S. Bellemin-Laponnaz, A. Pla-Quintana and A. Roglans, *ACS Catal.* **2023**, *13*, 3201-3210.
[338] S. Hameury, P. de Frémont and P. Braunstein, *Chem. Soc. Rev.* **2017**, *46*, 632-733.
[339] I. O. Koshevoy, L. Koskinen, M. Haukka, S. P. Tunik, P. Y. Serdobintsev, A. S. Melnikov and T. A. Pakkanen, *Angew. Chem. Int. Ed.* **2008**, *47*, 3942-3945.
[340] S.-K. Yip, C.-L. Chan, W. H. Lam, K.-K. Cheung and V. W.-W. Yam, *Photochem. Photobiol. Sci.* **2007**, *6*, 365-371.
[341] C. Sarcher, S. Bestgen, F. C. Falk, S. Lebedkin, J. Paradies and P. W. Roesky, *J. Organomet. Chem.* **2015**, *795*, 11-17.
[342] C. Sarcher, A. Lühl, F. C. Falk, S. Lebedkin, M. Kühn, C. Wang, J. Paradies, M. M. Kappes, W. Klopper and P. W. Roesky, *Eur. J. Inorg. Chem.* **2012**, *2012*, 5033-5042.
[343] X. He and V. W.-W. Yam, *Coord. Chem. Rev.* **2011**, *255*, 2111-2123.
[344] R. Visbal and M. C. Gimeno, *Chem. Soc. Rev.* **2014**, *43*, 3551-3574.
[345] C. E. Strasser and V. J. Catalano, *J. Am. Chem. Soc.* **2010**, *132*, 10009-10011.
[346] M. Baron, C. Tubaro, A. Biffis, M. Basato, C. Graiff, A. Poater, L. Cavallo, N. Armaroli and G. Accorsi, *Inorg. Chem.* **2012**, *51*, 1778-1784.

[347] T. Scattolin, G. Tonon, E. Botter, S. G. Guillet, N. V. Tzouras and S. P. Nolan, *Chem. Eur. J.* **2023**, *29*, e202301961.
[348] D. Iacopetta, J. Ceramella, C. Rosano, A. Mariconda, M. Pellegrino, M. Sirignano, C. Saturnino, A. Catalano, S. Aquaro, P. Longo and M. S. Sinicropi, *Appl. Sci.* **2021**, *11*, 5626.
[349] J. Belza, Z. Trávníček, J. Vančo, M. Čajan, J. Hošek and Z. Dvořák, *Organometallics* **2024**, *43*, 1155-1164.
[350] T. Zou, C.-N. Lok, P.-K. Wan, Z.-F. Zhang, S.-K. Fung and C.-M. Che, *Curr. Opin. Chem. Biol.* **2018**, *43*, 30-36.
[351] A. D'Amato, D. Iacopetta, J. Ceramella, R. Troiano, A. Mariconda, A. Catalano, M. Marra, C. Saturnino, C. Rosano, M. S. Sinicropi and P. Longo, *Eur. J. Med. Chem.* **2024**, *277*, 116757.
[352] D. Cao, Z. Liu, P. Verwilst, S. Koo, P. Jangjili, J. S. Kim and W. Lin, *Chem. Rev.* **2019**, *119*, 10403-10519.
[353] B. Xu, J. Yang, X. Jiang, Y. Wang, H. Sun and J. Yin, *J. Mol. Struct.* **2009**, *917*, 15-20.
[354] H. Abbas, *Comput. Theor. Chem.* **2012**, *992*, 55-58.
[355] B. Bertrand, A. de Almeida, E. P. M. van der Burgt, M. Picquet, A. Citta, A. Folda, M. P. Rigobello, P. Le Gendre, E. Bodio and A. Casini, *Eur. J. Inorg. Chem.* **2014**, *2014*, 4532-4536.
[356] K. N. Brinda, Z. Yhobu, J. G. Małecki, R. S. Keri, R. G. Balakrishna, D. H. Nagaraju and S. Budagumpi, *Int. J. Hydrogen Energy* **2023**, *48*, 10911-10921.
[357] G. Achar, S. C. R, S. A. Patil, J. G. Małecki and S. Budagumpi, *New J. Chem.* **2019**, *43*, 1216-1229.
[358] V. R. Naina, S. Gillhuber, C. Ritschel, D. Jin, Shubham, S. Lebedkin, C. Feldmann, F. Weigend, M. M. Kappes and P. W. Roesky, *Angew. Chem. Int. Ed.* **2025**, *64*, e202414517.
[359] V. R. Naina in *Coumarin based coinage metal complexes: Synthesis, luminescence and cytotoxicity studies*, *Vol.* Karlsruhe Institute of Technology, Cuvillier Verlag, Göttingen, **2023**.
[360] V. R. Naina, A. K. Singh, Shubham, F. Krätschmer, S. Lebedkin, M. M. Kappes and P. W. Roesky, *Dalton Trans.* **2023**, *52*, 12618-12622.
[361] H. Petersen, M. Ballmann, N. Krause and R. Weberskirch, *ChemCatChem* **2022**, *14*, e202200727.
[362] D.-H. Lee, J.-H. Kim, B.-H. Jun, H. Kang, J. Park and Y.-S. Lee, *Org. Lett.* **2008**, *10*, 1609-1612.
[363] S. Gaillard, A. M. Z. Slawin, A. T. Bonura, E. D. Stevens and S. P. Nolan, *Organometallics* **2010**, *29*, 394-402.
[364] D. Tapu, D. A. Dixon and C. Roe, *Chem. Rev.* **2009**, *109*, 3385-3407.
[365] H. V. Huynh, Y. Han, R. Jothibasu and J. A. Yang, *Organometallics* **2009**, *28*, 5395-5404.
[366] P. de Frémont, R. Singh, E. D. Stevens, J. L. Petersen and S. P. Nolan, *Organometallics* **2007**, *26*, 1376-1385.
[367] S. Orbisaglia, B. Jacques, P. Braunstein, D. Hueber, P. Pale, A. Blanc and P. de Frémont, *Organometallics* **2013**, *32*, 4153-4164.
[368] P. de Frémont, E. D. Stevens, M. R. Fructos, M. Mar Díaz-Requejo, P. J. Pérez and S. P. Nolan, *Chem. Commun.* **2006**, 2045-2047.
[369] P. de Frémont, N. Marion and S. P. Nolan, *J. Organomet. Chem.* **2009**, *694*, 551-560.
[370] R. Galassi, N. Sargentoni, L. Luciani, G. Manca and A. Ienco, *Inorg. Chim. Acta* **2024**, *560*, 121810.
[371] T. Söhnel, R. Brown, L. Kloo and P. Schwerdtfeger, *Chem. Eur. J.* **2001**, *7*, 3167-3173.
[372] V. W.-W. Yam and A. S.-Y. Law, *Coord. Chem. Rev.* **2020**, *414*, 213298.
[373] L. V. Inerrante and R. P. Messmer, *Inorg. Chem.* **1971**, *10*, 1174-1180.
[374] K. Cser and I. Vass, *Biochim. Biophys. Acta* **2007**, *1767*, 233-243.

[375] P.-A. Yin, Q. Wan, Y. Niu, Q. Peng, Z. Wang, Y. Li, A. Qin, Z. Shuai and B. Z. Tang, *Adv. Electron. Mater.* **2020**, *6*, 2000255.
[376] C. A. Smith, M. R. Narouz, P. A. Lummis, I. Singh, A. Nazemi, C.-H. Li and C. M. Crudden, *Chem. Rev.* **2019**, *119*, 4986-5056.
[377] A. Doddi, M. Peters and M. Tamm, *Chem. Rev.* **2019**, *119*, 6994-7112.
[378] Y. Pan, X. Jiang, Y.-M. So, C. T. To and G. He, *Catalysts* **2020**, *10*, 71.
[379] I. Ott, *Chapter 4 - Metal N-heterocyclic carbene complexes in medicinal chemistry*, *Vol. 75*, (Eds.: P. J. Sadler and R. van Eldik), Academic Press, **2020**, pp. 121-148.
[380] K. V. S. Ranganath, S. Onitsuka, A. K. Kumar and J. Inanaga, *Catal. Sci. Technol.* **2013**, *3*, 2161-2181.
[381] P. Schwab, R. H. Grubbs and J. W. Ziller, *J. Am. Chem. Soc.* **1996**, *118*, 100-110.
[382] P. Schwab, M. B. France, J. W. Ziller and R. H. Grubbs, *Angew. Chem. Int. Ed.* **1995**, *34*, 2039-2041.
[383] J. S. Kingsbury, J. P. A. Harrity, P. J. Bonitatebus and A. H. Hoveyda, *J. Am. Chem. Soc.* **1999**, *121*, 791-799.
[384] S. B. Garber, J. S. Kingsbury, B. L. Gray and A. H. Hoveyda, *J. Am. Chem. Soc.* **2000**, *122*, 8168-8179.
[385] J. A. Love, J. P. Morgan, T. M. Trnka and R. H. Grubbs, *Angew. Chem. Int. Ed.* **2002**, *41*, 4035-4037.
[386] T.-L. Choi and R. H. Grubbs, *Angew. Chem. Int. Ed.* **2003**, *42*, 1743-1746.
[387] P. Baczewska, K. Śniady, W. Kośnik and M. Michalak, *Catalysts* **2021**, *11*, 972.
[388] C. Malchau, D. V. Fries, Y. Mees, M. F. Jakobs, Y. Sun, S. Becker, G. Niedner-Schatteburg and W. R. Thiel, *Eur. J. Inorg. Chem.* **2022**, *2022*, e202200106.
[389] T. Scattolin and S. P. Nolan, *Trends Chem.* **2020**, *2*, 721-736.
[390] E. A. Martynova, N. V. Tzouras, G. Pisanò, C. S. J. Cazin and S. P. Nolan, *Chem. Commun.* **2021**, *57*, 3836-3856.
[391] H. D. Velazquez and F. Verpoort, *Chem. Soc. Rev.* **2012**, *41*, 7032-7060.
[392] P. P. Nair, A. Jayaraj and C. A. Swamy P, *ChemistrySelect* **2022**, *7*, e202103517.
[393] M. O. Karataş, A. Di Giuseppe, V. Passarelli, B. Alici, J. J. Pérez-Torrente, L. A. Oro, I. Özdemir and R. Castarlenas, *Organometallics* **2018**, *37*, 191-202.
[394] O. Halter and H. Plenio, *Eur. J. Inorg. Chem.* **2018**, *2018*, 2935-2943.
[395] J. M. Praetorius and C. M. Crudden, *Dalton Trans.* **2008**, 4079-4094.
[396] J. P. Morales-Cerón, P. Lara, J. López-Serrano, L. L. Santos, V. Salazar, E. Álvarez and A. Suárez, *Organometallics* **2017**, *36*, 2460-2469.
[397] G. Rivera, D. Ramírez, O. Martínez, S. Bernès, D. Garcia and J. Yreta, *J. Organomet. Chem.* **2025**, *1036*, 123718.
[398] R. Manguin, M. Galiana-Cameo, T. Kittikool, C. Barthes, J. Thongpaen, E. Bancal, S. Mallet-Ladeira, S. Yotphan, R. Castarlenas, M. Mauduit, J.-B. Sortais and O. Baslé, *Chem. Commun.* **2023**, *59*, 4193-4196.
[399] G. Sipos and R. Dorta, *Coord. Chem. Rev.* **2018**, *375*, 13-68.
[400] T. Rehm, M. Rothemund, J. K. Muenzner, A. Noor, R. Kempe and R. Schobert, *Dalton Trans.* **2016**, *45*, 15390-15398.
[401] E. Ö. Karaca, O. Çiftçi, İ. Özdemir, G. Yakali, M. Aygün, N. Gürbüz and İ. Özdemir, *Appl. Organomet. Chem.* **2019**, *33*, e4851.
[402] M. S. Viciu, O. Navarro, R. F. Germaneau, R. A. Kelly, W. Sommer, N. Marion, E. D. Stevens, L. Cavallo and S. P. Nolan, *Organometallics* **2004**, *23*, 1629-1635.

[403] M. Kaloğlu, N. Gürbüz, D. Sémeril and İ. Özdemir, *Eur. J. Inorg. Chem.* **2018**, *2018*, 1236-1243.
[404] X. Ma, S. G. Guillet, M. Peng, K. Van Hecke and S. P. Nolan, *Dalton Trans.* **2021**, *50*, 3959-3965.
[405] P. Cantero-López, D. Páez-Hernández and R. Arratia-Pérez, *Chem. Phys. Lett.* **2017**, *685*, 60-68.
[406] M. Heindl, J. Hongyan, S.-A. Hua, M. Oelschlegel, F. Meyer, D. Schwarzer and L. González, *Inorg. Chem.* **2021**, *60*, 1672-1682.
[407] S. Mai and L. González, *Chem. Sci.* **2019**, *10*, 10405-10411.
[408] J. E. Lewis and M. Maroncelli, *Chem. Phys. Lett.* **1998**, *282*, 197-203.
[409] P. Roy, F. Al-Kahtani, A. N. Cammidge and S. R. Meech, *J. Phys. Chem. Lett.* **2023**, *14*, 253-259.
[410] X. Zhang, Y. Wang and Z. Zhang, *J. Lumin.* **2024**, *267*, 120349.
[411] L. Stojanović and R. Crespo-Otero, *J. Phys. Chem. C* **2020**, *124*, 17752-17761.
[412] Y. Li, L. Jiang, W. Liu, S. Xu, T.-Y. Li, F. Fries, O. Zeika, Y. Zou, C. Ramanan, S. Lenk, R. Scholz, D. Andrienko, X. Feng, K. Leo and S. Reineke, *Adv. Mater.* **2021**, *33*, 2101844.
[413] I. Bhattacharjee, K. Hayashi and S. Hirata, *JACS Au* **2021**, *1*, 945-954.
[414] M. Gao, L. Yu, Q. Lv, F. Kang, Z.-H. Huang and R. Lv, *J. Materiomics* **2023**, *9*, 768-786.
[415] T. S. Jagodziński, *Chem. Rev.* **2003**, *103*, 197-228.
[416] T. Murai, *Thio-, Seleno-, Telluro-Amides*, (Ed. S. Kato), Springer Berlin Heidelberg, Berlin, Heidelberg, **2005**, pp. 247-272.
[417] R. C. Neuman, D. N. Roark and V. Jonas, *J. Am. Chem. Soc.* **1967**, *89*, 3412-3416.
[418] T. Lincke, S. Behnken, K. Ishida, M. Roth and C. Hertweck, *Angew. Chem. Int. Ed.* **2010**, *49*, 2011-2013.
[419] J. M. Goldberg, X. Chen, N. Meinhardt, D. C. Greenbaum and E. J. Petersson, *J. Am. Chem. Soc.* **2014**, *136*, 2086-2093.
[420] Tran, J. Zeng, H. Treutlein and A. W. Burgess, *J. Am. Chem. Soc.* **2002**, *124*, 5222-5230.
[421] H. Wang, L. Wang, J. Shang, X. Li, H. Wang, J. Gui and A. Lei, *Chem. Commun.* **2012**, *48*, 76-78.
[422] M. Iwata, R. Yazaki, I. H. Chen, D. Sureshkumar, N. Kumagai and M. Shibasaki, *J. Am. Chem. Soc.* **2011**, *133*, 5554-5560.
[423] M. A. Malik and P. O'Brien, *Chem. Mater.* **1991**, *3*, 999-1000.
[424] M. B. Hursthouse, M. A. Malik, M. Motevalli and P. O'Brien, *J. Mater. Chem.* **1992**, *2*, 949-955.
[425] M. Motevalli, P. O'Brien, J. R. Walsh and I. M. Watson, *Polyhedron* **1996**, *15*, 2801-2808.
[426] H. S. I. Sullivan, J. D. Parish, P. Thongchai, G. Kociok-Köhn, M. S. Hill and A. L. Johnson, *Inorg. Chem.* **2019**, *58*, 2784-2797.
[427] M. E. Robson and A. L. Johnson, *Dalton Trans.* **2024**, *53*, 11380-11392.
[428] K. Löhnwitz, M. J. Molski, A. Lühl, P. W. Roesky, M. Dochnahl and S. Blechert, *Eur. J. Inorg. Chem.* **2009**, *2009*, 1369-1375.
[429] I. Hartenbach and T. Schleid, *J. Solid State Chem.* **2003**, *171*, 382-386.
[430] H. Xiong, J. Xie and J. Dong, *Phys. Lett. A* **2020**, *384*, 126910.
[431] Y.-R. Xi, C.-C. Xu, S.-J. Yang, S.-C. Wang, W.-C. Sun, X.-K. Chen, G.-M. Tang, Y.-T. Wang and T. An, *J. Mol. Struct.* **2023**, *1272*, 134044.
[432] S. Karmegam, M. Kolikkaje and S. D. George, *J. Phys. Chem. C* **2024**, *128*, 14709-14716.
[433] S. van Bezouw, D. H. Arias, R. Ihly, S. Cambré, A. J. Ferguson, J. Campo, J. C. Johnson, J. Defillet, W. Wenseleers and J. L. Blackburn, *ACS Nano* **2018**, *12*, 6881-6894.

[434] K. Zhou, B. Qi, Z. Liu, X. Wang, Y. Sun and L. Zhang, *Adv. Funct. Mater.* **2024**, *34*, 2411671.
[435] A. Kolmakov, V. Stankevitch, N. Svechnikov, P. Dudin, N. Artemev, H. Berger, G. Clerc, G. Margaritondo, M. Kamada, S. Hirose, K. Kanno, I. Akimoto and T. Matsumoto, *J. Electron. Spectrosc. Relat. Phenom.* **1996**, *78*, 449-452.
[436] T. S. Prathima, K. Chanda and B. Mm, *Inorg. Chim. Acta* **2024**, *567*, 122038.
[437] Y.-H. Mao, M.-K. Hung, S.-T. Chung, S. Sharma, K.-W. Tsai and S.-A. Chen, *ACS Appl. Mater. Interfaces* **2024**, *16*, 60715-60731.
[438] G. Sheldrick, *Acta Crystallogr. C* **2015**, *71*, 3-8.
[439] G. Sheldrick, *Acta Crystallogr. A* **2008**, *64*, 112-122.
[440] O. V. Dolomanov, L. J. Bourhis, R. J. Gildea, J. A. K. Howard and H. Puschmann, *J. Appl. Crystallogr.* **2009**, *42*, 339-341.

8. Appendix

8.1 General abbreviations

λ	wavelength
°	degree
μM	micromolar
μs	microsecond
ΔE	energy difference
τ	lifetime
Å	angstrom
AACVD	aerosol-assisted chemical vapor deposition
Ar	aryl
ca.	approximately
CAAC	cyclic amino alkyl carbene
COD	1,5-cyclooctadiene
Coum	coumarin
CVD	chemical vapor deposition
DCM	dichloromethane
DippNHC	*N*,*N*'-2,6-bis(disopropylphenyl)imi-dazol-2-ylidene
DMSO	dimethylsulfoxide
eq.	equivalent
ESI	electro spray ionization
et al.	and co-workers
eV	electron volt
h	hour
HOMO	highest occupied molecular orbital
HRESI-MS	high resolution electro spray ionization mass spectrometry
HSAB	hard-soft acid-base
IC	internal conversion
i-PrNHC	*N*,*N*'-diisopropylimidazol-2-ylidene
IR	infrared
ISC	inter system crossing
K	kelvin
KC_8	potassium graphite
kg	kilogram
LUMO	lowest unoccupied molecular orbital

Mes	mesityl
MLCT	metal to ligand charge transfer
mM	millimolar
mmol	millimole
ms	millisecond
MS	mass spectrometry
NHC	*N*-heterocyclic carbene
nm	nanometer
NMR	nuclear magnetic resonance
NON	4,5-bis(2,6-diisopropylanilido)-2,7-di-*tert*-butyl-9,9-dimethylxanthene
OLED	organic light emitting diode
Ph	phenyl
PL	photoluminescence
PLE	photoluminescence excitation
PPh_3	triphenylphosphine
ps	picosecond
$PyPPh_2$	diphenyl-2-pyridylphosphine
rISC	reverse inter system crossing
SC-XRD	single crystal X-ray diffraction
S_n	singlet state
TADF	thermally activated delayed fluorescence
t-Bu	tertiary butyl
TEP	Tolman electronic parameter
TH	transfer hydrogenation
THF	tetrahydrofuran
THT	tetrahydrothiophene
TMEDA	tetramethylethylenediamine
TMS	trimethylsilyl
T_n	triplet state
UV	ultraviolet
Vis	visible
VR	vibrational relaxation
VT	variable temperature

8.2 NMR abbrevitations

MHz	megahertz
s	singlet
bs	broad singlet
d	doublet
dd	doublet of doublet
t	triplet
hep	heptate
J	coupling constant
m	multiplet
ppm	parts per million
δ	chemical shift

8.3 IR abbrevitations

br	broad
m	medium
s	strong
sh	shoulder
vs	very strong
w	weak

Curriculum Vitae (CV)

Name	Shubham
Date of birth	05.08.1999
Place of birth	Dehra, Himachal Pradesh (India)
Marital status	Single
Gender	Male
Nationality	Indian

Education

11/2021 - present	Ph. D. in Chemistry Institute of Inorganic Chemistry, Karlsruhe Institute of Technology (KIT), Karlsruhe, Germany Supervisor: Prof. Peter W. Roesky
06/2019 - 05/2021	Master of science in Chemistry Indian Institute of Technology, Delhi, (IITD) India Master thesis: “Synthesis of air and water stable low-valent germanium compounds”
07/2016 - 05/2019	Bachelor of science in Chemistry Panjab University (PU), Chandigarh, India

Conferences

1. 26.09.2022-28.09.2022: 21st Conference on Inorganic Chemistry, Marburg, Germany.
   Poster presentation: “Bisamidinate Ligand Stabilized Early-Late-Hetero-Tetranuclear Group IV-Au(I) Luminescent Complexes”; Shubham, C. Uhlmann, T. J. Feuerstein, T. P. Seifert, M. T. Gamer, R. Köppe, M. M. Kappes, P. W. Roesky.
2. 03.09.2023-07.09.2023: 6th EuChemS Inorganic Chemistry Conference, Vienna, Austria.
   Poster presentation: “Synthesis and Photophysical Properties of Phosphine Acetylide Amidinate Stabilized Copper(I) and Gold(I) Heterobimetallic Complexes”; Shubham, V. R. Naina, P. W. Roesky.
3. 14.07.2024-18.07.2024: 30th International Conference on Organometallic Chemistry, Agra, India.
   Poster presentation: “Synthesis and Photophysical Properties of Phosphine Acetylide Amidinate Stabilized Cu(I) and Au(I) Heterobimetallic Complexes”; Shubham, V. R. Naina, P. W. Roesky.
4. 16.09.2024-18.09.2024: 22nd Conference on Inorganic Chemistry, Munich, Germany.
   Poster presentation: “Luminescent Tetranuclear Cu(I) and Au(I) Heterobimetallic Complexes: A Phosphine Acetylide Amidinate Orthogonal Ligand Framework for Selective Complexation”; Shubham, V. R. Naina, P. W. Roesky.

Publications

1. V. R. Naina, A. K. Singh, Shubham, F. Krätschmer, S. Lebedkin, M. M. Kappes and P. W. Roesky, *Dalton Trans.* **2023**, *52*, 12618-12622. Heteroleptic Copper(I) Complexes with Coumarin-Substituted Aminodiphosphine and Diimine Ligands: Synthesis and Photophysical Studies.
2. Shubham, V. R. Naina and P. W. Roesky, *Chem. Eur. J.* **2024**, *30*, e202401696. Luminescent Tetranuclear Copper(I) and Gold(I) Heterobimetallic Complexes: A Phosphine Acetylide Amidinate Orthogonal Ligand Framework for Selective Complexation.
3. V. R. Naina, A. K. Singh, Shubham, J. Krämer, M. Iqbal and P. W. Roesky, *Inorg. Chem. Front.* **2024**, *11*, 6079-6088. Synthesis of Luminescent Coumarin-Substituted Phosphinoamide-Bridged Polynuclear Gold(I) Metallacycles and Reactivity Studies.
4. V. R. Naina, S. Gillhuber, C. Ritschel, D. Jin, Shubham, S. Lebedkin, C. Feldmann, F. Weigend, M. M. Kappes and P. W. Roesky, *Angew. Chem. Int. Ed.* **2025**, *64*, e202414517. Dye Induced Luminescence Properties of Gold(I) Complexes with Near Unity Quantum Efficiency.
5. Shubham, V. R. Naina, M. Iqbal and P. W. Roesky, Heterobimetallic Cu(I)-Rh(I) and Cu(I)-Ir(I) Complexes: Synthesis, Structural Characterization, Photophysical Studies and Catalytic Applications in Transfer Hydrogenation, Manuscript under preparation.

Acknowledgements

The acknowledgement section reminds me the past a few years of my Ph.D. I feel blessed that I have my colleagues, friends and family to support me throughout this journey.

Specifically, I want to thank…

…Prof. Dr. Peter W. Roesky for his guidance, constant support and encouragement during all the phases of my doctoral thesis. Without his supervision, I would not have found inspiration to work on various interesting topics. I am very grateful that I got an opportunity to pursue my doctoral studies in his working group.

…Prof. Dr. Silke Behrens for acting as the co-referee of my thesis.

…Dr. Michael Gamer for the help with solving crystal structures, providing the required glassware & deuterated solvents and for many other useful discussions.

…Sibylle Schneider for measuring my crystals and have patience to remeasure the bad ones. I am also grateful for all the absorption corrections done in time.

…Dr. Anna Stößer for helping me to chemicals; Petra Smie for recording mass spectrometry measurements, Ms. Kayas, Angie, Cornelia and Sing for their assistance with the paperwork; Ms. Berberich for the NMR measurements, Nicole Klassen for the elemental analyses, Mr. Munshi for repairing the glassware, Ms. Gabi for providing the chemicals and gas cylinders.

…All the current and former members of the Roesky group for their help and all the fun time. I especially want to thank…

…Vanitha for introducing me to the working environment here and helping me in and out of the lab. I am thankful for teaching me how to operate the instruments like UV-spectrometer, IR instrument and PL spectrometer.

…Dr. Akhil Kumar Singh and Dr. Debotra Sarkar for their help in my initial days.

…Iqbal for being a nice lab partner and all the discussions in general in and out of the lab. Even though we had arguments sometimes, it will not affect our bond.

…Sebastian, my first lab partner, for taking care of all the things in the lab and teach how to use the things properly. It would not be as entertaining in the lab without you.

…Aditi, Ria and Arjun for all the help and discussions about chemistry and also for the good times we had.

…Jin Da for being a good next lab neighbour and Xioafei Sun for discussions about chemistry and life.

…Elishua, Sebastian and Iqbal for proofreading my thesis.

…Steffi, Steven, Alicia, Nico, Maxim, David, Louis, Gerlinde and Victoria for all the breaks and discussions we had.

…Naina unwavering support and patience. Your help has been invaluable, and I truly believe that completing this work would not have been possible without you. I feel incredibly fortunate to have had you as my anchor throughout this journey.

…most importantly my family members without whom I wouldn´t have come so far in my life. Thank you for believing in me and my dreams and for all your love.